# Strain-tuned quantum dots and broadband photonic nanostructures for optical quantum information processing

Matteo Finazzer

## To cite this version:

Matteo Finazzer. Strain-tuned quantum dots and broadband photonic nanostructures for optical quantum information processing. Physics [physics]. Université Grenoble Alpes [2020-..], 2024. English. NNT : 2024GRALY014 . tel-04662572

HAL Id: tel-04662572
https://theses.hal.science/tel-04662572
Submitted on 26 Jul 2024

THÈSE

Pour obtenir le grade de

**DOCTEUR DE L'UNIVERSITÉ GRENOBLE ALPES**

École doctorale : PHYS - Physique
Spécialité : Physique de la Matière Condensée et du Rayonnement
Unité de recherche : PHotonique, ELectronique et Ingéniérie QuantiqueS

# Boîtes quantiques accordées par contrainte mécanique et nanostructures photoniques large bande pour le traitement quantique de l'information

# Strain-tuned quantum dots and broadband photonic nanostructures for optical quantum information processing

Présentée par :

**Matteo FINAZZER**

Direction de thèse :

| | |
|---|---|
| **Julien CLAUDON**<br>DIRECTEUR DE RECHERCHE, CEA - Centre de Grenoble | Directeur de thèse |
| **Jean-Michel GERARD**<br>INGENIEUR HDR, CEA CENTRE DE GRENOBLE | Co-encadrant de thèse |

Rapporteurs :

**OLIVIER KREBS**
DIRECTEUR DE RECHERCHE, CNRS DELEGATION ILE-DE-FRANCE SUD
**NICOLAS CHAUVIN**
CHARGE DE RECHERCHE HDR, CNRS DELEGATION RHONE AUVERGNE

Thèse soutenue publiquement le **5 mars 2024**, devant le jury composé de :

| | |
|---|---|
| **SIGNE SEIDELIN,**<br>PROFESSEURE DES UNIVERSITES, UNIVERSITE GRENOBLE ALPES | Présidente |
| **OLIVIER KREBS,**<br>DIRECTEUR DE RECHERCHE, CNRS DELEGATION ILE-DE-FRANCE SUD | Rapporteur |
| **NICOLAS CHAUVIN,**<br>CHARGE DE RECHERCHE HDR, CNRS DELEGATION RHONE AUVERGNE | Rapporteur |
| **ARMANDO RASTELLI,**<br>FULL PROFESSOR, JOHANNES-KEPLER-UNIVERSITÄT LINZ | Examinateur |
| **ISABELLE ROBERT-PHILIP,**<br>DIRECTRICE DE RECHERCHE, CNRS DELEGATION OCCITANIE EST | Examinatrice |

# Contents

# Introduction

Quantum information is a dynamic field that exploits the rules of quantum mechanics for information processing. A classical computer uses bits that are either in the 0 or 1 logical state. In contrast, a quantum bit is encoded on a two-level quantum system and can exist in a superposition of logical states. Furthermore, the application of the superposition principle to ensembles of qubits allows for entanglement, the creation of quantum correlation between various qubits. This allows for parallel computation and potentially solving certain problems much faster than classical computers [80]. In addition, a controlled quantum system can be leveraged to simulate another less-controlled system, and access important observables. Finally, flying qubits (possibly entangled) are also key to establish long haul quantum communications [47].

A qubit can be encoded on a matter system, that can belong either to the field of diluted atomic and molecular systems or to the field of condensed-matter. Prominent atomic systems include ions confined in an electrostatic trap [27] and individual Rydberg atoms trapped in arrays of optical tweezers [3]. Important condensed-matter systems include Josephson superconducting circuits [92] and spins carried by atomic impurities or trapped in QDs [78].

Alternatively, a qubit can be encoded on an optical field. One typically distinguishes continuous variables encoding (based on field quadratures) [25] and discrete variable encoding (based on photons) [94]. In the latter case, the quantum states are represented in finite-dimensional Hilbert spaces. Discrete photonic qubits can be encoded in polarization, path, time-bin, or even a combination of those. Like other quantum particles, photons can exist in superposition and entangled state, which is a crucial property for quantum communication and quantum computation protocols.

Optical photons are indeed very attractive flying qubits. They can travel over long distances without undergoing significant decoherence, making them ideally-suited for quantum communication protocols. For this reason photons are the workhorse of quantum key distribution (QKD), a technique that leverages the principles of quantum mechanics to secure communication channels [47]. QKD allows two parties to share a secret key securely, as any attempt to eavesdrop on the communication would disturb the quantum state, alerting the users to potential security breaches. In recent years there were a number of spectacular demonstrations of QKD ranging from fiber optics [173] to free space utilizing a satellite [110].

Quantum simulation is another promising field for photonic based quantum technologies. As a first example, ”boson sampling” is a quite specific quantum computational task which involves the sampling of the probability distribution of identical bosons scattered by a linear interferometer [1]. Simulating this process is highly demanding for classical computers, and belongs to the class of #P-hard problems [189]. That is however much easier handled by a quantum computer, and represents a first important benchmark for a quantum computing platform [26, 168, 178, 41, 29, 28, 166]. The photonic platform is well-suited for this task as the computation is performed by sending indistinguishable photons through a complex network of beam splitters: ideally the computational time is thus just the time taken by the photons to traverse the device and be detected (and acquiring sufficient statistics). In reality photon losses and decoherence in the system can result in an erroneous computation which must be repeated and thus lead to overall longer computational times.

More generally it has been shown that it is possible to achieve universal quantum computation via linear optics manipulation of the photons and single-photon detection [2, 93]. This paradigm is known as linear optic quantum computing (LOQC). Its main advantage is its simplicity: quantum gates only require beam splitters, phase shifters and single-photon detectors. LOQC allows to ”bypass” the need of photon interaction by relying heavily on photon interference via the Hong Ou Mandel (HOM) effect (which requires single photons with a high degree of indistinguishability). This has sprout efforts to develop programmable photonic quantum computers [13, 119, 108, 8, 23, 76, 42, 174]. Globally, the field benefits from the fast progress of integrated photonics [144]. Nevertheless LOQC is considered as poorly scalable, due to the limited reliability of the quantum gates. In order to solve this problem error correction mechanism are employed but they require large resource overheads. On the other hand significant efforts are conducted to implement photon interaction as a base for quantum computation. This can be achieved through the use of nonlinear crystals or other materials that exhibit non-linear optical effects [69, 111, 121] and could lead to more reliable quantum gates.

In this context, the ability to generate single-photon wavepackets with a high rate is crucial. Moreover these photons need to be in a pure quantum state (no multi-photon pulses) and indistinguishable from one another (same spatial and temporal mode). The development of single-photon sources follows two main tracks: i) heralded generation with a nonlinear process and ii) on-demand emission using artificial atoms.

For a long time, nonlinear sources of single photons have been the workhorse of quantum optics. They rely either on spontaneous parametric down conversion (SPDC), a $\chi^{(2)}$ process, or on four wave mixing (FWM), a $\chi^{(3)}$ process. For example, in SPDC a single photon from a pump laser beam incident on a nonlinear crystal generates two entangled photons. The generation is inherently probabilistic: the generation of entangled photon pairs for every incident photon is not guaranteed. However, when a pair is generated, the detection of one photon can be used to signal the presence of the other (heralding), effectively creating single-photon pulses [90]. These sources can operate at ambient temperature and offer a great photon indistinguishability. However, the number of generated photon pairs per pulse depends on the intensity of the input laser pulses and can be greater than one. To limit the probability of multipair emission, the input laser needs to be weak enough to generate mainly 0 or 1 pair per pulse. There is thus an intrinsic trade-off between brightness (the rate of photon generation) and purity.

To overcome this limitation, one can employ solid-state artificial atoms to generate single photons [206]. Owing to the Pauli exclusion principle, the excited state of a two-level system can only accommodate one excitation. In optically-active systems, the radiative decay to the ground state then leads to the emission of a single photon. Examples of artificial atoms include atomic defects such as color centers in diamond [103] or silicon [149] and semiconductor QDs [128], which are the focus of this PhD thesis.

A QDs is a nanoscale structure consisting of a semiconductor material embedded in a semiconductor matrix with a larger bandgap. The QD provides a three-dimensional confinement for electrons, resulting in quantized energy levels, akin to the energy levels of electrons in an atom. The size of the QD directly influences the energy spacing between these levels, with smaller dots having larger energy spacings. We will focus here on epitaxial InAs/GaAs QDs, which are obtained from a self-assembly process. For a long time, they offered the best performance among QDs. Recently, other fabrication routes have also led to high-quality emitters. For example, one can cite GaAs/AlGaAs QDs obtained from droplet etching and nanohole infilling [53] and InAsP/InP nanowire QDs [85]. At cryogenic temperature (4 K), eptiaxial QDs are remarkable solid-state emitters. They offer a close to unity radiative yield, a stable emission and a spectrally-narrow optical emission.

Nevertheless, building a single-photon source with a QD comes with several challenges. 1) Light extraction: A QD features a dipole-like emission pattern and is embedded in a large-index material. If nothing is done, only 2% of the emitted photons can be collected by a microscope objective. 2) Decoherence: as any solid-sate system, a QD is subject to various noises and unwanted interactions coming from the surrounding semiconductor crystal (phonons, fluctuating charge, fluctuating nuclear spins). These noises induce a spectral broadening of the QD transition and make the emitted photons distinguishable. 3) Emitter variability: the QD emission wavelength is extremely sensitive to the QD size. In general, two QDs will thus emit photons with distinct colours. This is a limitation for applications requiring the operation of several identical sources in parallel.

Challenge 3 can be addressed by using a tuning knob (e.g. electrical field, mechanical strain) to control the QD emission wavelength. Embedding the emitter in a photonic structure [116], such as a microcavity or a waveguide, allows addressing challenges 1 and 2. Microcavities are optical structures designed to resonantly enhance light-matter interactions. The selective acceleration of the spontaneous emission into the cavity mode — the famous Purcell effect — can be leveraged to dynamically funnel all the QD emission into the cavity mode. In addition, the global acceleration of the spontaneous emission process is particularly beneficial for improving the photon indistinguishability. However, microcavities offer a narrow operation bandwidth (as defined by the cavity spectral lineshape) which is not compatible with large emitter tuning. Waveguides, on the other hand, provide a broadband approach to light extraction. However, they typically lack the significant Purcell effect achieved in microcavities. This limitation hampers their ability to enhance the emission rate of quantum emitters. Nanocavities offer a best-of-both-worlds approach. Thanks to their ultrasmall mode volume, they provide a large Purcell acceleration with a modest optical quality factor ($Q$-factor) of about a few tens. This moderate $Q$-factor is advantageous for large operation bandwidth.

The quantum photonics team at CEA recently developed a new type of “nanopost” cavity, based on a segment of a photonic wire standing on a gold and silica mirror [97]. This design is the result of collaborative effort, with contributions from the group of Niels Gregersen (DTU, Denmark). A first generation of structures has been fabricated by Saptarshi Kotal and Alberto Artioli, former PhD student and postdoc in the team, respectively. They notably demonstrated the broadband Purcell acceleration of spontaneous emission, using a nonresonant optical excitation. During my PhD, I conducted the first demonstration of strictly resonant spectroscopy of a QD in a nanopost cavity. This was done during a stay (three months) in the group of Richard Warburton at Basel university. I conducted most of the experimental work and data analysis was done in collaboration with Maxime Gaignard (PhD student jointly supervised by Jean-Philippe Poizat and Julien Claudon). This is an important result since it proves the feasibility of resonant excitation and especially of the cross polarization rejection scheme on these small structures. In particular, it enables the fine optical characterization of the emitter (Finazzer$^\star$, Gaignard$^\star$ *et al.*, article in preparation).

The second axis of my PhD work aimed to tackle the challenge of tuning the emission wavelength of quantum dots without compromising their optical properties. To this end, I investigated QDs embedded in a tapered microwire (a ”photonic trumpet”) equipped with on-chip electrodes. Upon biasing with a DC voltage, an electrostatic force bends the photonic trumpet, which induces strain at the wire base where the quantum dots are embedded, enabling a controlled tuning of the emission wavelength. The device was also fabricated by Saptarshi Kotal and Alberto Artioli. Collaborating with Fabrice Donatini (Néel Institute), I conducted an in-depth study of the static tuning process. This work has been published recently (Finazzer *et al.*, Nano Lett. 2023).

Finally, on-chip electrodes also constitute an excellent tool to excite the vibration modes of a photonic trumpet. This capability is relevant for hybrid nanomechanics, a field that investigates the interaction of an artificial atom (here a quantum dot), with a mechanical resonator. We leveraged the broad operation bandwidth of the excitation scheme to investigate experimentally high-frequency resonances supported by the photonic trumpet. The study of dynamical actuation nicely complements and extends that of the static actuation. I contributed to this work, but the experimental effort was led by Rana Thanos (at the time postdoc in the team). A manuscript reporting this work was recently submitted (Tanos *et al.*, submitted).

The thesis is organized as follows:

In chapter 1 we explore the theoretical foundations of the artificial atom model, including discussions on the band structure of bulk semiconductors, the effects of confinement, the available states and their optical excitation. We also discuss the interaction of QDs with the surrounding environment, both as a source of noise and decoherence but also as mean to tune their properties. Finally we discuss the tailoring of spontaneous emission using photonic structures.

In chapter 2, we turn our attention to resonant excitation of QDs in nanopost cavities. With a detailed exploration of structure design, fabrication, and the theory of resonant excitation, we set the stage for experiments involving resonant linescans and intensity autocorrelation measurements.

In chapter 3, the spotlight turns to strain tuning of QDs embedded in a photonic wire antenna. Beginning with a theoretical background, we study an electrostatic actuation device and demonstrate energy shift of QD emission induced by mechanical strain. This experimental demonstration of strain tuning lays the foundation for practical applications in quantum photonic devices.

In chapter 4, our focus shifts to the electrostatic driving of nanowire vibration modes. We start with giving a theoretical background, exploring the principles of exciting vibration modes. We conduct extensive simulations which will guide the research into the experimental excitation and identification of vibration modes. We then push the research to high order modes approaching the sideband resolved regime.

# Chapter 1

# Quantum dots in photonic structures

## 1.1 Self-assembled quantums dots

This thesis work is centered around applications of QDs made of Indium Arsenide (InAs) that are embedded in a Gallium Arsenide (GaAs) matrix. Both materials are III-V semiconductors. These semiconductors are widely used in optoelectronics due to their direct and low energy bandgap, enabling efficient optical transitions.

### 1.1.1 Overview of the growth process

The most widespread method for obtaining self-assembled QDs is the Stranski-Krastanov method [68]. In the case of InAs/GaAs the principle is to grow InAs on a single-crystal, planar crystalline GaAs wafer. This growth is achieved by molecular beam epitaxy (MBE). Normally, growth occurs layer by layer, the surface remains flat: it is a two-dimensional growth. A typical case is GaAs/AlAs, as both materials have the same crystalline structure and lattice parameter. When we try to grow layers with different lattice parameters, initially, there is still 2D growth. However as the structure grows there is an accumulation of elastic energy due to the deformation of the epitaxial layer to adapt to the substrate's lattice parameter. There are two possible ways to relax: i) creation of a network of dislocations at the interface, ii) transitioning to a 3D geometry with the formation of nanometric islands.

For InAs/GaAs the lattice mismatch is $\approx 7\%$ and the predominant mechanis is the second one. The InAs layer initially adapts to the substrate, forming a coherent, planar layer on GaAs. Beyond a critical thickness of 1.7 InAs monolayers the stress due to lattice mismatch relaxes elastically

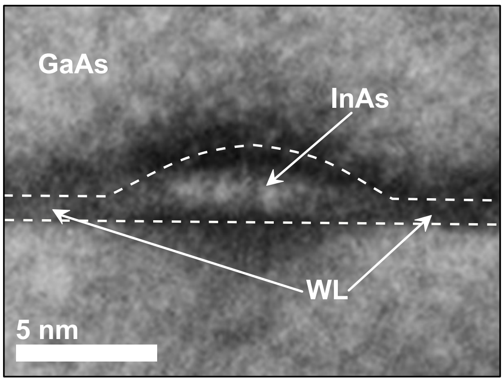

Figure 1.1: **TEM image of an InAs/GaAs QD cross-section.** In the image, we can identify the QD, with a the thin 2D InAs wetting layer (WL) on each side. The ensemble is embedded in GaAs. This image was obtained from A. Ponchet (CNRS/CEMES) Toulouse, captured on a sample fabricated by J.M. Gérard (France Télécom/CNET, 1993).

through a morphological transition. Three-dimensional islands appear on the residual 2D layer called the wetting layer. Once the InAs islands have been formed, they are covered (capped) by GaAs, which makes it possible to obtain optically-active structures called quantum dots. This encapsulation step modifies the morphology and composition of the dots due to the diffusion of GaAs into the InAs. Moreover the speed of the capping process influences the dimension and the symmetry of the dots [67].

### 1.1.2 Theoretical foundations of the artificial atom model

The theoretical study of the optical properties of QD is quite convoluted. In this section, we first introduce the properties of the bulk crystal. Then we can study the effect of confinement, both in the 2D wetting layer (WL) and into the 0D QD.

#### 1.1.2.1 Introduction to the band structure of bulk semiconductors

**The Bloch theorem.** GaAs and InAs are III-V direct bandgap semiconductors crystallizing in the Zinc-blende structure. Each unit cell consists of two atoms with 8 valence electrons. In principle we should solve the Schrödinger equation for all the atoms and the electrons of our system, but some clever approximation are made: first we consider a rigid crystal lattice (Born-Oppenheimer approximation) which allows to focus only on the electrons wavefunctions. Then, instead of solving the equations for all the electrons, we consider that every electron experiences an effective mean potential due to the lattice and all the other electrons (Hartree-Fock approximation). This leads to the equation:

$$\left(-\frac{\hbar^2}{2m}\nabla^2 + V(\mathbf{r})\right)\Psi(\mathbf{r}) = E\Psi(\mathbf{r}), \tag{1.1}$$

where the potential $V(\mathbf{r})$ is a periodic function with the same periodicity as the crystal lattice. From the Bloch theorem we know that the solutions of the eq. (1.1) can be written as:

$$\psi_{j,\mathbf{k}}(\mathbf{r}) = e^{-i\mathbf{k}\cdot\mathbf{r}}u_{j,\mathbf{k}}(\mathbf{r}). \tag{1.2}$$

The first factor is a plane wave, which characterizes translational invariance in the crystal, the second factor is the so called atomic function $u_{j,\mathbf{k}}(\mathbf{r})$, which has the same periodicity as the crystal lattice. So, plugging eq. (1.2) into eq. (1.1) we can derive an equation for the atomic functions:

$$\left(-\frac{\hbar^2}{2m}(\nabla - \mathbf{k})^2 + V(\mathbf{r})\right)u_{j,\mathbf{k}}(\mathbf{r}) = E_{j,\mathbf{k}}u_{j,\mathbf{k}}(\mathbf{r}). \tag{1.3}$$

For each value of $\mathbf{k}$ vector in the reciprocal lattice, there are thus many solutions indexed by $j$ with eigenvalues $E_{j,\mathbf{k}}$. The number of energy levels is high and define a band, that is the range of energy levels that electrons may occupy. For insulating materials and semiconductors, the bands are filled with electrons up to the top of the so-called valence band. The next-higher energy band is empty and is called the conduction band.

**Effective mass approximation.** GaAs and InAs are direct bandgap semiconductors, and the valence band maximum and the conduction band minimum lay at the same point $\Gamma$ that corresponds to the center of the Brillouin zone in $k$-space. To study the optical properties of these semiconductors we will consider transitions from the valence band to the conduction band. Since the momentum of optical photons is quite small all we need to know is the band structure in the vicinity of the $\Gamma$-point . In particular the energy around the $\Gamma$-point can be approximated by a Taylor expansion up to the second order. In the simple case of an isotropic k-dependence, this yields a parabolic approximation:

$$E_j(\mathbf{k}) \simeq E_j(0) + \left.\frac{\partial^2 E_j(\mathbf{k})}{\partial k^2}\right|_{\mathbf{k}=0} k^2. \tag{1.4}$$

The curvature of the parabola is given by the derivative term in eq. (1.4). Electron wavefunctions at the $\Gamma$-point are constructed as wavepackets of

Bloch functions and the curvature of the parabola controls the dispersion relation. This allows us to define an effective mass $m^*$ as:

$$\frac{\hbar^2}{2m^*} = \frac{\partial^2 E_j(\mathbf{k})}{\partial k^2}\bigg|_{\mathbf{k}=0}. \tag{1.5}$$

An electron in a band is thus characterized by his crystal momentum $\mathbf{k}$, the orbital angular momentum and his projection $|L, m_z\rangle$ and the spin with its projection $|\sigma, \sigma_z\rangle$. At the $\Gamma$-point, $\mathbf{k} = 0$ and the electronic states are completely described by the spin and angular momentum: $|L, m_z, \sigma, \sigma_z\rangle$.

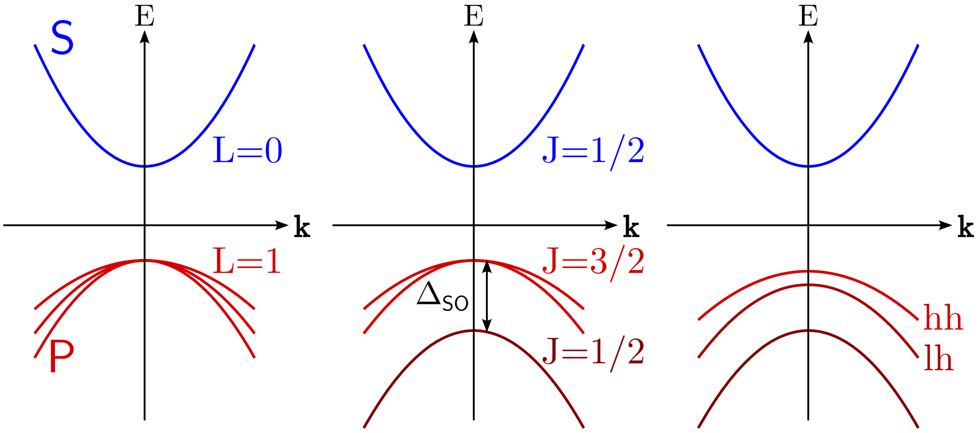

(a) (b) (c)

Figure 1.2: **Schematic representation of the band structure of an InAs crystal near the Γ point.** In **(a)** we see the band stucture before any correction is made. The conduction band is characterized by an orbital angular momentum of $L = 0$. The valence band has an orbital momentum $L = 1$ and features a threefold degeneracy. In **(b)** the spin-orbit coupling has the total angular momentum as eigenvalue. It partially removes the degeneracy of the valence band, pushing the doublet $J = \frac{1}{2}$ at lower energies. Finally in **(c)** the biaxial compressive stress splits the valence band in heavy-hole and light-holes, and increases the energy gap.

**Spin-orbit interaction.** For InAs the conduction band is characterized by $L = 0$; it is not degenerate and in an analogy with atomic physics is of type S. The valence band, however features $L = 1$; it is degenerate, with $m_z = -1, 0, 1$ it is thus of type P. The bands are shown in fig. 1.2.

Until now we have ignored the spin-orbit interaction, however in III-V materials the spin-orbit coupling is significant [146]. This is taken into account by the spin-orbit Hamiltonian:

$$\mathcal{H}_{SO} \propto \hat{L} \cdot \hat{\sigma}. \tag{1.6}$$

The total angular momentum $\hat{J} \equiv \hat{L} + \hat{\sigma}$ commutes with the spin-orbit Hamiltonian, so we can rewrite the electrons states in terms of the total angular momentum as $|J, j_z\rangle$. For the conduction band we have a doublet with $J = \frac{1}{2}$, while for the valence band we have the quadruplet $J = \frac{3}{2}$ and the doublet $J = \frac{1}{2}$. The effect of the spin-orbit is to lift the degeneracy between the quadruplet and the doublet, as shown in fig. 1.2b. The value of $\Delta_{SO}$ for GaAs is around 340meV [146], and thus we will ignore this band in the following.

The two remaining valence bands have different effective mass from which they are named heavy holes (hh) and light holes (lh) bands. The bi-axial compressive strain inherent to a self-assembled QD lifts the degeneracy between these two bands, as seen in fig. 1.2c [123]. In this case the splitting is of the order of several tens of meV [124]: it is important enough to allows us to consider just the heavy-hole band.

#### 1.1.2.2 Confinement and envelope function formalism

In the previous section we have shown how to describe the electrons in a bulk crystal in a simplified way. Our system actually consists of a QD, a 0D structure, a wetting layer, which provides a 2D confinement and a 3D GaAs matrix. In order to study the effects of confinement we use the envelope function formalism. It was first introduced by G. Bastard to study quantum well heterostructures and adapted next to quantum wire and QD heterostructures [14]. We expect our solution to be composed of three parts:

$$\Psi_{j,\mathbf{k}}(\mathbf{r}) = \Phi_{n,j}(\mathbf{r}) e^{i\mathbf{k}\cdot\mathbf{r}} u_{j,\mathbf{k}}(\mathbf{r}), \tag{1.7}$$

where the last two factors are like in eq. (1.2). The first factor is the envelope function, which results from the confinement of carriers in the nanostructure.

**Effect of confinement in the WL.** Let's start with the wetting layer. We can consider to a first approximation that it is perfectly smooth. In this case the charges are free to move in the $x$ and $y$ directions and confined in the $z$ direction. The envelope function only depends on $z$:

$$\Phi_{n,j}(\mathbf{r}) = \Phi_{n,j}(z), \tag{1.8}$$

which now corresponds to a localized state in the $z$ direction. The corresponding density of states thus has a stair-step profile. In the case of InAs/GaAs

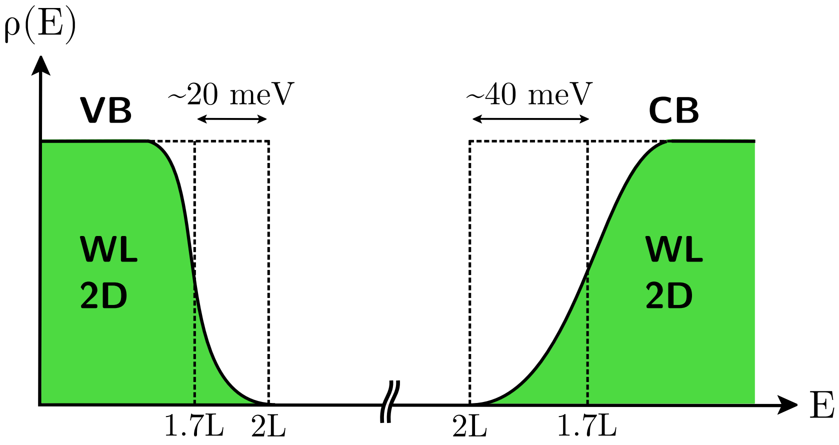

Figure 1.3: **Schematic representation of the density of states in the 2D wetting layer.** The rugosity of the wetting layer causes the step-like theoretical density to be smoothed out. As a reference, the dotted lines shows the theoretical position of the step for a perfect layer of thickness 1.7ML (the critical thickness), as shown in [67]. The figure is adapted from [30].

QD, the strong confinement along $z$ and the presence of bi-axial strain makes it possible to consider only heavy hole states for the valence band. Moreover, only the first $n = 1$ state is confined. The density of states thus features a single step.

In reality, the wetting layer is not perfectly smooth. It is made up of ”steps” of one to two atomic layers with an average value of 1.7 monolayers (ML). These defects behave like very flattened QDs. For a given band $j$ of the wetting layer it is necessary to then replace the 2D quasi-continuum by a distribution of more or less localized states [32, 143, 67]. This has the effect of softening the step profile of the ideal 2D density of states as illustrated in fig. 1.3.

**Effect of confinement in the QD.** As discussed at the beginning of this chapter a QD is a nanostructure that confines carriers in all three directions of space, leading to a discretization of accessible energy levels. The confinement potential associated with a realistic description of the QD is complex: self-assembled InAs/GaAs QDs generally have a flattened lens shape in the growth direction $z$ (the [001] direction of the crystal). In addition, they often exhibit ellipticity in the growth plane [31]. Moreover the composition is not uniform inside the QD, but rather it is made of InGaAs with different relative amounts of In and Ga across the structure. Even considering an in-plane rotational symmetry for the confinement potential, it is still not separable into a plane part and a vertical part due to the complex shape of the structure. This makes an analytical resolution impossible; a realistic calculation needs to be done numerically.

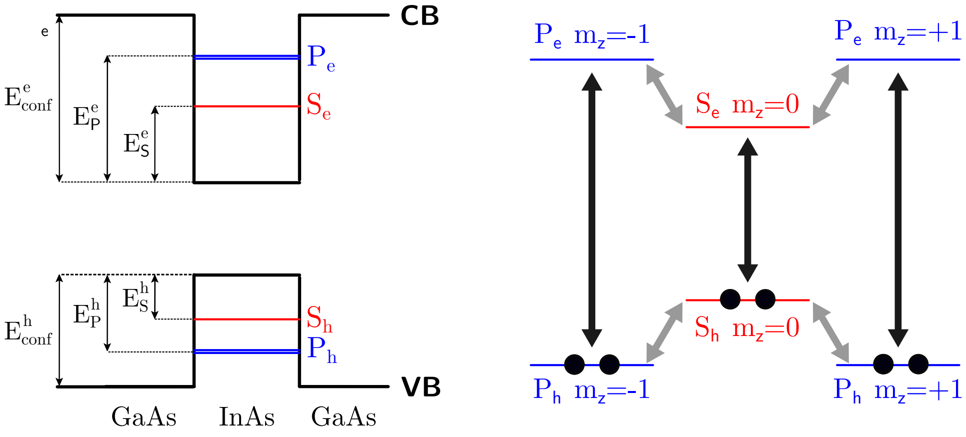

(a) (b)

Figure 1.4: **QD energy levels and allowed transitions.** **(a)** shows a simplified schematics of the QD energy levels. Note that VB corresponds to the heavy hole (hh) band of the strained material. We see that due to the shape and depth of the confinement potential only S and P states are available. For bigger QDs we can also have higher angular momentum levels (D). Dipole allowed transitions are shown in **(b)**. The transitions are divided in intraband (grey) and interband (black) and must satisfy selection rules dictated by symmetry and angular momentum conservation.

While a simplified treatment fails to precisely predict the energy levels, it can however illustrate the physics of the phenomena involved. Moreover a simplification can form the basis for a variational approach, as in [86]. The simpler way to approach the problem consists into treating the QD as a flattened cylinder. In this simplified geometry, the confinement potential is the product on an in-plane potential with a rotational symmetry times a vertical step-like potential.

We will use the envelope function formalism again, with a wavefunction as in eq. (1.7). This time the envelope function can be factorized into two parts. The first one describes the vertical confinement (along $z$). As in the case of the wetting layer, only the first state $n = 1$ is confined. The second part describes confinement in the transverse plane, with cylindrical symmetry. We describe this transverse part in the basis of the envelope eigenstates $|L, m_z\rangle$ associated with the $\hat{\mathbf{L}}^{\mathbf{2}}$ and $\hat{L}_z$ operators. The band structure of the semiconductor is taken in account by solving the Schrödinger equation within the effective mass approximation.

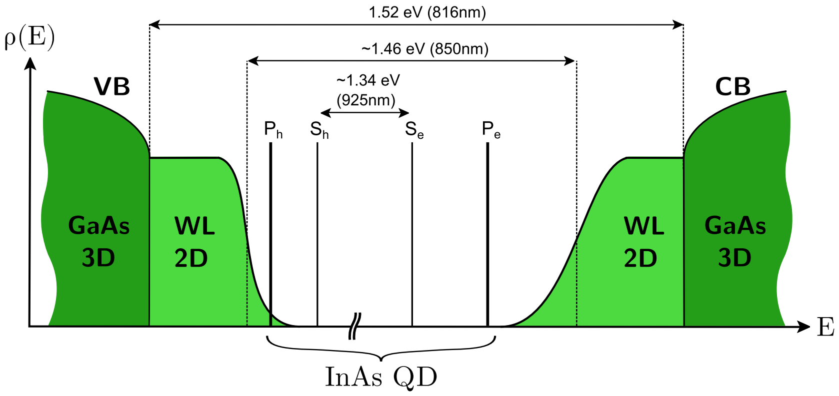

Figure 1.5: **Density of states of the QD with the surrounding 2D wetting layer.** This schematics illustrates the position of the QD discrete states with respect to the 2D and 3D continuum associated with the WL and GaAs respectively. The numbers are indicative of the mean gap values at $T = 4\text{K}$. The figure is adapted from [30].

Only a finite number of states can be confined within the InAs QD due to the finite depth of the confinement potential. For fairly small self-assembled InAs/GaAs QDs (emitting at a wavelength of less than 1µm), only those states that have an envelope function associated with $L = 0$ (S) and $L = 1$ (P) meet this condition. In a QD (contrary to an atom) the P states are doubly degenerate ($m_z = \pm 1$). The state $m_z = 0$ has higher energy. This comes from the shape of the dot: the state $m_z = 0$ extends into the $z$ direction, direction in which the flat QD has a much smaller dimension.

The QD energy levels are shown in fig. 1.4a. So we have succesfully introduced the electronic bands of a bulk semiconductor, the wetting layer, and the confined states in a QD. If we put everything together, we can describe the entire InAs/GaAs system according to the diagram shown in fig. 1.5. The values shown in the figure are average values at cryogenic temperature ($T = 4\text{K}$). Exact values depend on the growth details and on morphology of the QDs.

### 1.1.3 Optical properties

In this section we describe the optical transitions between the QD energy levels. As a first thing, let's return to the energy levels of the QD. We see that the semiconductor band structure provides a S conduction band and a P valence band, of which we just retain the heavy hole one. The confinement provides a discretization of the levels into the band with his own S$_{e,h}$ an P$_{e,h}$ orbitals, belonging to the envelop function. This energy structure is shown in fig. 1.4a.

In the dipole approximation, the Hamiltonian describing an interaction with the electromagnetic field has the form:

$$H_I = \frac{e}{m_0}\mathbf{A}\cdot\mathbf{p}, \tag{1.9}$$

where $e$ is the elementary charge, $m_0$ the mass of the free electron, $\mathbf{A}$ the vector potential associated with the electromagnetic field and $\mathbf{p}$ the momentum operator. We expect $\mathbf{A}$ to have vanishingly small variation across the QD since the QD is more than 20 times smaller than the wavelength of infrared light. The probability for the transition between an initial state $|i\rangle$ to a final state $|f\rangle$ is controlled by the matrix element:

$$\begin{aligned}\langle f|\, H_I\, |i\rangle \sim & \frac{e}{m}\mathbf{A}\cdot\langle\chi_f|\,\mathbf{p}\,|\chi_i\rangle\cdot\langle u_f|\,u_i\rangle + \\ & \frac{e}{m}\mathbf{A}\cdot\langle\chi_f|\chi_i\rangle\cdot\langle u_f|\,\mathbf{p}\,|u_i\rangle\,,\end{aligned} \tag{1.10}$$

which is the sum of two terms. The first one is associated with with intraband transitions, in which two distinct envelop states $|\chi_i\rangle$ and $|\chi_f\rangle$ are coupled. Typically, a transition between the conduction states $S_e$ and $P_e$ for a InAs QD has an energy of the order of $\simeq$ 10meV. The second term is associated with interband transitions.

The fact that the incoming light carries an angular momentum of one gives rise to selection rules, which are summarized in fig. 1.4b. Our main focus here is on interband transitions.The scalar product of the envelop functions restricts the transitions to envelope states with the same symmetry (S or P in the case of our system). Furthermore the dipole term imposes a variation in the total angular momentum projection. These selection rules determine which pairs of states are coupled to light.

#### 1.1.3.1 Excitonic states

To characterize an elementary excitation, we need to describe the conduction state of one electron and the valence states of the remaining N - 1 electrons. In solid state the absent electron from the valence band is described by means of a fictitious particle: the hole. This quasi-particle has the same characteristics as electrons, but with opposite signs.

**Neutral excitons.** The mechanism of spontaneous emission involves the radiative recombination of an electron in a conduction state with a hole in

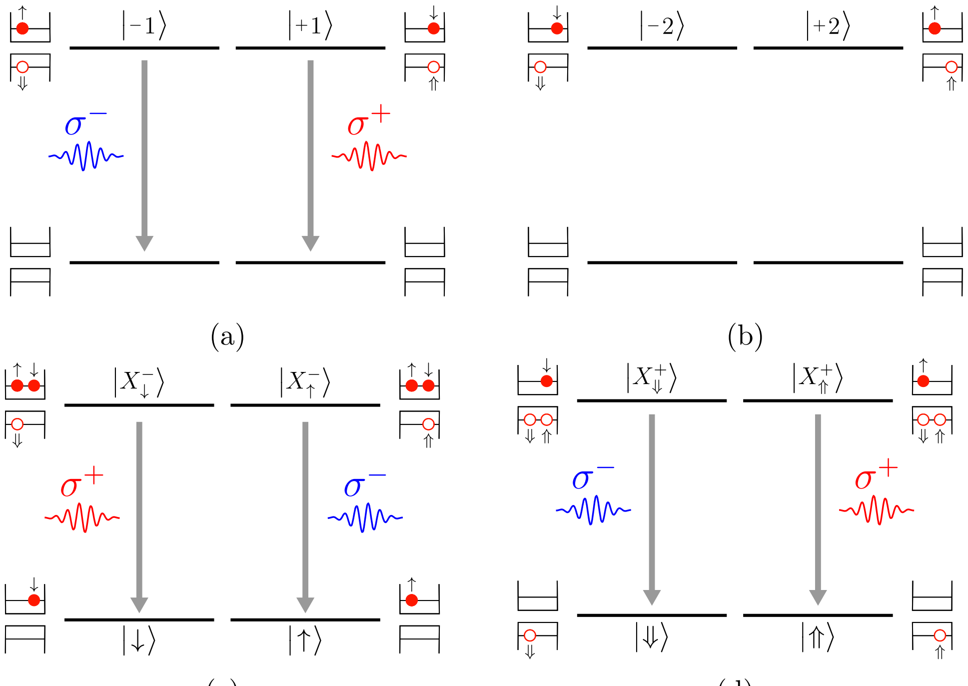

(a) (b)

(c) (d)

Figure 1.6: **Neutral excitons and trions.** Schematics of the excited states of QD's S level in an ideal QD, without considering exchange interaction and asymmetries in geometry or stress in the QD. Starting from a neutral QD we can have two bright excitons states (a) which recombine emitting circularly polarized photons. Then, in (b) we have two dark excitonic states which are not optically-active but can be reached from a bright excitonic state via a spin-flip process. The QD can be charged, starting with a negative charge we have two negative trion states (c) and for a positive charge two positive trions (d). The trions remain degenerate even when considering exchange interaction and asymmetries due to the Kramers theorem. The degeneracy can be lifted adding a magnetic field. There is one last important S shell complex which is the biexciton, shown in fig. 1.7.

the valence states. For this we need to consider a two-body representation of the electron-hole pair states confined in the QD. So, holes in the valence band have $|J_h = \frac{3}{2}, J_{h,z} = \pm\frac{3}{2}\rangle$, and can form up to four states with the corresponding electrons in the conduction band:

$$|\uparrow,\Downarrow\rangle \equiv |j_z=-1\rangle \tag{1.11}$$
$$|\downarrow,\Uparrow\rangle \equiv |j_z=+1\rangle \tag{1.12}$$
$$|\uparrow,\Uparrow\rangle \equiv |j_z=+2\rangle \tag{1.13}$$
$$|\downarrow,\Downarrow\rangle \equiv |j_z=-2\rangle \tag{1.14}$$

where we have introduced the notation $|\uparrow\rangle \equiv |J_e=+1/2, j_{e,z}=+1/2\rangle$, $|\downarrow\rangle \equiv |J_e=+1/2, j_{e,z}=-1/2\rangle$ for the electrons states, and $|\Uparrow\rangle \equiv |J_h=+3/2, j_{e,z}=+3/2\rangle$, $|\Downarrow\rangle \equiv |J_h=+3/2, j_{e,z}=-3/2\rangle$ for the holes. According to the interband selection rules, only pair states with $j_z=\pm1$ can be coupled to light. The radiative recombination of the states $|\uparrow,\Downarrow\rangle$ and $|\downarrow,\Uparrow\rangle$ will therefore result in the emission of circularly polarized photons. These optically-active states are the so-called bright exciton states and the process is schematized in fig. 1.6a. The states $|\uparrow,\Uparrow\rangle$ and $|\downarrow,\Downarrow\rangle$ on the other hand have $|j_z=\pm2\rangle$ and cannot lead directly to photon emission or absorption: they are called dark excitons (see fig. 1.6b). Dark excitons cannot be created directly by a resonant optical excitation. However, a bright exciton can be converted into a dark one by a spin-flip process. Furthermore, in non-resonant optical excitation schemes, the spin memory of the excitation is often lost, which can lead to a population of dark excitons in the QD.

Our model for the QD reduced a multiparticle problem into a single particle one by using a mean field approach. The introduction of the hole as a fictitious particle, requires us to consider the effect of the Coulomb interaction between the electron and the hole. In self-assembled QDs such as InAs/GaAs QDs the Coulomb binding energy between electron and hole provides a weak correction to the energy of the electron-hole pair, which is essentially determined by confinement. While the energy corrections are overall small, the exchange interaction lifts the degeneracy between the dark exciton and the bright excitons, as was shown in fig. 1.7.

**Biexciton.** The QD can host two electron-hole pairs in the S shell: this excitonic complex is called a bi-exciton. Due to the Pauli exclusion principle, the two electrons must be in a singlet state; the pair of holes should fulfill the same condition. We can thus write the bi-exciton state as:

$$|XX\rangle = \frac{1}{\sqrt{2}}(|\uparrow\downarrow\rangle - |\downarrow\uparrow\rangle) \otimes (|\Uparrow\Downarrow\rangle - |\Downarrow\Uparrow\rangle). \tag{1.15}$$

The energy of the bi-exciton is:

$$E_{\mathrm{XX}} = 2E_X + E_{\mathrm{C}}, \tag{1.16}$$

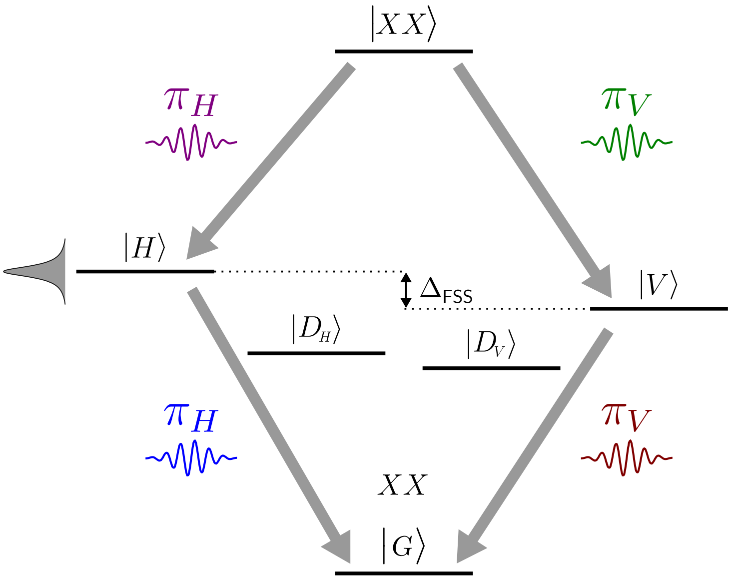

Figure 1.7: **Biexciton radiative cascade, in the presence of a fine structure splitting.** The biexciton $|XX\rangle$ decays following one of two paths, resulting in the emission of two entangled linearly polarized photons. In general, the decay $|XX\rangle \rightarrow |H\rangle$ or $|V\rangle$ and $|H\rangle$ or $|V\rangle \rightarrow |G\rangle$ have a different transition energy even without FSS due to the Coulomb interaction in the biexciton. This energy can be both positive or negative. All the four excitons have in general different energies. The break of degeneracy between the bright and dark exciton states comes from an exchange interaction. Moreover, asymmetry in the geometry or strain in the QD lead to a FSS between the two bright excitons. This asymmetry causes a splitting of the dark excitons as well, albeit a less important one.

where $E_X$ is the energy of the exciton and $E_\mathrm{C}$ is the Coulomb interaction energy. The bi-exciton state can decay through the emission of two photons. While the simultaneous emission of two photons at the energy $E_\mathrm{XX}/2$ is an allowed process, it is very weak and generally not observed experimentally. Bi-exciton recombination follows instead a cascaded process composed of two single-photon emission processes, involving an intermediate exciton state, as sketched in fig. 1.7. Due to the Coulomb interaction the energy of the two emitted photons is in general different. That is a good news in practice since it means that the two emitted photons can be spectrally separated. The bi-exciton is a non-degenerate state, with a total angular momentum of 0 which in theory means that the two emitted photons are circularly polarized with opposite polarization. Since there are two possible paths, the spontaneous emission of the bi-exciton can be described by the entangled photon state:

$$|\psi\rangle \Rightarrow \frac{1}{\sqrt{2}}(|\sigma^+_{XX}\rangle\,|\sigma^-_X\rangle + |\sigma^-_{XX}\rangle\,|\sigma^+_X\rangle), \tag{1.17}$$

where $|\sigma^\pm_{XX}\rangle$ ($|\sigma^\pm_X\rangle$) represents a circular polarized photon from the $|XX\rangle \to |X\rangle$ ($|X\rangle \to |G\rangle$) transition.

In reality the QD doesn't have a cylindrical symmetry. The true eigenstates are linear combination of the two exciton states:

$$|H\rangle = \frac{1}{\sqrt{2}}(|\uparrow\Downarrow\rangle - |\downarrow\Uparrow\rangle) \tag{1.18}$$

$$|V\rangle = \frac{1}{\sqrt{2}}(|\uparrow\Downarrow\rangle + |\downarrow\Uparrow\rangle). \tag{1.19}$$

They are not, in general, degenerate and they relax by emitting linearly polarized light, see fig. 1.7. The difference in energy between the two excitonic states is called the fine structure splitting (FSS). One of the main consequence of a nonzero FSS is that the photons emitted along the two paths become distinguishable. This will affect the emission of entangled photons. Moreover, while the relaxation of the bi-exciton state still produces an entangled photon state, the FSS introduces a random phase difference for each realization:

$$|\Psi\rangle = \frac{1}{\sqrt{2}}\left(|\pi_H\pi_H\rangle + e^{i\phi}\,|\pi_V\pi_V\rangle\right), \tag{1.20}$$

where $\phi = \frac{E_{\mathrm{FSS}}\tau}{\hbar}$ is a phase which depends on the FSS and the time $\tau$ elapsed between the first and second photon. This time is random and varies between sudsequent emission processes: this spoils the time-integrated entanglement [172, 82]. Since an exciton has a finite lifetime, and thus a finite linewidth (supposing a radiatively-limited linewidth) the effect of the FSS has to be evaluated in comparison to the linewidth (see fig. 1.7). Note that the dark excitons also feature a FSS, albeit with a smaller value. We will see in the following that there exists ways to tune the optical properties of the dots, and thus, for instance correct, or at least mitigate, the asymmetries leading to the FSS and restore the time-integrated entanglement.

**Trions.** Finally there are other states that need to be considered. A QD can be in a charged state, that is, contain a hole or an electron in its ground state. It is then possible to create an electron-hole pair in a charged QD, we call this state a trion. As seen before, we need to take in account the Pauli principle when there are multiple fermions in the same state. So, if we start with a negatively-charged QD we can have two negative trions:

$$|X_{\uparrow}^{-}\rangle = \frac{1}{\sqrt{2}}(|{\uparrow\downarrow}\rangle - |{\downarrow\uparrow}\rangle) \otimes |{\Uparrow}\rangle \tag{1.21}$$

$$|X_{\downarrow}^{-}\rangle = \frac{1}{\sqrt{2}}(|{\uparrow\downarrow}\rangle - |{\downarrow\uparrow}\rangle) \otimes |{\Downarrow}\rangle\,. \tag{1.22}$$

Starting with a positively charged QD gives the two positive trions:

$$|X_{\Uparrow}^{+}\rangle = |{\uparrow}\rangle \otimes \frac{1}{\sqrt{2}}(|{\Uparrow\Downarrow}\rangle - |{\Downarrow\Uparrow}\rangle) \tag{1.23}$$

$$|X_{\Downarrow}^{+}\rangle = |{\downarrow}\rangle \otimes \frac{1}{\sqrt{2}}(|{\Uparrow\Downarrow}\rangle - |{\Downarrow\Uparrow}\rangle). \tag{1.24}$$

One of the interesting properties of the trions, which we will use in this thesis, concerns the degeneracy. Kramers' theorem states that a system containing an odd number of fermions (in this case, electrons and holes) remains at least twice degenerate if it is described by a time-reversal symmetric Hamiltonian. This is the the case for the Coulomb exchange interaction and also for the Hamiltonian describing the stress on the QD. Thus the trion states remain degenerated, even in the presence of structutral or strain asymmetries. An important exception is an Hamiltonian which depends on the magnetic field, since the magnetic field is antisymmetric with respect to time inversion. In addition, trion states are always bright.

#### 1.1.3.2 Quasi continuum of mixed QD-WL states

So far we have considered the coonfined states hosted by the QD. Recalling the diagram in fig. 1.5, we have the bulk states in the GaAs, then we have a constant density of nonlocalized states in the wetting layer which due to the rugosity of the surface has a smooth edge. There are a family of mixed states that we haven't discussed: they involve both the wetting layer and the QD.

These are mixed pairs where one of the carriers is localized in the QD and the other one is delocalized in the WL. These states behave like a 2D - 0D quasi-continuum. The quasi-continuum of crossed states overlaps with the $\mathrm{P}_e$ $\mathrm{P}_h$ interband transition of the QD, basically extending the 2D continuum down to the highly localized excited states of the QD. This is shown in the diagram in fig. 1.8. The $\mathrm{S}_e$ $\mathrm{S}_h$ transitions remain spectrally isolated from this quasi-continuum (by a few tens of meV). The quasi-continuum is very important since it provides a relaxation mechanism, for pairs created into the wetting layer (see section 1.1.4.1), to reach the Pe Ph states.

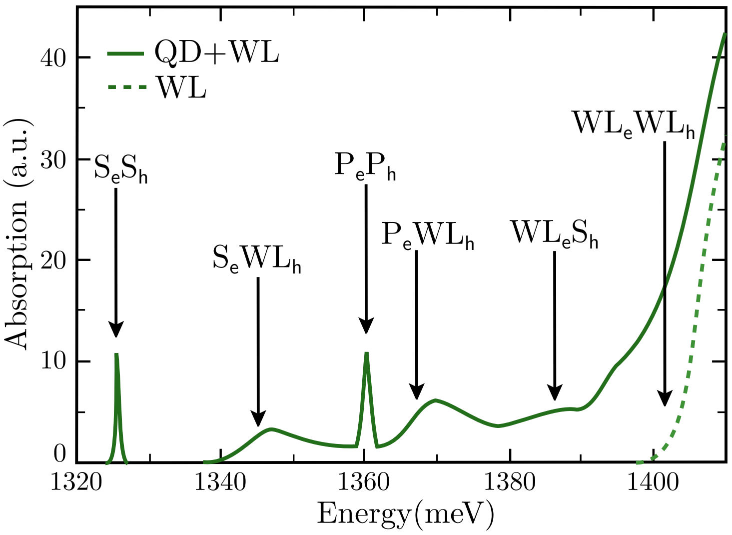

Figure 1.8: **Quasi continuum 2D-0D.** Calculation of the interband absorption spectrum for a system composed of a WL and a QD. The contribution of the WL alone is showed in dashed line. The various peaks correspond to the different transitions coupling WL and/or QD states and are indicated by the black arrow. The figure is adapted from [190].

## 1.1.4 Optical excitation techniques

### 1.1.4.1 Non resonant excitation

In the case of non-resonant excitation, we generally excite our system with energies below the GaAs bandgap energy ($E_g = 1.52$eV) but above the wetting layer bandgap energy ($E_g = 1.46$eV). This excitation scheme is shown in fig. 1.9. Free carriers are injected by a non resonant laser into the the wetting layer.

In semiconductors in general relaxation through acoustic phonons is inefficient, the energy mismatch between electron states being much too large [22, 16].

In bulk, planar and 1D structures, the main energy relaxation channel is the irreversible emission of longitudinal optical (LO) phonons through the Fröhlich coupling and next through acoustic phonons, made possible by the presence of a continuum of final states. Within their lifetime ($\simeq 1$ ns) carriers thermalize at their band edges and decay radiatively there. Despite its effectiveness, this electron-phonon coupling is weak, and is usually well described by the Fermi golden rule.

Going to 0D, this mechanism is no longer possible. As shown in [77] LO phonons in a QD are always in a strong coupling regime and form an (in

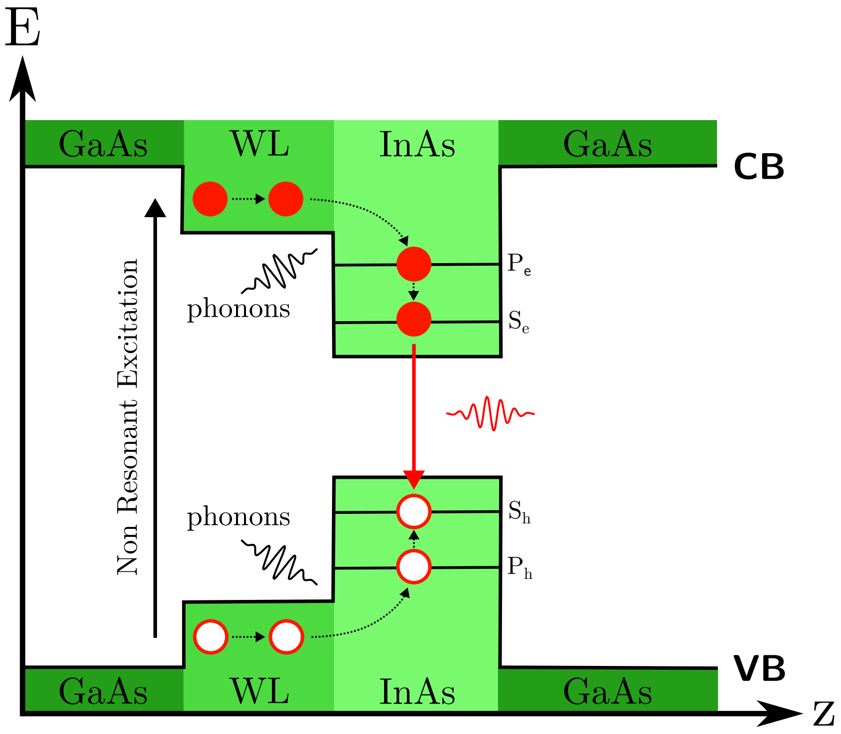

Figure 1.9: **Non resonant optical excitation.** The non resonant laser (left black arrow) creates electron-holes pairs into the WL. The electrons (holes) relax into the lower (higher) energy band of the QD system $S_e$ ($S_h$). Finally the electron-hole pair can recombine by emitting a photon. Figure adapted from [30].

theory) everlasting mixed electron-phonon mode called polaron. Because the optical phonons shows very little dispersion, one would expect that the LO phonon assisted relaxation in semiconductor quantum dots could be efficient only if the energy of the phonon would match the energy transition. This represents an unavailable relaxing channel for QD due to the scarcity of final states satisfying both energy and momentum conservation. This phenomenon goes by the name of ”photon bottleneck” [16].

However the capture of carriers by the QD and its photo-luminescence (PL) emission show the existence of fast ($\simeq$ 10 ps) capture and relaxation mechanisms for the QD systems [65]. How to explain this contradiction? As a first step it is worth briefly talk about how the electron-hole pair is captured by the QD. This process is not based just on diffusion: as discussed in [65], during the growth process, following the formation of the InAs/GaAs island, GaAs experiences a strain which is essentially a biaxial compression (enhanced bandgap) between the 3D islands and biaxial tension (reduced bandgap) near the top or the bottom of an island. These strain fields generate channels which drain the carriers toward the islands, making the capture process much more efficient.

Regarding the relaxation process two possible mechanisms have been proposed.

- **Relaxation exploiting Auger effect.** In [65] a possible sequence of relaxation is based on the Auger effect. To briefly explain it let's restate the photon bottleneck problem: the electron-hole pair, once is trapped near the QD cannot relax by itself into the ground state due to energy conservation and lack of suitable channels. However the presence of another carrier can provide such a channel: for instance the energy lost by the relaxation of the electron in the pair can kick one electron in the continuum of states (2D WL or 3D GaAs) where it can quickly relax by standard electron-phonon scattering.

- **Instability of LO phonons.** Another possibility is illustrated in [191] and is based on the fact that the crystal anharmonicity drives the instability of LO phonons. This leads to a decay of polaron states which otherwise would be everlasting. By such a mechanism a single electron in an excited dot state can relax down to the ground state even if the electron energy difference differs from the optical phonon energy.

It is reasonable to believe that both of this processes contribute to the fast relaxation seen in QD systems.

The advantage of non resonant excitation is that the excitation laser is usually spectrally quite far from the emission of the dots, and thus easily filtered out. However this excitation technique has several drawbacks. The incoming laser creates many electron-hole pairs, which contribute to spectral diffusion. Residual charges undergo trapping and de-trapping processes in defects and barriers near the QD [17, 52]. These fluctuations influence the QD's emission energy through the quantum-confined Stark effect. In order to mitigate these effects one needs to lower the excitation power. Actually we will see in section 2.5.3, that a low-power non resonant laser can lead to a stabilization of spectral diffusion. In that case the power is so low that the emission of the QD is not relevant.

Another drawback is that the photon emission follows a random process of carrier relaxation, from the capture by the QD down to the relaxation to the lowest S energy levels. This introduces a jitter in the photon emission which impacts the temporal indistinguishability of subsequently emitted photons.

#### 1.1.4.2 Resonant excitation

Resonant excitation is a coherent excitation of the TLS. The advantages of this excitation method are the suppression of some of the occurring dephasing processes, in particular those related to unnecessary charges in the QD environment. Moreover in resonant excitation pairs are created directly into the TLS virtually eliminating the time-jitter of non resonant excitation. This is especially important when one wants the QD to emit strictly identical single photons from one excitation pulse to the next. Nevertheless, local charge environment fluctuations, are still a problem even resonance excitation. This can lead to spectral wandering and blinking as we will see in section 2.5.3.

From a technical point of view, resonance excitation is more difficult to implement, since, compared to non-resonant excitation, the exciting scattered laser can not be filtered out spectrally. One technique to get rid of the laser is to filter it out in polarization. This requires a sample with a smooth surface which will not change the polarization of the laser upon reflection. Provided that the sample is suitable, it is essential to have a good quality setup and well aligned polarization optics. This can lead to suppression ratios up to $10^6$ as seen in section 2.5.2. The downside of this technique is that half of the light emitted by the QD will be lost due to having the same polarization of the laser.

### 1.1.5 Tuning the QD optical emission

The mechanism of formation of QDs produces a random distribution of dots, with different geometrical dimensions, which leads to different resonance frequencies, and asymmetries. As a result two distinct QDs generally emit photon at distinct wavelengths. In many cases we are interested in applications where photons produced from different QDs needs to interfere. A mechanism to tune the QD emission wavelength is thus required.

#### 1.1.5.1 Temperature

Temperature affects the structure of crystals: an increase in temperature leads to an expansion of the crystal lattice, resulting in an increase in the interatomic distances. This leads to a change in the band gap. Therefore temperature can be used as a tuning mechanism for QD. From the work in [51] we can see that shifts as large as 1.4 nm can be obtained with a temperature ranging from 10 K to 40 K, without loss in intensity. The heat can be provided by a laser, or resistors, in which case it can be applied locally. Tuning with temperature is relatively simple to implement and it is also reversible. The main disadvantage is that it becomes at some point detrimental for the emission efficiency and introduces thermal phonons which, interacting with excitons, increase the dephasing.

#### 1.1.5.2 Magnetic field

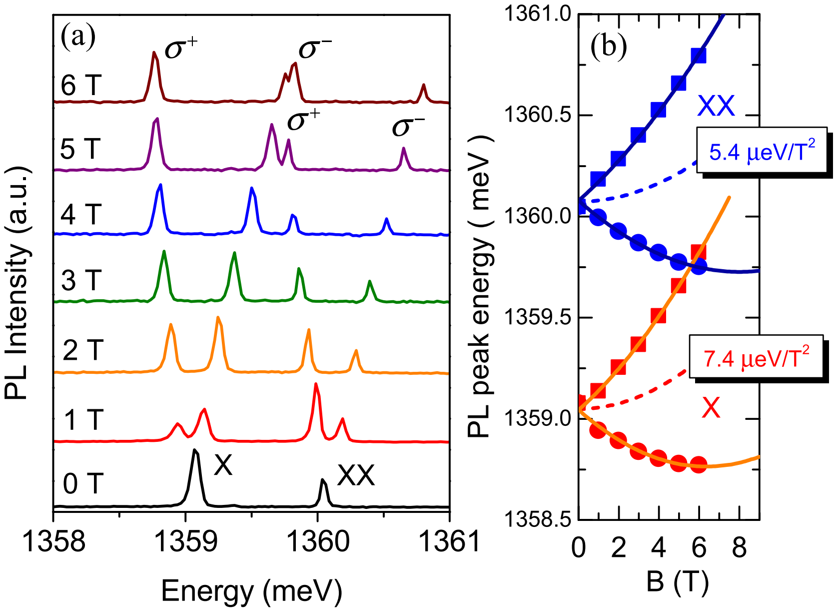

Figure 1.10: **Magnetic field tuning.** **(a)** Magneto-PL spectra measured from $B = 0$ up to 6 T in the Faraday geometry. **(b)** B-dependent energy shifts of the X and XX lines. Solid and dashed lines are fitting curves using a quadratic B dependence. Figure reproduced from [187].

A magnetic field can be used to tune the emission of a QD. The effect of the magnetic field on the QD is double. On one side we have the Zeeman effect, which can be described by a perturbation Hamiltonian such as:

$$H_M = -\mu \cdot \mathbf{B}, \tag{1.25}$$

where $\mu$ is the magnetic moment of the exciton, which is proportional to the total angular momentum $J$. The Zeeman effect causes the splitting of the doublet of the bright exciton states (see fig. 1.10), as well as for the trions. The effect is linear in the applied field.

In addition there is the diamagnetic shift, an increase in energy caused by changes in the spatial confinement, and in the electron-hole Coulomb interaction. Indeed magnetic field squeezes the exciton wave function, which in turn enhances the binding energy. So, the diamagnetic shift causes an increase of the energy which is proportional to $B^2$ for a neutral exciton as a first approximation.

This is illustrated in fig. 1.10, where both the diamagnetic shift and the Zeeman splitting are shown for an exciton state. The maximum shift obtained is around 1 meV but it requires a strong magnetic field of about 6 T.

### 1.1.5.3 Electric field

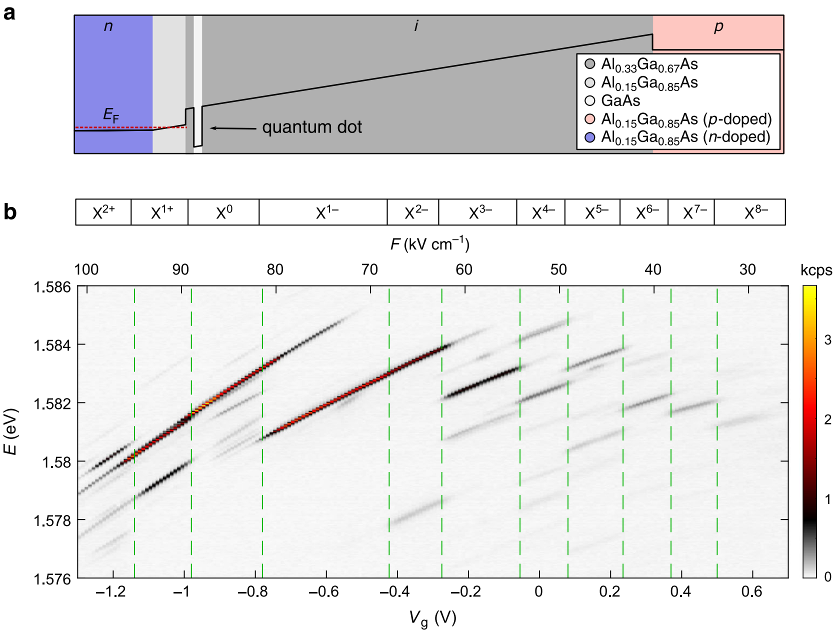

Figure 1.11: **Tuning the wavelength and charge state of single GaAs quantum dots.** **(a)** Schematic band structure (conduction band) of the diode hosting charge-tunable GaAs QD. **(b)** The PL emitted by an exemplary single quantum dot as a function of the gate voltage, $V_g$. (Positive gate voltage indicates a forward bias.) The corresponding electric field, F, is plotted as an additional x-axis on top. The emission spectrum shows several plateaus corresponding to different charge states of the QD. We observe narrow PL-linewidths on highly charged excitons where up to eight additional electrons occupy the QD. Figure reproduced from [205].

In a real QD, the confinement potential, even if as a first approximation has a cylindrical symmetry, shows a dependency in $z$. In general the wavefunction of the electrons and the holes are different, mainly due to their difference in the effective mass. This means that the mean position of the hole is different from the mean position of the electron. This results in a permanent dipole moment for an exciton in a QD. Moreover, the presence of the electric field modifies the confinement potential of the QD, which affects the energy levels of confined electrons and holes, with the effect of tuning the QD emission. This is the so called quantum-confined Stark effect. When the field is weak, this effect can be treated perturbatively. The odd terms of the energy correction vanish due to symmetry consideration, which leaves at lower order a dependency of the field squared. So, the effect of the electric field on the QD energy can be written as [59]:

$$E = E_0 + pF + \beta F^2. \tag{1.26}$$

Here, $p$ is the permanent exciton dipole moment of the QD and $\beta$ is the polarizability of the state.

There have been multiple demonstrations of QD tuning in recent years [54, 24]. One of the most impressive is shown in [205]. Incidentally fig. 1.11 shows that an electric field can be used to charge the QD by tunneling in and out electrons. The main disadvantage of the electric field tuning is that, for large electric fields, the increasing electron and hole wavefunctions separation leads to PL quenching [54].

#### 1.1.5.4 Mechanical strain

Mechanical strain significantly impacts the band structure of a semiconductor, which leads to modification of the energy bandgap. For this reason, stress can be used as a mechanism for tuning the optical properties of a QD [162, 161]. Compared to other tuning mechanism, strain tuning preserves the quality of the QD optical emission.

Quantum optics applications require the ability to control the excitonic emission energy as well as the FSS. This requires the combination of multiple and independent ”tuning knobs”. For instance electric field can be combined with strain [186]. The control over FSS requires two degrees of freedom. Indeed to obtain the greater reduction the perturbation must be applied along the direction aligned with the polarization axis of the exciton emission [164, 183].

Strain alone can provide multiple of such tuning knobs. For instance a complete control over strain in the $xy$ plane provides 3 tuning knobs, via the three components of the stress tensor $\epsilon_{xx}$, $\epsilon_{yy}$, $\epsilon_{xy}$. With that one can achieve the FSS correction and the tuning of the exciton emission as shown in fig. 1.12 [184].

We will see in chapter 3 a device that leverages strain to tune the QD emission.

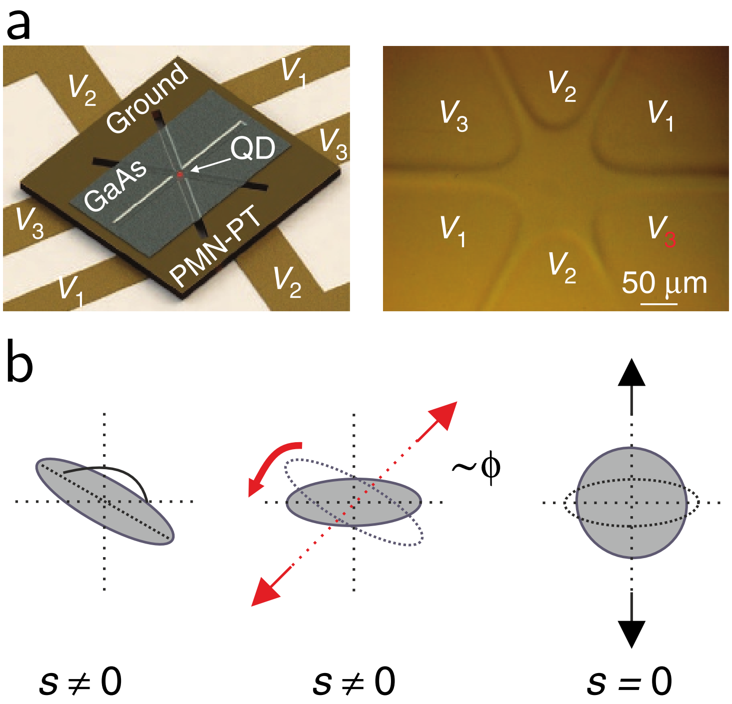

Figure 1.12: **Full control of the in-plane strain.** **(a)** Sketch of a 6-legged device with a GaAs nanomembrane bonded on it (left panel). The PL is measured from QDs located at the central gap between the six legs. Voltages ($V_1$,$V_2$,$V_3$) are applied to pairs of aligned legs to avoid lateral displacements of the active structure. An optical picture of the central gap of a 6-legged device is shown (right panel). **(b)** Sketch of the QD anisotropy for a QD with $s \neq 0$ (left panel). The deviations from a circle indicate the existence of an in-plane anisotropy in the QD confining potential. The anisotropy can be aligned along the actuating direction of leg-2 with leg-1 ($V_1$). Finally, the anisotropies can be fully compensated with leg-2 ($V_2$). Reprinted from [184].

### 1.1.6 Sources of decoherence

As seen in the previous section a QD is not an isolated system and interacts with its environment. QDs are quite sensitive to electric field, magnetic field and strain. In QDs we can have charge noise resulting in a fluctuating electric field, spin-flips which in the environment resulting in a fluctuating magnetic field, and the interaction with phonons which represents a fluctuating stress on the semiconductor lattice. All of them can lead to dephasing and decoherence of optical and spin states.

Charge noise arises from the fluctuation of charge occupation in the environment of the QD. This leads to fluctuations in the electric field experienced by the QD. The electric field shifts the optical transition energy via the quantum-confined Stark effect. In general, charge noise occurs at frequencies that are much smaller than the QD emission rate. This results in random fluctuations of the central energy of the emitted photons, a process often called spectral wandering.

The QD is coupled to lattice vibration (phonons). This interaction is associated with the deformation potential, which couples the QD bandgap energy to the crystal strain. Theory and experiments had shown that for s shell excitons, the longitudinal acoustic phonons represent the greatest source of decoherence [60, 148]. At first order the coupling to phonons leads to acoustic siebands that surround a central zero-phonon emission line. At second order, phonon coupling also induces an homogeneous broadening of the zero-phonon line. These features strongly depend on the temperature.

Spin noise is typically the result of fluctuations in the nuclear spins of the host material. This results in a fluctuating magnetic field (the Overhauser field). This magnetic field induces a shift in the QD energy levels. This noise has usually a lower amplitude than the charge noise, but is present over a larger bandwidth [101]. More important is the effect over an electron or hole spin: the resulting hyperfine interaction causes a fast spin dephasing.

### 1.1.7 Summary on self-assembled QDs

In this first section we have discussed the electronic properties of self-assembled QDs. We first discussed the band structure and shown how the confinement in three dimension leads to the development of the artificial atom model. This two-level system (TLS) system can host several excitonic complexes such as the exciton, the trion and the biexciton, which we will encounter throughout this thesis. We have also seen the characteristics of real structures, in particular the FSS and its impact on the emission of entangled photon pairs. We have seen how to excite this artificial atom and introduced non-resonant and resonant excitation, two important techniques used all throughout this thesis. Finally we have seen how to control the QD emission using temperature, electric field, magnetic field and strain. In particular strain is a very powerful tool for a comprehensive tuning of a QD optical properties.

In the next section we will continue along this path, this time looking at the photonic environment surrounding the QD. We will see how the QD emission can be accelerated and funneled into a specific mode. This is particularly important to improve some of the weak points of artificial atoms in the bulk, such as the low extraction efficiency and the impact of noise from its environment.

## 1.2 Photonic structures for spontaneous emission control

A single photon source (SPS) based on a QD exploits the exciton recombination through spontaneous emission. This emission features a dipole-like emission pattern, and, because we are dealing with a material of high refractive index, the majority of it is trapped by total internal reflection, especially in a planar geometry (see fig. 1.13). In this section, we will introduce microcavities and waveguides which enable the funneling all photons into a selected mode that can be efficently coupled to external collection optics.

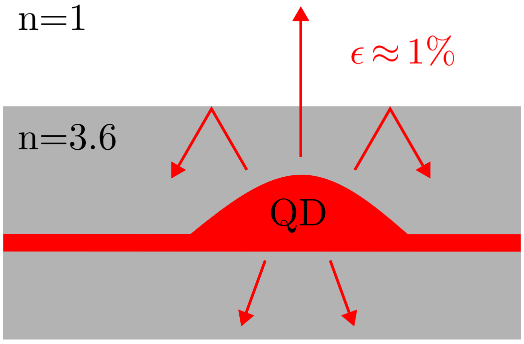

Figure 1.13: **Light collection for planar structures.** A QD is embedded in a high refractive index planar structure. The extraction efficiency $\epsilon$ is quite low due to total internal reflection. Moreover, half of the light is emitted downwards and lost into the substrate.

### 1.2.1 Strategies for spontaneous emission control

Spontaneous emission (SE) is a purely quantum effect involving an emitter in an excited state which relaxes by emitting a photon. The system is thus composed of the emitter and the electromagnetic field. The latter is constituted by a large reservoir of harmonic oscillators representing all the modes with which the emitter can couple to. The treatment of SE requires a quantum description of both the emitter and the field.

The challenge of spontaneous emission control consists in engineering the photonic environment of the emitter in order to suppress the coupling to all unwanted modes and/or strongly enhance the coupling to one preferred mode.

We will consider two systems leading to single-mode spontaneous emission: i) optical microcavities that support descrete resonant modes and ii) single-mode waveguides that support only a single familly of guided modes. We note $\Gamma_M$ the SE rate into the mode M of interest (cavity mode or guided mode). In addition, the QD is also coupled to a continuum of background modes. The SE rate into these modes is denoted $\Gamma_B$. The fraction of SE into mode of interest, $\beta$, is given by:

$$\beta = \frac{\Gamma_M}{\Gamma_M + \Gamma_B}. \tag{1.27}$$

Two main strategies can be employed to bring $\beta$ close to unity: i) the microcavity approach, which exploits the Purcell effect to selectively enhance $\Gamma_M$ (see [63]); ii) the single-mode waveguide approach, inhibiting SE in other modes using a 3D photonic crystal [202] or dielectric screening effect in high-index-contrast waveguides [37].

Combining these two approaches is also possible, such as slow modes in photonic crystal waveguides [5] and nanocavities [97]. All these concepts will be detailed in the following sections.

### 1.2.2 Optical microcavities

A first strategy to control spontaneous emission is to embed the emitter into an optical cavity which increases the zero-point fluctuations and spectral density of states associated with the cavity mode. This strategy makes it possible to accelerate spontaneous emission via resonant coupling between the emitter and a cavity mode. This acceleration is quantified by the Purcell factor $F_p$. It is defined as the ratio between $\Gamma_M$, the spontaneous emission rate in the mode of interest $M$, and $\Gamma_0$ the emission rate in an unstructured environment that serves as a reference (for a QD one usually considers the bulk semiconductor):

$$F_p = \frac{\Gamma_M}{\Gamma_0}. \tag{1.28}$$

Despite the fact that it was originally introduced for optical cavities, where emission acceleration can be very large, it is easily generalized and used in other structures, such as waveguides.

Historically the acceleration of spontaneous emission was first predicted in the context of the engineering of spin relaxation, by spontaneous emission in the microwave spectral range [21]. The first experimental demonstration of the Purcell effect came in 1983 within the research group led by S. Haroche [70]. This involved the coupling of a single Rydberg atom with a microwave cavity. In the solid-state the Purcell acceleration was first demonstrated in 1998 with InAs QDs integrated into a micropillar (see [64, 62]).

In the following we introduce the theoretical bases of cavity quantum electrodynamics, which describes the light-matter interraction in an atom-cavity system.

#### 1.2.2.1 Weak and strong coupling regimes

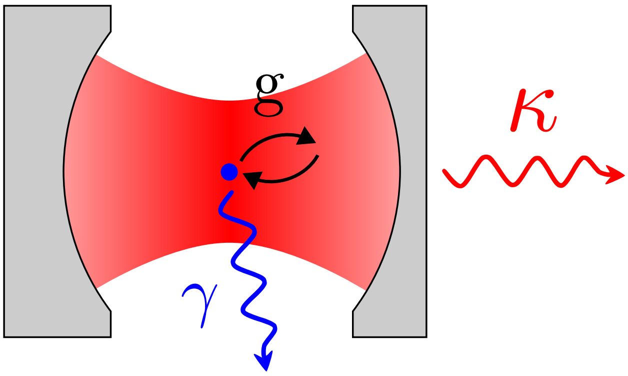

Figure 1.15: **An atom coupled to a single cavity mode.** $g$ is the coupling constant of the dipole-interaction Hamiltonian. There are two loss channels: spontaneous emission of the atom into other modes that the cavity one (rate $\gamma$) and cavity losses (rate $\kappa$).

An optical cavity confines light in all three directions of space, thus discretizing the density of optical modes accessible to photons emitted by the emitter. The study of an emitter placed in an optical cavity constitutes a complex system which couples the evolution of the emitter, the electromagnetic field inside the cavity and the electromagnetic field continuum. The Hamiltonian describing the coupling between the cavity and the atom is the Jaynes-Cummings Hamiltonian:

$$\hat{H}/\hbar = \omega_{at}\hat{\sigma}^{+}\hat{\sigma}^{-} + \omega_{c}\hat{a}^{\dagger}\hat{a} + ig(\hat{a}^{\dagger}\hat{\sigma}^{-} - \hat{\sigma}^{+}\hat{a}). \tag{1.29}$$

Here, $g$ is the coupling strength, $\omega_{at}$ is the frequency of the TLS, $\omega_c$ the resonance frequency of the cavity, $\hat{\sigma}^{-}$ ($\hat{\sigma}^{+}$) is the lowering (rising) operator for the atom and $\hat{a}$ ($\hat{a}^{\dagger}$) is the annihilation (creation) operator for a photon in the cavity mode.

The study of such a system makes use of the master equation formalism:

$$\dot{\rho} = -\frac{i}{\hbar}[\hat{\mathcal{H}}, \rho] + \mathcal{L}_{\text{cav}} + \mathcal{L}_{\text{se}} \tag{1.30}$$

The $\mathcal{L}.$ are Lindblad operators that describe the interaction of the system with the surroundings. Here they represents the cavity damping (rate $\kappa$) and emission into other modes that the cavity mode (rate $\gamma$).

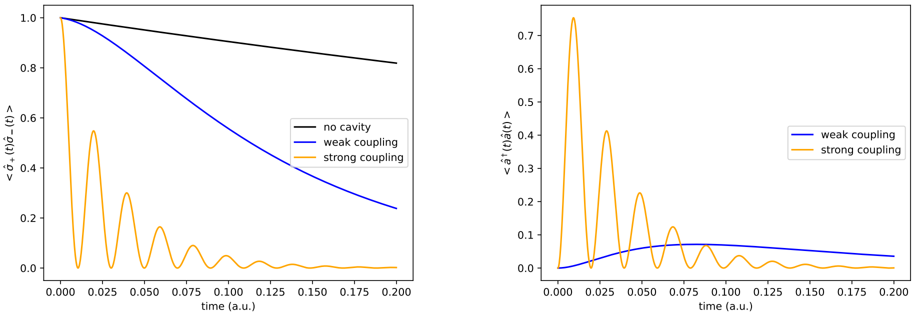

(a) (b)

Figure 1.16: **Light-matter interaction regimes.** Simulation of a TLS coupled to a cavity, using the Python package `QuTip` to solve the Lindblad master equation eq. (1.30). Three regimes are studied: the QD not coupled to the cavity, the weak coupling regime ($\kappa \gg g$) and the strongly coupled regime ($\kappa \ll g$). In all cases $\gamma \ll \kappa$. **(a)** shows the time evolution of the population of the atom excited state. **(b)** shows the time evolution of the cavity photon population.

To give an extensive treatment of the emitter/cavity system is not the scope of this section, however eqs. (1.29) and (1.30) allows us to grasp the physical meaning of the relevant quantities. As a starting point, we consider an excited emitter and an empty cavity. Depending on the hierarchy between the coupling strength and the loss rates, we can identify two main regimes:

- **Weak coupling regime**: when $g \ll \kappa$ a photon emitted by the atom into the cavity mode escapes into the free-space continuum before it can be reabsorbed by the emitter. This regime will be further discussed later.

- **Strong coupling regime**: When $g \gg \kappa$ the photons emitted by the emitter can be reabsorbed before they escape the cavity. This phenomenon is called Rabi oscillations [126]. Figure 1.16a shows the coherent exchange of an elementary excitation between the emitter and the cavity. The damping of the oscillation is due to losses (here mainly cavity losses). The eigenstates of the Hamiltonian are a combination of the emitter and the cavity excited states. These are called dressed states and provide non linearities exploitable at very low photon numbers. This phenomenon can be very useful for realizing coherent couplings and entangled quantum systems [79, 153, 145].

#### 1.2.2.2 Purcell effect

In the weak coupling regime, the cavity losses dominate over the coupling strength so that a photon emitted into the cavity will leave it before being reabsorbed. From the emitter point of view, the lossy cavity is just a continuum of modes whose density of states has a Lorentzian profile. As seen in fig. 1.16a the cavity induces an acceleration of the spontaneous emission: this is the Purcell effect.

The Purcell effect can be calculated analytically (see [66]), giving:

$$F_p = \frac{\Gamma_{\mathrm{C}}}{\Gamma_0} = \frac{3}{4\pi^2}\left(\frac{\lambda}{n}\right)^3 \frac{Q}{V_{\mathrm{eff}}}, \tag{1.31}$$

where $\Gamma_{\mathrm{C}}$ is the spontaneous emission rate into the cavity mode, and

$$V_{\mathrm{eff}} = \frac{\iiint n^2(\vec{r})|\vec{E}(\vec{r})|^2\, d^3\vec{r}}{n^2 \max\left(\left|\vec{E}(\vec{r})^2\right|\right)} \tag{1.32}$$

is the effective volume of the cavity, and

$$Q \equiv 2\pi \frac{\text{energy stored in the cavity}}{\text{energy lost per optical cycle}} = \frac{\omega_c}{\kappa} \tag{1.33}$$

is the quality factor. Note that $\Gamma_C$ can be derived from the coupling strength and from the atom and cavity damping:

$$\Gamma_C = \frac{4g^2}{\kappa + \gamma}. \tag{1.34}$$

It is therefore possible to accelerate the emission rate by increasing the quality factor $Q$ and reducing the effective volume $V_{\mathrm{eff}}$ of the cavity mode under consideration. Accelerating spontaneous emission is important because the emitter has less time to interact with its surrounding, thus making the system more resilient to noise. Note that this effective acceleration increases the linewidth of the emitted photons. The coupling of the emitter with the cavity has a positive impact on the $\beta$ factor. Indeed the latter reads:

$$\beta = \frac{\Gamma_C}{\Gamma_C + \Gamma_B} = \frac{F_p}{F_p + \frac{\Gamma_B}{\Gamma_0}}, \tag{1.35}$$

where $\Gamma_B$ represents the emission in other channels which are not the cavity mode (B stands for background). We see that increasing the Purcell factor reduces the relative importance of these unwanted channels.

Given the importance of the enhancement of spontaneous emission of a quantum emitter, many strategies have been pursued for improving the Purcell factor. This has led to a variety of optical cavities with interesting designs, which will be explored in the next section.

### 1.2.2.3 Examples of optical cavities

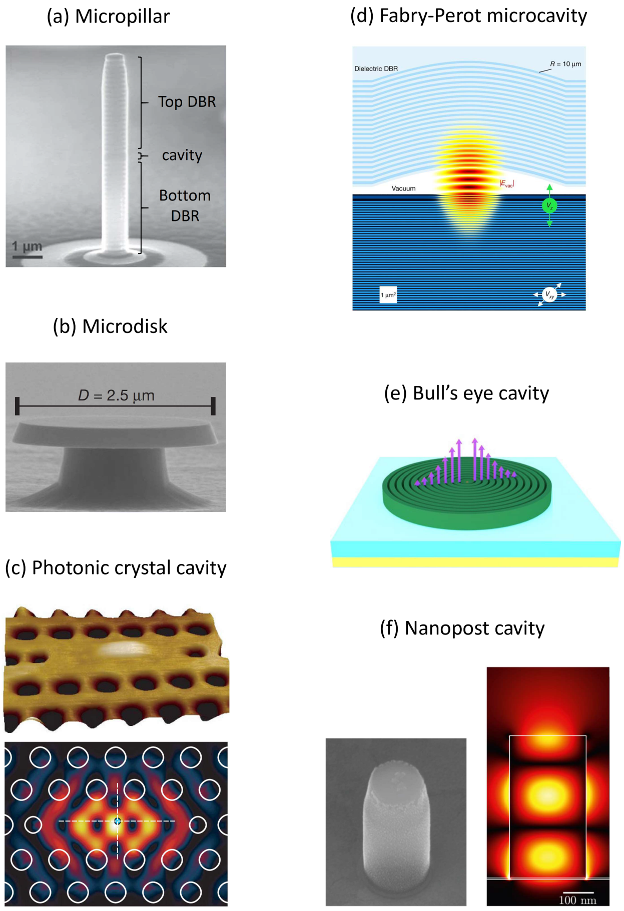
(a) Micropillar

(b) Microdisk

(c) Photonic crystal cavity

(d) Fabry-Perot microcavity

(e) Bull's eye cavity

(f) Nanopost cavity

Figure 1.17: **Examples of optical cavities.** **(a)** scanning electron microscope (SEM) image of a micropillar cavity containing a QD placed between two AlGaAs/GaAs Bragg mirrors (adapted from [152]). **(b)** SEM image of a microdisk cavity (adapted from [169]). **(c)** Top: atomic force microscope (AFM) image of a L3 photonic crystal cavity. The bright contrast at the surface corresponds to a few manometer high deformation, which reveals the presence of a buried QD. Bottom: calculated field map of the resonant mode (adapted from [79]). **(d)** Sketch of an open tunable Fabry-Perot microcavity, which also shows the mode field map (adapted from [135]). **(e)** Sketch of a bullseye cavity (adapted from [114]). **(f)** Left: SEM image of a nanopost cavity (adapted from [97]). Right: calculated field map of the resonant mode [84].

**Micropillar.** Micropillar cavities consist of two Bragg mirrors produced by planar epitaxy using alternating layers of refractive index $n_1$ and $n_2$ (GaAs and AlGaAs materials are often used) with a thickness of $\lambda/4n_i$ ($i = 1, 2$, $\lambda$ is the wavelength at cavity resonance). The micropillar is formed by dry etching. The emitter is positioned in a thicker layer $\frac{\lambda}{n_1}$ between the two Bragg mirrors, where the cavity mode is confined. The reflectivity of the Bragg mirrors is controlled by adjusting the number of layers. In general, the two mirrors do not have the same number of layers, resulting in a highly reflective lower mirror and an upper mirror with higher transmission. This degrades the quality factor $Q$ but allows photons to be extracted preferentially towards the top of the structure, rather than towards the substrate.

The diameter of the micropillar is a crucial parameter in these structures. It needs to be small enough to minimize the mode effective volume. However, diameters of less than $1 - 2\,\mu$m reduce the quality factors. Indeed for an ideal structure, $Q$ is approximately constant with respect to the diameter but degrades below $\approx 4\lambda/n$. However, in practice, for small pillars, losses are dominated by surface roughness scattering resulting from imperfect fabrication [156, 107]. Effective volumes achieved in the literature are of the order of $V_{\text{eff}} \approx 10(\lambda/n)^3$ and quality factors up to $Q = 10^4 - 10^5$ [117, 154].

**Photonic-crystal cavities.** Photonic crystals are photonic structures which use a periodic arrangement of subwavelength structures to control the propagation of light via interference phenomena. The periodic arrangement aims to emulate the band structure arising in crystal lattices. In particular it is possible to create a structure with a photonic bandgap, a wavelength range where light propagation is impossible. The interesting part is that the properties of the structure can be completely engineered acting on the spacing and dimensions of the elements composing the photonic crystal. The photonic crystal can extend in 3D, or in lower dimensions. For instance a Bragg mirror is a 1D photonic crystal. From a practical point of view 3D crystals are very difficult to fabricate. Most of the structures are defined on 2D membranes as they are much simpler to work with. Photonic crystal cavities are obtained by inserting a local defect into a membrane where holes are periodically etched [49].

There are many types of photonic crystal cavities, but one of the most successful and widespread is the one obtained by removing three holes from a triangular periodicity membrane, as seen in fig. 1.17. These structures can achieve very low effective volumes of the order of $(\lambda/n)^3$ and thanks to the photonic bandgap, strongly reduce emission in free-space modes [4].

In theory one could fabricate cavities with very high quality factors. In practice the limiting factor is the sensibility to manufacturing defects, which is more constraining that in micropillars. Nevertheless quality factors as high as $Q = 3 \cdot 10^4$ has been obtained in GaAs membranes [153]. Silicon cavities working at telecom wavelength reached a quality factor of $Q = 2 \cdot 10^6$. This was possible due to the longer wavelength (around 1.55 $\mu$m) which permits photonic crystals with bigger structures and the more mature fabrication technology for silicon [106].

**Microdisks.** Microdisks are thin dielectric disks with a diameter of $1 - 10\ \mu$m and a thickness close to $\lambda/n$. Optical confinement is based on total internal reflection and the structure supports the so-called gallery modes. The gallery modes are localized at the periphery of the disk. The disk stands on a pedestal with a smaller diamter. From an optical point of view the modes are quite isolated from the substrate which enables very high quality factors. Effective volumes are generally larger than with the other approaches but this is compensated by higher quality factors. The drawback of microdisks is the light collection, indeed the light propagates in the plane of the disk which makes photon extraction tricky.

**Bullseye.** This cavity employs a circular Bragg grating around the emitter, which serves at the same time to suppress the emission into unwanted modes and to provide Purcell acceleration. It can be etched in a planar structure [104] or defined in a suspended membrane [158]. Moreover, the introduction of a dielectric spacer and of a bottom metallic reflector further improves the performance [114, 197].

This cavity combines a moderate quality factor $Q \approx 120$ and a small effective mode volume $V_{\text{eff}} \approx 0.4(\lambda/n)^3$. This allows for broadband operation, while the emission is a single-lobe, weakly divergent radiation pattern providing excellent out-coupling toward fibers or free-space collection optics.

**Open Fabry-Pérot microcavity.** An open Fabry-Perot microcavity is formed by a bottom planar Bragg mirror and top concave dielectric Bragg mirror (see fig. 1.17) [135]. One of the main differences in comparison to the previous structures is the much larger effective mode volume $V_{\text{eff}} \approx 60(\lambda/n)^3$. The $Q$ factor is determined by the mirror reflectivities of the two mirrors and can be engineered to reach $Q \approx 4 \cdot 10^5$ for cavities containing an active layer with QDs in the bottom AlAs/GaAs structure. Here the cavity can be adapted to the emitter: lateral displacement of the top mirror allows centering the cavity mode around any emitter, whereas vertical displacement allows for a fine tuning of the cavity resonance. One of the greatest assets of the cavity is the light collection: it produces a Gaussian output beam which can be coupled with high-efficiency to an optical fiber (see [179]).

#### 1.2.2.4 Summary on optical cavities

Cavities are a great tool for the control of spontaneous emission. The Purcell acceleration offers many advantages: it increases the light extraction efficiency, the emitter radiative yield and makes the emitter less sensitive to external noise sources.

The accelerated emission has paved the way for the generation of highly indistinguishable photons [165]. However, this approach comes with certain limitations. For instance, the emitter must be precisely tuned to the resonance of the cavity mode, both spectrally and spatially.

These difficulties can be overcame thanks to deterministic manufacturing processes. These techniques involve precise spatial and spectral control of QDs prior to etching the cavity. The spatial control can be achieved a posteriori utilizing scanning electron microscopes [11] or atomic force microscopes [79] to locate the QD prior to the definition of the cavity. One of the most promising approaches to resolve both issues (spatial and spectral control) comes from P. Senellart's group. Here the cavity is defined via a deterministic in situ lithography technique, allowing for the simultaneous determination of the QD's position and energy at $T = 10\text{K}$ via photoluminescence. Subsequently, another laser is employed to define an etching hard mask by exposing a photosensitive resist deposited on the sample's surface. These methodologies facilitate the production of high-quality single QD cavities but are complex and require significant fabrication process and technological resources.

To relax the spectral constrain we note that the Purcell factor as in eq. (1.31) depends on both the quality factor and the effective volume. In a cavity with a very small mode volume, one can decrease the quality factor while preserving a large Purcell factor. A modest quality factor directly yields a broad operation bandwidth. This approach has been developped by our group and will be presented more in detail in chapter 2, which is dedicated to nanopost cavities.

### 1.2.3 Waveguides

A possible strategy to achieve a broadband spontaneous emission control is to rely on a waveguide. We sill see that tight transverse confinement yields a significant spontaneous emission rate into the guided mode. However, achieving single-mode emission generally requires to also supress spontaneous emission into the continuum of free-space modes.

#### 1.2.3.1 Emission rate into the guided mode

The generalized Purcell factor for a waveguide reads:

$$F_p = \frac{\Gamma_{\text{wg}}}{\Gamma_0} = \frac{3}{4\pi}\frac{(\lambda/n)^2}{S_{\text{eff}}}\frac{n_g(\omega)}{n}, \tag{1.36}$$

where $\Gamma_{\text{wg}}$ is the rate of emission into the waveguide, $n_g$ is the group index and

$$S_{\text{eff}} = \frac{\iint n^2(\vec{r})|\vec{E}(\vec{r})|^2\, d^2\vec{r}}{n^2 \max\left(\left|\vec{E}(\vec{r})^2\right|\right)}. \tag{1.37}$$

$S_{\text{eff}}$ is the effective area of the guided mode which describes the waveguide's ability to confine light in the plane transverse to $z$. We can see an analogy between the Purcell factor in cavities eq. (1.31) and in the waveguides eq. (1.36): the spatial confinement of the mode has a similar expression and is characterized by the volume $V_{\text{eff}}$ for the optical cavities and an area $S_{\text{eff}}$ for the waveguides. The quality factor is replaced by the factor $n_g/n$. In order to increase the Purcell factor we can thus minimize $S_{\text{eff}}$ which depends both on the cross section and the refracting index difference between the waveguide and the surrounding. Increasing $n_g$ (slow light) yields a flatter dispersion curve which corresponds to a higher density of states.

In the next section we will explore some of the designs used for waveguides.

#### 1.2.3.2 Examples of waveguides

**Photonic crystal waveguides.** A photonic crystal waveguide is created by defining a line defect in a photonic crystal. These are usually defined on 2D photonic crystal membrane of thickness $\approx \lambda/n$ where light is confined thanks to a combination of total internal reflection in the vertical direction and distributed Bragg reflection in the membrane plane. Photonic crystal waveguides are very interesting for the control of spontaneous emission. The photonic bandgap can in theory completely inhibit the coupling with the free space continuum; this can lead to $\beta$ factors close to 1 [109, 120]. This is true for an ideal structure, in reality manufacturing imperfections degrade the performance of the photonic crystal causing transmission losses and thus limiting $\beta$. The photonic crystal waveguides have typically quite small mode surface $S_{\text{eff}} \approx 1/3(\lambda/n)^2$ and can reach very high group index up to $n_g = 300$

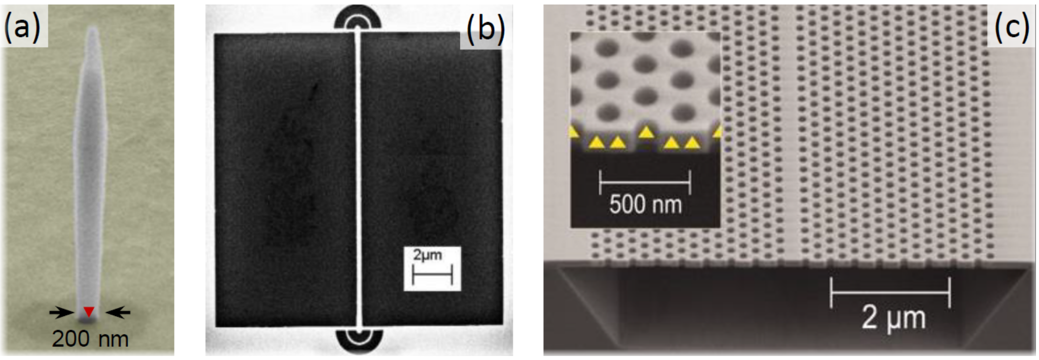

Figure 1.18: **Examples of photonic waveguides for control of SE. (a)** Tilted SEM view (false colors) of a photonic wire designed for out-of-plane emission into free-space (adapted from [37]). **(b)** Top SEM view of a suspended in-plane photonic wire with grating outcouplers [39]. **(c)** Tilted SEM view of a cleaved W1 photonic crystal waveguide [157].

in a silicon waveguide [192]. These two characteristics can be exploited to increase the Purcell factor as seen in eq. (1.36). However relying on high group index for increasing SE generally implies a reduced bandwidth and greater sensitivity to manufacturing precision which can lead to the formation of localized photonic states [157]. In order to preserve the bandwidth, and relax fabrication constraints, it is interesting to use a moderate group index. As an example in [6] a photonic crystal waveguide with $n_g \approx 60$ already yields a very large $F_p \approx 10$. P. Lodahl's group succeeded in achieving $\beta > 0.89$ over a spectral range of 20nm with a GaAs structure [118].

**Dielectric photonic wire waveguides.** These structures consist of a dielectric cylinder that can be obtained by etching a planar sample or directly by epitaxial growth. These nanowires have a high refractive index relative to the background medium, which ensures transverse confinement by total internal reflection. The confinement is optimized for diameters around $d \simeq \lambda/n$ which leads to a diffraction-limited mode surface $S_{\text{eff}} \simeq 1/4(\lambda/n)^2$.

We also have $n_g/n \approx 1$, which leads to $\Gamma_g/\Gamma_0 \approx 1$. The spontaneous emission into the guided mode is thus significant, even if there is no acceleration of spontaneous emission compared to the bulk case. In addition, a dielectric screening effect suppresses the emission into the continuum of free space modes.

The key feature of photonic nanowires is their broadband character: a large beta factor is maintained over a wide spectral range, which can go up to $\Delta\lambda > 100$ nm as calculated for an infinite wire [57]. In addition these waveguides offer a very simple structure that is robust to fabrication imperfections. Finally the broadband character of photonic wire means that they are compatible with tuning mechanisms, possibly over a large range. One of this tuning mechanism makes use of strain and will be extensively discussed in chapter 3.

Another key feature of these structures is the far field emission control. Indeed once the light is efficiently coupled to the wire we then need a way to collect it. With proper engineering of the nanowire ends one can achieve highly directive emission and a Gaussian beam profile. Two main strategies have been pursued, based on a needle shaped and a trumpet shaped tip [72, 37]. The needle shaped tip adiabatically expands the guided mode in the background. This also brings the effective index close to one, which suppresses the reflectivity of the top facet. For small taper angles ($<$ a few degree) one obtains a directive far-field emission with a Gaussian profile. In the case of a trumpet shaped tip the wire diameter slowly increases in order to adiabatically expand the guided mode inside the structure. The wire then ends with a flat surface that is covered with an antireflection coating. The trumpet shape has proven to be as efficient as the needle like but more robust to manufacturing imperfections (there is a larger tolerance on the taper angle). In all cases the structure stands on a gold-silica mirror to also collect the photons that are emitted downwards.

The major drawback of dielectric waveguides is that they not provide a significant acceleration of spontaneous emission. Indeed simulations have shown that for a dipole perpendicular to the wire axis and for an optimal wire diameter $\Gamma_{\mathrm{WG}} = 0.9\Gamma_0$ is achieved. The above-mentioned mirror improves the situation [58, 38] when located at a proper distance from the emitter in order to exploit contructive interference from the reflected light. Under these conditions, a Purcell factor $F_p \simeq 1.5$ has been measured [20].

#### 1.2.3.3 Summary on waveguides

The SE control in waveguides is based on the inhibition of SE into the 3D continuum of nonguided modes. This involves the engineering of the photonic environment around the emitter. On one side unwanted emission channels are suppressed, on the other a single-mode electromagnetic environment is created around the emitter.

The main advantage of waveguides in comparison to microcavities is the broad operation bandwidth. This is a crucial asset for the realization of tunable sources of single photons, or for the realization of sources of entangled photon pairs that exploit the radiative cascade of the QD biexciton.

Moreover, they can offer efficient coupling into photonic circuits or highly directive far-field emission, with a Gaussian angular profile.

On the other hand, this approach usually offers low Purcell factor, which is an important tool in the realization of indistinguishable photon sources.

### 1.2.4 Conclusion

The first part of this chapter introduced the concepts used throughout the whole thesis. We have seen (section 1.1) that QDs are excellent artificial atoms and that there are many interesting excitonic states that can be produced and manipulated (section 1.1.3.1). We discussed in section 1.1.4 the techniques used to excite the QDs: non resonant excitation (will be employed in chapters 3 and 4) and resonant excitation (makes the core of chapter 2). We have also explored the main methods for tuning the optical properties of QDs in section 1.1.5. More precisely we focused on stress tuning (the focus of chapter 3). Finally we have introduced the main decoherence mechanisms in section 1.1.6.

In the second part of this chapter we have seen that photonic structures can greatly benefit QDs-based emitters. More specifically we have introduced the two main approaches to spontaneous emission control: photonic cavities and waveguides.

In this thesis we will investigate two types of broadband photonic structures. In chapter 2 we investigate a new type of optical nanocavity based on a nanopost design. We will demonstrate the first resonant excitation of a QD embeded in such a structure. In chapter 3 we consider a tapered nanowire waveguide (a photonic trumpet) that is equipped with on-chip electrodes. These generate a force that bends the nanowire. The resulting strain field is leveraged to tune the QD emssion wavelenght. Chapter 4 goes beyond quantum photonics and uses the electrodes to excite the vibration modes of the wire. In these experiments, changes in the QD emission wavelength are used to detect the vibration. One exploits also here the broad operation bandwidth of the nanowire.

# Chapter 2

# Resonant excitation of a QD in a nanopost cavity

## 2.1 Introduction

We have seen in chapter 3 that both microcavities and waveguide structures enable to efficiently collect the emission of an embedded QD. A microcavity relies on the Purcell effect, which also enables an acceleration of the total radiative rate, which in turn eases the emission of indistinguishable photons. However, to reach a significant Purcell effect, microcavities typically feature quality factors of a few $10^3$. This translates into a narrow operation bandwidth, which can be a limitation for some devices. For example, it limits the spectral range over which an emitter can be tuned while preserving the emission brightness. In contrast, waveguides generally feature a much broader operation bandwidth, but typically lack Purcell acceleration of spontaneous emission. They are thus fully compatible with broadband emitter tuning, but the emission of indistinguishable photons is challenging with these systems.

In this chapter we aim for a best-of-both-worlds approach and investigate a photonic structure that offers a broadband Purcell acceleration of spontaneous emission. Our strategy relies on a nanocavity. Indeed, the Purcell factor scales as $Q/V$, the ratio of the quality factor over the mode volume. An ultrasmall $V$ (approaching the diffraction limit) yields a significant Purcell factor even for a modest $Q$ of about a few tens. This modest $Q$ is desirable, as it directly translates into a broad operation bandwidth.

Specifically we investigate a nanopost cavity, a structure that was designed in the frame of a collaboration between CEA and DTU (group of Niels Gregersen). A first generation of devices was fabricated at CEA and investigated under non-resonant QD excitation.

The promising results of the first generation of the device stimulated further theoretical investigation which provided a deeper understanding of the complex photonic properties of the device, well explored in [84] and discussed as well in this chapter. Moreover this encourages us to continue investigations, with the prospect of using these devices for the generation of indistinguishable single photons. For this, the natural next step consists of an optical characterisation in resonant excitation. This is indeed a powerful tool for a fine characterization of the emitter. In this chapter we present the first resonant spectroscopy of a QD embedded in a nanopost cavity.

This chapter starts with a discussion of the design principles, briefly discussing the simpler model which led to the fabrication of the first (and current) generation. It then expands to discuss the simulations which allowed to gain a deeper insight of devices on the optical properties of the structure. In section 2.3 the fabrication process is briefly discussed. Then in section 2.4 we show the measurement to obtain the lifetime of the transition. The core of the chapter is section 2.5 which discusses the resonant excitation measurements. The work done on resonant excitation has been performed in University of Basel in the group of prof. Richard Warburton. This successful collaboration has been possible thanks to the EU funded QUDOT-TECH project.

## 2.2 Structure design

In this section we will discuss the design principles leading to the realization of the nanopost nanocavity. The design and theoretical work is the result of a prolific collaboration with the group of Niels Gregersen at Technical University of Denmark (DTU).

If we remove the anti-reflection coating from the design of fig. 3.1 and then cut the nanowire, we are left with a cylinder, resembling fig. 2.1a. This structure is made of a GaAs cylinder over a $SiO_2$-Au mirror. The presence of the $SiO_2$ here is necessary in order to avoid the coupling to surface plasmon polaritons which would hamper the reflectivity of the guided mode ($HE_{11}$) at the bottom [58]. The modal reflectivity of the bottom mirror is 0.9. The nanocavity's top facet acts as a second mirror and, surprisingly, the modal reflectivity appears to be larger than the reflectivity for a planar interface, $(n-1)^2/(n+1)^2 = 0.3$, for the optimum diameter. In simple words, the tightly confined mode $HE_{11}$ has large $k_{/\!/}$ components that help getting a strong reflection at the GaAs/air interface. This device is thus a cavity with the fundamental mode $HE_{11}$ shown in fig. 2.1b for the resonant wavelength $\lambda_c$. We can see the presence of three anti-nodes, and the emitters are here

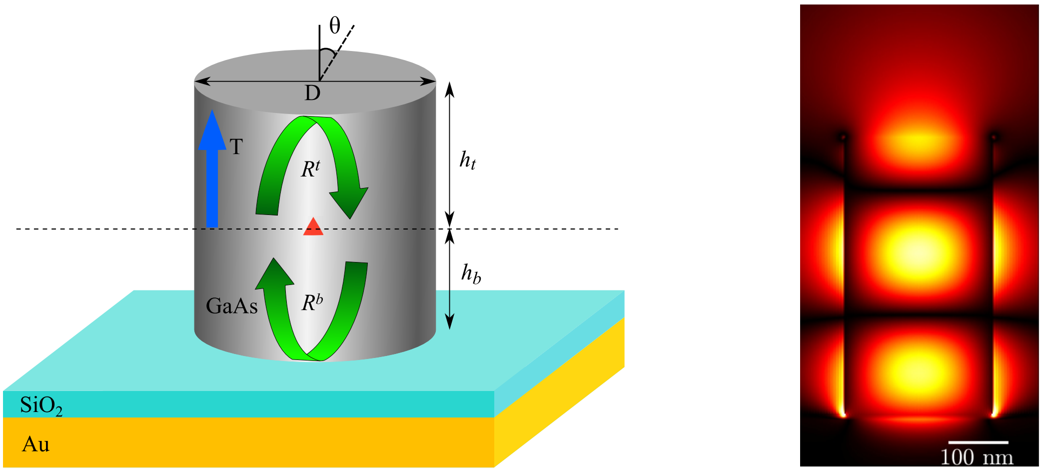

(a) (b)

Figure 2.1: **Nanopost nanocavity. (a)** shows a schematics of the nanocavity. **(b)** shows a simulation of the in plane electric field (absolute value) associated with the resonant cavity mode. This mode features 3 electric field antinodes. **(b)** is reproduced from [84].

located at the first one.

The enhancement of spontaneous emission is measured by the Purcell factor:

$$F_P \equiv \frac{\Gamma_C}{\Gamma_0}, \tag{2.1}$$

where $\Gamma_C$ is the rate of spontaneous emission in the cavity mode and $\Gamma_0$ is the rate of spontaneous emission in the bulk.

Following the derivation given in [96] a first way to study and gain insight on this system is by using a simplified single mode model (SMM) followed by 1D Purcell factor calculation. The nanocavity is treated like an infinite waveguide, the effective refractive index of the supported mode can be computed from the refractive index of the material and the diameter of the waveguide. Then the infinite cylinder is cut and both the top and bottom reflectivity can be obtained by electrostatic FEM simulations. Finally the system can be studied with a Fabry-Pérot 1D model, which gives:

$$F_P \equiv \frac{\Gamma_C}{\Gamma_0} = Re\left[\frac{(1+|r_t|)(1-|r_b|)}{1-|r_t r_b|}\right]\frac{\Gamma_{HE_{11}}}{\Gamma_0}, \tag{2.2}$$

where $\Gamma_{HE_{11}}$ is the rate of emission into $HE_{11}$ guided mode. This equation shows that the Purcell factor can be engineered acting on reflectivity of the top and bottom mirrors as well as $\Gamma_{HE_{11}}$. $r_b$ should be as high as possible

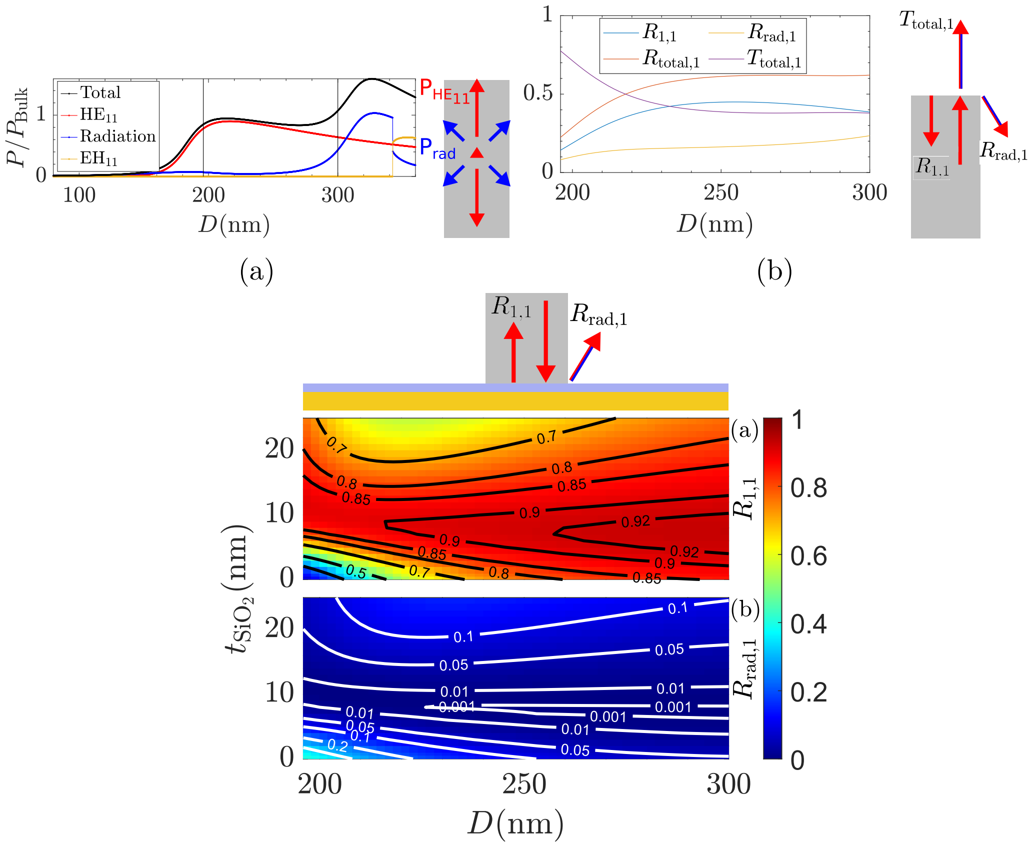

(a)

(b)

(c)

Figure 2.2: **Infinite nanowire and reflectivity at the two wire ends. (a)** is a plot of the power emitted in various channels in the infinite nanowire as a function of the diameter, D. In **(b)** we plot the reflection and transmission of the fundamental mode at the top interface as a function of the diameter, D. **(c)** shows the (top) modal reflection and (bottom) reflection into radiation mode of the fundamental mode as a function of both the diameter and the silica layer thickness ($t_{\mathrm{SiO_2}}$). Each plot shows a sketch of the studied emission channels. Reproduced from [84].

in order to limit the radiative losses. For this reason a thin layer of SiO$_2$ is necessary as seen in fig. 2.2c. We can see also that $r_b$ doesn't show a strong dependence on the diameter. However $r_t$ depends on the mismatch between the effective index of $HE_{11}$ and the refractive index of the backgroud, and thus on the cavity diameter. In general the larger the diameter the larger $r_t$, as seen in fig. 2.2b. The last factor $\Gamma_{HE_{11}}$, the spontaneous emission into the guided mode will favor a more compact mode and thus a smaller diameter as seen in fig. 2.2a for an infinite long nanowire. The interplay between these two effects gives an optimum for a diameter of $D = 240$nm. For this diameter and a $SiO_2$ thickness of 7 nm, which corresponds to the parameters of the fabricated device, we find a Purcell factor of $\approx 6.5$ and a collection efficiency of $\approx 0.4$.

Thus far we have discussed the Purcell factor but not on the collection efficiency $\epsilon$. In the design of SPS the Purcell factor is usually related to the fraction of the light that is emitted into the cavity mode [63], commonly called $\beta$:

$$\beta \equiv \frac{\Gamma_C}{\Gamma_C + \Gamma_{rad}} = \frac{Fp}{Fp + \frac{\Gamma_{rad}}{\Gamma_0}} \,, \tag{2.3}$$

where and $\Gamma_{rad}$ is the emission in (usually unwanted) radiative modes. The claim is that efficiency is proportional to the beta factor:

$$\epsilon = \Gamma_C \beta, \tag{2.4}$$

where $\Gamma_C$ is the collection efficiency of cavity mode emission by our set-up, that is governed by the numerical aperture (NA) of the first objective.

Thus for low $Q$ cavities one way to maximize the collection efficiency is to maximize the Purcell factor. This is a well established paradigm [198] for the design of SPS as we can see in microcavity pillars [198, 196, 165, 44] and also on open cavities approaches [179]. However for very high $Q$ cavities, the collection efficiency can be affected by imperfections (e.g. scattering by sidewall roughness) ([12]). Equation (2.4) is usually a good approximation to make when the light emitted into radiation modes is lost. This is however not always the case, such as in circular Bragg cavity (also known as ”bullseye”) for which high collection efficiency is obtained in a wavelength range significantly broader ($\approx$ 100nm) than the typical resonance linewidth ($\approx$ 10nm) [203, 114, 196].

The work done in [97] has shown that even for nanocavities the collection efficiency is approximately constant on a larger range for detuning bigger than the resonance width. The SMM doesn't accurately describe the nanocavity mode, due to the coupling of $HE_{11}$ to weakly guided or non-guided modes upon reflection on the facets. This has required further analysis performed using a fourier modal method (FMM) Fourier Modal Method [198], in order to gain physical insight into the role of non-guided and radiation modes.

A thoroughly analysis has been performed in [84]. This analysis shows a quite different picture for what concerns the efficiency, which is much higher than the prediction of the SMM thanks to additional transmission channels to the far-field, whose beneficial contributions are dominating over the resonant cavity effect, as shown in fig. 2.3b. The far-field emission results mainly

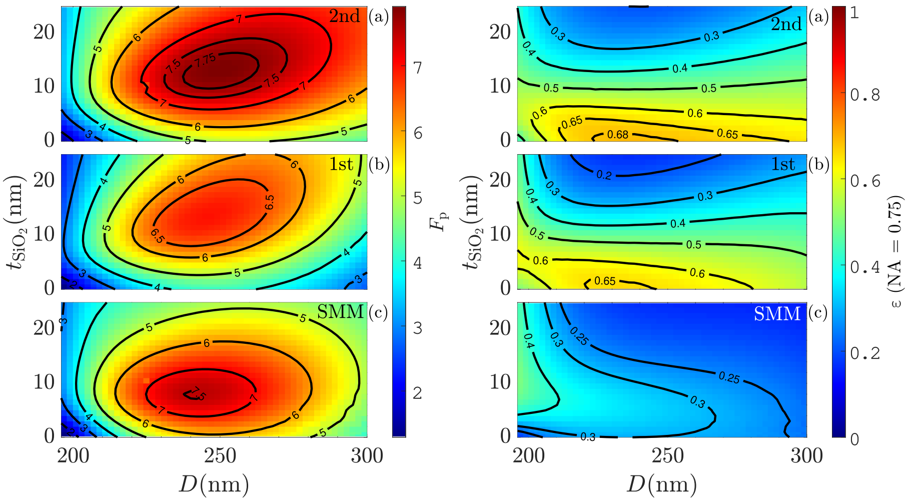

(a) (b)

Figure 2.3: **Simulation of the Purcell factor and collection efficiency.** Simulations of the Purcell factor are shown on the left while the far field collection efficiency ($\Gamma_C$) is shown on the right. The simulations take in account three distinct scenarii: QD at the 2nd antinode **(a)**, at the 1st antinode **(b)** and at any antinode using the SMM **(c)**. For each scenario a map is constructed as a function of the diameter, $D$, and the thickness of silica layer $t_{\mathrm{SiO_2}}$. The device studied in this chapter has been designed using the SMM, it features thus a 7 nm $\mathrm{SiO_2}$ layer, has a diameter of 230 nm and is placed at the first antinode. Reproduced from [84].

from 3 channels, associated with the scattering of $HE_{11}$ at the wire ends: 1) direct transmission by the top facet, 2) backscattering from the top facet and reflection on the gold-silica mirror and 3) scattering at the connection with the mirror. The far-field angular profile depends on the interference between these channels. To understand the physics behind one can look at the far field emission in fig. 2.4. Figure 2.4b shows the far field emission for the fundamental mode, while fig. 2.4c shows the far field emission for the scattered radiation. In fig. 2.4a we see the phase between the fundamental mode and the scattered radiation, for both TE and TM modes; $\beta = \sqrt{nk_0^2 - k_\perp^2}$ is the propagation constant and $k_0 = \frac{2\pi}{\lambda}$ is the free space wavenumber. The ratio $\frac{\beta}{k_0}$ goes from 1 (light directed vertically upwards) to 0 (light more and more tilted). For higher values of $\frac{\beta}{k_0}$ there is constructive interference between the direct transmission and the background radiation. For the light that propagates horizontally, the phase difference is closer to $\pi$, and thus there is destructive interference. The net remarkable result is that the in-

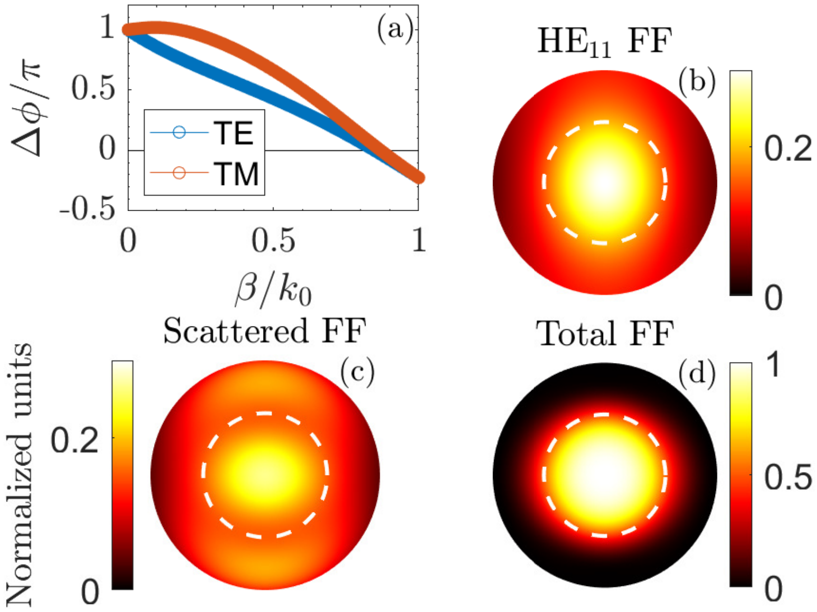

Figure 2.4: **Far field emission.** **(a)** phase difference between the direct transmission of the fundamental mode and the background continuum for TE and TM modes as a function of the propagation constant, $\frac{\beta}{K_0}$. **(b)** The far-field of the fundamental mode. **(c)** The far-field of the background continuum. **(d)** The total far-field. The white dotted line indicates NA = 0.75. The scale of **(b)** **(c)** is different from **(d)**. Reproduced from [84].

terference between the fundamental mode and the radiation modes focuses the far-field, as can be seen in fig. 2.4d. Moreover, the contribution from the scattered light, decouples the efficiency from the Purcell factor, which remains high over a large detuning (see fig. 2.3b) so that eq. (2.4) is not valid anymore. Finally contributions from radiative and evanescent modes influence also the Purcell factor. In general, the effect of these modes on the two antinodes, shows both positive and negative deviations across the parameter space (fig. 2.3a) compared to the SMM.

If we want to maximise the Purcell factor we will place the emitter at the second antinode and with a $SiO_2$ thickness of $\simeq 12$ nm we would achieve a Purcell factor of 7.75 with a diameter of $\simeq 250$ nm. Incidentally, for this particular case, the collection efficiency is also improved. On the other end if the goal is to maximise the emission efficiency we want to reduce the $SiO_2$ thickness, allowing to achieve $\epsilon = 0.68$ for no silica and a diameter of $\simeq 230$ nm. Note that the second antinode offers in general the better performances both for the Purcell factor and far field emission efficiency.

To conclude, the traditional Fabry-Pérot SMM, which typically provides an excellent description of the physics for cavity-based SPS significantly underestimates the achievable performance of the nanopost structure. Moreover since the efficiency is now decoupled from the Purcell factor future designs can achieve better performances for both of them, even if simulations have shown that the maximum of values for Purcell factor and collection efficiency are obtained for very different sets of parameters.

## 2.3 Fabricated device

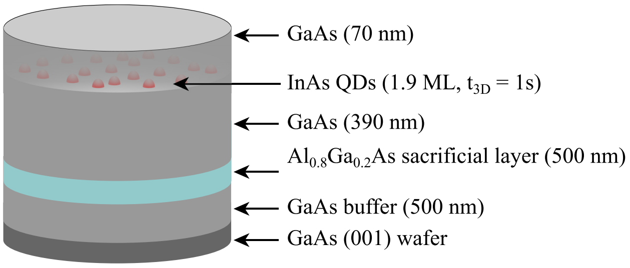

Figure 2.5: **Planar heterostructure grown by MBE.**

The section describes the fabrication process of nanowire nanocavities for broadband Purcell enhancement. The growth was done by Yann Genuist (CNRS/Institut Néel), and the clean room processing was performed by Saptarshi Kotal and Alberto Artioli.

The process begins with the growth of planar heterostructures on a semi-insulating (001) GaAs wafer using molecular beam epitaxy. The planar sample consists of a layer of self-assembled InAs QDs embedded in GaAs, resting on a sacrificial layer of $Al_{0.8}Ga_{0.2}As$ (see fig. 2.5). The substrate temperature is controlled, and arsenic-rich environment is maintained during the growth to prevent surface roughening.

After the epitaxial growth, the next step is to deposit the high reflectivity mirror, consisting of a Au and dielectric $SiO_2$ layers. Before deposition, the epitaxial sample undergoes thorough cleaning and treatment to ensure high-quality mirror deposition. A 7nm $SiO_2$ layer is deposited using electron-beam evaporation, followed by a 250nm Au layer using electron-beam metal evaporation, with a 3nm Ti layer for adherence.

The flip-chip process involves bonding the planar sample mirror-side down on a new GaAs substrate using SU-8 2005 epoxy-based photoresist. The growth wafer is partially removed by mechanical polishing and then fully removed using a $H_2O_2$ and $C_6H_8O_7$ solution. This exposes the AlGaAs sacrificial layer, which is removed by concentrated HF (50%).

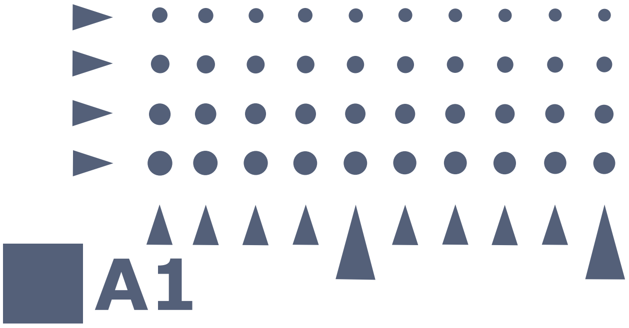

Figure 2.6: **Unit cell layout.** This pattern is repeated in both directions in order to cover the entire surface and then used to generate the lithography mask for the nanocavity sample. On the sample, a cell is indexed using a letter and a number visible in the bottom left. Within the cell we find 40 nano cavities arranged in a 10 × 4 matrix. The nano cavities nominal diameter ranges from 500 nm (bottom left) to 110 nm (top right), in steps of 10 nm moving left to right. The arrows are used for easy optical alignment and to better navigate across the sample.

To define nanostructures from a planar heterostructure using a top-down approach, a mask is defined to encompass the entire sample design layout. The mask is created from a pattern of unit cells shown in fig. 2.6.

A positive electron-beam resist is spin coated on the top of the sample. Electron-beam lithography is utilized to precisely pattern the mask on the sample's resist. Once developed the exposed resist is removed and a layer of nickel (Ni) is deposited, creating a protective hard mask for selective etching. The residual resist is removed, leaving just the Ni; at this point reactive ion etching (using $SiCl_4$, $BCl_3$ and Ar as reactants) is employed to define the desired nanostructures. Laser interferometry is utilized to determine the etch endpoint accurately. Finally, a solution of 10% $HNO_3$ will remove the Ni mask residues.

The fabrication process is completed, in fig. 2.7 we can see SEM images of the nanocavity sample after the fabrication process.

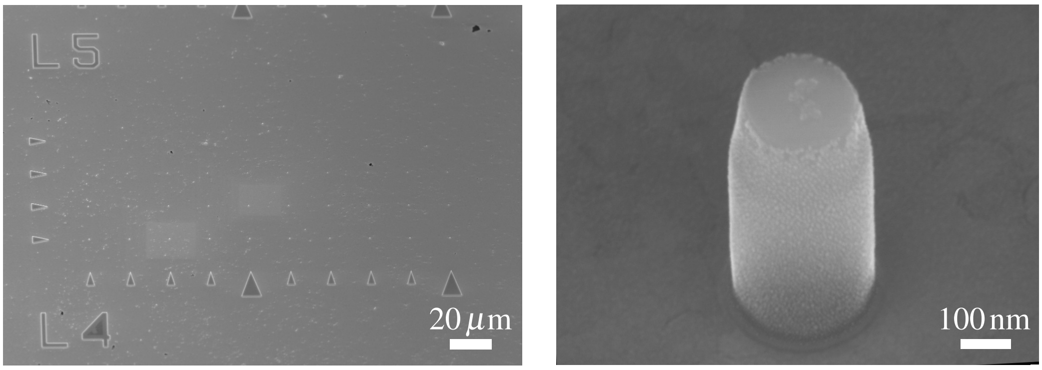

Figure 2.7: **SEM images of the fabricated nanocavity sample. (Left)** Top view of the unit cell schematized in fig. 2.6. **(Right)** close up image of a fabricated nanocavity (tilted view).

## 2.4 Preliminary characterization under non resonant excitation

In this section we perform a preliminary analysis under non resonant excitation. The objective is to identify a line that is suitable for resonant excitation studies. We search for a structure, and particularly for a QD emission line with the following characteristics: i) emission from a trion transition, ii) bright emission, iii) shows Purcell enhancement, iv) relatively isolated.

Our goal is to find a ”line” well isolated and suitable to be studied in resonant excitation. We focus on a trion transition because it features a simpler level structure as compared to a neutral exciton (no dark states, no fine structure splitting).

The lifetime is obtained using the setup in fig. 2.8, the laser excitation pulse is at 835 nm wit a power $P = 10\% P_{\mathrm{sat}}$. In fig. 2.9b is shown a typical lifetime histogram. The lifetime is obtained via a fit with the IRF curve in fig. 2.9a convoluted to an exponential decay. This gives a lifetime of 0.34 ns. The lifetime of the QDs in bulk is obtained from lifetime measurements on the square espace of 1.65 ns [96]. From these two measurements, using eq. (2.1) we obtain a Purcell factor of 4.9. This transition was choosen due to its spectral isolation and brightness both in non-resonant and resonant excitation. The measurement was done at Néel Institute with Maxime Gaignard.

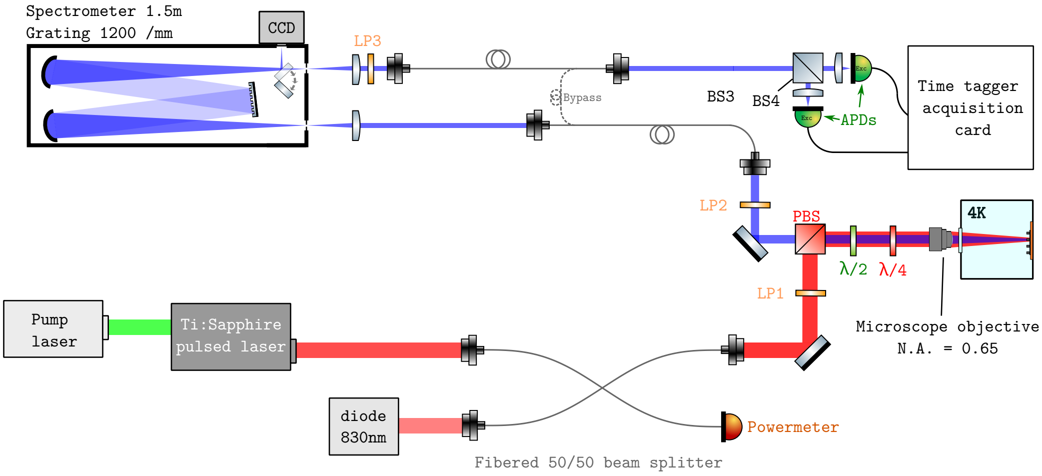

Figure 2.8: **Setup for nonresonant characterization.** The setup is easily re-configurable to perform lifetime measurements, non resonant, resonant and phonon assisted excitation, autocorrelations and HOM interferometry. Here it is used to perform a lifetime measurements. The excitation part consists of a pulsed Ti-sapphire laser and a laser diode (not used). The laser passes through a `LP` and a `PBS`. After that is sent and focused on to the sample via an objective. On the way back the laser excitation is removed and half of the signal passes through the `PBS` and goes through a monochromator. The laser cross polarization rejection is useful to prevent too much power to enter the monochromator. The light is then sent to a `BS` and finally to the `APDs`. The measure is a start/stop measure, the start being the trigger of the pulsed laser. The `APDs` are in a Hambury Brown and Twiss (HBT) configuration, but we're just interested in counts; rather than remove (and disalign) the `BS` two start/stop measurements are done by the time tagger and subsequently summed.

## 2.5 Resonant excitation

Resonance fluorescence is an excitation technique to study a TLS; it consists in using a laser which resonates with the optical transition. This allows interacting directly with a specific excitonic transition. Here ”directly” is the key word: in non resonant excitation electron-hole pairs are created into the wetting layer and randomly fall into the QD potential where they recombine at a later time. In pulsed operation the resonant pumping allows to eliminate the time jitter given by the migration of the electron-hole pair; this is essential for achieving a good indistinguishability. Furthermore, this is a ”clean” excitation scheme, which only creates electron-hole pairs in the QD. In contrast, non resonant excitation yields spurious e-h pairs around the QD,

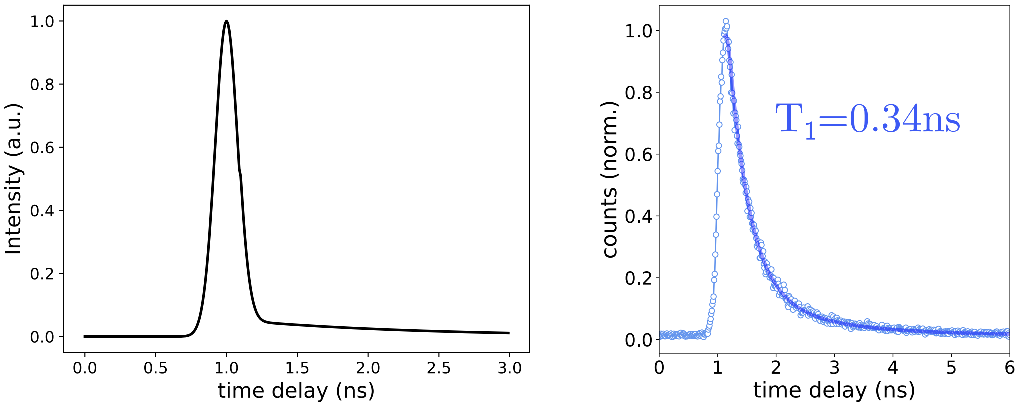

(a) (b)

Figure 2.9: **Photo-luminescence lifetime. (a)** Impulse response function (IRF) of the setup, measured with a pulsed laser. **(b)** Lifetime histogram, the fit is a convolution between the IRF and an exponential decay.

which often degrade its spectral linewidth.

We focus here on cw resonant spectroscopy, which allows for a fine characterization of the QD spectral properties. In order to be able to perform such experiments we need a tunable and narrow bandwidth laser, where narrowband means much smaller than the linewidth of the transition we want to study (we used a laser with a 300 kHz linewidth). The great challenge is that the laser used for excitation needs to be filtered out. Since it has (by definition) the same wavelength than that of the excitonic transition, it can't be filtered out spectrally. Instead we can use polarization ([100]). The excitation laser is thus linearly polarized and removed from the collected light with a polarization filter. One major problem is that there is no guarantee that the reflected laser light will still be linearly polarized. This depends on the surface of the sample and for the nanocavity, on the effect of the nanopillars on the scattered laser. Even if the surface doesn't substantially alter the polarization, the rejection is still a technically difficult step, requiring good quality optics and precise alignment.

As seen in section 1.1.3.1 the emission from a transition in a QD is also polarized. Let's suppose that we want to do RF on an exciton, due to the FSS the two exciton states have a different energy. To excite one transition I will preferably align on the corresponding dipole direction, in order to maximize the coupling, however also the emission will be in the dipole direction and thus will be filtered out. A solution is to excite with a laser polarisation making a 45° angle with respect to the exciton dipole and to align the polarization rejection at 90° with respect to the exciton dipole. In this way the laser can be properly rejected and light collected at the expense of a halved collection efficiency. As seen in section 1.1.3.1 the light from the trion is circularly polarized, the excitation is then independent of the dipole direction, however, still, half of the light will be lost in the process of laser rejection by cross polarization. The trion allows us to not bother with the FSS and so a suitable trion line will be employed in the rest of section.

RF is an essential tool for the employment of photon source in QI. In this section, I will discuss the development of this technique made during my PhD. The setup used is discussed in section 2.5.2. In section 2.5.3, I will describe the RF scans which provides information about the linewidth, in particular Gaussian noise and homogeneous broadening. In section 2.5.4, I will discuss second order correlation measurements and especially blinking of the QD source, and ways to improve it.

### 2.5.1 Theory of resonant excitation for a two level emitter

In order to gain insight into the performed experiments we would like to construct a theoretical model for our system. The interaction between light and matter has been extensively studied, we are interested in the case of a coherent beam of light exciting a QD close a transition, such as the system can be studied as a TLS. A brief treatment will be given following [74].

**Atom-field Hamiltonian.** The Hamiltonian of the system is composed by three parts: the atom, the field and the interaction term:

$$\begin{aligned} \mathcal{H} &= \frac{1}{2}\hbar\omega_{ge}\hat{\sigma}_z && +\hbar\sum_{\mathbf{k},s}\omega_{\mathbf{k}}\left(\hat{a}^{\dagger}_{\mathbf{k},s}\hat{a}_{\mathbf{k},s}+\frac{1}{2}\right) && -\hat{\mathbf{d}}\cdot\hat{\mathbf{E}} && (2.5)\\ &= \mathcal{H}_{\text{atom}} && +\mathcal{H}_{\text{field}} && +\mathcal{H}_{\text{int}} && (2.6)\end{aligned}$$

The atom is modelled as a TLS constituted by a ground state $|g\rangle$ and an excited state $|e\rangle$. These two levels are separated by an energy $\hbar\omega_{ge}$. We have introduced the Pauli operator $\hat{\sigma}_z = |e\rangle\langle e| - |g\rangle\langle g|$.

The field is described on a basis of propagating plane waves with a propagation constant $\mathbf{k}$, an angular frequency $\omega_{\mathbf{k}}$ and a transverse polarization $\mathbf{e}_{\mathbf{k},s}$ identified by the index $s = 1$ or 2. The field Hamiltonian is the sum of independent harmonic oscillators.

Finally, the light-matter interaction is treated in the dipole approximation. $\hat{\mathbf{E}} = \mathbf{e}_{\mathbf{k},s}E_{zpf}(\hat{a}_{\mathbf{k},s} + \hat{a}^{\dagger}_{\mathbf{k},s})$ is the electric field operator at the atom location (set at $\mathbf{r} = \mathbf{0}$). $\hat{\mathbf{d}}$ is the dipole operator associated with the $|g\rangle \leftrightarrow |e\rangle$ transition. In general, $\hat{\mathbf{d}}$ can be written as:

$$\hat{\mathbf{d}} = \mathbf{d_{eg}}\hat{\sigma}_+ + \mathbf{d_{eg}}^*\hat{\sigma}_- \tag{2.7}$$

with the lowering and raising operators:

$$\hat{\sigma}_- \equiv |g\rangle\langle e| \tag{2.8}$$

$$\hat{\sigma}_+ = \hat{\sigma}_-^\dagger = |e\rangle\langle g| \tag{2.9}$$

$\mathbf{d_{eg}}$ is the strength of this transition. For a linear optical dipole $\mathbf{d_{eg}} = d_{eg}\mathbf{e}_d = \mathbf{d_{eg}}^*$.

**Semiclassical model.** In the following we consider an intense laser field that impinges on the atom. We describe it as a single mode ($\mathbf{k}$, $\mathbf{e}_{\mathbf{k},s}$) of angular frequency $\omega_f$ that is placed in a coherent state $|\alpha(t)\rangle = e^{-i\omega_f t}|\alpha(0)\rangle$, with $\alpha(0) = |\alpha|e^{-i\phi}$. In the following we treat this light field as a classical field: all field operators are replaced by their expectation value. In particular the classical electrical field reads:

$$\mathbf{E}(t) = \mathbf{e}_{\mathbf{k},s}E_0\cos(\omega_f t + \phi), \tag{2.10}$$

with the amplitude $E_0 = 2|\alpha|E_{zpf}$. This procedure leads to the Hamiltonian:

$$H_{atom} + \hbar\omega_f|\alpha|^2 - \hbar\Omega_R(\hat{\sigma}_+ + \hat{\sigma}_-)(e^{i(\omega_f t+\phi)} + e^{-i(\omega_f t+\phi)}) \tag{2.11}$$

and we have introduced the Rabi angular frequency:

$$\hbar\Omega_R = E_0 d_{eg}(\mathbf{e}_{\mathbf{k},s}.\mathbf{e}_d) \tag{2.12}$$

The first term in eq. (2.11) remains unaffected, the second term gives an overall constant that is not important for the dynamics of the system and can be ignored. The third term, represents the interaction of the field with the atom and is now expressed entirely in terms of operators ($\hat{\sigma}_+$ and $\hat{\sigma}_-$) acting on the atom.

Now that the field part is traced out, we focus on the TLS. The Hamiltonian in eq. (2.11) can be written in matrix form:

$$\mathcal{H}_{\text{TLS}} = \frac{\hbar}{2}\begin{bmatrix} -\omega_{ge} & -\Omega_R\left(e^{i\left(\omega_f t+\phi\right)} + e^{-i\left(\omega_f t+\phi\right)}\right) \\ -\Omega_R\left(e^{i\left(\omega_f t+\phi\right)} + e^{-i\left(\omega_f t+\phi\right)}\right) & \omega_{ge} \end{bmatrix}. \tag{2.13}$$

In order to obtain the evolution of the system we can use the Liouville equation:

$$\dot{\rho} = -\frac{i}{\hbar}[\mathcal{H}_{\text{TLS}}, \rho], \tag{2.14}$$

where $\rho$ is the density matrix given in the $\{|g\rangle, |e\rangle\}$ basis by:

$$\rho = \begin{bmatrix} \rho_{gg} & \rho_{ge} \\ \rho_{eg} & \rho_{ee} \end{bmatrix}. \tag{2.15}$$

**Rotating wave approximation.** The Hamiltonian in eq. (2.13) has, however, an explicit time dependence which prevents a straightforward analytical solution. In order to eliminate this time dependence we introduce the rotating frame of light. The transformation into the rotating frame corresponds to the unitary transformation represented by the operator:

$$U(t) = exp\left[\frac{i\omega_f t}{2}\hat{\sigma}_z\right] = \begin{bmatrix} e^{-\frac{i\omega_f t}{2}} & 0 \\ 0 & e^{\frac{i\omega_f t}{2}} \end{bmatrix}. \tag{2.16}$$

Applying the transformation we obtain:

$$\mathcal{H}_{\text{TLS}} \rightarrow \tilde{\mathcal{H}}_{\text{TLS}} = U(t)\mathcal{H}_{\text{TLS}}U^\dagger(t) + i\hbar\frac{d}{dt}(U)U^\dagger \tag{2.17}$$

$$\rho \rightarrow \tilde{\rho} = U(t)\rho U^\dagger(t) \tag{2.18}$$

where, expanding the first term, we obtain:

$$U(t)\mathcal{H}_{\text{TLS}}U^\dagger(t) = \frac{\hbar}{2}\begin{bmatrix} -\omega_{ge} & -\Omega_R\left(e^{i\phi} + e^{-i\left(2\omega_f t+\phi\right)}\right) \\ \Omega_R\left(e^{i\left(2\omega_f t+\phi\right)} + e^{-i\phi}\right) & \omega_{ge} \end{bmatrix}. \tag{2.19}$$

We see that the unitary transformation $U(t)$ eliminates the terms oscillating at $\omega_f$ and introduces "fast" oscillating terms at $2\omega_f$. Here we are interested in the resonant excitation, where $\omega_f \approx \omega_{ge}$. In this condition and with $\Omega_R \ll \omega_f$ we can neglect the fast oscillating term. This is known as *secular approximation* or *rotating wave approximation*. The transformed Hamiltonian now reads:

$$\tilde{\mathcal{H}}_{\text{TLS}} = \frac{\hbar}{2}\begin{bmatrix} \omega_f - \omega_{ge} & -\Omega_R e^{i\phi} \\ -\Omega_R e^{-i\phi} & -\omega_f + \omega_{ge} \end{bmatrix} = \frac{\hbar}{2}\begin{bmatrix} -\delta & -\Omega_R e^{i\phi} \\ -\Omega_R e^{-i\phi} & \delta \end{bmatrix}, \tag{2.20}$$

where we have introduced the detuning $\delta \equiv \omega_{ge} - \omega_f$. Now we can write a new Liouville equation for the transformed Hamiltonian and density matrix:

$$\dot{\tilde{\rho}} = -\frac{i}{\hbar}[\tilde{\mathcal{H}}_{\text{TLS}}, \tilde{\rho}]. \tag{2.21}$$

**Introduction of the Lindblad master equation.** This model represents the idealized case of a closed system, in which the dynamics of the TLS is completely determined by the incoming field strength and the detuning from the TLS transition. In reality there are other processes which contribute to the evolution of the TLS, such as, for example, spontaneous emission and pure dephasing. These processes arise from the interaction of the TLS with the surrounding. In order to take them into account one has to move to the theory of open quantum systems.

The theory of open quantum systems considers the evolution of the system as well as the environment and the interaction between the two. In order to make the problem treatable one can try to trace out the evolution of the environment and retain only the effects on the system part. This usually requires some assumptions on the environment and the result is a so-called master equation. Depending on the assumptions that are made one can obtain different master equations. In our case, the approximations are:

- **Separability:** it requires that the state of the environment does not significantly change as a result of the interaction with the system. Moreover the system and the environment need to remain separable throughout the evolution. These assumptions are justified if the interaction is weak and if the environment is much larger than the system. In summary:
  $$\rho_{\text{tot}}(t) \approx \rho(t) \otimes \rho_{\text{env}}. \tag{2.22}$$
- **Markov approximation:** the time-scale of decay for the environment ($\tau_{\text{env}}$) is much shorter than the smallest time-scale of the system dynamics ($\tau_{\text{sys}}$). This approximation is often deemed a "short-memory environment" as it requires that environmental correlation functions decay on a time-scale fast compared to those of the system.
- **Secular approximation:** stipulates that elements in the master equation corresponding to transition frequencies satisfy $|\omega_{ab} - \omega_{cd}| \ll \frac{1}{\tau_{\text{sys}}}$, i.e., all fast-rotating terms in the interaction picture can be neglected.

This leads to the Lindblad master equation in the rotating frame of light:

$$\dot{\tilde{\rho}} = -\frac{i}{\hbar}[\tilde{\mathcal{H}}_{\text{TLS}}, \tilde{\rho}] + \hat{\mathcal{L}}(\tilde{\rho}), \tag{2.23}$$

where $\hat{\mathcal{L}}$ is the Lindbladian super operator, defined as:

$$\hat{\mathcal{L}}(\rho) = \sum_n (L_n \rho L_n^\dagger - \frac{1}{2} L_n^\dagger L_n \rho - \frac{1}{2} \rho L_n^\dagger L_n) \tag{2.24}$$

and the $L_n$ are Lindblad jump operators. Through these operators one can describe interaction with the environment. For example, for spontaneous emission the jump operator reads:

$$L_{se} = \sqrt{\Gamma_{\mathrm{rad}}}\hat{\sigma}_- \tag{2.25}$$

where $\Gamma_{\mathrm{rad}}$ is the rate of spontaneous emission.

Another effect that can be captured by the master equation formalism is the pure dephasing. In this case the associated operator is:

$$L_{pd} = \sqrt{\frac{\gamma^*}{2}}\hat{\sigma}_z \tag{2.26}$$

where $\gamma^*$ is the rate of pure dephasing.

We can rewrite the eq. (2.23) in matrix form (assuming $\phi = 0$ for simplicity):

$$\begin{aligned} \frac{d}{dt}\begin{bmatrix} \rho_{gg} & \rho_{ge} \\ \rho_{eg} & \rho_{ee} \end{bmatrix} = -\frac{i}{\hbar}\begin{bmatrix} \frac{\Omega_R\hbar(-\rho_{eg}+\rho_{ge})}{2} & -\frac{\hbar(2\Delta\rho_{ge}+\Omega_R\rho_{ee}-\Omega_R\rho_{gg})}{2} \\ -\frac{\hbar(-2\Delta\rho_{eg}-\Omega_R\rho_{ee}+\Omega_R\rho_{gg})}{2} & \frac{\Omega_R\hbar(\rho_{eg}-\rho_{ge})}{2} \end{bmatrix} \\ + \begin{bmatrix} \Gamma_{rad}\rho_{ee} & \frac{\rho_{ge}(-\Gamma_{rad}-2\gamma^*)}{2} \\ \frac{\rho_{eg}(-\Gamma_{rad}-2\gamma^*)}{2} & -\Gamma_{rad}\rho_{ee} \end{bmatrix}. \end{aligned} \tag{2.27}$$

Since $\rho$ is an Hermitian matrix $\rho_{eg} = \rho_{ge}^*$; moreover $\rho_{ee} = 1 - \rho_{gg}$, so the evolution of the system consists of 2 coupled first-order differential equations. It is useful to define the total dephasing rate:

$$\Gamma = \frac{\Gamma_{\mathrm{rad}}}{2} + \gamma^*. \tag{2.28}$$

Alternatively this relation can be rewritten as:

$$\frac{1}{T_2} = \frac{1}{2T_1} + \frac{1}{T_2^*}, \tag{2.29}$$

where $T_2 = 1/\Gamma$ is the total dephasing time, $T_1 = 1/\Gamma_{\mathrm{rad}}$ is the radiative decay time and $T_2^* = 1/\gamma^*$ is the pure dephasing time.

**Stationary state.** When the system is in the stationary state, the master equation reads:

$$\dot{\tilde{\rho}} = 0 = -\frac{i}{\hbar}[\tilde{\mathcal{H}}_{\mathrm{TLS}}, \tilde{\rho}] + \hat{\mathcal{L}}(\tilde{\rho}) \tag{2.30}$$

The intensity $I$ of the light emission by the TLS is proportional to the population of the excited state $\rho_{ee}$. It is given by:

$$\rho_{ee} = \frac{1}{2}\frac{\frac{\Omega_R^2}{\Gamma\Gamma_{rad}}}{\frac{\delta^2}{\Gamma^2}+1+\frac{\Omega_R^2}{\Gamma\Gamma_{rad}}}. \tag{2.31}$$

This equation is a Lorentzian function of the detuning $\delta$. At resonance ($\delta = 0$) the intensity of the emission is given by:

$$I \propto \frac{1}{2}\frac{P}{P+P_0} \tag{2.32}$$

where we have defined the two quantities (which have the dimensions of power):

$$P \equiv \hbar\Omega_{\mathrm{R}}^2 \qquad P_0 \equiv \hbar\Gamma\Gamma_{rad} \tag{2.33}$$

Moreover, the full width at half maximum (FWHM) ($\Delta E$) is given by

$$\Delta E = \frac{2\hbar}{T_2}\sqrt{1+\frac{P}{P_0}} \tag{2.34}$$

These two equations eq. (2.32) and eq. (2.34) can be used to calculate $T_2$.

## 2.5.2 Resonant excitation setup

This section describes the resonant excitation setup at Basel University. It uses a cross-plarization scheme to reject stray light from the excitation laser.

### 2.5.2.1 Microscope head and laser rejection

The experimental setup used for resonant excitation is shown in Figure 2.10. The sample is mounted on a sample holder, which provides a lens for focusing at the top and space for piezoelectric actuators. The sample holder is then attached to a structure which is inserted into a cylinder. The cylinder is first vacuumed for 1 day and then filled with helium at a pressure of 5 mbar. The cylinder is then inserted into a liquid Helium Dewar. The helium in the cylinder transfers heat from the sample to the liquid helium bath.

On top of the Dewar there is the optical setup for the resonant excitation and laser rejection. The laser passes through a quarter wave plate (QWP), then it enters the cylinder and it is finally focused on the sample. Part of the laser light is reflected, in addition to the light emitted by the QD in the sample. Going back this light encounters again the QWP and the PBS. The QWP is used to compensate the change in polarization resulting from the

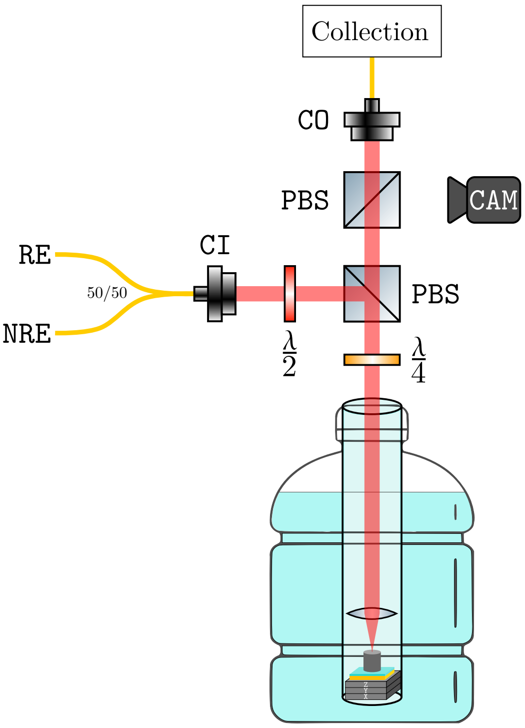

Figure 2.10: **Resonant excitation setup.** The nanocavity sample is located on the bottom of a transport Dewar, inside a low pressure He filled cylinder. On top of the cylinder is mounted a microscope for resonant excitation with laser rejection via cross polarization. The sample is mounted on piezoelectric actuators to control its position with respect to the pump beam. The `HWP` and `QWP` are mounted on rotating stages. The resonant laser `RE` enters from the left (a non resonant laser `NRE` can also be added via a fiber beam splitter `FBS`), is reflected downwards by a `PBS`, rotated by the `QWP` and focused on the sample by the lens `L`. The scattered laser, together with the sample emission exits the cylinder and is rotated again by the `QWP`. The angle of the `QWP` is adjusted in order to compensate the change in polarization resulting from the scattering from the sample. This leaves just the light emitted by the sample to pass through the `PBS` and being collected. In reality the `PBS` is not a perfect component and there is leakage of light of the unintended polarization passing through or being reflected. The addition of the `HWP` ensures that the input polarization is in the right direction, preventing some of this leakage. The second `PBS` further improves on the laser rejection, while also being used during alignment where it reflects the light on the camera `CAM`.

scattering from the sample. In this way the laser reflection can be filtered out by the PBS, while part of the emission of the QD pass straight through.

Ideally one QWP and a PBS would suffice to build a laser rejection scheme. In practice though, the PBS lets some light with unwanted polarization passing through or being reflected. In order to reduce these ”leaks” as much as possible, the input laser passes through a HWP which fixes the axis of polarization before being reflected by the first PBS. Moreover another PBS is added above the first one, which allows further rejection of laser light. In addition, to improve laser rejection, the second PBS is used during alignment: the QWP angle is changed by $\frac{\pi}{4}$ allowing the light to pass through the first PBS and be then reflected into a camera.

The laser rejection provided by this setup has been measured on 4 different points on the sample surface. For a given input power, the HWP and QWP are adjusted in order to first maximize the transmission power to the outer coupler ($P_{\mathrm{MAX}}$) and then to extinct it as much as possible ($P_{\mathrm{MIN}}$). The ratio $P_{\mathrm{MIN}}/P_{\mathrm{MAX}}$ gives the extinction rate. The four different points on the sample surface are: a random point on the gold mirror, a $230-$nm-diameter nanocavity, a $500-$nm-diameter nanocavity and the square mesa structure. For the first three cases laser rejection is $> 10^6$, while being $\approx 10^6$ for the mesastructure. These values are very promising and not expected for a non planar sample, furthermore they compare well with state-of-the-art laser rejection [138, 100].

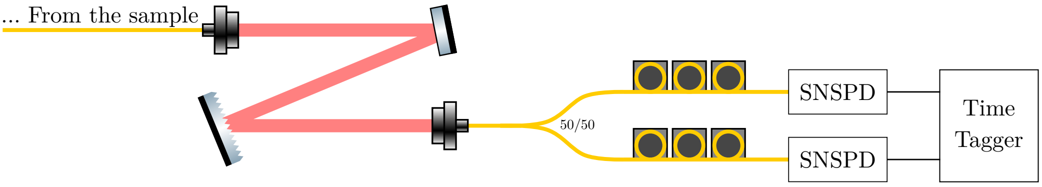

Figure 2.11: **Light collection stage.** Light from the sample is filtered in free space by a grating and sent to a fiber BS and to two SNSPDs. Note that there is a polarization controlled stage before each of the SNSPDs. Finally the time tagger can be configured in different ways, acting as a correlator for $g^{(2)}$ measurements (section 2.5.4), or to perform a linescan (section 2.5.3).

Since the excitation uses a resonant laser mixed with a non resonant one (as explained in section 2.5.3), the collected signal contains a small amount of emission from other QDs, not just the one being resonant with the laser. For that reason the light collected by the microscope is sent to a filter, shown in fig. 2.11, which has a free spectral range (FSR) of around 50GHz. The light is then splitted in half and sent to the supercondactive nanowire single photon detectors (SNSPDs). A time tagger collects the electrical pulses from the

SNSPD and can be configured to perform $g^{(2)}$ measurements (section 2.5.4), or to perform a linescan (section 2.5.3).

#### 2.5.2.2 Laser stabilization

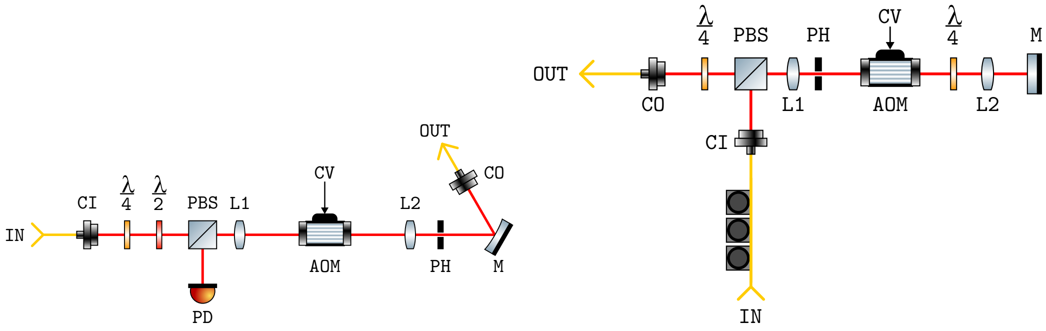

(a) Single pass (b) Double pass

Figure 2.12: **AOM based laser stabilization systems.** `CI` and `CO` are the input and output fiber couplers, `L1` and `L2` focus the laser into the AOM. The AOM is aligned in order to extract the first order scattering, the remaining orders are filtered by the pinhole (`PH`). The input `CV` controls the contrast of the diffraction grating, and thus the amount of light in the first order. In the single pass configuration **(a)** the light passes just once into the AOM. Meanwhile in the double pass configuration **(b)** the light is reflected back into the AOM by the mirror `M`. The double passage on the $\frac{\lambda}{4}$ plate rotates the light by $\frac{\pi}{2}$ in order to it to pass through the `PBS`. The double passage allows for a better rejection of the unwanted diffracted orders, which is critical for low power control.

The lasers used in the experiments are a `TOPTICA` tunable laser for the resonant excitation, and a non tunable laser at 830 nm for the non resonant excitation. In the beginning of our measurement campaign we realized that the power reaching the sample was drifting at a considerable level. The main reason was the laser polarization drifts, since free space light passes through a linear polarizer (LP) before being coupled to a fiber. Moreover, light polarization in fibers is quite sensitive to strain so every time a small change was made to the optics, the power sent to the sample was changed. For these reasons we used a stabilization system based on an acoustic optical modulator (AOM).

An AOM is a device in which a pressure wave is applied to a crystal creating differences in the refractive index through the crystal itself. For a standing wave we have a grating with a contrast dependent on the pressure

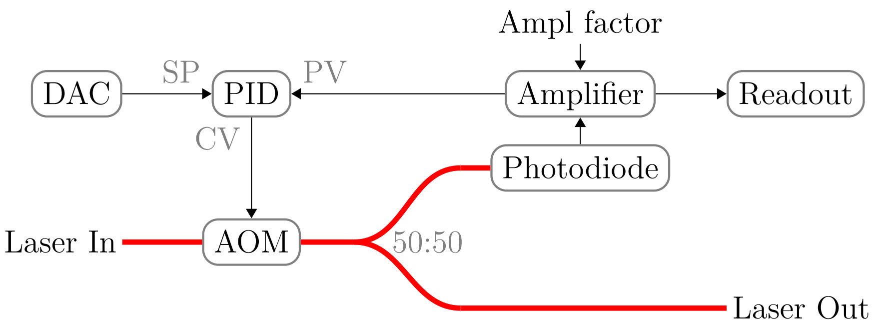

Figure 2.13: **Schematics of the laser stabilization system.** The Laser passes through the AOM system (see fig. 2.12), through the fiber BS and is collected on one end. The other branch of the BS is used for the feedback loop. The laser signal is collected by a photodiode, the current signal is amplified and fed into the process variable (PV) port of a PID system. The PID system compares the PV input with the provided set point (SP) in order to generate the proper control variable (CV) output to control the AOM. The inputs of the system are the DAC voltage and the amplification factor which together allow to cover all the output power range of the AOM system. The output is the power measured by the photodiode.

wave amplitude. The laser is thus diffracted by the grating and we collect the first order refraction. The amount of power diffracted into the first order depends on the contrast of the grating. In fig. 2.12 we can see two realizations of such a circuit, both of them used for our measurements. In fig. 2.12a we see the simpler configuration. We note that the light enters the AOM with a defined polarization, since the response is polarization dependent. When it comes to fine tuning of the power, it is very important to be able to filter out light diffracted in the unneeded orders, so the pinhole aperture is crucial, as well as the distance from the pinhole to the collimating lens `L2`. In the circuit in fig. 2.12b the light makes a double passage on the AOM. In order to extract the light on a different branch than the input one, the light is rotated by $\frac{\pi}{2}$ and a PBS is used. The advantage of a double pass circuit is a greater range of output powers attainable and a better rejection of unwanted diffracted orders compared with similar sized single pass. This comes at the cost of a more complex circuit, harder to align.

We want the AOM system of fig. 2.12 to stabilize the laser, and we do this with a feedback loop, as seen in fig. 2.13. The output of the AOM system is measured by a photodiode and then amplified; the electrical signal is then sent on a proportional integral derivative (PID) controller. The PID compares this signal with a provided set point in order to generate the proper driving signal to control the AOM circuit. The laser output power depends thus on the set point defined by the DAC and on the amplification factor of the amplifier.

### 2.5.3 Line scans

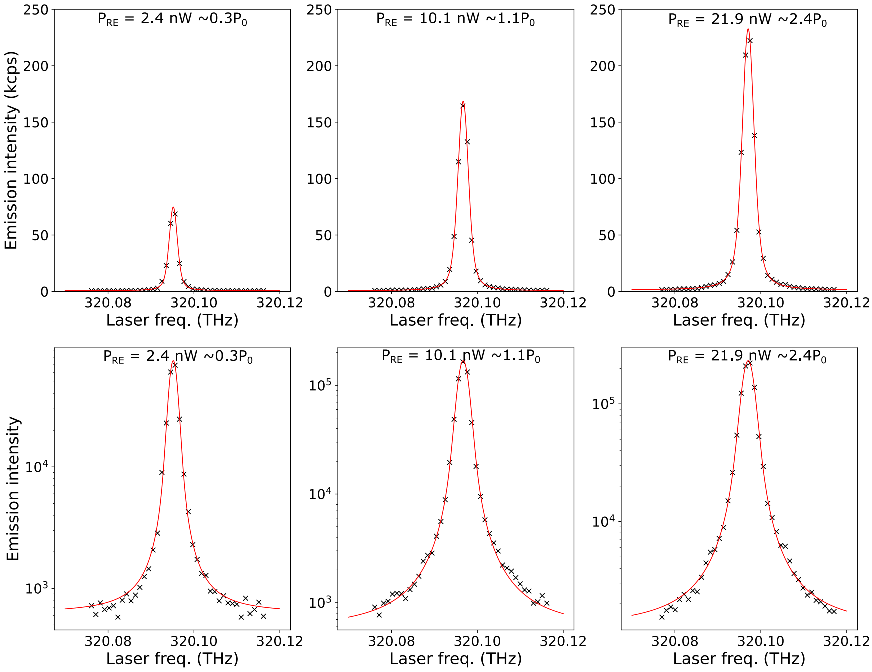

Figure 2.14: **Resonant excitation scans for different RE power.** The non-resonant laser power is fixed at 160 nW ($2\% P_{\mathrm{sat}}$). The experimental data are fitted using a Voigt function. In order to estimate the quality of the fit at resonance and around the side wings, the data and the fit are shown in linear scale (top row) and in logarithmic scale (bottom row).

In order to study the behavior of the TLS we spectrally sweep the tunable laser over the QD resonance. According to eq. (2.31) a Lorentzian function is expected expected in the case of an homogeneously-broadened emitter. The measurements are shown in fig. 2.14. As we can see the curve is not a Lorentzian but it is actually a Voigt function ($V(x; \sigma, \gamma)$), which is the convolution between a Lorentzian and a Gaussian:

$$V(x;\sigma,\gamma) \equiv \int_{-\infty}^{\infty} G(x';\sigma)L(x-x';\gamma)\,dx' \tag{2.35}$$

$$G(x;\sigma) \equiv \frac{e^{-x^2/(2\sigma^2)}}{\sigma\sqrt{2\pi}} \qquad L(x;\gamma) \equiv \frac{\gamma}{\pi(x^2+\gamma^2)}. \tag{2.36}$$

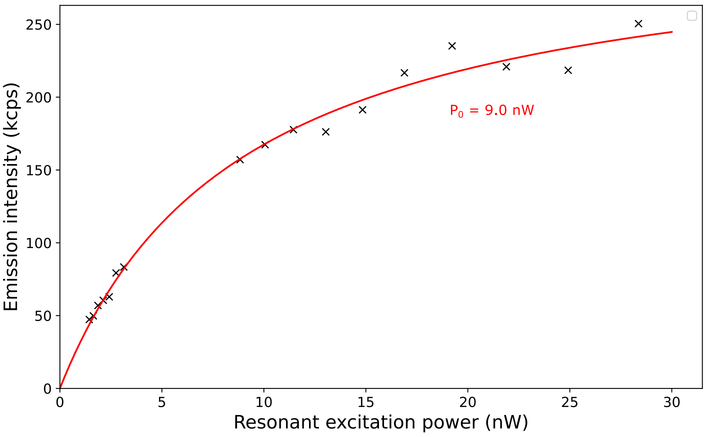

Figure 2.15: **Emission intensity saturation curve.** Evolution of the emission intensity as resonance as a function of the RE power. The curve is fitted using eq. (2.32) in order to get $P_0 = 9.0\,\text{nW}$. The non-resonant excitation laser is kept at 160 nW. The data points between 5 to 10 nW were not correctly acquired due to an error in the acquisition script.

**Spectral wandering.** We attribute the Gaussian component to spectral wandering which arises from defects, impurities, and trapped charges present in the proximity of the QD, as seen in the study conducted by [17, 89]. The influence of these perturbations depends on their time scale compared to the radiative time of the emitter. For "slow modulation" the spectral wandering mirrors the statistical spreading of the perturbations which is here taken as Gaussian noise, and thus gives rise to a Gaussian broadening. Conversely, within the "fast modulation" domain, the perturbations act on the timescale of the radiative emission or faster. These do not affect the energy of the transition since they average to 0 over the transition time, but perturb the evolution of the excited state, introducing what is called as pure dephasing. The effect of fast modulation (pure dephasing) is taken into account in the evolution of the TLS via a Lindblad operator (eq. (2.26)) in the master equation. This results into a Lorentzian broadening.

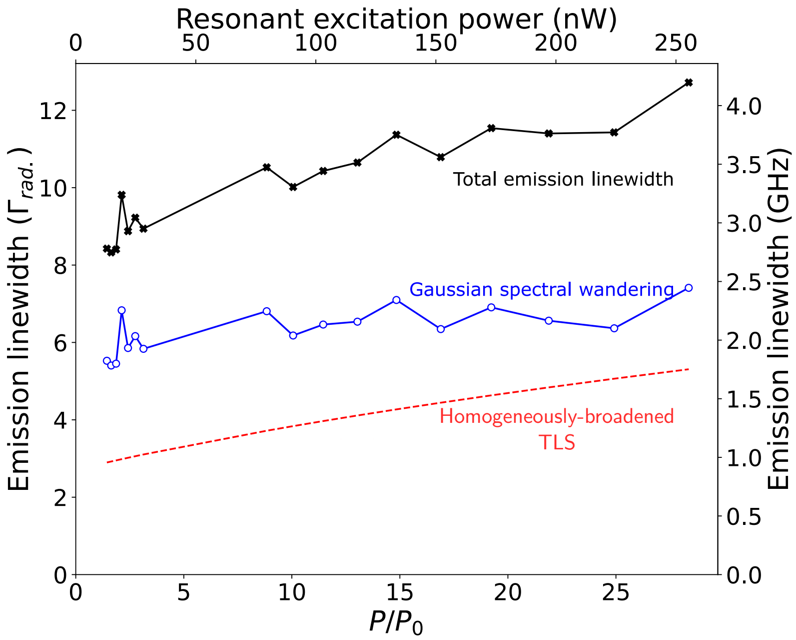

Figure 2.16: **Emission linewidth.** The linewidth of emission as a function of the RE power. The linewidth features a Lorentzian contribution from a TLS (which comprises the radiative decay, the pure dephasing and power broadening) and a Gaussian spectral wandering. The value for $P_0$ comes from the fit in fig. 2.15. From this measurement one can deduce the time $T_2$ using eq. (2.34).

The scans in fig. 2.14 are thus fitted with a Voigt function from which we can recover the Gaussian and Lorentzian parts. The Lorentzian part is attributed to the natural linewidth in collaboration with the pure dephasing, while the Gaussian contribution comes from slower noise. Supposing the same Gaussian noise for the different linewidth scans and fitting with a Voigt function, we obtain a Gaussian noise with a FWHM of $2.08 \pm 0.03$ GHz.

Performing several linescans at different laser powers we can obtain a saturation curve such as in fig. 2.15, which can be fitted using eq. (2.32) to get $P_0$. Then from the same data set we can get the Lorentzian part of FWHM (fig. 2.16) from which, via eq. (2.34) we can obtain the time $T_2 = 360 \pm 5$ ps. The time $T_2$ gives the homogeneous linewidth of the transition, since $T_1$ is known from lifetime measurements, we can get $T_2^* = 740$ ps using eq. (2.29). The homogeneous broadening reduces the $T_2$ below the radiative limit, which is $2T_1 \approx 680$ ps.

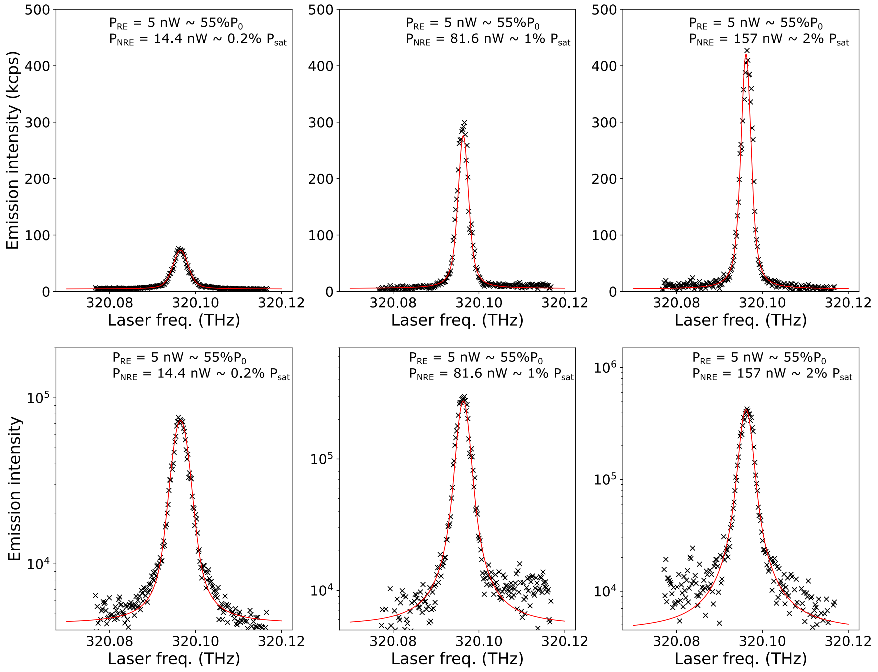

Figure 2.17: **Resonant excitation scans for different non resonant powers.** Scans over the QD resonance for different values of non resonant power. Increasing the non-resonant power causes a great enhancement of the emission intensity. The resonant laser power is fixed at 5 nW ($55\% P_{\mathrm{sat}}$). The experimental data are fitted using a Voigt function. The data and the fit are shown in linear scale (top row) and in logarithmic scale (bottom row).

**Noise reduction.** In order to reduce the spectral wandering noise, we have tried to add a non-resonant laser, as seen in fig. 2.17. The idea is that the addition of a non resonant laser will constantly create charges into the semiconductor matrix, which would provide a more stable charge environment, and hopefully reduce the fluctuations ([150]). On the other hand the laser needs to be attenuated enough in order to not influence the emission of QD via non resonant excitation. As shown in fig. 2.18 the addition of the non resonant laser greatly benefits the emission intensity. Note that the extra counts do not come from the non resonant laser, which by himself, cause a barely visible emission, comparable to dark counts. Moreover we can see that we obtain a narrower linewidth thanks to the reduction of the Gaussian component. To obtain more insights into the emission process, we also

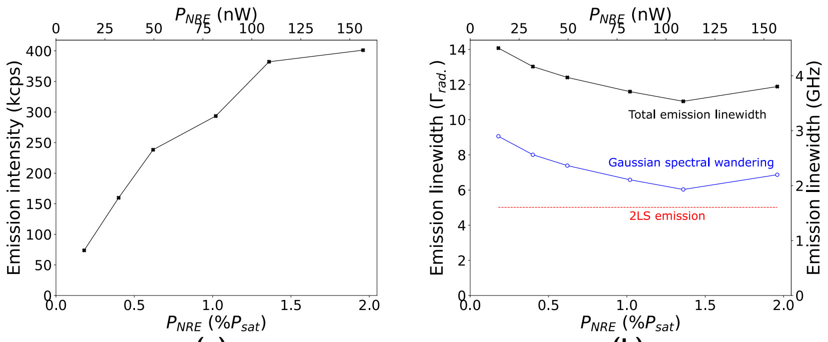

**(a)** **(b)**

Figure 2.18: **Effects of the non resonant laser on the intensity and linewidth.** **(a)** Emission intensity as a function of non resonant laser power. **(b)** Linewidth as a function of non resonant laser power. The total linewidth is made of contribution from the lorentzian emission (radiative and dephasing) of the TLS (in dashed red) and a Gaussian spectral wandering (blue).

performed intensity autocorrelation measurements.

## 2.5.4 Intensity autocorrelation measurements

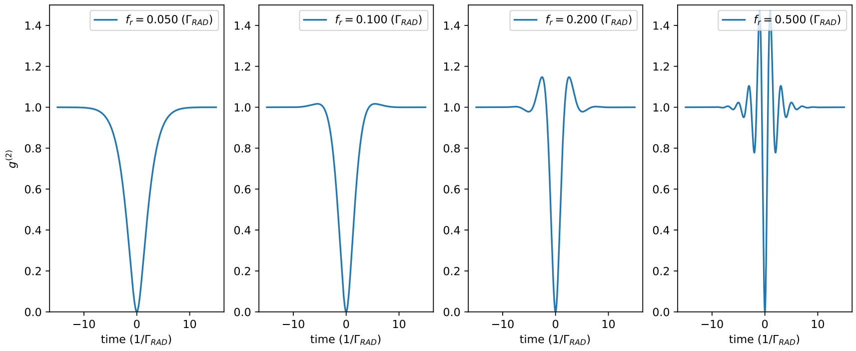

Figure 2.19: **Effect of Rabi frequency over intensity correlation simulations.** $g^{(2)}$ simulations for different values of Rabi frequency $f_r$. The radiative rate $\Gamma_{\mathrm{rad}}$ is fixed to 1 in units of $f_r$ and $\gamma^* = 0$. We see that the amplitude and frequency of oscillations increase with the Rabi frequency and the detuning. The time unit is $1/\Gamma_{\mathrm{rad}}$.

An important tool for the characterization of SPS is the intensity autocorrelations, or $g^{(2)}$. The $g^{(2)}$, for a stationary system, is defined at follows:

$$g^{(2)}(\tau) = \frac{\langle : I(t)I(t+\tau) : \rangle}{\langle : I(t) : \rangle \langle : I(t+\tau) : \rangle} = \frac{\langle a^\dagger(t)a^\dagger(t+\tau)a(t+\tau)a(t)\rangle}{\langle a^\dagger(t)a(t)\rangle\langle a^\dagger(t+\tau)a(t+\tau)\rangle}, \tag{2.37}$$

where $I(t)$ is the intensity operator and $\langle : : \rangle$ represents the expected value using normal order for creation and annihilation operators. Going back to the TLS treatment given in section 2.5.1, the $g^{(2)}$ can be expressed in terms of the raising and lowering operators of the emitter:

$$g^{(2)}(\tau) = \frac{\langle \hat{\sigma}^+(t)\hat{\sigma}^+(t+\tau)\hat{\sigma}^-(t+\tau)\hat{\sigma}^-(t)\rangle}{\langle \hat{\sigma}^+(t)\hat{\sigma}^-(t)\rangle\langle \hat{\sigma}^+(t+\tau)\hat{\sigma}^-(t+\tau)\rangle}. \tag{2.38}$$

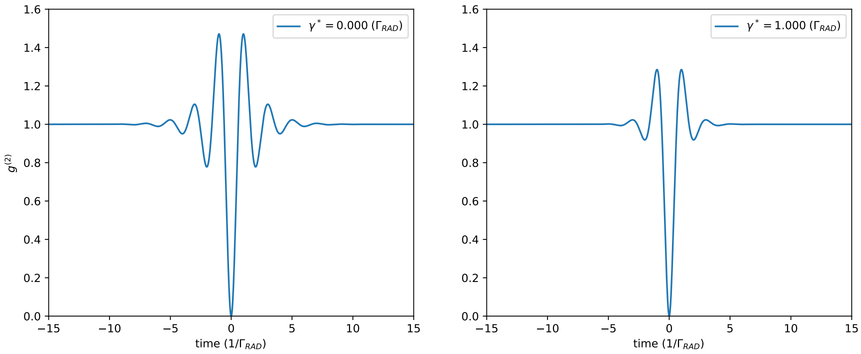

Figure 2.20: **Effect of the dephasing rate on intensity correlation.** $g^{(2)}$ simulations for different values of dephasing $\gamma^*$. $\Gamma_{\text{rad}}$ is fixed to 1 and $f_r = 0.5\Gamma_{\text{rad}}$. We see that the effect of increasing $\gamma^*$ is to dampen the amplitude of the oscillations.

We are interested to see what shape has the $g^{(2)}$ in our model. For that we can simulate the system using a python simulation toolbox called `QuTip` ([88]). Note that `QuTip` is dimensions agnostic, and assumes $\hbar \equiv 1$, so in fig. 2.19 we fix $\Gamma_{\text{rad}} = 1$ which effectively acts as frequency reference quantity. We then put $\gamma^*$ to 0 and we look at the effect of the Rabi frequency and the detuning on the $g^{(2)}$. The $g^{(2)}$ shows the characteristic antibunching dip around 0, at low powers $g^{(2)}$ is 1 just outside the dip, while increasing the power we start to see oscillations due to the fact that the TLS gets more and more coherently driven. The detuning of the laser from resonance further increases the antibunching ripples and the frequency of the oscillations. To understand the role of $\gamma^*$ we can fix the value of the Rabi frequency and make $\gamma^*$ vary, as shown in fig. 2.20. Pure dephasing induces a faster reduction of the dipole of the TLS. This smooths out the oscillations in the autocorrelation function.

Finally we know from linescans that the emitter undergoes spectral wandering. The fast part causes an homogeneous broadening of the line, and it is thus taken in account by the pure dephasing operator within the Lindblad equation. The slow part is not considered in the model, and it causes the resonance frequency to drift from the initial value. That could be included as a time dependent term in the Hamiltonian, a perturbation on the detuning with a stochastic evolution. In a first and preliminary approach, we simulate a $g^{(2)}$ many times with a detuning term drawn from the estimated noise distribution. In order to see the effects on the $g^{(2)}$ we simulate the TLS at 0 detuning, $\Gamma_{\text{rad}}$ and $\gamma^*$ comes from experiments and the noise is the Gaussian part of the linescans fits. The results are shown in fig. 2.21 where a low power (fig. 2.21a) and a high power (fig. 2.21b) regime are simulated. For both powers the addition of the noise decreases the coherence time, and for high power, it can slightly enhance the antibunching due to the Rabi oscillations.

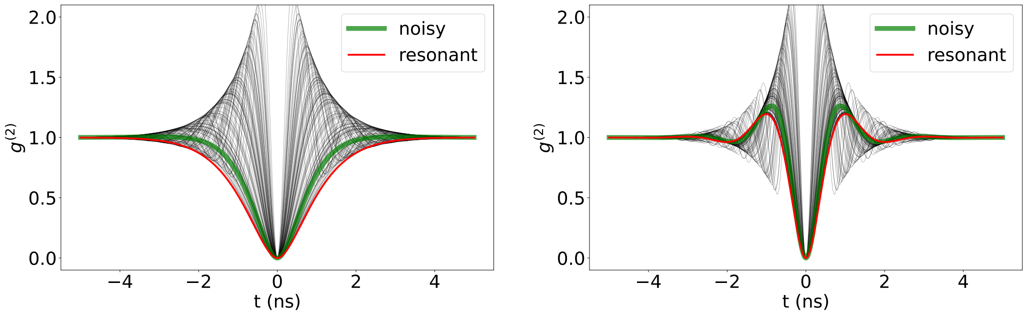

(a) (b)

Figure 2.21: **Preliminary simulation of the impact of low-frequency noise on $g^{(2)}$** Simulation of the intensity correlation function $g^{(2)}$ in presence of spectral wandering. The two figures are obtained for Rabi frequency $f_r = 0.1$ (**(a)**) and $f_r = 0.5$ (**(b)**). The red curve is the $g^{(2)}$ with no noise, while the black curves represent a $g^{(2)}$ where the noise has caused a detuning between the QD and the laser. The thick green curve shows the total effect of the inhomogeneous noise on the $g^{(2)}$.

Moving to the experiments, we realize that the $g^{(2)}$ shape is not flat as we will expect fig. 2.25. We can see that the expected antibunching dip at 0 is present. However a clear bunching is also oberved at short delays, with a g(2) that peaks around 5 and the correlation drops to 1 on a timescale of hundreds of ns, which is much slower than $T_2$.

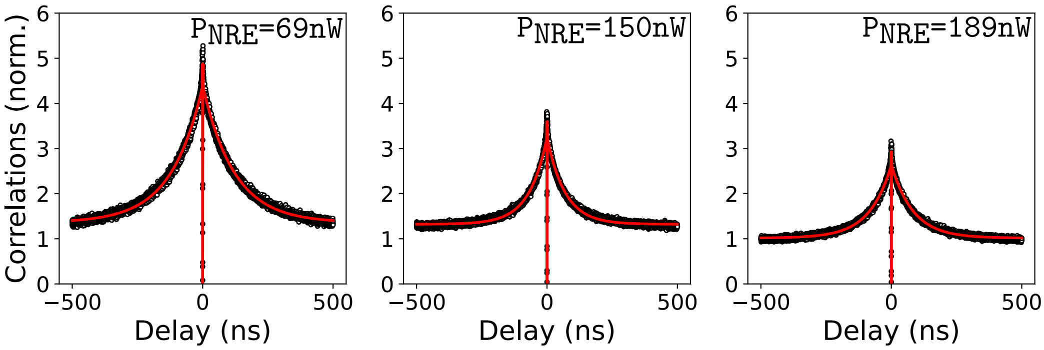

Figure 2.25: **Intensity autocorrelation measurements at long delays.** Measurements of $g^{(2)}$ for long time delays, taken at different values of the non-resonant laser power. The RE power is 20 nW ($2.2P_0$) for all the measurements. Increasing the non resonant laser power significantly decreases the blinking. The curves are fitted with eq. (2.40).

We attribute this effect to blinking. This is a common phenomenon which causes intermittent fluctuations in the emission intensity of QDs over time. It is characterized by periods of bright emission (on-states) followed by periods of no emission or very weak emission (off-states). These on-off fluctuations can happen on various timescales. The mechanism behind is complex and can involve several factors. First of all QDs are sensitive to their local environment, which can include changes in temperature, impurities and defects. These fluctuations can lead to changes in the quantum dot's electronic structure, affecting its emission properties and causing blinking. Another contribution arises from the charging and discharging of the QD with trapped charges. When a charge is present, the QD emission is shifted to another energy, leading to a quench in the resonant excitation and thus in the detected signal (off state) ([137]). When the trapped charge is released, the emission can resume, leading to an on-state. In a first approach, the effect of blinking can be modeled using the so called telegraphic-noise. Telegraphic noise, refers to a type of noise or signal variation that resembles a telegraph-like pattern of alternating high and low states. This phenomenon is often observed in electronic systems and data transmission, where the signal fluctuates between discrete levels. Following [43] let's make the assumption that the intensity emission of the whole system comes from the TLS ($I_{\text{on}}(t)$) and the blinking via a telegraphic stochastic process ($S(t)$), so that

$$I(t) = I_{\text{on}}(t)S(t). \tag{2.39}$$

Under the assumption that $I_{\text{on}}(t)$ and $S(t)$ are statistically independent, the

$g^{(2)}$ becomes

$$g^{(2)}(\tau) = \left(1 + \frac{t_{\text{off}}}{t_{\text{on}}} e^{-|\tau|\left(\frac{1}{t_{\text{on}}}+\frac{1}{t_{\text{off}}}\right)}\right) g^{(2)}_{\text{on}}(\tau), \tag{2.40}$$

where $g^{(2)}_{\text{on}}$ is the autocorrelation function of the TLS. The effect of the telegraphic noise is thus to multiply $g^{(2)}_{\text{on}}$ by a function which depends on the two characteristic times of the telegraphic noise $t_{\text{on}}$ and $t_{\text{off}}$. A measure of blinking is given by the factor $B \equiv \frac{t_{\text{off}}}{t_{\text{on}}}$, whereas the timescale is given by: $\frac{1}{\tau_{\text{B}}} = \left(\frac{1}{t_{\text{on}}} + \frac{1}{t_{\text{off}}}\right)$.

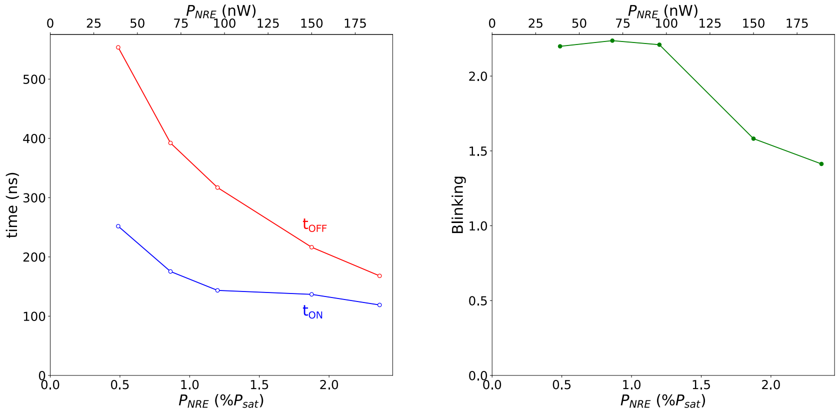

(a) (b)

Figure 2.28: **Characteristic times of blinking as a function of non resonant laser power.** **(a)** shows the characteristic times ($t_{\text{on}}$, $t_{\text{off}}$) of the telegraphic noise as a function of non resonant laser power. **(b)** shows the corresponding blinking. The resonant laser power is $P_{\text{RE}} = 5$ nW $= 55\% P_0$.

We can then try to fit the data for the $g^{(2)}$ at long delays with the formula in eq. (2.40). As shown in fig. 2.25 the fit works very well. As for the RF scan, we have tried to see if the addition of a non-resonant laser could mitigate the blinking. For this reason we have performed several scans, changing the non resonant power, while keeping RF power fixed. The measurements shown in fig. 2.25 shows that blinking greatly improves with the addition of the non-resonant laser. We can summarize the action of the non-resonant laser in fig. 2.18 where we see the evolution of $t_{\text{on}}$ and $t_{\text{off}}$ as a function of non-resonant laser power. Both of them decrease with the increasing of non resonant laser power. As shown in fig. 2.18 the blinking intensity $B$ also decreases as well as the timescale. This experiment allows us to find an appropriate value for the power of non resonant laser, one that reduces the blinking, without being too much powerful to cause significant emission.

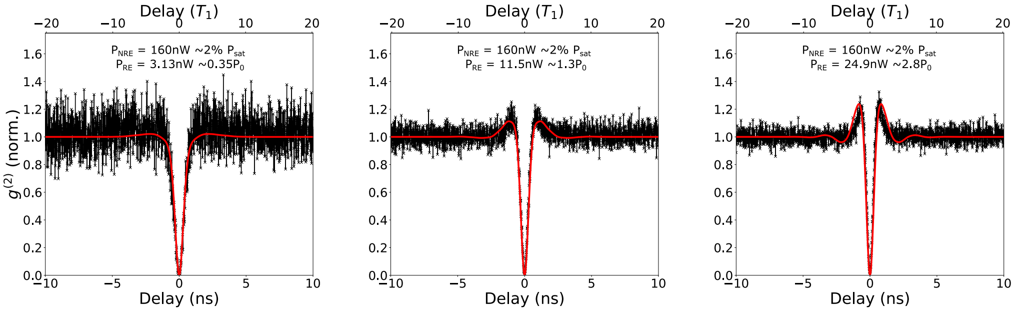

Figure 2.29: **Intensity correlation at different RE power.** The intensity correlation function $g^{(2)}_{\text{on}}$ (the effect of blinking is removed) is measured at short delays for different values of the RE power. Increasing the power we can see the emergence of Rabi oscillations. The red curve corresponds to the numerical simulation of the $g^{(2)}$.

We can fit the $g^{(2)}$ using the model discussed in section 2.5.1. For that we already know the value of $T_1$ from the section 2.4, and $T_2$, $T_2^*$ and $P_0$ from section 2.5.3. We make use of a python library called `QuTip` in order to obtain numerical simulations of our $g^{(2)}$. The spectral wandering is tricky to be inserted directly into the Hamiltonian. However we have seen in section 2.5.3 that the Gaussian part of the linewidth enlargement is due to "slow" noise which acts on a timescale larger than the timescale of the emission. This means that the $g^{(2)}$ is the result of many $g^{(2)}$ taken at different detunings, the detuning being a random variable with a Gaussian distribution. We can see the effect of this noise on a $g^{(2)}$ in fig. 2.21. With this we are able to obtain the fits in fig. 2.29, which shows that the model is able to satisfactorily fit the data. Future work is planned to investigate the impact of spectral wandering on the $g^{(2)}$.

## 2.6 Conclusion

In this chapter we have studied a novel photonic structure, simple in its conception, yet rich of interesting properties and promising as a photonic device.

**Photonic structure.** From a photonic point of view the nanopost design has shown high emission acceleration and collection efficiency across a wide spectral range. One potential application of this nanocavity is to create a bright and tunable source of indistinguishable single photons, possibly by using a piezo actuator to apply mechanical stress on QDs. Following these promising results, an extensive numerical analysis has shown that the traditional Fabry-Pérot single mode model underestimates the performance of nanopost structures as SPS. Indeed, perhaps surprisingly, light scattered into radiation modes, which is usually ignored, participates into Purcell enhancement and improves collection efficiency. This scattering mechanism also decouples collection efficiency from the Purcell factor. These results suggest the potential for unconventional SPS design, particularly in non-resonant conditions. Moreover, the simplicity of the device, makes it appealing for use with emerging material systems that may not be as technologically mature as established III-As semiconductors.

**Resonant excitation spectroscopy.** From a technical point of view, it is the first time that RE measurements have been done on such a structure. This is by no means trivial, since a good laser rejection is needed. This means, first that the scattering on the sample surface needs to change the polarization in an homogeneuos way. Moreover the optical setup needs to be carefully assembled and aligned in order to obtain a good laser rejection. This result is essential for the future of these structures in building a bright and tunable source of indistinguishable single photons. This has solely been possible thanks to the expertise of the group of prof. Richard Warburton.

**Coherence times.** The RF laser scans have given access to the linewidth of the QD emission. This has prompted us to construct a model for the emission linewidth and to determine the various factors that contribute.

In this regard we've been able to obtain the dephasing time $T_2$. The ratio $T_2/2T_1 \simeq 0.52$ is relatively far from the ideal radiative limit of $T_2/2T_1 = 1$ During his PhD at Néel Institute, Maxime Gaignard measured a Hong Ou Mandel visibility of 80% for photons separated by 3 ns emitted by exactly the same device. This suggests $T_2/2T_1 = 0.8$. Our measurements are however integrated over relatively long periods of time ($\approx 1$ minute for a linewidth scan). This discrepancy could also come from other sources of noise with a Lorentzian spectral density, slow enough to not cause pure dephasing but affecting photons emitted on larger timescales than the lifetime of the transition.

Finally, by precisely measuring and fitting the emission line profile, we were able to measure the spectral wandering of the emission line. Due to slow modulations of the perturbations, it has a Gaussian shape with a full width at half maximum of 2.08 GHz which shows no correlation with the resonant excitation power.

**Blinking and nonresonant excitation.** The measurement of the autocorrelation at long delays shows that the QD is blinking. However this effect can be greatly mitigated by the addition of a non-resonant laser, which has the effect of creating a more stable charge environment around the emitter. This is a precious tool for more advanced experiments with these structures. It is also a reminder that the charge control is crucial for having good sources of single photons and that new designs would need to tackle this problem.

**Perspectives.** These RE measurements have permitted a better characterization of the system. The mitigation of the blinking opens the doors to other experiments (such as four wave mixing spectroscopy) which will allow for an even better understanding of the device. There are two main directions of improvements: from a photonic point of view (as discussed in section 2.2) thanks to more precise simulations, is worth experimenting with different geometric parameters in order to get higher collection efficiency or Purcell factors. From a technical point of view, in order to improve on the spectral wandering we can think of new designs. These are usually based on the addition of an electric field which should allow to evacuate the trapped charges. This can be done for instance via electrodes connected to a PIN junction ([165, 135]).

# Chapter 3

# Electrostatic strain tuning of QDs embedded in a photonic wire antenna

This chapter is adapted from the article: Matteo Finazzer, Rana Tanos, Yoann Curé, Alberto Artioli, Saptarshi Kotal, Joël Bleuse, Yann Genuist, Jean-Michel Gérard, Fabrice Donatini, and Julien Claudon. "On-Chip Electrostatic Actuation of a Photonic Wire Antenna Embedding Quantum Dots". In: *Nano Letters* 23.6 (2023). Publisher: ACS Publications, pp. 2203–2209

## 3.1 Introduction

Quantum dot (QD) embedded in photonic structures feature key assets for photonic quantum technologies [115]. In particular, this solid-state platform can generate various non-classical states of light on-demand, with high brightness and fidelity [163, 81, 181]. However, applications requiring multiple sources in spectral resonance face a significant challenge. Whatever the growth technique, two given QDs generally slightly differ by their geometry or alloy composition, resulting in distinct emission wavelengths. Spectral tuning of the QD emission is mandatory to overcome this limitation. Among various possible 'tuning knobs', such as temperature [50], electrical [55] and magnetic [155] fields, mechanical stress stands out. This approach, usually implemented with a piezo actuator [122], offers a large tuning range while preserving the excellent QD optical properties [56, 201, 182, 34]. In practice, maintaining the source brightness upon spectral tuning requires a broadband photonic structure such as an optical nanocavity [112, 113, 195, 95, 71, 141], a microlens [75] or a waveguide [36, 151, 133, 6, 176]. Whereas piezo actuators were successfully integrated with most of these platforms [98, 48, 129, 159], an alternative strategy can be employed to strain photonic wire antennas. When a force is applied on the free end of a nanowire, it bends. As a result, QDs embedded near the anchored end experience a large strain. This modifies their bandgap energy, leading to the desired spectral tuning. Recently, this idea was demonstrated by simply pushing the top part of a photonic trumpet with a micro-manipulator tip [188].

In this chapter, we build on this proof-of-principle experiment and demonstrate a practical, integrated device in which on-chip electrodes generate an electrostatic bending force. Control over the amplitude and bending direction is achieved thanks to two distinct bias configurations. This enables to blueshift or redshift the emission of any individual QDs embedded in the wire.

The chapter is structured as follows: in section 3.2 we will briefly discuss the ideas behind the design and the relevant geometrical and physical quantities, used through the chapter. In Section 3.3 we provide the theoretical framework on which the design is based. The mechanics of the device is analyzed using the Euler-Bernoulli beam theory, which allows us to identify the relevant geometrical parameters and their influence on the device behavior. Moreover the effect of strain on QD light emission is discussed. Finally finite elements method (FEM) simulations are used to investigate the different components of the device in order to have a complete picture on the mechanics, electrostatic and electrical behavior of the device. The investigated device we fabricated by Saptarshi Kotal and Alberto Artioli. The steps of the fabrication process are discussed in section 3.4, as well as the mask design and the sample layout. Finally section 3.5 covers the sample characterization and the experimental results.

## 3.2 Device concept

As shown in fig. 3.1a, we consider a photonic trumpet, a conical nanowire antenna that efficiently funnels the emission of embedded QDs into a Gaussian output beam [133, 170]. The antenna is here made of GaAs, stands on a planar silica/gold mirror and features a top $Si_3N_4$ antireflection layer (thickness: 115 nm) (fig. 3.1b). The trumpet is oriented along the 'vertical' $\hat{\mathbf{z}}$ axis. Through the paper, we set dimensions equal to the ones of the investigated devices: height $h = 16.4\,\mu$m, bottom radius $r_b = 130$ nm and top radius $r_t = 800$ nm. Close to its base, the trumpet embeds a single sheet of self-assembled InAs QDs. The vertical QD location is precisely controlled ($z_{\mathrm{QD}} = 95$ nm), but their lateral location in the trumpet cross-section is

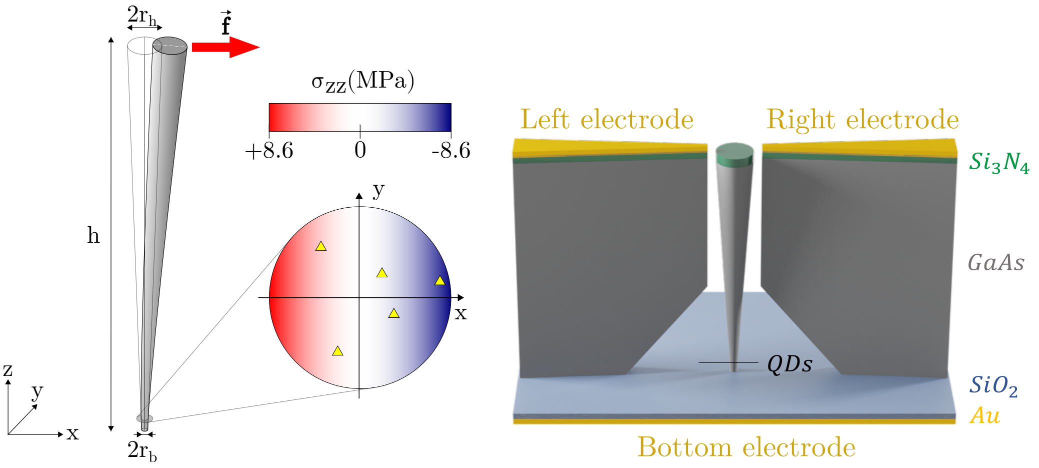

(a) (b)

Figure 3.1: **Device concept.** (a) Applying a force $\mathbf{f} = f_x\hat{\mathbf{x}}$ on the trumpet top facet generates stress in the QD cross-section. Map of the longitudinal stress component ($\sigma_{zz}$) in the QD section, calculated for $f_x = 1$ nN. The triangles represent randomly-located QDs. (b) Schematics of the device: three on-chip electrodes generate an electrostatic bending force.

random.

In our device, the bending force is generated by three on-chip electrodes fig. 3.1b. The bottom gold mirror serves as a first, planar electrode (B). In addition, two needle-like electrodes (left, L and right, R) are located close to the top facet, at a distance of $d_L = d_R = 550$ nm. We first consider bias configuration R: R is biased at a potential $V_{\text{dc}}$, whereas all other electrodes are grounded. This setting establishes a highly inhomogeneous electrical field between the tip of R and the bottom plane. The large relative permittivity of GaAs ($\epsilon_r = 12.9$) enables the build-up of a strong dielectric polarization of the trumpet, which is then attracted towards the tip of R — the area of most intense electric field. We will see in the next section that free carriers associated with non-intentional doping of GaAs further increase the trumpet polarization and thus the applied force.

The electrostatic force features a roughly quadratic voltage dependence: whatever the sign of $V_{\text{dc}}$, the trumpet is always attracted toward the right electrode in configuration R. We achieve control over the bending direction by using the mirror-symmetric bias configuration L. A potential $V_{\text{dc}}$ is applied to the left electrode, whereas all other electrodes are grounded. The trumpet is then attracted towards L. The inversion of the bending direction reverses the stress map and enables obtaining red and blue shifts for any QD location, thereby doubling the spectral tuning range.

## 3.3 Theoretical background

In this section, we first introduce a simple analytic model to describe the stress in a bended photonic trumpet and the resulting energy shift of a strain-tuned QD (sections 3.3.1 and 3.3.2). The second part of the section discusses FEM simulations which provide a complete picture of the whole device. First mechanical simulations allow to validate the predictions made by the theoretical model. Then the electrical behavior of the sample is studied. Finally the electrostatic simulations provide the strength of the applied force to feed the mechanical model.

### 3.3.1 Euler-Bernoulli beam theory

A beam is a structure which responds to a force applied laterally with respect to its main axis and where the mechanical response is dominated by bending. If the lateral deflection is small and shear stresses can be neglected, these kind of structures can be studied using the Euler-Bernoulli beam theory, which is a simplification from the more general theory of linear elasticity. Therefore, the theory can be used to study the physics of the bending of a tapered beam.

The geometry is the one of the fig. 3.1a: the conical trumpet is anchored at its base ($z = 0$) and its top facet ($z = h$) is free. At $z = h$, one applies a transverse force $\mathbf{f} = f_x\hat{\mathbf{x}}$ on the top facet center (with an associated moment $\mathbf{M}_{\mathrm{O}} = hf_x\hat{\mathbf{y}}$) which leads to a deflection $\mathbf{u} = u(z)\hat{\mathbf{x}}$ of the neutral axis of the beam. The scalar deflection $u(z)$ satisfies the static Euler-Bernoulli equation:

$$\frac{d^2}{dz^2}\left[YI_y(z)\frac{d^2u(z)}{dz^2}\right] = 0. \tag{3.1}$$

Here, $Y$ is the Young modulus of the beam material; $I_y(z)$ is the second moment of area with respect to the $y$ axis. For a beam that features a circular cross-section of radius $r(z)$, $I_y(z)$ reads

$$I_y(z) = \frac{\pi}{4}r(z)^4. \tag{3.2}$$

We consider here a linear taper for which the cross-section radius at height $z$, $r(z)$, increases linearly from $r(0) = r_b$ to $r(h) = r_t$ according to

$$r(z) = r_b\Big[1 + \delta(z/h)\Big], \tag{3.3}$$

with $\delta = r_t/r_b - 1$ being a parameter that characterizes beam tapering. By successive integration of eq. (3.1) and taking into account the set of four boundary conditions:

$$\frac{d}{dz}\left[YI_y\frac{d^2u}{dz^2}\right](L) = -f_x, \quad \frac{d^2u}{dz^2}(L) = 0, \quad \frac{du}{dz}(0) = 0, \quad u(0) = 0, \tag{3.4}$$

one obtains the beam deflection $u(z)$. It reaches a maximum at the level of the top facet $(z = h)$:

$$u(h) = \frac{4}{3\pi}\frac{h^3}{Yr_b^3r_t}f_x. \tag{3.5}$$

Compared to a cylindrical beam of identical bottom radius, beam tapering (with $\delta > 0$) reduces the free end displacement $u(h)$ by a factor of $(r_t/r_b)$. For the geometry considered in main text, one obtains $u(h) = 12.4\,\mathrm{nm}$ for $f_x = 1\,\mathrm{nN}$. The normalized deflection profile is given by:

$$\frac{u(z)}{u(h)} = (z/h)^2\left(\frac{1+\delta}{1+\delta(z/h)}\right)^2\left(\frac{3-(z/h)+2\delta(z/h)}{2+2\delta}\right). \tag{3.6}$$

The longitudinal stress $\sigma_{zz}$ is deduced from eq. (3.6) using

$$\sigma_{zz}(x, z) = -Yx\frac{d^2u(z)}{dz^2}. \tag{3.7}$$

We note that $\sigma_{zz}$ does not depend on $y$. The stress reaches a maximum (in absolute value) at the base $(z = 0)$ for the two symmetric sidewall points satisfying $|x| = r_b$. At $x = +r_b$, the stress is compressive for $f_x > 0$ and reaches

$$\sigma_{zz}(r_b, 0) = -\frac{4}{\pi}\frac{h}{r_b^3}f_x. \tag{3.8}$$

For a given applied force, the maximum stress *at the base* is thus identical for tapered and untapered beams having identical $r_b$. Put in another way, beam tapering has no impact on the stress at the base $(z = 0)$.

When $z \neq 0$ the general expression for the stress inside the tapered beam is:

$$\sigma_{zz}(x, z) = -\left(\frac{4hf_x}{\pi r_b^3}\right)\left(\frac{x}{r(z)}\right)\left(\frac{1-z/h}{(1+\delta z/h)^3}\right), \tag{3.9}$$

As illustrated in fig. 3.1a, half of a given cross section is stretched $(\sigma_{zz} > 0)$, whereas the other one is compressed $(\sigma_{zz} < 0)$. The stress is null on the $x = 0$ diameter and reaches a maximum in absolute value for the two circumference points with $x = \pm r(z)$.

| | $Y$ (GPa) | $\nu$ | $\epsilon_r$ |
|---|---|---|---|
| GaAs | 85.9 | 0.31 | 12.9 |
| $Si_3N_4$ | 250 | 0.23 | 7.5 |
| $SiO_2$ | 70 | 0.17 | 3.9 |
| Au | 70.0 | 0.44 | – |

Table 3.1: Material parameters.

Beam tapering profoundly affects the longitudinal stress distribution in the trumpet:

$$\frac{\sigma_{zz}(x,z)}{\sigma_{zz}(r_b,0)} = \left(\frac{x}{r(z)}\right)\left(\frac{1-z/h}{(1+\delta z/h)^3}\right). \tag{3.10}$$

This can be directly traced back to the $r(z)^4$ dependence of $I_y(z)$.

We compared this analytic model to finite-element simulations performed with the linear elasticity module of the software COMSOL. All materials are supposed to be isotropic from a mechanical point of view; their Young modulus ($Y$) and Poisson coefficient ($\nu$) are given in table 3.1. A transverse force $\mathbf{f} = f_x\hat{\mathbf{x}}$ with a magnitude $f_x = 1\,\mathrm{nN}$ is applied at the top facet center of a conical GaAs trumpet. In a first simulation, we used the same boundary condition as in Euler-Bernoulli calculation: the bottom facet is clamped. One then obtains an excellent agreement between analytic and finite element simulations: the stress $\sigma_{\mathrm{zz}}$ at the QD level (95 nm above the clamped base) is 4% smaller in the simulation, while the top facet deflections $u(h)$ are almost identical. We additionally investigated the effect of a deformable GaAs and Au substrate. These changes have a minor impact on the calculated stress in the QD section. For a conical trumpet, Euler-Bernoulli beam theory thus offers an excellent estimate of the stress in the QD section.

### 3.3.2 Energy shift of the QD emission

We have seen in the previous section that the stress tensor in a bended trumpet is dominated by the $\sigma_{\mathrm{zz}}$ component. This mechanical stress can impact the QD emission energy in many ways. Through the deformation potentials [19], the resulting strain affects the bandgap energy of the QD material. Since strain also affects the band energy of the barrier material, this will also change the confinement potential seen by electrons and holes. Strain also modifies the physical dimensions of the QD, hence the confinement energy. Finally, for some crystalline directions, stress can also induce a piezoelectric effect, which impacts the QD emission through the quantum-confined Stark effect.

At lowest order the energy shift experienced by a QD is related to the stress by a linear relation: a given QD located at $x_{\mathrm{QD}}$ undergoes an energy shift $\Delta E = s\sigma_{\mathrm{zz}}(x_{\mathrm{QD}})$. The leading contribution to the tuning slope $s$ is the change in the bandgap energy of the QD material. Here, the trumpet longitudinal $z$ axis coincides with the growth direction. For an uniaxial stress applied along this direction, $s$ reads [171, 10]

$$s = \Big[a_{\mathrm{QD}}(1-2\nu_{\mathrm{GaAs}}) + b_{\mathrm{QD}}(1+\nu_{\mathrm{GaAs}})\Big]/Y_{\mathrm{GaAs}}. \tag{3.11}$$

Here, $Y_{\mathrm{GaAs}} = 85.9\mathrm{GPa}$ and $\nu_{\mathrm{GaAs}} = 0.31$ are the Young modulus and Poisson ratio of GaAs, respectively; $a_{\mathrm{QD}}$ and $b_{\mathrm{QD}}$ are the hydrostatic and shear deformation potentials of the QD, respectively. We assume an $\mathrm{In_{0.5}Ga_{0.5}As}$ alloy composition and perform a linear interpolation between InAs and GaAs [194] to obtain $a_{\mathrm{QD}} = -7.2$ eV and $b_{\mathrm{QD}} = -1.9$ eV. Equation (3.11) then yields $s = -61\,\mu\mathrm{eV.MPa}^{-1}$. For example, a tiny force of 1 nN, which is the typical magnitude of the force obtained via electrostatic actuation, already generates $\sigma_{zz} = -8.6\,\mathrm{MPa}$ ($\epsilon_{zz} = -0.01\,\%$) for $x_{\mathrm{QD}} = r(z_{\mathrm{QD}})$. The corresponding spectral shift $\Delta E = 530\,\mu\mathrm{eV}$ exceeds the QD radiative linewidth ($\sim 0.7\,\mu\mathrm{eV}$) by nearly three orders of magnitude. Trumpet bending is thus an efficient way to tune the emission of embedded QDs. In this example, the minute wire deflection (top facet deflection of 12 nm, bending angle below 0.05°) does not affect light collection.

### 3.3.3 Electromechanical numerical simulations

We evaluate in this section the electrostatic bending force and the maximal QD spectral shift. To obtain a correct order of magnitude, it is necessary to take into account the free carriers in GaAs that result from non-intentional p-type doping. Given the size of our device, 3D numerical simulations combining semiconductor physics, electrostatics and linear elasticity are too computationally demanding. Therefore, we adopt a simplified, cascaded approach:

1. First we describe the electrode stack using an analytic 1D model.

2. Next we perform 3D electrostatic simulations and evaluate the bending force in two limit cases:

    - **Dielectric trumpet**: no free-carriers, but already significant dielectric polarization, yielding a minimal value for the bending force.

- **Metallic trumpet**: maximal polarization associated with free carriers, yielding an upper bound for the bending force.

Our weakly doped semiconductor ($p \sim 10^{15}$ cm$^{-3}$) lays between these two extreme cases.

3. Finally, we plug these results into linear elasticity simulations (using the finite elements method software COMSOL) to obtain the stress in the QD section. One then deduces the maximal spectral shift using the tuning slope established in section 3.3.2, which can be compared to experimental results.

#### 3.3.3.1 1D model of the electrode stack

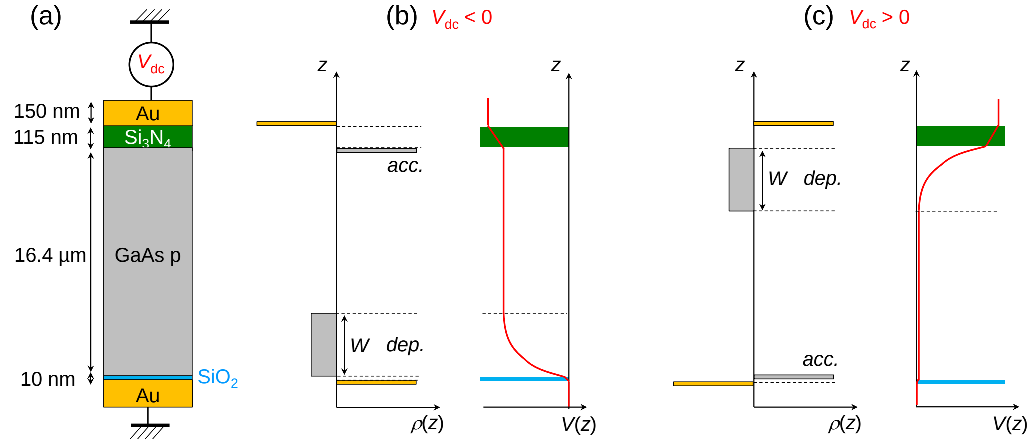

Figure 3.2: (a) Structure of the on-chip electrodes and bias configuration. (b) Sketches of the volume charge density $\rho(z)$ distribution and of the electrostatic potential $V(z)$ for a top bias $V_{\mathrm{dc}} < 0$. (c) Same sketches for a bias $V_{\mathrm{dc}} > 0$. Note the exchange of the location of the depleted (dep.) and accumulation (acc.) sections.

The complete electrode stack (top to bottom: Au-$Si_3N_4$-GaAs-$SiO_2$-Au) is shown in fig. 3.2(a). Earlier Hall measurements have revealed a non-intentional p-type doping of GaAs. The electrode stack consists of two face-to-face Metal-Insulator-Semiconductor structures, that we describe with a simple 1D model. Since we consider large applied voltages $V_{\mathrm{dc}}$, we also neglect the built-in potential associated with the difference in the work functions of Au and GaAs (flatband configuration for $V_{\mathrm{dc}} = 0$). For a negative applied voltage, holes accumulate close to the $Si_3N_4$-GaAs interface whereas the bottom GaAs-$SiO_2$-Au structure is in the depletion regime (fig. 3.2(b)). For a positive voltage, the situation is reversed, as shown in fig. 3.2(c). For voltages that typically exceed the bandgap of GaAs (1.5 V at cryogenic temperature), and for perfectly insulating layers, the depleted zone should be accompanied by an inversion layer (a very thin layer populated by minority carriers — electrons in the present case). I-V measurements show that our structure features significant leakage currents ($\sim 10\,\mathrm{nA}$ for $V_{\mathrm{dc}} = -5$ V and $\sim 20\,\mathrm{nA}$ for $V_{\mathrm{dc}} = +5$ V, at cryogenic temperature) that we attribute to imperfect dielectric barriers (see section 3.5.1). Modeling the insulating layer as a parallel resistor-capacitor association, we estimate a minimum escape rate for the electrons on the order of $1/(10\,\mathrm{ms})$. This largely exceeds the thermal generation rate of minority carriers, which is vanishing small at cryogenic temperature. We thus suppose that the inversion layer is absent and that all the voltage drop in the semiconductor is accommodated by the depletion layer. The latter features a width $W$ for a total charge per unit area $Q_{\mathrm{W}} = -|q|N_{\mathrm{A}}W$ ($q$ is the electron charge and $N_{\mathrm{A}}$ the acceptor concentration). Within these hypotheses, the width $W$ of the depletion layer is set by the condition:

$$|V_{\mathrm{dc}}| = \frac{|q|N_{\mathrm{A}}W}{C_{\mathrm{Si_3N_4}}} + \frac{|q|N_{\mathrm{A}}W^2}{2\epsilon_{\mathrm{GaAs}}} + \frac{|q|N_{\mathrm{A}}W}{C_{\mathrm{SiO_2}}}. \tag{3.12}$$

In this equation, the three terms are the potential drops across the $Si_3N_4$, depletion and $SiO_2$ layers ($\Delta V_{\mathrm{Si_3N_4}}$, $\Delta V_{\mathrm{dep}}$ and $\Delta V_{\mathrm{SiO_2}}$, respectively); $C_{\mathrm{Si_3N_4}} = \epsilon_{\mathrm{Si_3N_4}}/t_{\mathrm{Si_3N_4}}$ and $C_{\mathrm{SiO_2}} = \epsilon_{\mathrm{SiO_2}}/t_{\mathrm{SiO_2}}$ are the capacitance per unit area associated with the two dielectric layers; $\epsilon_i$ and $t_i$ are the dielectric constant of the considered material ($i$ = $Si_3N_4$, GaAs and $SiO_2$, see material parameters in table 3.1). For $|V_{\mathrm{dc}}| = 10\,V$ and $N_{\mathrm{A}} = 10^{15}\,\mathrm{cm}^{-3}$, one obtains $W = 3.5\,\mu$m, $\Delta V_{\mathrm{dep}} = 8.8\,\mathrm{V}$, $\Delta V_{\mathrm{Si_3N_4}} = 1\,\mathrm{V}$ and $\Delta V_{\mathrm{SiO_2}} = 0.2\,\mathrm{V}$. The potential profiles are sketched in fig. 3.2(b) and (c) for $V_{\mathrm{dc}} < 0$ and $V_{\mathrm{dc}} > 0$, respectively.

#### 3.3.3.2 Electrostatic bending force

We next evaluate the bending force and the maximum stress in the QD section using finite element simulations that are performed with the software COMSOL. Figure 3.3a shows the geometry, as derived from SEM observations, that is implemented in simulations. We consider in the following a trumpet that is located in the middle of the two electrodes. It is then sufficient to discuss one of the bias configurations, for example R (R biased at $V_{\mathrm{dc}}$, L and B grounded). By symmetry, the other configuration yields an opposite bending force. In the simulation, we impose the potential at the surface of the metallic Au parts. For the grounded electrode L, the surface potential of the semiconductor is set to 0. For electrode R, the semiconductor part features a space charge zone and a neutral part whose properties are fixed by the 1D model. Finally we examine two limit cases for the trumpet:

- **Purely dielectric trumpet**: the static relative permittivity of GaAs is $\epsilon_r = 12.9$.
- **Metallic trumpet**: this case is treated by taking the limit $\epsilon_r \to \infty$ for the trumpet material, in practice $\epsilon_r = 10^4$.

We consider here 'small' top facet displacements: the maximum top facet displacement ($\sim 20$ nm) is much smaller than the facet-electrode distance ($\sim 500$ nm). This allows us to decouple electrostatics and linear elasticity simulations. Using the electrostatics module of COMSOL, we first evaluate the total force $\mathbf{f}$ and the bending moment $\mathbf{M}_{\mathrm{O}}$ that are experienced by the trumpet (the point O is the center of the clamped base of the trumpet). We are interested in the $y$-component of the bending moment, $M_{\mathrm{O},y} = \mathbf{M}_{\mathrm{O}}.\hat{\mathbf{y}}$. Since the contribution associated with the vertical force component is negligible, $M_{\mathrm{O},y} = z_f f_x$. This expression defines the altitude $z_f$ at which an equivalent point-like force is applied. The force distribution takes large values 'far' from the QD section. According to Saint-Venant principle, one can replace the distributed electrostatic force by a point-like force to calculate the maximal stress in this section, $\sigma_{\mathrm{zz,max}}$. In order to check the validity of the decoupling between the mechanical and electrostatic simulations we have benchmarked the faster, cascaded approach against a multiphysics simulation that couples the electrostatics and linear elasticity modules: they yield identical results within a few percents. We note that $\sigma_{\mathrm{zz,max}}$ can also be determined using the analytic expression in eq. (3.9) by replacing $(hf_x)$ by the moment of the electrostatic force $M_{\mathrm{O},y} = (z_f f_x)$.

For a modest voltage $V_{\mathrm{dc}} = -10\,\mathrm{V}$, we estimate the moment of the electrostatic force to be 5 nN.$\mu$m for a dielectric trumpet and 22 nN.$\mu$m for a metallic one. Our weakly doped trumped lays between these two limit cases.

#### 3.3.3.3 Maximum QD spectral shift

Finally, one deduces the maximum QD spectral shift

$$\Delta E_{\mathrm{max}}(V_{\mathrm{dc}}) = |s\sigma_{\mathrm{zz,max}}(V_{\mathrm{dc}})|$$

using the stress tuning slope $s = -61\ \mu\mathrm{eV.MPa}^{-1}$ (see eq. (3.11)). Figure 3.3b shows the calculated maximal spectral shift as a function of the

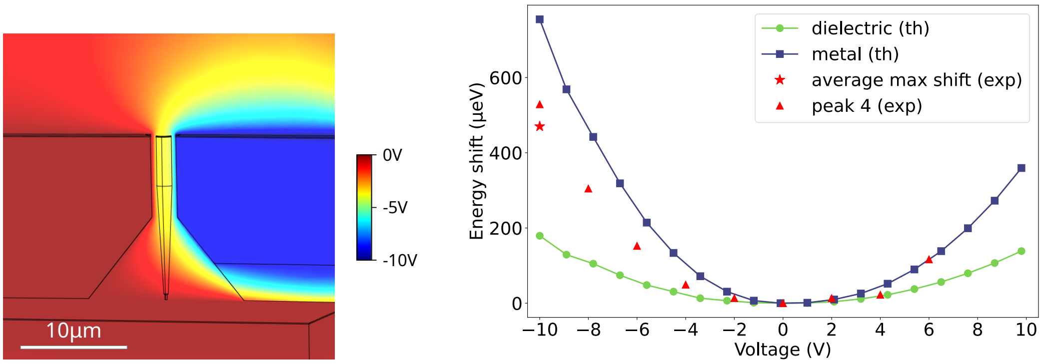

(a) (b)

Figure 3.3: (a) Geometry used in electrostatics and linear elasticity simulations. Geometrical parameters are given in the main text. The figure also shows an example of calculated potential distribution in the electrode plane (configuration R, $V_{dc} = -10$ V, dielectric trumpet). (b) Calculated maximum spectral shift as a function of $V_{dc}$. We consider two limit cases: i) purely dielectric trumpet and ii) metallic trumpet. The triangles correspond to measurements on the QD emission line 4, which exhibits the maximum shift in fig. 3.10a. The star indicates the mean of the maximum experimental shifts (taken at $V_{dc} = -10$ V) measured over all the studied devices.

bias $V_{dc}$ for the two limit cases discussed above (purely dielectric trumpet and metallic trumpet). A purely dielectric trumpet already experiences a significant bending force. However, a metallic structure always experiences a larger force. This is expected, as dielectric polarization is smaller than the metallic one (dielectric screening leads to a partial screening of external electrical fields, whereas a metal ensures a perfect screening). The model also predicts an asymmetry between positive and negative bias voltages, which directly reflects the distinct potential distributions in the electrode stack. This asymmetry is almost negligible in the dielectric case, which leads to a roughly parabolic voltage dependence. In contrast, it is more pronounced in the metallic case.

In the section 3.5, we discuss experimental results. We will see that the model developed in this section provides a good estimate of the device performance.

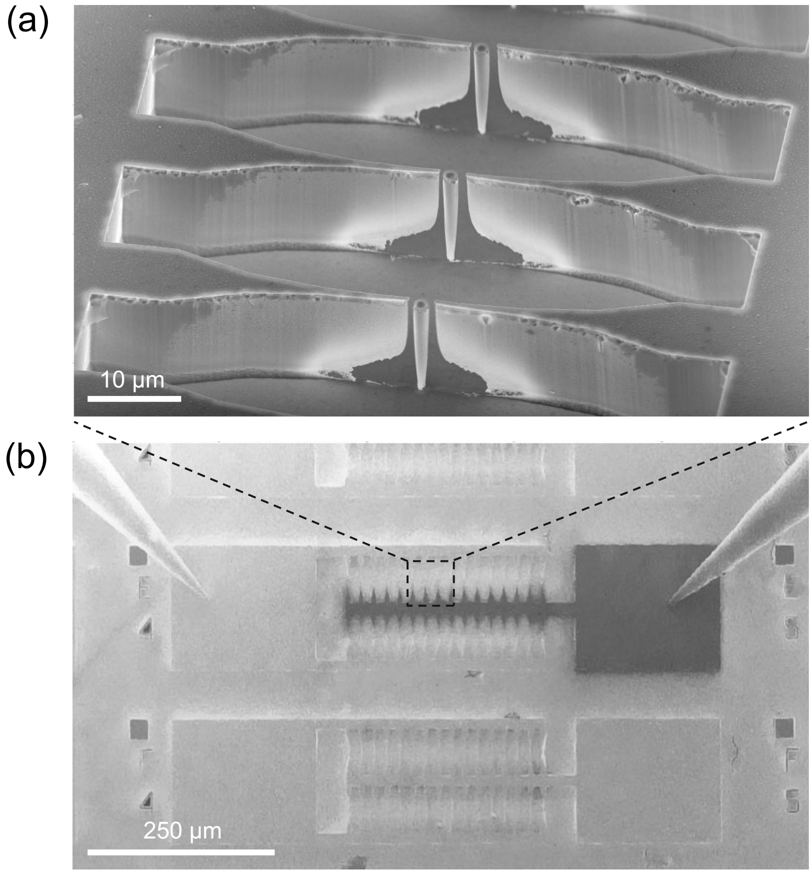

Figure 3.4: **Scanning electron microscope images of the fabricated device.** (a) Side view of photonic trumpets flanked by on-chip electrodes. (b) Top view of a device subfield contacted with two tips. The left pad and the bottom electrode are grounded; the right pad is biased at potential $V_{\mathrm{dc}} > 0$, which reduces secondary electron emission and yields a dark contrast.

## 3.4 Fabricated device

Figure 3.4 shows a SEM image of the investigated device. The device was fabricated in the team by Yann Genuist (MBE growth), Saptarshi Kotal (mask design and clean room processing) and Alberto Artioli (mask design and clean room processing). The fabrication process is described in fig. 3.5. We start with the molecular beam epitaxy growth of a structure over a (001) GaAs wafer. We grow a GaAs layer containing a single sheet of self-assembled InAs QDs over a 500 nm-thick $\mathrm{Al_{0.8}Ga_{0.2}As}$ sacrificial layer. The QDs are formed during the fast (1s) deposition of 1.9 monolayers of InAs, immediately followed by GaAs capping. These growth conditions lead to a QD areal

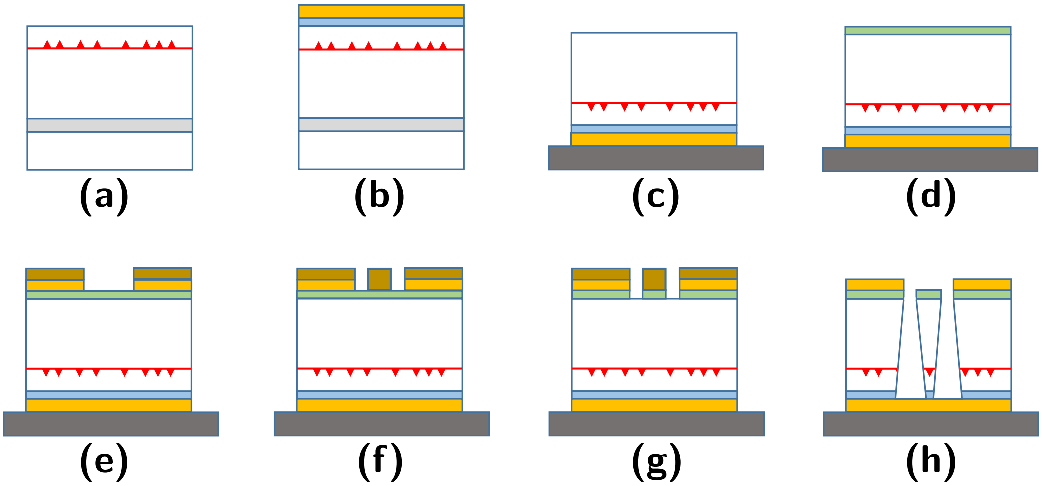

Figure 3.5: **Overview of the fabrication steps.** **(a)** MBE growth of a planar heterostructure. **(b)** Deposition of a $SiO_2$-Au mirror. **(c)** Flip-chip process. **(d)** Deposition of the $Si_3N_4$ layer, which acts as an anti-reflection coating over the trumpets, and as electrical insulation between Au electrodes and GaAs. **(e)** EBL step 1 and deposition of Au to define the electrodes and alignment markers, and deposition of Ni hard mask. **(f)** EBL step 2 and deposition of Ni mask over trumpets **(g)** ICP etching of $Si_3N_4$ . **(h)** ICP etching of GaAs and removal of Ni hard mask (see [96]).

density of a few 100 $\mu m^{-2}$ and to ‘small’ lens-shape QDs, with an ensemble luminescence that peaks around 920 nm ($\approx 1.35$ eV) ([67]). After deposition of the $SiO_2$-Au mirror, the sample is flip-chipped on a host substrate and the growth substrate and the sacrificial layer are removed. We next deposit a 115 nm-thick $Si_3N_4$ layer by sputtering. It will serve as an antireflection coating for the trumpet top facet and provide electrical isolation for the top electrodes. The device geometry is next defined by top-down processing. Two aligned levels of electron-beam lithography followed by metal deposition and lift-off define the electrodes and their contact pads (Ti (5 nm)/Au (150 nm)/Ni (180 nm)) as well as the trumpet top facet (Ni (180 nm)). In a RIE-ICP chamber we next etch the $Si_3N_4$ layer (gases: Ar, $CH_2F_2$, $SF_6$). Subsequent GaAs etching is performed in the same chamber (gases: Ar, $BCL_3$, $SiCl_4$) and allows defining the trumpets and the suspended electrodes in a single step. To this end, the process was carefully optimized to offer a controlled and constant under-etching angle. Finally, residues of the Ni hard mask are removed with nitric acid diluted in water.

Across the wafer we patterned a series of subfields (see fig. 3.6). Each subfield features 32 trumpets with nominally identical top radius as shown in

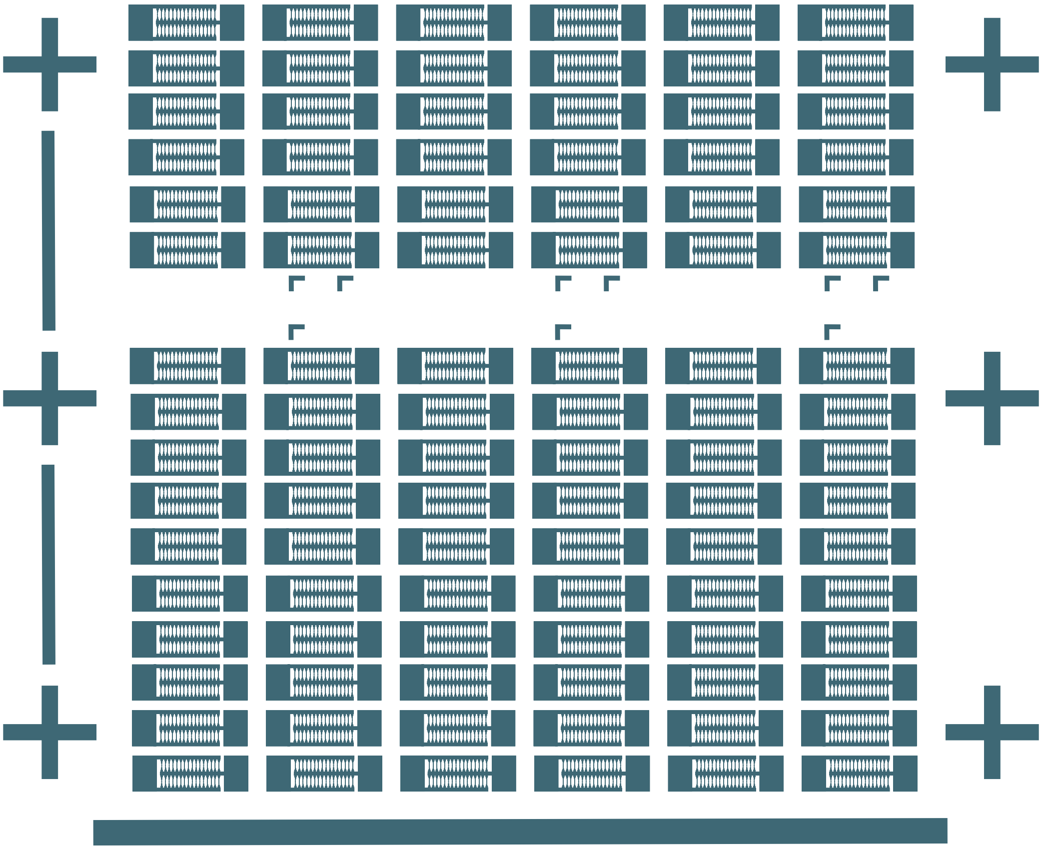

Figure 3.6: **Lithography mask design for trumpets.** Each subfield consist of 32 devices with identical top diameter.

fig. 3.7. Each trumpet is flanked by a pair of electrodes that are connected to two contact pads. The experiments described in this chapter are conducted on devices that belong to the same subfield and thus feature identical top diameter.

## 3.5 Experimental demonstration of strain tuning

### 3.5.1 Preliminary electrical characterization

Figure 3.8b presents a typical I-V measurement performed at room temperature. The electrical connection is made using micromanipulators which are then connected to a semiconductor parameter analyzer (Agilent 4155C). As shown in fig. 3.8a, the bottom mirror is grounded whereas the top gold elec-

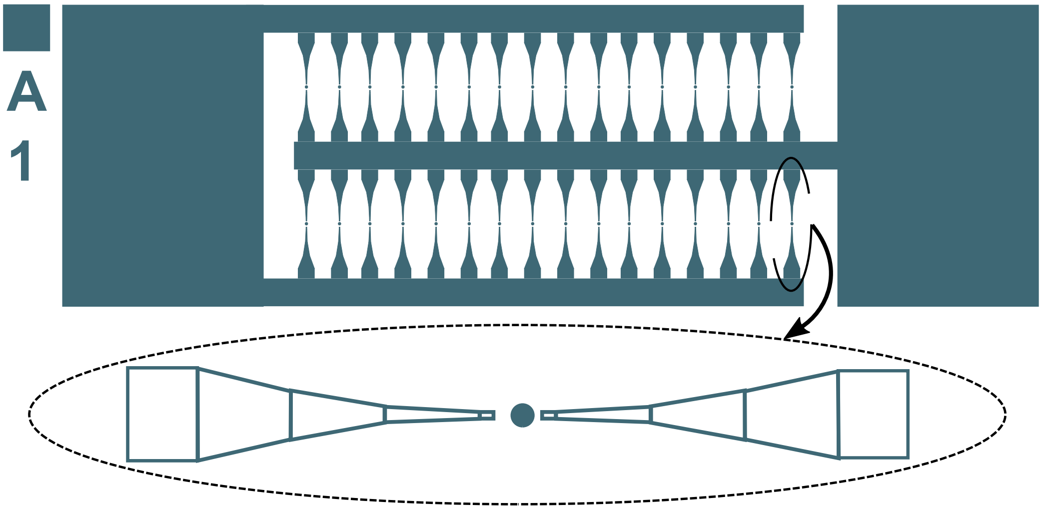

Figure 3.7: **Basic lithography mask motif for electrostatically-actuated trumpets.** This motif is replicated over a 22 by 6 matrix to fill a 6 x 5.5 mm sample. **(inset)** Electrode geometry, divided into five sections in order to define a dedicated dose to each.

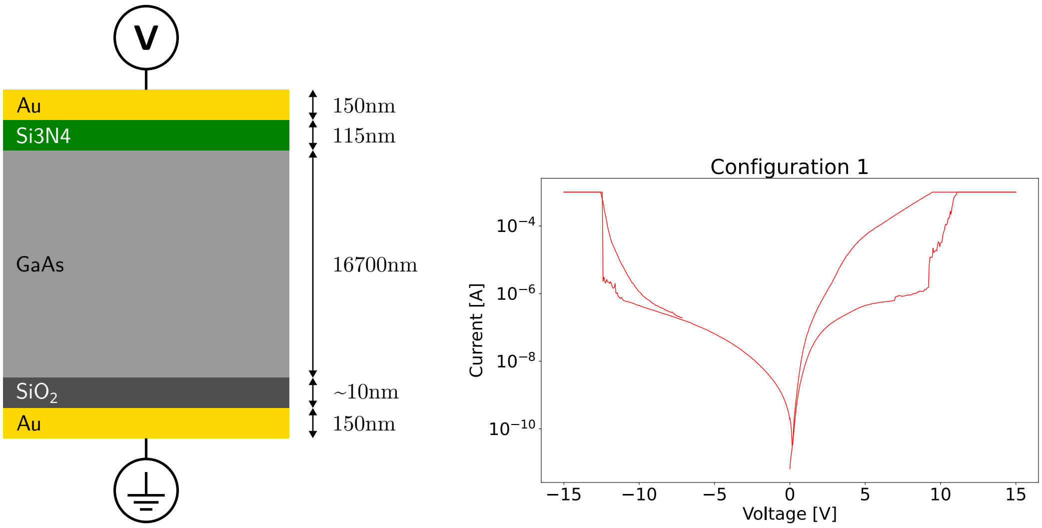

(a)

(b)

Figure 3.8: (a) Bias configuration for $I-V$ measurements. (b) Typical $I-V$ curve measured at room temperature. The absolute value of the current $|I|$ is plotted with a logarithmic scale. We impose a 1 mA-limit on the source current to protect the device.

trode is biased at $V_{\mathrm{dc}}$. Starting from $V_{\mathrm{dc}} = 0$ V and increasing the voltage bias, one observes a threshold at $\sim +10$ V above which the current increases sharply with a step-like behavior. From this point, ramping down the voltage leads to a different I-V branch, with a smaller voltage threshold and a larger current. A similar behavior is observed for negative voltages, albeit with a slightly larger threshold and a less pronounced hysteresis. After this initial cycle, the I-V curves do not show any significant hysteresis and are stable on a time scale of a few hours. However, the structure generally 'heals' itself overnight, leading to a reset of the I-V features.

The device always features significant leakage currents. We note that the leakage current is generally smaller for negative voltages. This observation is also valid at cryogenic temperatures. For $|V_{\mathrm{dc}}| > 10$ V, we attribute the sharp increase in the current to the dielectric breakdown of the $SiO_2$ and $Si_3N_4$ layers, combined with an avalanche mechanism in the depleted region discussed in section 3.3.3.1. Subsequent SEM inspections have shown that such current surges can severely damage the electrodes. In the experiments presented in the following section, the bias voltage is thus kept between $-10$V and $+6$ V to protect the device.

## 3.5.2 Experimental setup

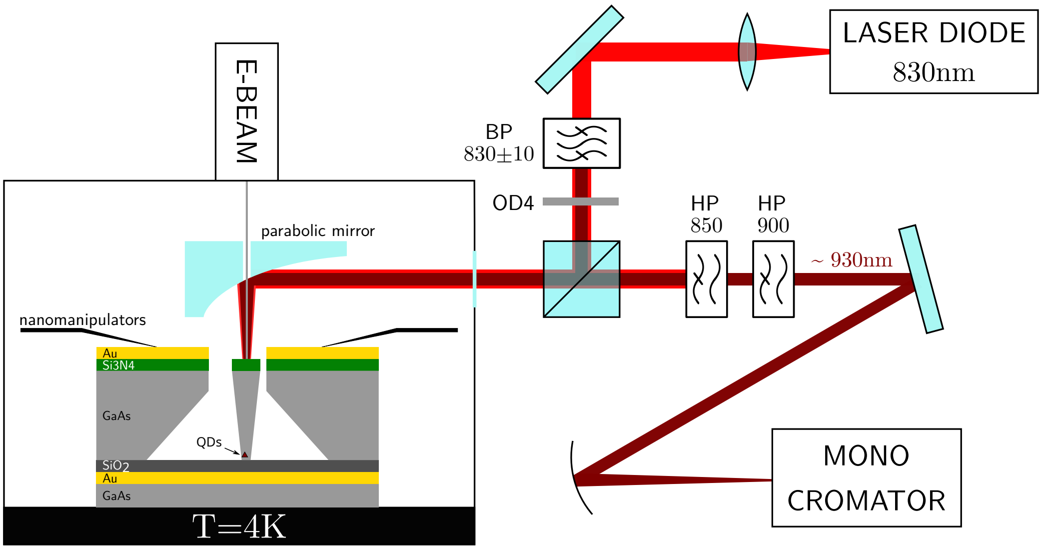

Figure 3.9: **SEM and micro photoluminescence setup.** Schematics of the setup used for the static actuation of the trumpet (designed by Fabrice Donatini). The SEM, which is equipped with the nanomanipulators, allows for rapid testing of the different structures.

The setup used for static tuning experiments is shown in fig. 3.9. The device chip is mounted on a cryogenic sample holder ($T = 5$ K) in a SEM chamber equipped with an optical access. Moreover 4 nanomanipulators allows for a fast device characterization. The QDs luminescence is excited by a continuous wave laser tuned to $\lambda_{\mathrm{exc}} = 830$ nm, in the absorption continuum associated with the QD wetting layer. The laser is focused on a single trumpet device with a parabolic mirror (focal length: 3 mm). The same mirror collects the device luminescence, which is focused on the entrance slit of a grating spectrometer using a concave mirror (focal length: 200 mm, magnification: ×67). The grating spectrometer (600 grooves per mm, focal length: 55 cm) is equipped with a Si charge-coupled device (CCD) camera (2048 pixels, pitch: 13.5 $\mu$m). Experiments are conducted around 920 nm (1.348 eV) and the width of the entrance slit is 100 $\mu$m. Considering a uniform illumination, this defines an upper bound of 420 $\mu$eV for the spectral resolution (the internal magnification of the spectrometer is ×1). When the trumpet image at the entrance of the spectrometer becomes smaller than the CCD pixel size, the latter imposes a lower bound on the resolution. We take a typical limit that corresponds to two CCD pixels or 120 $\mu$eV. The actual resolution is found between these two values; it depends on the exact size of the trumpet image at the entrance of the spectrometer.

The bottom Au mirror is grounded and the two top electrodes are contacted with movable tips (see fig. 3.4(b)). After placing the tips, the imaging electron-beam is shut down when performing experiments: the associated charges indeed impact both the QD optical emission and the electrostatic actuation.

### 3.5.3 Demonstration of strain tuning

We first investigate spectral tuning in configuration R (R biased at $V_{\mathrm{dc}}$, L grounded). In order to limit leakage current and preserve the device integrity, $V_{\mathrm{dc}}$ is kept between $-10$ V and $+6$ V (see section 3.5.1). Figure 3.10a shows a reference micro photoluminescence spectrum acquired when all electrodes are grounded (no applied force). It features sharp peaks associated with the recombination of excitonic complexes trapped in various QDs. Figure 3.10b is a zoom on the QD emission line 4 for various $V_{\mathrm{dc}}$. A clear spectral shift is visible, without noticeable degradation of the intensity nor spectral broadening. From a fit to a Lorentzian spectral profile we determine the central emission energy $E_0$ and deduce the spectral shift $\Delta E_{\mathrm{dc}} = E_0(V_{\mathrm{dc}}) - E_0(0)$. Figure 3.10c shows the voltage dependence of $\Delta E_{\mathrm{dc}}$ for the 5 QD lines identified in panel (a). Strikingly, distinct QD lines can exhibit very different $\Delta E_{\mathrm{dc}}$, which can be of opposite signs. Such a dispersion directly reflects the inhomogeneity of

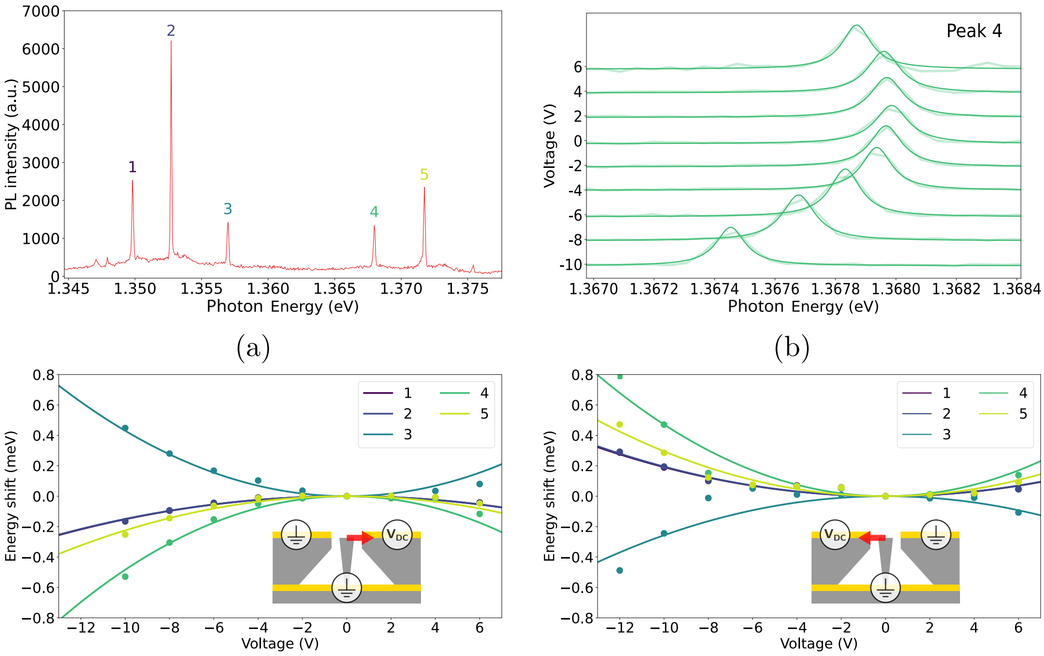

(a) (b)

(c) (d)

Figure 3.10: **Static spectral tuning.** (a) Reference microphotoluminescence spectrum, measured when all electrodes are grounded. (b) Spectra of the QD emission line 4 for $V_{\mathrm{dc}}$ ranging between $-10$ V and $+6$ V (configuration R). The transparent solid lines correspond to measurements; the plain solid lines are fit to Lorentzian line-shape. (c) Spectral shifts $\Delta E_{\mathrm{dc}}$ of individual QD emission lines versus $V_{\mathrm{dc}}$ in configuration R. (d) Same plot in configuration L. Dots are experimental points and solid lines are fit to a parabolic law centered at $V_{\mathrm{dc}} = 0$.

the stress profile in the QD section (Figure 3.1a). Figure 3.10d shows similar measurements in configuration L. Compared to configuration R, all QDs exhibit a spectral shift of opposite sign: as the trumpet bends in the opposite direction, the zone previously under tensile stress is now compressed, and vice versa. The absolute value of the shifts are slightly smaller in configuration L. Due to a fabrication imperfection, the trumpet is slightly closer to electrode R, which explains the observed asymmetry. One can also remark that the curves associated with QD lines 1 and 2 are superimposed: they very likely belong to the same QD, as distinct excitonic complexes feature similar response to strain [102].

In our experiments, $V_{\mathrm{dc}}$ is kept between $-10$ V and $+6$ V to limit leakage current and to preserve the device integrity. Overall, the measured spectral shifts are correctly reproduced by a quadratic voltage law centered at $V_{\mathrm{dc}} = 0$ (solid lines in Figures 3.10c and 3.10d). A close inspection reveals that negative $V_{\mathrm{dc}}$'s systematically lead to slightly larger spectral shifts than positive ones. We attribute this feature to an asymmetry in the electrostatic bending force. To compare experimental and predicted shifts, we introduce $\Delta E_{\mathrm{max}}$, the largest absolute spectral shift that is achieved considering all the QDs embedded in a given device. For $V_{\mathrm{dc}} = -10$ V in configuration R, QD line 4 exhibits $\Delta E_{\mathrm{max}} = 530\ \mu$eV. In order to gain statistics, we repeated this experiment in 6 nominally identical trumpets with the same bias configuration ($\sim 40$ distinct emission lines in total). The average maximum shift is 470 $\mu$eV. This value exceeds the estimation for a purely dielectric trumpet (180 $\mu$eV), but remains smaller than the predicted value in the metallic case (750 $\mu$eV). We conclude that free carriers in GaAs significantly contribute to the electrostatic force. For a given value of $V_{\mathrm{dc}}$, experimental data sometimes reveal an asymmetry between the absolute shifts obtained in configurations R and L (for example, typically 20 % when comparing figs. 3.10c and 3.10d). Our simulations show that it can be explained by a small misalignment (a few tens of nanometers) of the photonic trumpet with respect to the central position. This leads to an imbalance between the forces exerted in the two configurations.

### 3.5.4 Quantum dot linewidth

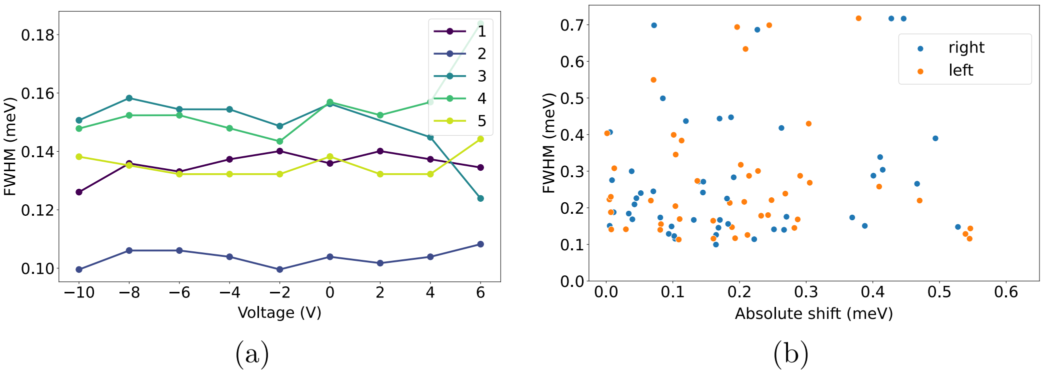

(a) (b)

Figure 3.11: (a) QD linewidth (FWHM) as a function of the applied voltage $V_{\mathrm{dc}}$ in configuration R (the data corresponds to the 5 spectral lines investigated in the Fig. 3 in the main text). (b) QD linewidth as a function of the absolute spectral shift $|\Delta E_{\mathrm{dc}}|$ measured at $V_{\mathrm{dc}} = -10$ V.

Figure 3.11a shows the FWHM as a function of the applied voltage $V_{\mathrm{dc}}$, for the five QD lines investigated in fig. 3.10 (configuration R, fig. 3.10c). In all cases, the linewidths remain constant when $V_{\mathrm{dc}}$ is varied between $-10$ V and $+6$ V. This feature is confirmed in several nominally-identical devices. Within this voltage range, strain tuning does not induce any measurable broadening of the QD linewidth (within the spectral resolution of the experiment). Outside this voltage range, we however sometimes observe a spectral broadening. It is correlated with the sharp increase in the leakage current that has been discussed in section 3.5.1. We believe that these currents induce an extra noise on the QDs. We note that the data do not reveal a significant redshift of the QD emission, which excludes a simple heating process.

Figure 3.11b shows the QD linewidth as a function of the absolute spectral shift $|\Delta E_{\mathrm{dc}}|$. Since large $|\Delta E_{\mathrm{dc}}|$ are obtained for QDs that are located close to the wire sidewall, such a plot can be used to reveal sources of decoherence that are hosted by the wire surface. To gain statistics, we consider all the QD emission lines (without any selection) originating from 6 distinct, nominally identical devices. Measurements have been performed in configurations R and L, for $V_{\mathrm{dc}} = -10$ V. We observe significant linewidth fluctuations from QD to QD, with a mean value of 200 $\mu$eV. Many QD emission linewidths are found within the resolution window given in section 3.5.2. Quite surprisingly, there is no clear correlation between the QD linewidth and the spectral shift. In particular, it is possible to observe large shifts for narrow QD emission lines.

This observation is of course bounded by the experimental spectral resolution. In the future, it would be very interesting to run a similar experiment using resonant QD optical excitation. The latter offers a much better spectral resolution and minimizes excitation-induced QD decoherence.

## 3.6 Conclusion and perspectives

The electrostatic actuation scheme demonstrated in this work can tune independently several devices embarked on the same chip. Blue and red shifts of magnitude 0.5 meV has been demonstrated; this represents a key asset for the scale-up to applications requiring multiple sources operated in parallel. In practice, the choice of moderately off-axis QDs (radial distance below $r_b/2$) will preserve a reasonable tuning range without compromising the excellent light extraction offered by photonic nanowires [20]. As demonstrated in very similar structures [132, 136, 91], a clean, resonant QD excitation is also desirable in order to optimize the spectral coherence of the emitted photons.

**Towards a larger tuning range.** In the present device, the tuning range is limited by the maximum applied voltage. The latter is in turn imposed by

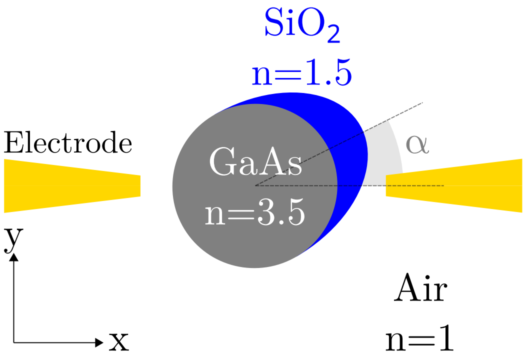

Figure 3.12: **Generation of an anisotropic inplane strain with an asymmetric shell.** An example of an asymmetric shell surrounding a trumpet. The shell is made of a low refractive index material in order to maintain the optical symmetry, while breaking the mechanical symmetry.

the appearance of leakage currents. In a future device, realistic improvements in the quality of the dielectric materials ($SiO_2$ and $Si_3N_4$), possibly combined with an increase of their thicknesses, should allow multiplying the maximum voltage by a factor of 10. This will increase the applied force and consequently the tuning range by two orders of magnitude. The quality of the dielectric materials can be largely improved. Indeed, the dielectric breakdown field of electronic-grade $Si_3N_4$ is about $10^7$ kV.cm$^{-1}$, a value that is compatible with a bias of 100 V. In the first device, the $Si_3N_4$ was deposited by sputtering at room temperature. Switiching to plasma-enhanced chemical vapor deposition (PECVD) deposition should largely increase the material quality. At the same time, this represents an opportunity to investigate the response of self-assembled QDs to large ($|\epsilon_{zz}| \sim 1\,\%$) tensile or compressive strains [15].

**Fine structure splitting correction.** So far, we have discussed mainly the tuning of the QD emission wavelength. However, strain can also be employed to adjust other optical properties of QDs, such as the FSS. In self-assembled InAs QDs, the FSS typically amounts to a few tens of meV. For the emission of entangled photon pairs based on the recombination of a neutral biexciton, the FSS should be brought below 1 $\mu$eV. However the stress in the z direction affects photons emitted in both polarization in the same way, rather we are interested in the components $\epsilon_{xx}$ and $\epsilon_{yy}$ of the stress tensor. In the device shown in Figure 3.1a simulations have shown that these two components are indeed present, but the symmetry of the system make them equal. In order to compensate for the natural asymmetry of the QD, one can immerse the QD in a strain field that features an in-plane anisotropy [183]

($\epsilon_{xx} \neq \epsilon_{yy}$). In a wire with a circular section, the stress is locally uniaxial along $z$, which leads to $\epsilon_{xx} = \epsilon_{yy}$.

Figure 3.12 shows one possible approach to make $\epsilon_{xx} \neq \epsilon_{yy}$. The trumpet is covered by a shell of $SiO_2$. Due to the large contrast in refractive indexes between GaAs and $SiO_2$, the optical properties are not significantly affected; on the other hand the shell changes dramatically the mechanical properties of the trumpet, especially the in-plane strain associated with bending. Simulations has shown that the shell induces a mechanical anisotropy (shown $\epsilon_{xx} \neq \epsilon_{yy}$). To maximise the in-plane strain anisotropy, the direction of deflection should be different from the direction of the deposition of the shell and with an angle $\alpha$ comprised between 20 and 70 degrees.

**Collective optical effects.** The single-mode electromagnetic environment defined by a photonic wire [20, 131] combined with the specific stress pattern associated with trumpet bending is also particularly well suited to explore collective effects, such as superradiance [73]. Indeed, the presence of tensile and compressive stress in a cross section facilitates the tuning of two distinct QDs into resonance. This capability is illustrated in fig. 3.13. In this context, a supplementary pair of electrodes in the y direction, would offer a vectorial control over the bending direction, enabling to control the orientation of the stress gradient in the wire cross-section. This could allow for the tuning of up to 3 distinct QDs into resonance.

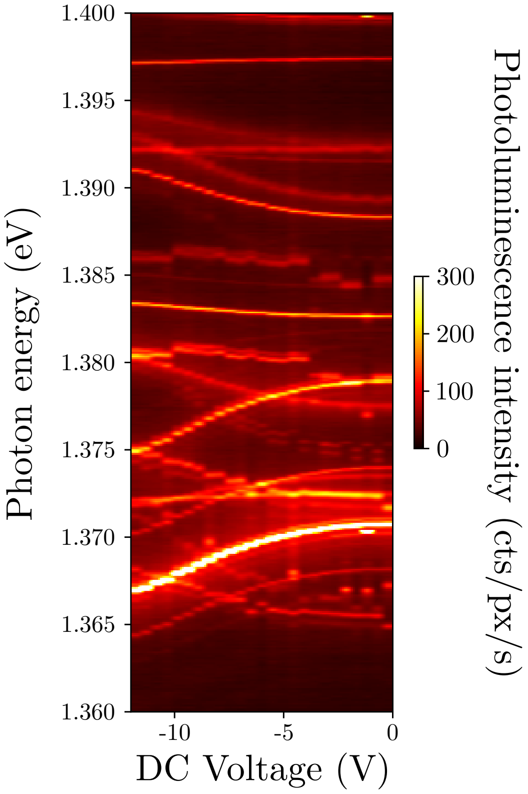

Figure 3.13: **Photo-luminescence spectrum of a QDs located at the base of another trumpet as a function of electrode bias.** Some QDs experience positive strain and some other a negative one, this shifts the emission in opposite directions in this way two emission lines belonging to different QDs are brought to the same energy. The data were acquired using the setup described in section 4.4.1, the scans are automatized, allowing for longer time integration of the signal and higher resolution in electrode polarization. The measurement is performed on another device, in which the trumpet is largely off-axis.

# Chapter 4

# Electrostatic driving of the nanowire high order vibration modes

This chapter represents the natural progression from the work done in [125] where the exploration of a dynamical regime was proposed as one of the main perspectives. This chapter is adapted from the submitted (under review) manuscript: ”High-order nanowire resonances for high-frequency, large coupling strength quantum dot hybrid nanomechanics” by Rana Thanos, Hajer Tlili, Yoann Curé, Matteo Finazzer, Alberto Artioli, Saptarshi Kotal, Yann Genuist, Pierre Verlot, Joël Bleuse, Jean-Michel Gérard, and Julien Claudon. The experimental work has been led by Rana Thanos. I contributed with the realization of a physical support for the sample and the electrical interconnections. This allowed the sample to be used without the help of nanomanipulators and thus outside the SEM setup (section 3.5.2) which is not adapted to perform photoluminescence measurements with the precision required in this work. Moreover I participated in the discussions and helped on the data analysis.

## 4.1 Introduction

Recent years have witnessed the blossoming of hybrid systems that couple a two-level system (TLS) to a mechanical resonator [180]. Leveraging the TLS to achieve quantum control over the oscillator motion [139, 35] enables addressing fundamental questions, such as the exploration of the quantum-classical boundary. From a more applied perspective, hybrid systems can also be employed to realize quantum-enhanced sensors and could play a key role in the architecture of quantum information devices [147]. In a rich landscape of practical implementations [139, 35, 7, 142, 175], hybrid systems based on optically-active TLS [204, 130, 177, 140] open specific opportunities. For instance, they could interface a long-lived mechanical memory with flying photons, and enable microwave-to-optical conversion of photons through optomechanical wavemixing [199, 83]. Among solid-state quantum light emitters, semiconductor quantum dots (QDs) stand out for their remarkable optical properties [115, 163]. Key assets include a nearly-ideal radiative yield [87, 20], highly-stable emission and close-to-lifetime-limited spectral linewidth [99]. Furthermore, the extreme sensitivity of the QD bandgap energy to mechanical strain [18, 123] gives birth to large, built-in coupling to mechanical vibrations [200, 127, 204, 130, 160]. Most envisioned applications demand a large mechanical frequency, which exceeds the emitter spectral linewidth. To achieve this goal, QDs have been recently coupled to high-frequency oscillators such as surface acoustic wave resonator [83] or the Lamb modes of a doubly-clamped cantilever [193]. Whereas the hybrid system formed by a single QD in a vibrating nanowire has enabled many early demonstrations in the field [204, 130, 10, 132, 91], most investigations so far focused on the low-frequency (sub-MHz) fundamental flexural mode.

In this chapter we'll present a comprehensive exploration of hybrid nanomechanics for a vibrating nanowire. In particular we delve into the dynamical interplay of quantum dots (QDs) and the vibration modes supported by the structure. In the first section we introduce a model for the interaction of the QD embedded in the nanowire with the strain induced by the nanowire's vibration modes. Then in the second section we dive deep into the theoretical foundations of vibration modes and the analogies with 1D harmonic oscillators. Moreover we explore the electrostatic excitation of vibration modes, both in the DC and AC configurations. Here, finite-element simulations showcase how off-axis nanowires can excite all families of vibration modes. Equipped with this theoretical background we will then introduce the principle of the experiment. Here we will take a closer look at our experimental setup, discuss a wide-range frequency scan, and demonstrate the successful fit of vibration-broadened QD emission spectra. In the next section we explore how the QD ensemble becomes a probing tool, allowing us to discriminate between the transverse stress profile. For this we will make use of finite-element simulations in order to unveil the footprint of different vibrating modes. This journey through hybrid nanomechanics of the nanowire bring us to two remarkable vibration modes. In that section we will shine a spotlight on the high-order flexural mode $F_{7x}$ and the intriguing longitudinal resonance $L_1$ and uncover the unique characteristics that make them interesting from an hybrid-nanomechanics point of view. Finally we will discuss the scaling of mechanical Q-Factor and coupling strength with the mode order. We will then see how to obtain the coupling strength, discussing the important case of $F_{7x}$.

## 4.2 Hybrid nanomechanics with a QD in a vibrating nanowire

The vibration modes of a microwire fall into three families: flexural (F), torsional (T) and longitudinal (L). Our device features an elliptical base, due to a slight anisotropy of the etching. Therefore, we distinguish between flexural modes that are polarized along the major ellipse axis $x$ axis ($F_x$ modes) and flexural modes that are polarized along the minor axis $y$ ($F_y$ modes). In the following, the mode order is indicated with an integer index $n$ (n = 1 corresponds to the first mode of each family). The mode shape associated with $F_{1x}$, $F_{1y}$, $T_1$ and $L_1$ is shown in fig. 4.1.

As the wire vibrates, the embedded QDs experience an oscillating strain that modulates their bandgap energy according to the Bir-Pikus Hamiltonian [18]. We consider here self-assembled InAs QDs which feature a large (a few %), built-in compressive biaxial strain. Their fundamental optical transition involves conduction electrons and heavy holes (valence band mixing is negligible in our QDs [40]). At first order in perturbation theory, they are thus sensitive to the local hydrostatic $\epsilon_h = \epsilon_{xx} + \epsilon_{yy} + \epsilon_{zz}$ and tetragonal shear strain $\epsilon_{sh} = 2\epsilon_{zz} - \epsilon_{xx} - \epsilon_{yy}$ associated with the vibration. Locally, the stress tensor associated with $F$- and $L$-modes is dominated by the longitudinal component $\sigma_{zz}$. The associated strain components directly impacts the QD bangap energy. In contrast, the shear stress components $(\sigma_{xz}, \sigma_{yz})$ associated with $T$-modes are weakly coupled to the QD. However, the elliptical base also results in a significant $\sigma_{zz}$ stress for $T$-modes. Figure 4.1b shows that the stress distribution in the QD section strongly depends on the nature of the mode.

Formally, the interaction between a given QD and a given vibration mode $m$ is described by the Hamiltonian:

$$\mathcal{H}/\hbar = \omega_{\text{eg}} \hat{\sigma}^\dagger \hat{\sigma} + \Omega_m \hat{b}_m^\dagger \hat{b}_m + g_m \hat{\sigma}^\dagger \hat{\sigma} (\hat{b}_m^\dagger + \hat{b}_m). \tag{4.1}$$

The first term describes the QD, which is modelled as a two-level system whose ground state $|g\rangle$ and excited state $|e\rangle$ are separated by an energy $E_{\text{eg}} = \hbar\omega_{\text{eg}}$; $\hat{\sigma} = |g\rangle\langle e|$ is the lowering operator. The vibration mode is treated as a 1D harmonic oscillator of angular frequency $\Omega_m$ and effective mass $m_{\text{eff}}$; $\hat{b}_m$ is the associated phonon annihilation operator. The third term couples the QD energy to oscillator reduced position $\hat{b}_m^\dagger + \hat{b}_m = \hat{x}/x_{\mathrm{zpf}}$, with $x_{\mathrm{zpf}} = \sqrt{\hbar/(2m_{\mathrm{eff}}\Omega_m)}$ the rms value of the zero-point position fluctuations. The associated coupling strength reads:

$$g_m = (\partial_x \omega_{\mathrm{eg}}) x_{\mathrm{zpf}}. \tag{4.2}$$

The modulation parameter $\partial_x \omega_{\mathrm{eg}}$ is equal to $\frac{1}{\hbar}\left[a\partial_x \epsilon_h + b\partial_x \epsilon_{sh}\right]$, with $a$ and $b$ the deformation potentials of the QD material. In this chapter, a 'large' wire vibration is driven by a classical voltage source: the vibration mode is thus treated in the classical limit. A sinusoidal vibration of amplitude $x_{\mathrm{ac}}$ then induces a modulation of the QD transition energy with an amplitude:

$$E_{\mathrm{ac}} = \hbar g_m \frac{x_{\mathrm{ac}}}{x_{\mathrm{zpf}}}. \tag{4.3}$$

Such a modulation broadens the QD photon emission spectrum, as we will see in section 4.4.2.

## 4.3 Excitation of vibration modes: theoretical background

In this section we provide some theoretical background for the description of vibration modes.

### 4.3.1 Vibration modes as 1D harmonic oscillators

In the frame of linear elasticity, the nanowire supports a discrete, infinite set of independent vibration modes. We adopt here a classical perspective and focus below on a given vibration mode, with a free-running angular frequency $\Omega_m$. The associated displacement field can be factorized as:

$$\mathbf{u}(\mathbf{r}, t) = \mathbf{u}_m(\mathbf{r}) x(t), \tag{4.4}$$

where $\mathbf{u}_m(\mathbf{r})$ is the modal displacement field (or mode shape) and $x(t)$ a scalar coordinate. Here, we chose to normalize $\mathbf{u}_m(\mathbf{r})$ such that $\max_{\mathbf{r}} |\mathbf{u}_m(\mathbf{r})| = 1$. In practice, $\Omega_m$ and $\mathbf{u}_m(\mathbf{r})$ are determined using a finite-element software (see section 4.3.3). Thanks to the factorization of $\mathbf{u}(\mathbf{r}, t)$, the 3D vibration mode can be described as an effective 1D harmonic oscillator of position $x(t)$. This oscillator features an effective mass:

$$m_{\mathrm{eff}} = \int \rho(\mathbf{r}) |\mathbf{u}_m(\mathbf{r})|^2 \mathrm{d}^3\mathbf{r}, \tag{4.5}$$

where $\rho(\mathbf{r})$ is the volumetric mass density. We also introduce the effective spring constant:

$$k_{\text{eff}} = m_{\text{eff}}\Omega_m^2. \tag{4.6}$$

The time evolution of $x(t)$ is governed by the equation of motion of a damped harmonic oscillator:

$$\ddot{x}(t) + \frac{\Omega_m}{Q_m}\dot{x}(t) + \Omega_m^2 x(t) = \frac{1}{m_{\text{eff}}}F_{\text{eff}}(t). \tag{4.7}$$

Here, the mechanical quality factor $Q_m$ parameterizes mechanical damping. External driving is included by considering an effective driving force $F_{\text{eff}}(t)$ that will be discussed in the next paragraph. We neglect thermal fluctuations, which are much smaller than the driven oscillation amplitude. Note that eq. (4.7) is analogous to the equation for a classical damped harmonic oscillator, where the mass is replaced by the effective mass $m_{\text{eff}}$ and the force by $F_{\text{eff}}(t)$.

In the following, we consider a driving force $F_{\text{eff}}(t) = F_{\text{ac}}\cos(\omega t)$ and recall textbook results regarding the amplitude resonance of a driven harmonic oscillator. In the steady state, $x(t)$ oscillates in time according to: $x(t) = x_{\text{ac}}(\omega)\cos(\omega t + \varphi(\omega))$. As discussed later, our measurements are not sensitive to the phase $\varphi(\omega)$. We focus on the amplitude response of the oscillator, which is given by:

$$x_{\text{ac}}(\omega) = \frac{F_{\text{ac}}}{k_{\text{eff}}} \frac{1}{\sqrt{\left(1 - \frac{1}{2Q_m^2} - \left(\frac{\omega}{\Omega_m}\right)^2\right)^2 + \frac{1}{Q_m^2} - \frac{1}{4Q_m^4}}}. \tag{4.8}$$

For $Q_m \geq 1/\sqrt{2}$, $x_{\text{ac}}(\omega)$ features a resonance peak centred at

$$\omega_r = \Omega_m\sqrt{1 - \frac{1}{2Q_m^2}}. \tag{4.9}$$

In the low-loss limit ($Q_m \gg 1$), $\omega_r$ is very close to the free-running frequency $\Omega_m$. In the vicinity of the resonance frequency ($|\omega - \Omega_m| \ll \Omega_m$), the resonance peak is well approximated by the square root of a Lorentzian profile:

$$x_{\text{ac}}(\omega) \approx \frac{F_{\text{ac}}\Omega_m}{2k_{\text{eff}}} \frac{1}{\sqrt{(\omega - \Omega_m)^2 + \left(\frac{\Omega_m}{2Q_m}\right)^2}}. \tag{4.10}$$

At $\frac{1}{\sqrt{2}}$-level, the resonance curve features a total linewidth $\Delta\omega = \Omega_m/Q_m$.

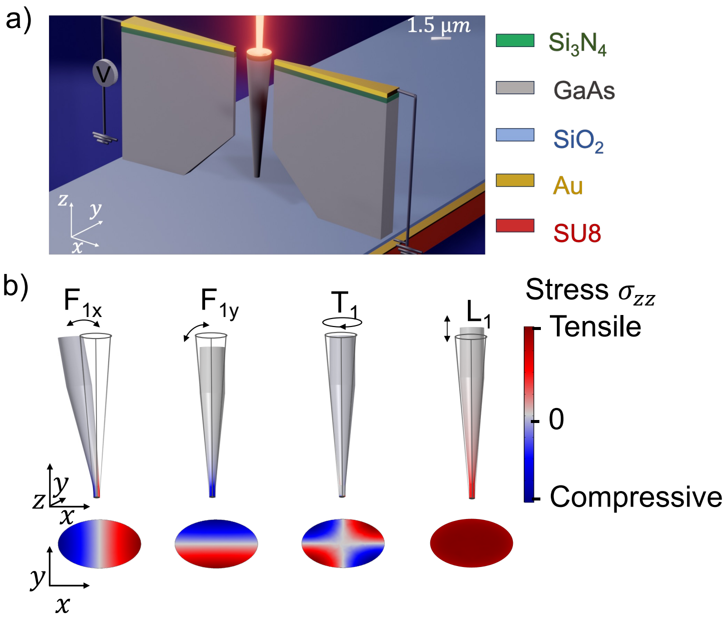

Figure 4.1: **Strain-coupled QD-nanowire hybrid system. (a)** Device schematics: a set of on-chip electrodes drive the mechanical resonances of the nanowire. They are detected by measuring the time-averaged photoluminescence spectrum of embedded QDs (red beam). **(b)** Calculated displacement profile of the first vibration modes of each family: $F_{1x}$, $F_{1y}$, $T_1$ and $L_1$. The colors represent the stress component $\sigma_{zz}$ for a maximum displacement of 1 nm. For each mode, we also show the distribution of $\sigma_{zz}$ in the QDs cross-section.

### 4.3.2 Electrostatic excitation of vibration modes

Mechanical vibrations are driven by applying an electrostatic force on the nanowire thanks to three on-chip electrodes (fig. 3.1b). As shown in fig. 4.1a, one of the top needle electrodes is biased at a potential $V(t) = V_{\mathrm{dc}} + V_{\mathrm{ac}}\cos(\omega t)$, whereas the other needle electrode and the bottom gold plane are grounded. We choose here a negative DC bias in order to limit leakage currents and typically operate the device with $|V_{\mathrm{ac}}| \ll |V_{\mathrm{dc}}|$ (see section 3.5.1. This immerses the wire into an inhomogeneous electrostatic force field that is proportional to $V(t)^2$ and features a DC and an AC part.

Locally, on the wire, an infinitesimal volume $\delta V$ experiences a force $\delta\mathbf{F}(\mathbf{r},t) = \mathbf{f}(\mathbf{r},t)\delta V$. The force volumic density can be decomposed as

$$\mathbf{f}(\mathbf{r},t) = \mathbf{f}_{\mathrm{dc}}(\mathbf{r}) + \mathbf{f}_{\mathrm{ac}}(\mathbf{r},t), \tag{4.11}$$

where the first term is the static contribution and the second term the time varying one. In our measurements, $|V_{\mathrm{dc}}| \gg |V_{\mathrm{ac}}|$. The DC part of the force field is then proportional to $V_{\mathrm{dc}}^2$, whereas the AC part scales as $2V_{\mathrm{dc}}V_{\mathrm{ac}}$. This reflects on the excerted force: the typical amplitude of $\mathbf{f}_{\mathrm{dc}}$ is much larger than that of $\mathbf{f}_{\mathrm{ac}}$.

**DC force field.** The static component $\mathbf{f}_{\mathrm{dc}}(\mathbf{r})$ induces a static bending of the wire (the result of static bending for the wire investigated in this chapter is shown in section 3.5). Furthermore, the external force field $\mathbf{f}_{\mathrm{dc}}(\mathbf{r})$ “dresses” the oscillator. In the perturbative regime, and to lowest order, the gradient of $\mathbf{f}_{\mathrm{dc}}(\mathbf{r})$ leads to an additional spring constant for the oscillator. For example, we consider the mode $F_{1x}$ that vibrates along the direction parallel to the unitary vector $\hat{\mathbf{x}}$. The spring constant due to the gradient of the dc force reads:

$$k_{\nabla} = -\int \partial_x(\mathbf{f}_{\mathrm{dc}}(\mathbf{r}) \cdot \hat{\mathbf{x}})|\mathbf{u}_{F_{1x}}(\mathbf{r})|^2 \mathrm{d}^3\mathbf{r}. \tag{4.12}$$

Note that $k_{\nabla}$ can be either positive or negative. A similar expression is obtained for $F_{1y}$ by changing $x$ into $y$ in eq. (4.12). As shown in section 4.7, this effect induces a measurable shift of the resonance frequency of $F_{1x}$ and $F_{1y}$.

**AC force field.** We now focus on the oscillating part $\mathbf{f}_{\mathrm{ac}}(\mathbf{r}, t)$, which is dominated by a driving at the angular frequency $\omega$ (the driving at the $2\omega$-harmonic can be neglected). The effective force that appears in eq. (4.7) is given by:

$$F_{\mathrm{eff}}(t) = \int \mathbf{f}_{\mathrm{ac}}(\mathbf{r}, t) \cdot \mathbf{u}_m(\mathbf{r}) \mathrm{d}^3\mathbf{r}. \tag{4.13}$$

This expression clearly highlights that the driving force depends on the vectorial overlap between the external force field density $\mathbf{f}_{\mathrm{ac}}(\mathbf{r}, t)$ and the mode shape $\mathbf{u}_m(\mathbf{r})$. We did not compute $F_{\mathrm{eff}}$ for all the modes. Instead, we employed FEM simulations to compute the total force and torque applied to the microwire in the static (DC) case. This provides a good indication of the ability of our actuation scheme to drive the various vibration modes. These calculations are detailed in the next section.

### 4.3.3 Finite-element simulations of the static force field

In this section, we present numerical simulation for the magnitude and direction of the force and torque applied on the nanowire via the electrostatic excitation. This allows us to study the effect of an off-axis nanowire location.

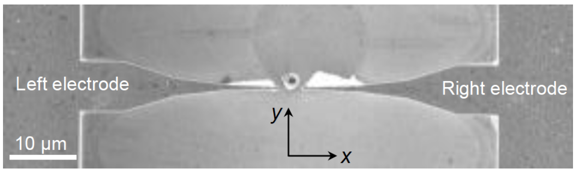

Figure 4.2: **Investigated device.** Top SEM view of the investigated nanowire. Note the offset of the nanowire along the $y$ direction.

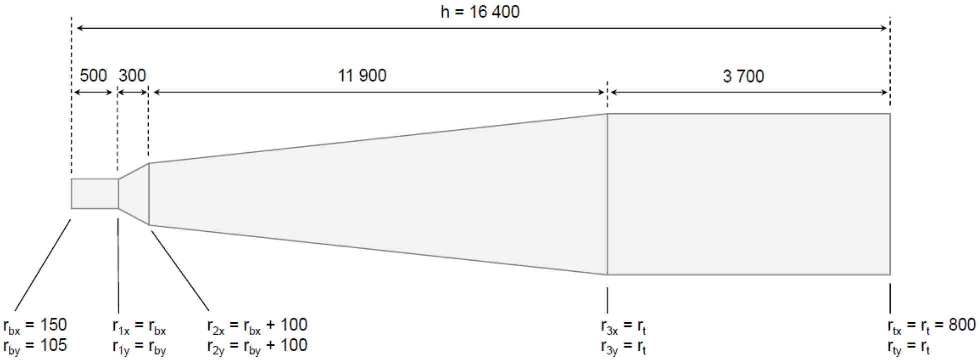

(a)

Figure 4.3: **Geometry used in finite-element simulations.** This geometry is derived from SEM observation. Distances in nm, not to scale.

**Simulated geometry.** Figure 4.2 shows a SEM picture of the investigated device. Globally, its geometry is identical to one of the device presented in chapter 3. There is however an important difference: in chapter 3, the center of the nanowire top facet was located on the $x$-axis defined by the two top electrodes, in a central position. The top facet is offset by $\sim 200$ nm in the $x$ direction and $\sim 600$ nm in the $y$ direction (see fig. 4.2). This asymmetric location yields additional components for the force field experienced by the nanowire, as discussed in section 4.3.2. For details regarding nanofabrication, see the previous chapter in section 3.4.

Simulations are based on the geometry obtained from the SEM inspection and shown in fig. 4.3. The structure features a total height of 16.4 $\mu$m. The top facet is circular (radius $r_t = 800$ nm), as defined by e-beam lithography. The bottom end is elliptical due to a slight anisotropy of the etching process: we measure $r_{bx} = 150$nm and $r_{by} = 105$nm. While this was not an important detail for strain tuning in chapter 3 it has a much greater importance for the dynamics as discussed in section 4.2. SEM inspection also reveals that the structure deviates from an ideal conical shape. To account for this, we introduce 3 intermediate sections (fig. 4.3). The wire is made of GaAs, which is treated as an isotropic material (Young modulus, $Y = 85.9$ GPa; Poisson ratio, $\nu = 0.31$; volumic mass, $\rho = 5.316\,\mathrm{kg.m}^{-3}$). In the simulation, the wire base is rigidly anchored. We have checked that including the first layers of the substrate (200 nm of gold, on 5 $\mu$m of SU8 resist) does not significantly changes the predictions.

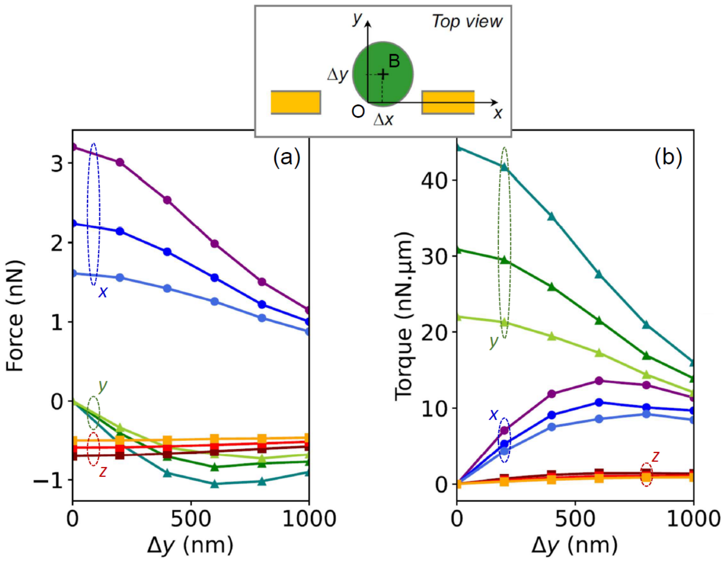

Figure 4.4: **Finite element simulations.** **(a)** Calculated components of the total static force $\mathbf{F}_{\mathrm{dc}}$ versus the $y$-offset $\Delta y$. **(b)** Calculated components of the total moment $\mathbf{M}^{\mathrm{B}}_{\mathrm{dc}}$ versus $\Delta y$. In both cases, we consider three values for the $x$-offset: $\Delta x = 0,\ 100,\ 200$ nm and use $V_{\mathrm{dc}} = -10$ V.

**Force and torque on a nanowire in an asymmetric location.** We employ finite-element simulations (COMSOL) to investigate the impact of the asymmetric wire location on the electrostatic force. Starting from the symmetry point O (on the $x$ axis, in-between the two top electrodes), the center of the wire base B is offset by $\Delta x$ and $\Delta y$. We use here the same model as in section 3.3.3.2 and recall that free carriers in the wire provide an important contribution to the force. We consider here the metallic case, which gives an upper bound for the force. We first focus on $\mathbf{F}_{\mathrm{dc}}$, the total force experienced by the wire. fig. 4.4a shows the dependence of its three components as a function of $\Delta x$ and $\Delta y$ for $V_{\mathrm{dc}} = -10$ V. At a centered location ($\Delta x = \Delta y = 0$), the force features an $x$-component (towards the biased electrode) and a $z$-component (towards the substrate). Increasing $\Delta y$ gives birth to a significant $y$-component, which points towards the electrodes. We next consider the total moment calculated at the center of the wire base

B, $\mathbf{M}^{\mathrm{B}}_{\mathrm{dc}}$. In fig. 4.4b, its three components are plotted as a function of $\Delta x$ and $\Delta y$. In addition to the bending moments oriented along the $x$ and $y$ axes, simulations reveal a longitudinal moment (oriented along $z$). This last component only exists for $\Delta y \neq 0$ and arises because of the inhomogeneity of the force field.

These simulations provide information on the ability of electrostatic actuation to drive the various modes. We stress that, in all rigour, one should compute the overlap between the force field and the mode shape to extract the effective driving force (eq. (4.13)). Nevertheless, the calculations yield a reasonnable estimate, in particular for the first modes of each family.

To conclude, the complex force field allows us to induce the following deformations on the nanowire: flexion along $\hat{\mathbf{x}}$, flexion along $\hat{\mathbf{y}}$, axial deformation (along $\hat{\mathbf{z}}$) and torsion (rotation of axis $\hat{\mathbf{z}}$). This tells us that we should be able to excite the following first order modes: $F_{1x}$, $F_{1x}$, $L_1$, $T_1$. We also see that the contributions associated with the two flexions largely dominate the other ones.

## 4.4 Principle of the experiment

### 4.4.1 Experimental setup

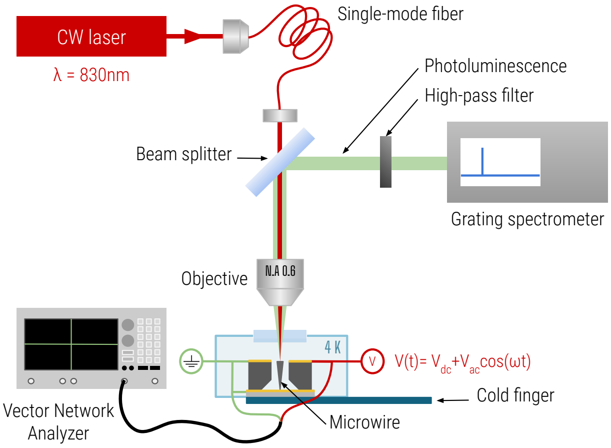

Figure 4.5: **Schematics of the experimental setup.**

Experiments are performed in a micro-photoluminescence setup that is schematized in fig. 4.5. The sample is mounted on the cold finger of a liquid helium flow cryostat ($T \approx 4\,\mathrm{K}$) which is continuously pumped to mantain a pressure ($P \approx 10^{-6}$ mbar). The cryostat is equipped with an optical access. To excite the QD luminescence, we employ a Ti-Sapphire laser operated in cw mode. The excitation wavelength ($\lambda_{\mathrm{exc}} = 830\,\mathrm{nm}$) is tuned 10 nm above the bandgap of GaAs, in the absorption continuum of the wetting layer of the QDs. This nonresonant excitation scheme enables us to simultaneously light up all the QDs that are embedded in the nanowire. After spatial filtering with a single-mode fiber, the laser beam is focused on a single nanowire with a microscope objective (focal length: 5 mm, numerical aperture: 0.6). The same objective collects the device luminescence, which is focused on the entrance slit of a grating spectrometer with a lens (focal length: 75 mm, magnification: ×25). The grating spectrometer (1200 grooves per mm, focal length: 64cm) is equipped with a Si CCD camera (1024 pixels, pitch: $26\,\mu$m). The width of the entrance slit is $100\,\mu$m. Considering a uniform illumination, this defines an upper bound of $140\mu$eV for the spectral resolution (the internal magnification of the spectrometer is ×1). When the nanowire image at the entrance of the spectrometer becomes smaller than the CCD pixel size, the latter imposes a lower bound on the resolution. We take a typical limit that corresponds to two CCD pixels or 70 $\mu$eV. The actual resolution is found between these two values; it depends on the exact size of the trumpet image at the entrance of the spectrometer. We drive the wire mechanical vibration by applying a bias $V(t) = V_{\mathrm{dc}} + V_{\mathrm{ac}} \cos(\omega t)$ to one of the needle-like electrodes (the other needle electrode and the bottom plane are both grounded). The signal $V(t)$ is generated by a spectrum analyser (Agilent E50613) and is routed to the sample with a $50\Omega$ BNC coaxial cable.

### 4.4.2 Principle

To perform a mechanical spectroscopy of the device, we scan the driving frequency $\omega/(2\pi)$ while measuring the QD photoluminescence spectrum (integration time $\sim$ 1s). Far from a mechanical resonance, the wire is at rest and the luminescence spectrum consists of sharp spectral lines that are associated with the recombination of excitonic complexes trapped in QDs (neutral and charged excitons, neutral biexciton). Approaching the resonance we expect a spectral broadening from the stress induced shift in the lines (as shown in fig. 4.6). Quantitative analysis of vibration-broadened spectra aims at determining the modulation amplitude $E_{\mathrm{ac}}$ for relevant QD emission lines. When the mechanical frequency is much smaller than the QD radiative rate ($\Gamma_{\mathrm{rad}}/(2\pi) = 160$ MHz for a typical exciton lifetime of 1 ns), the QD emis-

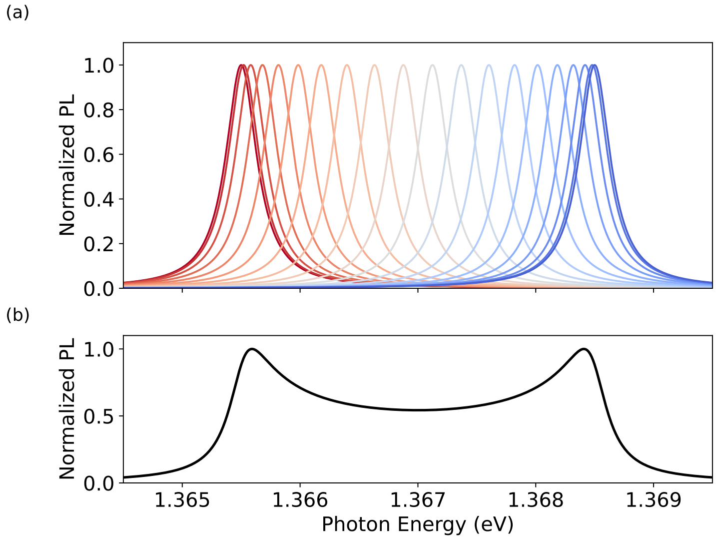

Figure 4.6: **Calculation of the vibration-broadened spectrum. (a)** the photoluminescence emission of a QD embedded in vibrating nanowire consists in a Lorentzian profile whose central frequency oscillates in time. **(b)** the final spectrum is obtained time averaging, as in eq. (4.14). Here $E_{\mathrm{ac}} > \delta E$ so that we observe the characteristic camelback lineshape.

sion spectrum adiabatically follows the mechanical oscillation. We describe the QD emission as a Lorentzian profile whose central frequency oscillates in time: $E_{\mathrm{eg}}(t) = E_{\mathrm{dc}} + E_{\mathrm{ac}}(\omega)\cos(\omega t)$. Here, $E_{\mathrm{dc}}$ includes the static shift induced by the static part of the electrostatic force field. Since we employ continuous wave (CW) excitation and do not record the photon arrival time, we discarded a phase term that is not relevant for our experiments. We also assume that the spectral linewidth $\delta E$ remains constant in the course of the oscillation. Time averaging then yields the emission spectrum:

$$S(E,\omega) = I_{\mathrm{int}}\left(\frac{\omega}{2\pi}\right)\int_{-\frac{\pi}{\omega}}^{+\frac{\pi}{\omega}} \frac{\delta E}{2\pi}\frac{1}{(E - E_{\mathrm{eg}}(t))^2 + (\delta E/2)^2}\mathrm{d}t, \tag{4.14}$$

where the scaling factor $I_{\mathrm{int}}$ corresponds to the spectrally-integrated intensity. When $E_{\mathrm{ac}}$ exceeds $\delta E$, eq. (4.14) yields a "camelback" lineshape (see fig. 4.6), with two peaks that are approximately separated by $2E_{ac}$. Since $E_{ac}$ is proportional to the vibration amplitude $x_{ac}$, it is clear that the brodenand QD spectrum directly reflects the amplitude response of the oscillator.

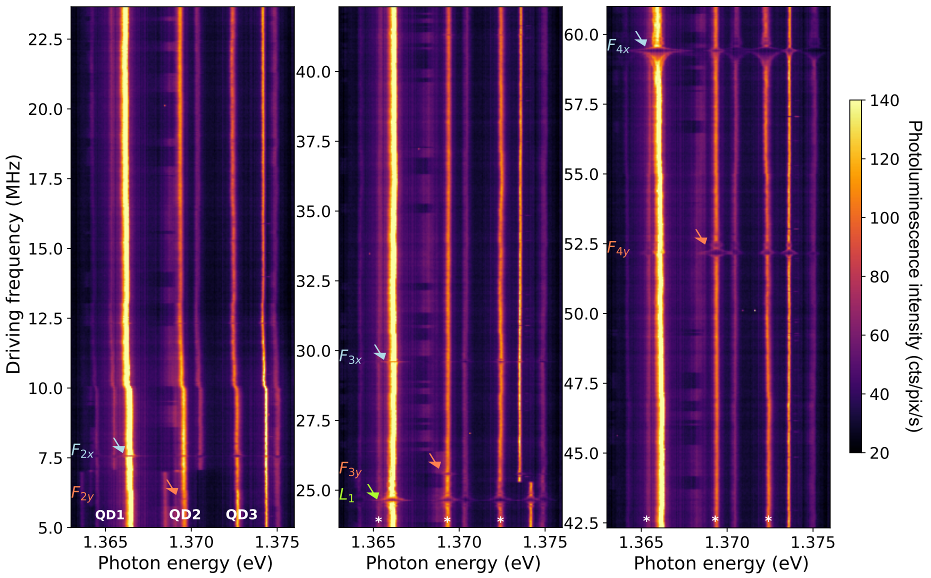

Figure 4.7: **Example of wide-range frequency scan.** Measured photoluminescence intensity (color coded) versus the photon energy and the driving frequency $\omega/(2\pi)$. The driving frequency increases from 5 MHz up to 61 MHz by steps of 5 kHz and the measurement is performed for $V_{\mathrm{dc}} = -10$ V and $V_{\mathrm{ac}} = 1$ V. Total measurement time: 4h.

### 4.4.3 Example of widerange frequency scan

Figure 4.7 shows QD photoluminescence spectra as the driving frequency is varied from 5 MHz and up to 61 MHz by steps of 5 kHz. The discrete resonances of the nanowire stand on a very clean background. This is typically the case up to $\sim$ 120 MHz. Mode identification will be discussed in section 4.5. It is based on the modulation pattern of the various QDs embedded in the microwire. This experimental fingerprint is complemented by finite-element simulations.

The total scan lasted 4 hours: this measurement is thus also an excellent test of the QD spectral stability. However, fig. 4.7 reveals that some QD lines can exhibit significant spectral jumps (*e.g.* close to 7 MHz).In the following we will mostly discuss QD lines 1, 2 and 3.

### 4.4.4 Fit of vibration-broadened QD emission spectra

This section discusses the fit process, which is illustrated for the flexural mode $F_{4x}$. The left panel in fig. 4.8a shows the measured QD photoluminescence spectra when scanning the driving frequency across the mechanical

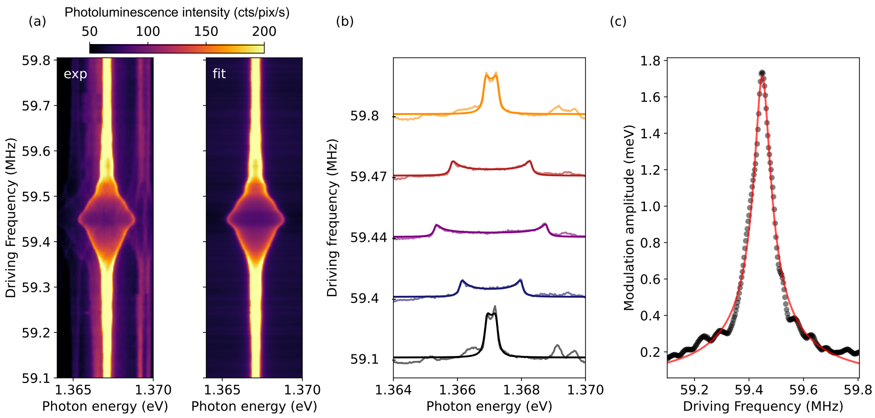

Figure 4.8: **Fit procedure - mode $\mathbf{F_{4x}}$. (a)** Left panel: Measured photoluminescence intensity (color-coded) versus the photon energy and the driving frequency $\omega/(2\pi)$ (zoom on line QD1). Right panel: fit. **(b)** Linecuts for selected $\omega/(2\pi)$ (transparent solid lines: experimental data, plain solid lines: fit). **(c)** Mechanical spectrum: modulation amplitude $E_{\text{ac}}$ of QD1 versus $\omega/(2\pi)$ (disks: experiment, red solid line: fit). Driving parameters: $V_{\text{dc}} = -6$ V and $V_{\text{ac}} = 0.63$ V.

resonance $F_{4x}$. We zoom here on the brightest QD line 1, which dominates the spectra. We fit the measurement to a broadened Lorentzian profile, as given by eq. (4.14). The fit parameters are: the unperturbed peak energy, the QD linewidth, the integrated intensity and the modulation amplitude ($E_{\text{dc}}$, $\delta E$, $I_{\text{int}}$ and $E_{\text{ac}}$, respectively) plus a constant background. The fit process runs as follows. We first select a driving frequency "far" from the mechanical resonance. This allows us to determine $E_{\text{dc}}$, $\delta E$, $I_{\text{int}}$ as well as the background level. We next fix these quantities (within ±5% on account of possible experimental drifts). For all driving frequencies we next adjust $E_{\text{ac}}$ in order to reproduce the experimental spectra. The right panel in fig. 4.8a demonstrates that this procedure accurately reproduces the emission of QD1. The fit quality is confirmed by the linecuts shown in fig. 4.8b. When the wire vibrates, the QD spectrum features a characteristic camel back shape (see fig. 4.6). Figure 4.8c shows the modulation amplitude of QD1 as a function of $\omega/(2\pi)$. Since $E_{\text{ac}}(\omega) \propto x_{\text{ac}}(\omega)$, this plot directly reflects the amplitude response of the oscillator. In the low-loss limit and close to the resonance peak, the latter is well approximated by the square root of a Lorentzian:

$$x_{\text{ac}}(\omega) \propto \frac{1}{\sqrt{(\omega - \Omega_m)^2 + \left(\frac{\Omega_m}{2Q_m}\right)^2}}. \tag{4.15}$$

A fit to the modulation amplitude response then yields the resonance frequency $\Omega_m/(2\pi) = 59.45\,\mathrm{MHz}$ and the mechanical quality factor $Q_m = 1030$.

### 4.4.5 Linear dependence of the vibration amplitude on $V_{ac}$

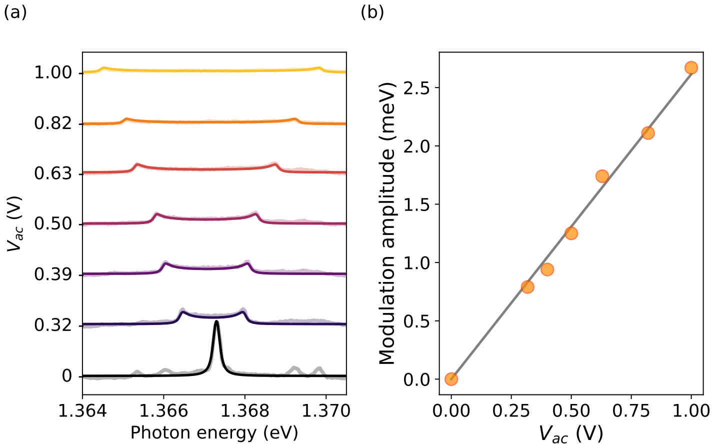

Figure 4.9: **Impact of $V_{\mathrm{ac}}$ on the vibration amplitude.** **(a)** Measured photoluminescence spectra of QD line 1 for increasing values of $V_{\mathrm{ac}}$, when driving the mode $F_{4x}$ at resonance ($V_{\mathrm{dc}} = -6$ V). Transparent solid lines: experimental QD spectra, plain solid lines: fit. **(b)** Modulation amplitude $E_{\mathrm{ac}}$ of QD1 as a function of $V_{\mathrm{ac}}$. The disks are deduced from experimental data and the solid line is a linear fit.

The measurements presented in this chapter are performed in the linear vibration regime. In particular, we have checked that $V_{\mathrm{ac}}$ does not affect the resonance frequency nor the mechanical $Q$-factor. We have also checked that the vibration amplitude is proportional to $V_{\mathrm{ac}}$. As an example, we consider here the mode $F_{4x}$. fig. 4.9a shows the spectra of QD1 when $F_{4x}$ is driven at resonance for increasing values of $V_{\mathrm{ac}}$. From a fit of the data, we determine the modulation amplitude $E_{\mathrm{ac}}$. This quantity — proportional to the vibration amplitude — is plotted versus $V_{\mathrm{ac}}$ in fig. 4.9b. As expected, $E_{\mathrm{ac}}$ is proportional to $V_{\mathrm{ac}}$.

## 4.5 Identification of the vibration modes

Mode identification is based on the measured modulation pattern of the embedded QDs. This experimental information is complemented by finite element simulations.

### 4.5.1 The QD ensemble as a probe for the transverse stress profile

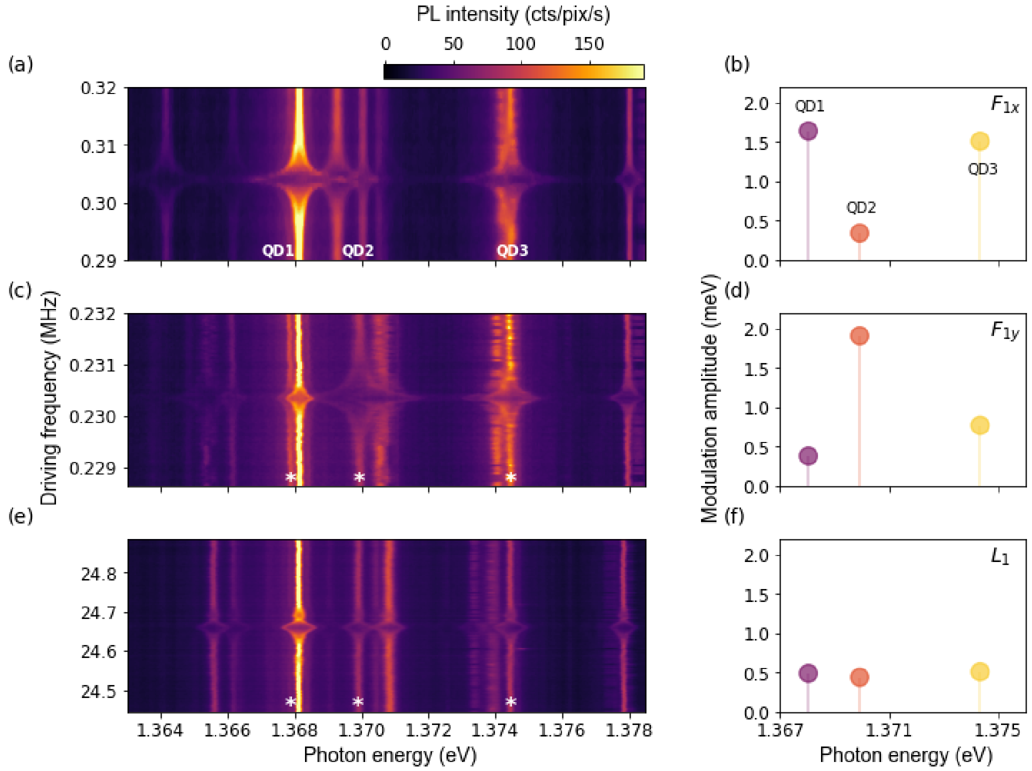

Figure 4.10: **Identification of three families of vibration modes.** Flexural mode $F_{1x}$: **(a)** Measured photoluminescence intensity (color-coded) versus the photon energy and the driving frequency $\omega/(2\pi)$. **(b)** Modulation amplitude $E_{\mathrm{ac}}$ of QD lines 1, 2 and 3, when $F_{1x}$ is driven at resonance ($\omega/(2\pi) \approx 305$ kHz). **(c)** and **(d)**: Similar plots for the flexural mode $F_{1y}$. **(e)** and **(f)**: Similar plots for the longitudinal mode $L_1$. We fix $V_{\mathrm{dc}} = -5$ V for all measurements; $F_{1y}$ **(a,b)** is driven with $V_{\mathrm{ac}} = 64$ mV, $F_{1x}$ **(c,d)** with $V_{\mathrm{ac}} = 57$ mV and $L_1$ **(e,f)** with $V_{\mathrm{ac}} = 199$ mV.

The left panels in fig. 4.10 show closeups on the $F_{1x}$, $F_{1y}$ and $L_1$ resonances, which peak at 304 kHz, 230.5 kHz and 24.65 MHz, respectively. In all cases the wire vibration is revealed by a simultaneous blurring of QD emission lines. Strikingly, driving $F_{1x}$, $F_{1y}$ or $L_1$ yields very different modulation patterns for the various QD lines (fig. 4.10). The embedded, pointlike QDs probe the strain at various (random) locations in the wire cross section. The observed modulation pattern thus directly reflects the transverse strain distribution, which we leverage for unambiguous mode identification.

In fig. 4.10, we selected three spectral lines (QD1, 2 and 3) on account of their spectral stability and their contrasted response to the various vibration modes. The right panels **(b)**, **(d)** and **(f)** show the modulation amplitude of these lines when $F_{1x}$, $F_{1y}$ and $L_1$ are driven at resonance. When exciting $F_{1x}$, QD2 is much less modulated than QD1 and 3. This reflects the inhomogeneity of the stress pattern (fig. 4.1b) and implies that QD2 is closer to the $y$-oriented minor diameter than QD1 and 3 [10]. Driving $F_{1y}$ completely reverses the modulation pattern: QD2 is much more modulated than the two other lines. Roughly speaking, the stress distribution of $F_{1y}$ is obtained by rotating the one of $F_{1x}$ by $\frac{\pi}{2}$. Thus, QD1 and 3 are much closer to the $x$-oriented major diameter than QD2. When driving $L_1$, all QDs exhibit a similar modulation. This reflects the very homogeneous stress distribution of this mode. In the following, mode identification is also backed by finite-element simulations.

### 4.5.2 Finite element simulations of vibration modes

We perform FEM mechanical simulations in order to find the resonance frequency of the supported vibration modes. The predicted resonance frequencies provide guidelines for mode identification and complement the measurement of the QDs modulation pattern. The calculated frequencies are listed in table 4.1. Overall, we obtain a good agreement between numerical simulation and measurements. We stress that the considered frequency span covers 3 orders of magnitude and that we directly plugged the wire geometry as derived from SEM observation, without any adjustment. For a given mode, we define the relative error $\epsilon = |\Omega_m^{\mathrm{sim}}/\Omega_m^{\mathrm{exp}} - 1|$. The average error for the $F_x$ family (7 modes) is $\bar{\epsilon} = 8\%$. For the $F_y$ family (5 modes), $\bar{\epsilon} = 16\%$. Finally, we obtain $\epsilon = 7\%$ for $L_1$.

| | Exp. | Simulations | | | |
|---|---|---|---|---|---|
| | $\frac{\Omega_m}{2\pi}$ (MHz) | $\frac{\Omega_m}{2\pi}$ (MHz) | $m_{\mathrm{eff}}$ (pg) | $u_{\mathrm{zpf}}$ (fm) | $\frac{\lvert g_m^{\max}\rvert}{2\pi}$ (MHz) |
| $F_{1y}$ | 0.230 | 0.183 | 49.2 | 30.5 | 0.37 |
| $F_{1x}$ | 0.307 | 0.251 | 48.9 | 26.1 | 0.41 |
| $T_1$ | – | 4.07 | 37.3 | 7.43 | 0.15 |
| $F_{2y}$ | 6.04 | 7.01 | 29.0 | 6.42 | 1.07 |
| $F_{2x}$ | 7.56 | 7.82 | 30.1 | 5.97 | 1.09 |
| $L_1$ | 24.7 | 26.5 | 88.9 | 1.89 | 1.59 |
| $F_{3y}$ | 25.6 | 30.1 | 9.98 | 5.28 | 1.85 |
| $F_{3x}$ | 29.6 | 32.6 | 10.9 | 4.86 | 1.80 |
| $F_{4y}$ | 50.5 | 60.8 | 6.93 | 4.46 | 2.64 |
| $F_{4x}$ | 59.4 | 65.7 | 7.76 | 4.06 | 2.48 |
| $F_{5y}$ | – | 99.1 | 5.41 | 3.96 | 3.34 |
| $F_{5x}$ | 102 | 107 | 6.24 | 3.55 | 3.08 |
| $T_2$ | – | 120 | 10.43 | 2.59 | 0.15 |
| $F_{6y}$ | 134 | 144 | 4.35 | 3.67 | 3.89 |
| $F_{6x}$ | 146 | 154 | 5.22 | 3.23 | 3.57 |
| $L_2$ | – | 174 | 21.00 | 1.51 | 2.08 |
| $T_3$ | – | 190 | 5.77 | 2.77 | 0.20 |
| $F_{7y}$ | – | 194 | 3.47 | 3.53 | 4.23 |
| $F_{7x}$ | 189 | 208 | 4.38 | 3.04 | 3.92 |

Table 4.1: **Finite-element modelling of vibration modes.** The measured experimental frequencies are shown in the first column (Exp.); for $F_{1x}$ and $F_{1y}$ we show the low-$V_{\mathrm{dc}}$ value.

## 4.6 Two remarkable modes

### 4.6.1 The high-order flexural mode $F_{7x}$

This section discusses the excitation and detection of the the highest resonance identified so far. The modulation pattern of QD1, 2 and 3 shown in fig. 4.11c is characteristic of the $F_x$ family. We identify this mode as the high-order flexural mode $F_{7x}$, which features 7 displacement antinodes (see fig. 4.11a).

As we can see in fig. 4.11b an unstable spectral line is present close to QD1. It is stable on the timescale of the measurement of $F_{7x}$, but was for example absent in the measurement of $F_{4x}$ (fig. 4.8). The left panel in fig. 4.12a shows the measured QD photoluminescence spectra when scanning

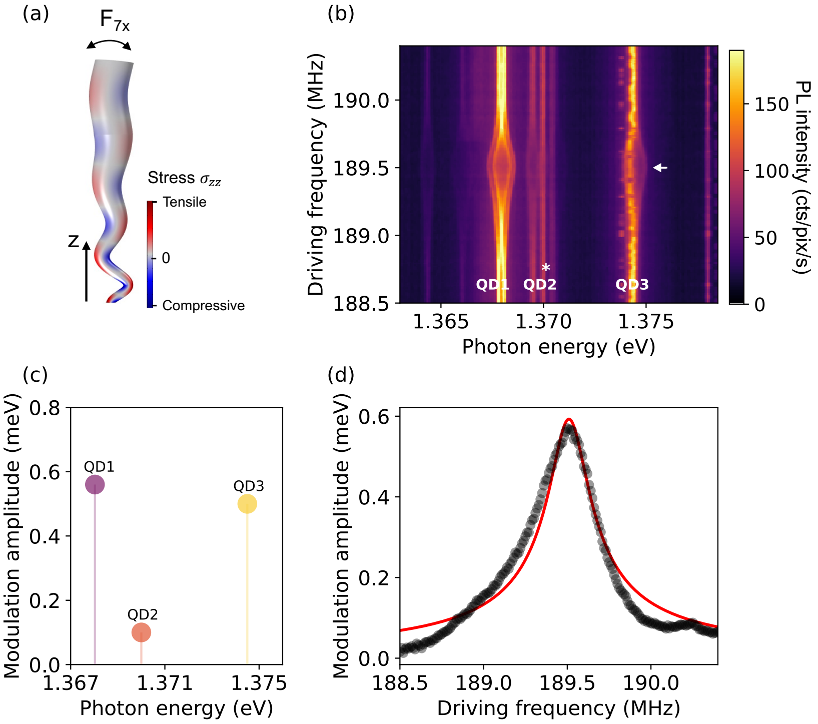

Figure 4.11: **Mechanical spectroscopy of the high-order flexural mode $\mathbf{F_{7x}}$.** **(a)** Calculated mode shape of $F_{7x}$ (not to scale); the $\sigma_{zz} > 0$ stress component is color-coded. **(b)** Measured photoluminescence intensity (color-coded) versus the photon energy and the driving frequency $\omega/(2\pi)$. In this measurement, an unstable emission line is close to QD1. **(c)** Modulation amplitude $E_{ac}$ of QD lines 1, 2 and 3, when $F_{7x}$ is driven at resonance ($\omega/(2\pi) = 189.5$ MHz). **(d)** Mechanical spectroscopy of $F_{7x}$ : modulation amplitude Eac of QD1 versus the driving frequency $\omega/(2\pi)$ (disks: experimental data, solid line: fit). Driving parameters: $V_{dc} = 5$ V, $V_{ac} = 1$ V.

the driving frequency across the mechanical resonance $F_{7x}$. The fit process is similar to the one described in section 4.4.4, except that the measured spectra are now fit to a sum of two broadened Lorentzian profiles. An excellent agreement with the experimental data is also achieved in this case, as shown by the right panel in fig. 4.12a and the linecuts in fig. 4.12b. This demonstrate the robustness of the fit approach.

We focus on QD1 and determine $E_{\mathrm{ac}}$ for the various driving frequencies $\omega/(2\pi)$ (fig. 4.11d). The fit of the data yields the mechanical resonance frequency $\Omega_m/(2\pi) = 189.5$ MHz and the mechanical quality factor $Q_m = 800$. So far, most experiments with QD-nanowire hybrid systems have involved

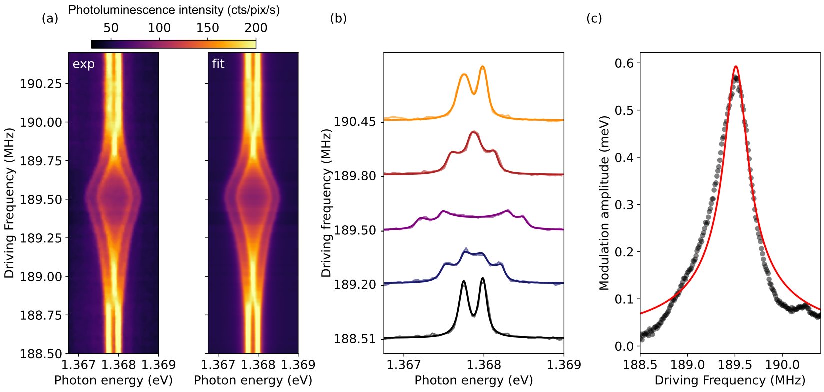

Figure 4.12: **Fit procedure - mode $\mathbf{F_{7x}}$ (a)** Left panel: Measured photoluminescence intensity (color-coded) versus the photon energy and the driving frequency $\omega/(2\pi)$ (zoom on QD line 1, note the presence of a nearby QD line). Right panel: fit. **(b)** Linecuts for selected $\omega/(2\pi)$ (transparent solid lines: experimental data, plain solid lines: fit). **(c)** Mechanical spectrum: modulation amplitude $E_{\mathrm{ac}}$ of QD1 versus $\omega/(2\pi)$ (disks: experiment, red solid line: fit). Driving parameters: $V_{\mathrm{dc}} = -5$ V and $V_{\mathrm{ac}} = 1$ V.

the fundamental flexural mode ($F_{1x}$ or $F_{1y}$). The resonance frequency of $F_{7x}$ is typically one thousand times larger. Furthermore, it exceeds the QD radiative rate ($\Gamma_{\mathrm{rad}}/(2\pi) = 160\,\mathrm{MHz}$). This will enable the future exploration of a new interaction regime for QD-nanowire hybrid systems, beyond the purely adiabatic regime.

These considerations call for a comment regarding data analysis. Whereas the adiabatic model is perfectly suited to describe low-frequency resonances such as $F_{1x}$, $F_{1y}$ and $L_1$, the mode $F_{7x}$ would require a more refined treatment. In our experiments, deviations from the adiabatic model are likely blurred by i) additional QD decoherence due to the nonresonant optical excitation and ii) the spectral resolution of the setup which vastly exceeds the mechanical frequency. As a result, the adiabatic model provides an excellent description of the QD emission spectrum, even for $F_{7x}$.

### 4.6.2 The longitudinal resonance $L_1$

We have seen that the wire also supports longitudinal vibration modes (fig. 4.10a). These are particularly interesting for hybrid nanomechanics. Indeed, the coupling strength $g_m$ weakly depends on the QD location and reaches a maximum value on the wire axis. From a photonic point of view this location simultaneously maximizes the coupling to the fundamental guided mode [20]

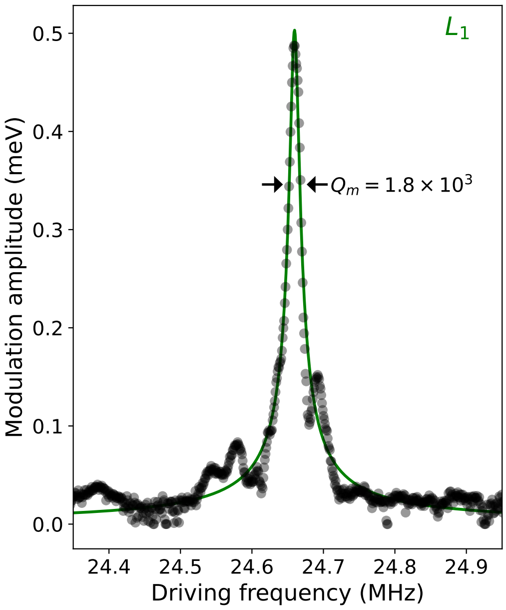

Figure 4.13: **Mechanical spectroscopy of $\mathbf{L_1}$.** Modulation amplitude $E_{\mathrm{ac}}$ of QD1 versus the driving frequency $\omega/(2\pi)$. Disks: value obtained from the fit of the experimental spectrum; solid line: fit to the amplitude response of a driven harmonic oscillator. The arrows indicate the linewidth at $\frac{1}{\sqrt{2}}$-level. Driving parameters: $V_{\mathrm{dc}} = -5$ V, $V_{\mathrm{ac}} = 199$ mV.

and the distance to the sidewall — host of potential decoherence sources. fig. 4.13 shows the resonance curve of $L_1$. This mode resonates at 24.65 MHz and features a quality factor of 1760, close to the one of the fundamental flexural modes $F_{1x}$ and $F_{1y}$. Similarly than for flexural modes, higher-order longitudinal resonances are particularly interesting for nanomechnanics. Finite element simulations predicts that $L_2$ resonates around 175 MHz. We indeed observe a feature in this frequency range, but on a large spectral bandwidth and with a lot of spectral rebounds. To a much smaller extend, such rebounds are already visible in the resonance curve of $L_1$ (fig. 4.13). We suspect here a coupling with substrate modes or a strain-coupling between neighbouring structures [45, 46]. We stress that the structure is glued on the host substrate using 4 $\mu$m of SU8 resist, a relatively soft material (its Young Modulus, 4 GPa, is much smaller that of GaAs, 85.9 GPa). Whereas the investigation of collective vibration modes in a very interesting topic on his own [45, 46], the investigation of higher-order longitudinal modes will require a new device with a hard bonding layer.

## 4.7 Scaling of the mechanical Q-factor with the mode order

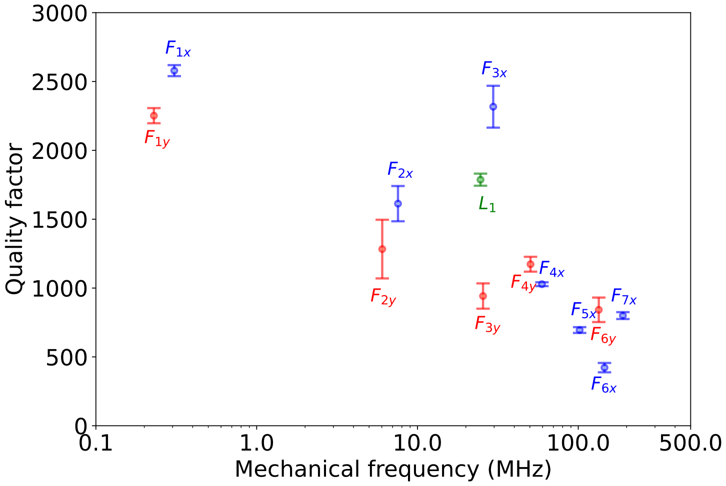

Figure 4.14: **Mechanical Q-factors.** Measured $Q$-factor and resonance frequency $\Omega_m/(2\pi)$ for the vibration modes identified in this work. Measurement conditions: $F_{1x}$, $V_{\rm dc} = -0.4$V; $F_{1y}$, $V_{\rm dc} = -2$V; $F_{2y}$ to $F_{5x}$, $V_{\rm dc} = -10$V; $F_{6y}$ to $F_{7x}$, $V_{\rm dc} = -5$ V.

We identified all the series of flexural modes between $F_{1x}$ and $F_{7x}$, which unveils the dependence of the quality factor $Q_m$ on the mode frequency. Detailed investigation revealed that special care should be taken with the fundamental resonance $F_{1x}$, which is very sensitive to the DC bias (see section 4.7). For the fundamental mode, we use the low-$V_{\rm dc}$ value, $Q_m = 2500$, as a reference. For all higher-order modes, $Q_m$ features an almost negligible dependence on $V_{\rm dc}$. fig. 4.14 shows that the quality factor is surprisingly robust when resonance frequency increases: from $F_{1x}$ to $F_{7x}$, $\Omega_m/(2\pi)$ is multiplied by $\sim 10^3$ and $Q_m$ only drops by a factor of 3. The series of flexion modes along $y$ ($F_{1y}$ and $F_{5y}$) follow a very similar trend.

**Impact of $V_{\rm dc}$ on the fundamental flexural modes.** We first focus on the voltage dependence of the resonance frequency of $F_{1x}$ (fig. 4.15b). When $V_{\rm dc}$ varies from $-0.4$ V to $-12$ V, $\Omega_m/(2\pi)$ decreases by $\sim 8\%$. Furthermore, the shift of the resonance frequency exhibits a quadratic voltage dependence (dashed line). We attribute this behavior to the spatial dependence of the DC part of the external force field. In the perturbative regime, the gradient $\partial_x(\mathbf{f}_{\rm dc}(\mathbf{r}).\hat{\mathbf{x}})$ introduces an additional spring constant $k_\nabla$, which is given by

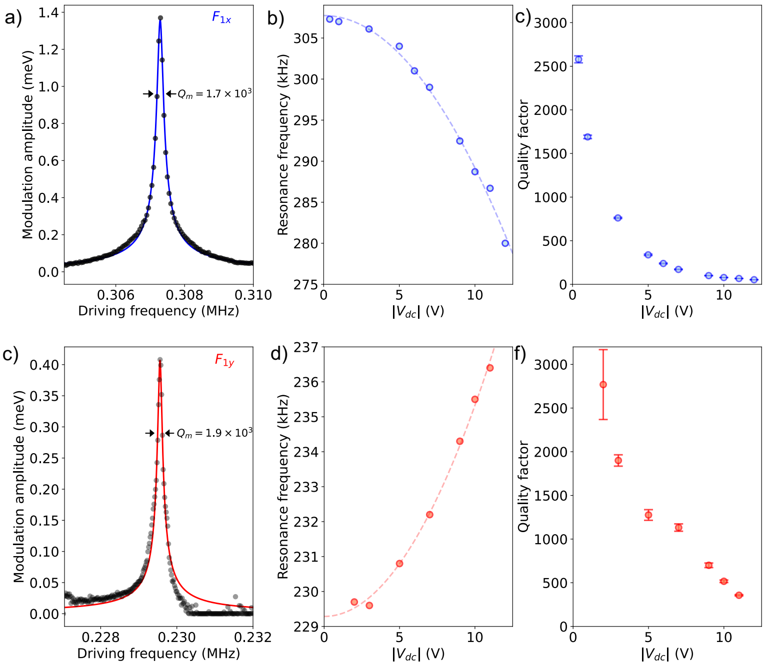

Figure 4.15: **Impact of $V_{\mathrm{dc}}$ on the fundamental flexural modes. (a)** Mechanical resonance of $F_{1x}$: Modulation amplitude $E_{\mathrm{ac}}$ of QD1 versus the driving frequency $\omega/(2\pi)$. Disks: value obtained from the fit of the experimental spectrum; solid line: fit to the amplitude response of a driven harmonic oscillator. Arrows indicate the linewidth at $\frac{1}{\sqrt{2}}$-level. **(b)** Resonance frequency $\Omega_m/(2\pi)$ as a function of $|V_{\mathrm{dc}}|$ ($V_{\mathrm{dc}} < 0$). Disks: experimental data; dashed line: fit to a quadratic law. **(c)** Mechanical $Q$-factor as a function of $|V_{\mathrm{dc}}|$. **(d)**, **(e)**, **(f)**: Similar plots for $F_{1y}$. Driving conditions: mode $F_{1x}$ (top panels): in **(a)** $V_{\mathrm{dc}} = -1$ V, in all panels (a, b, c) $V_{\mathrm{ac}} = 57$ mV; mode $F_{1y}$ (bottom panels): in **(d)** $V_{\mathrm{dc}} = -2$ V, $V_{\mathrm{ac}} = 162$ mV, in **(e)** and **(f)** $V_{\mathrm{ac}} = 63$ mV except for the data point at $V_{\mathrm{dc}} = -2$ V, taken at $V_{\mathrm{ac}} = 162$ mV.

eq. (4.12) (section 4.2). This yields a relative change in the resonance frequency $\delta\Omega_m/\Omega_m \approx k_\nabla/(2k_{\mathrm{eff}})$. Since $\mathbf{f}_{\mathrm{dc}}(\mathbf{r}).\hat{\mathbf{x}}$ increases with $x$, $k_\nabla < 0$ and $\delta\Omega_m < 0$, which is also consistent with the observation. Furthermore, the DC electrostatic force — and thus its gradient — scales as $V_{\mathrm{dc}}^2$, hence the observed quadratic frequency shift. Figure 4.15e shows the voltage dependence of the resonance frequency of $F_{1y}$. In this case, the frequency *increases* quadraticaly up to $\sim 3\%$ when $|V_{\mathrm{dc}}|$ increases. Compared to $F_{1x}$, the $y$-polarized mode experiences a projected force gradient of opposite sign, with weaker amplitude.

We now turn to the voltage dependence of the mechanical quality factors

$Q_m$ of modes $F_{1x}$ and $F_{1y}$ (figs. 4.15c and 4.15f, respectively). Since the amplitude of the effective driving force scales as the product $V_{\rm dc}V_{\rm ac}$, one could naively expect that $V_{\rm dc}$ and $V_{\rm ac}$ play a symmetric role. This is not always the case. As shown in fig. 4.15, both the resonance frequency $\Omega_m/(2\pi)$ and the quality factor $Q_m$ of the fundamental flexural modes depend on $V_{\rm dc}$. In both cases, $Q_m$ decreases dramatically when $|V_{\rm dc}|$ increases. Considering for example $F_{1x}$, $Q_m$ exceeds 2500 for $V_{\rm dc} = -0.4$ V and drops down to 53 for $V_{\rm dc} = -12$ V. The origin of these supplementary mechanical losses is not yet fully elucidated, but we suspect free-carriers, located in particular in the nearby electrode stacks. Indeed, electrical measurements reveal a highly nonlinear I-V curve, with a resistance that strongly depends on $V_{\rm dc}$ (section 3.5.1). For all other modes, the impact of $V_{\rm dc}$ on $\Omega_m/(2\pi)$ and $Q_m$ is almost negligible.

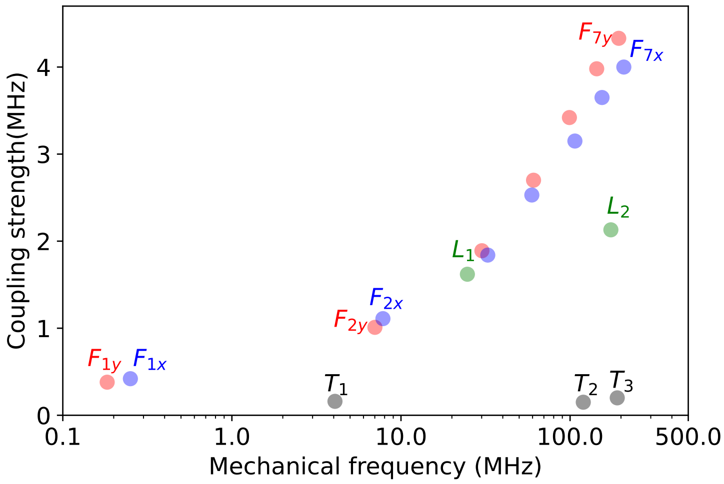

Figure 4.16: **Coupling strength.** Calculated maximal coupling strength $g_m^{\rm max}/(2\pi)$ as a function of the mechanical frequency $\Omega_m/(2\pi)$. For flexural modes, this maximum value is achieved on the sidewall. For longitudinal modes, $g_m$ is maximum on the wire axis and features a much weaker spatial dependence.

**Scaling of the coupling strength with the mode order.** We can obtain a numerical estimate of the coupling strength $g_m$ via FEM simulations. As discussed in section 4.2 the coupling constant is defined as: $g_m = (\partial_x\omega_{\rm eg})x_{\rm zpf}$, with $x_{\rm zpf} = \sqrt{\hbar/(2m_{\rm eff}\Omega_m)}$ the rms value of the zero point fluctuations of the oscillator position. For our self-assembled QDs, $\partial_x\omega_{\rm eg} = \frac{1}{\hbar}\Big[a\partial_x\epsilon_h + b\partial_x\epsilon_{sh}\Big]$. Here, $\epsilon_h = \epsilon_{xx} + \epsilon_{yy} + \epsilon_{zz}$ is the hydrostatic shear strain and $\epsilon_{sh} = 2\epsilon_{zz} - \epsilon_{xx} - \epsilon_{yy}$ is the tetragonal shear strain; $a$ and $b$ are the deformation potentials of the QD material. We consider a QD made of $\mathrm{In}_{0.5}\mathrm{Ga}_{0.5}\mathrm{As}$ and perform a linear interpolation between the deformation potentials of pure InAs and pure GaAs [194] to obtain $a = -7.5\,\mathrm{eV}$ and $b = -1.9\,\mathrm{eV}$. This immediately yields $\partial_x \epsilon_h$ and $\partial_x \epsilon_{sh}$. The effective mass $m_{\mathrm{eff}}$ can for example be obtained from the time-averaged elastic energy $\langle W_{\mathrm{el}} \rangle_t = \frac{1}{4} m_{\mathrm{eff}} \Omega_m^2 x_{ac}^2$. Owing to the inhomogeneous strain distribution in the wire cross-section, $g_m$ generally depends on the QD location. In table 4.1, we give the maximum value of the coupling strength $|g_m^{\max}|$. For flexural and torsional modes, the maximum value is achieved on the sidewall. For longitudinal modes, it is reached on the wire axis.

Figure 4.16 shows the maximum value $g_m^{\max}$ in the QD section for the investigated modes. For flexural modes, $g_m$ increases linearly with the distance to the neutral diameter and reaches a maximum on the sidewall. For $F_{7x}$, $g_m^{\max}/(2\pi)$ is as high as 3.9 MHz: this is the largest value reported so far for a QD-based hybrid system. In particular, it exceeds the state-of-the-art of high-frequency QD-hybrid systems [193, 83] by nearly two orders of magnitude. Such an improvement results from the combination of two key factors. First, the longitudinal uniaxial stress applied along $z = [001]$ optimizes the QD energy shift. Indeed, the shifts associated with hydrostatic and tetragonal shear strains add constructively [171]. Second, fig. 4.16 demonstrates that increasing the mode order vastly increases the coupling strength. Such a favourable scaling can be understood from a simple analytical model that considers QDs located at the anchoring end of a cylindrical wire. Due to the increase in the curvature radius with the mode order, $\partial_x \omega_{eg} \propto \Omega_m$; in parallel, $x_{\mathrm{zpf}} \propto 1/\sqrt{\Omega_m}$, which leads to $g_m \propto \sqrt{\Omega_m}$ for this simple case.

Note that here the coupling strength is estimated using finite-element simulations, another way to obtain the coupling strength would be by measuring the actual physical displacement and use eq. (4.3).

## 4.8 Conclusion

We leveraged an on-chip actuation technique to explore the high-order vibration modes of a GaAs nanowire that embeds self-assembled inas QDs. The QDs microphotoluminescence spectrum allows to optically detect mechanical vibration and to identify the mode nature. More specifically, we conduct a comprehensive characterization of flexural vibrations over the $200\,\mathrm{kHz} - 200\,\mathrm{MHz}$ frequency span and identify a mode that resonates close to 189.5 MHz, with a quality factor as high as 800. The QD-mode coupling strength — calculated using finite-element simulations — reaches 3.9 MHz: this is the highest value reported so far for a QD-hybrid system. Beyond flexural resonances, longitudinal modes are also particularly promising: close-to-axis QD locations simultaneously optimize both the coupling strength and the photonic properties [20]. Whereas $L_1$ was clearly identified in the present device, the $L_2$ resonance is blurred, likely by hybridization with modes supported either by the substrate or by nearby nanowires [45, 46].

The massive increase in the resonance frequency achieved thanks to higher-order modes brings QD-nanowire hybrid systems very close to the so-called resolved-sideband regime [9], in which the mechanical frequency $\Omega_m/(2\pi)$ exceeds the total QD linewidth $\delta E/h$. Under resonant optical excitation, a self-assembled InAs/GaAs QD embedded in a photonic trumpet features $\delta E/h$ as low as 1 GHz [132]. Over the years, bottom-up nanowire QDs have also demonstrated impressive progress: in state-of-the-art InAsP/InP structures, $\delta E/h$ now reaches 300 MHz [105]. Spectrally-resolved phonon sidebands enable frequency conversion based on optomechanical wave mixing [199, 83]. In this context, QD-nanowire systems offer a large coupling strength and an excellent optical interfacing between the QD and external collection optics [36, 151, 131].

Control of the wire motion by optical means is another important perspective of this work. For example, a selective driving of the low-frequency sideband cools down the mechanical mode, which constitutes a first step towards the generation of quantum states of motion. This first step is in fact already quite challenging: whereas cavity optomechanics exploits the circulation of many photons to boost the effective coupling strength [33], a hybrid system operates with at most one quanta. This imposes stringent constraints on $g_m$ and $Q_m$: in the resolved sideband regime $(g_m/\Omega_m)^2 Q_m$ should exceed 1 to enable efficient mode cooling [200]. Considering the mode $F_{7x}$ identified in this chapter, we obtain a value of 0.2 that approaches the cooling threshold. Looking ahead, shrinking the nanowire length down to the submicron range appears as a simple yet powerful strategy to further boost $g_m$ by one order of magnitude. Mode cooling then becomes possible with $Q_m \sim 10^3$.

# Conclusion and perspectives

In the following, we summarize the main results and discuss the perspectives associated with each chapter.

**Nanopost optical cavity.** In chapter 2 we have studied a novel optical nanocavity based on a nanopost design. Despite its simplicity, it offers a large extraction efficiency and a broadband acceleration of spontaneous emission. Specifically we extended the study done in [97] by performing resonant excitation spectroscopy of a QD embedded in the nanocavity. From a technical point of view, it is the first time that RE measurements have been done on such a structure. These measurements have been performed with a confocal microscope using a cross-polarization scheme for laser rejection. We found a laser rejection exceeding $10^6$, quite impressive for such a structured sample. During this study, we gained a lot of expertise in optical resonance spectroscopy, in particular in the way of building up and align the optical setup.

We investigated a trion emission line experiencing a Purcell acceleration by a factor of 4.9 ($T_1 = 340\,\mathrm{ps}$). We observed that an additional weak, non resonant laser is crucial to obtain a resonance fluorescence signal. Such a behaviour has been observed by other groups and is attributed to a stabilization of the QD charge environment. We performed two types of measurements: linescans and intensity auto-correlation measurements. Linescans reveal a significant spectral broadening, that we attribute to a low-frequency spectral wandering. A fit to a Voigt profile yields a Gaussian contribution (assumed to account for all the spectral wandering) and a Lorentzian one (assumed to account for homogeneous broadening, including power broadening). Our model yields a spectral wandering with a full width at half maximum of 2 GHz which shows no correlation with the resonant excitation power. We attribute it mainly to charge noise and will discuss possible improvements in the following section. In the low-power limit, we obtain a ratio $T_2/2T_1 \simeq 0.5$ that is far from the radiative limit of $T_2/2T_1 = 1$. During his PhD at Néel Institute, Maxime Gaignard measured a Hong Ou Mandel visibility of 80%

for photons separated by 2 ns emitted by exactly the same device. This suggests that $T_2/2T_1 \simeq 0.8$ and that our model overestimates pure dephasing. A possible explanation would be a contribution to spectral wandering with a Lorenztian profile. We now turn our attention to intensity auto-correlation. At long delays, the measurements reveal that the QD is blinking on a typical timescale of a few hundreds of ns. This effect can be partially mitigated by increasing the non-resonant laser power.

Nanocavities are interesting in particular to realize bright and broadly-tuneable sources of indistinguishable single photons. We discus below future directions and first focus on the improvement of the QD spectral properties and next discuss spectral tuning.

A recent theoretical study, conducted in collaboration with the group of Niels Gregersen (DTU), suggests straightforward improvements of the cavity design. Indeed, the second antinode of the cavity mode offers in general better performances both for the Purcell factor and for the far-field collection efficiency. The Purcell factor can reach 7.7, which is of course beneficial to maximize the photon indistinguishability. In addition, this second antinode is more favorable to limit decoherence due to thermal vibration. Indeed, previous work in the team has shown that nanowire structures are highly sensitive to this spectral broadening mechanism. Even if the short height of the nanopost reduces a lot the number of low-frequency modes (say below 1 GHz), preliminary numerical studies reveal that the first flexural mode (500 MHz) could lead to a significant line broadening for a QD located on the first antinode. These simulations also show a significant improvement when moving the QD to the second antinode, which is located farther from the anchoring point. Regarding the low-frequency charge noise, the application of an electrical field on the QD is an established technique to control the charge environment of the QD [165, 135]). Still in collaboration with the DTU group, we investigated several nanocavity designs that are compatible with electrical contacts. This should improve the control over the low-frequency noise. Beyond InAs self-assembled QDs, GaAs QDs have also recently demonstrated appealing performance, in particular photon interference from two distinct QDs without any Purcell acceleration [185, 205]. The design and fabrication process could be easily adapted in order to define an AlGaAs nanocavity around these GaAs QDs.

Finally, wavelength tuning of a QD embedded in a nanopost cavity can also be achieved by mechanical strain. It is unlikely that the electrostatic actuation demonstrated with photonic trumpets will work with a $0.5\,\mu$m-high nanowire. Instead, we plan to glue the nanopost structure on a planar piezo actuator [184], and to transfer the mechanical strain from the planar piezo to the nanowire.

**Electrostatically-actuated photonic trumpet.** In chapter 3, we demonstrated the strain-tuning of QDs embedded in a photonic wire antenna. In this device, the antenna is flanked by two needle-like electrodes and the bottom mirror serves as a third electrode. Biasing one of the needle electrode with a DC voltage whereas the other electrodes are grounded leads to an electrostatic force that bends the nanowire and immerses the QDs in a strain field. Biasing the other needle-like electrode bends the nanowire in the opposite direction. The emission of a given QD can thus be blue- and red-shifted, with a maximum absolute shift of 0.5meV for $V_{\text{dc}} = -10\text{V}$. In another device, in which the trumpet is largely off-centred, we achieved a shift as large as 2.5 meV for a similar voltage.

In the present device, the tuning range is limited by the maximum applied voltage. The latter is in turn imposed by the appearance of leakage currents. We suspect here a bad quality of the dielectric layers (in particular $Si_3N_4$ that was deposited at low temperature for technical reasons). In a future device, realistic improvements in the quality of the dielectric materials, possibly combined with an increase of their thicknesses, should allow multiplying the maximum voltage by a factor of 10. This will increase the applied force and consequently the tuning range by two orders of magnitude. Another simple idea is to bring the trumpet closer to one of the electrodes. One then increases a lot the bending force, but looses the ability to significantly bend the structure in the other direction.

The ability to tune independently several devices embarked on the same chip represents a key asset for the scale-up to applications requiring multiple sources operated in parallel. This will require a clean, resonant QD excitation to optimize the spectral coherence of the emitted photons. We note here that strain tuning can be included in a feedback mechanism in order to stabilize the QD emission with respect to low frequency drifts.

In addition to tuning of the QD emission wavelength, strain can also be employed to adjust other optical properties of the QDs, such as the FSS. This is crucial for the emission of polarization-entangled pairs of photons, emitted by the radiative cascade of the bi-exciton. In order to compensate for the natural asymmetry of most QDs, one can immerse the QD in a strain field that features an in-plane anisotropy [183] ($\epsilon_{xx} \neq \epsilon_{yy}$). In a wire with a circular section, bending yields equal strain components $\epsilon_{xx}$ and $\epsilon_{yy}$. A non-symmetric shell of $SiO_2$ breaks this symmetry and creates an in-plane mechanical anisotropy while preserving the optical symmetry of the nanowire

[61](the refractive index of GaAs is much larger than that of $SiO_2$).

Finally, the single-mode electromagnetic environment defined by a photonic wire [20, 131] combined with the specific stress pattern associated with trumpet bending is also particularly well suited to explore collective effects, such as superradiance [73]. Indeed, the presence of tensile and compressive stress in a given wire cross-section facilitates the tuning of two distinct QDs into resonance. In this context, a supplementary pair of electrodes would offer a vectorial control over the bending direction, enabling to control the orientation of the stress gradient in the wire cross-section. This could allow for the tuning of up to 3 distinct QDs into resonance.

**High-order nanowire vibration modes.** We have shown in chapter 4 that on-chip electrodes also constitute a very convenient tool to excite the vibration modes of the nanowire. This capability is relevant for hybrid nanomechanics, a line of research that investigates and exploits the coupling between a quantum system (here the QD) and a mechanical oscillator. In our experiments, the QDs microphotoluminescence spectrum is leveraged to optically detect mechanical vibration and to identify the mode nature. Starting from the sub-MHz fundamental flexural mode, we have shown that high-order flexural resonances enable a dramatic increase of both the mechanical frequency and the hybrid coupling strength. In particular, we identify a flexural mode that resonates close to 190 MHz — a value that exceeds the QD radiative rate — with a mechanical quality factor as high as 800. For a QD located at the stress maximum, the hybrid coupling strength reaches 3.9 MHz, the highest value reported so far for a QD hybrid system.

The massive increase in the resonance frequency achieved thanks to higher-order modes brings QD-nanowire hybrid systems very close to the so-called resolved-sideband regime [9], in which the mechanical frequency exceeds the total QD linewidth. Under resonant optical excitation, a self-assembled InAs/GaAs QD embedded in a photonic trumpet indeed features a linewidth as low as 1 GHz [132]. In the resolved-sideband regime, Raman transitions appear as spectrally-resolved satellites on the side of the bare QD emission. Driving these transitions with a narrow laser enables a control over the phonon population of the mode. To enter deeply into the sideband regime, a decrease of the nanowire height will help in increasing both the mechanical frequencies and the spectral separation between the various resonances. Another benefit of the size reduction is the increase in the hybrid coupling strength, due to the decrease in the effective mass of the oscillator.

In this respect, the nanopost optical cavity can be seen as an extremely short nanowire. As such, the structure investigated in the first chapter is also interesting in the context of hybrid nanomechanics. Indeed, finite-element simulations predict that the fundamental $F_1$ mode resonates close to 500MHz and that the $F_2$ resonance should occur close to 2 GHz. During my stay at Basel, we tried to measure the Brownian motion of theses modes, using a technique similar to the one employed in [134] (a cw narrow laser is tuned on the flank of the QD transition and Brownian motion generates noise on the resonant PL signal at the vibration frequency, that can be deduced from a Fourier analysis of the signal). At the time, we did not found any evidence of any vibrational mode. However, recent advances in the group of Richard Warburton have shown that high-frequency modes (frequency larger than the QD radiative rate) require specific detection condition. The laser power should be increased such that the Rabi frequency matches the mechanical frequency [167]. This result likely explains the lack of signal in the first experiments; another experimental run will be soon scheduled. Beyond flexural resonances, longitudinal modes are also very interesting for future experiments. In that case, close-to-axis QD locations simultaneously optimize both the coupling strength and the photonic properties [20]. We estimate that with a mechanical quality factor of the order of 1000, the hybrid coupling strength in nanopost structures should enable a cooling of the mechanical mode. This constitutes a first, important step towards the all-optical manipulation of the mechanical state.

# List of Publications

- “A nanowire optical nanocavity for broadband enhancement of spontaneous emission” Saptarshi Kotal, Alberto Artioli, Yujing Wang, Andreas Dyhl Osterkryger, Matteo Finazzer, Romain Fons, Yann Genuist, Joël Bleuse, Jean-Michel Gérard, Niels Gregersen, Julien Claudon. In: App. Phys. Lett. 118, 194002 (2021). https://doi.org/10.1063/5.0045834

- “On-Chip Electrostatic Actuation of a Photonic Wire Antenna Embedding Quantum Dots” Matteo Finazzer, Rana Tanos, Yoann Curé, Alberto Artioli, Saptarshi Kotal, Joël Bleuse, Yann Genuist, Jean-Michel Gérard, Fabrice Donatini, and Julien Claudon. In: Nano Letters 23, 2203–2209 (2023). https://doi.org/10.1021/acs.nanolett.2c04813

- “High-order nanowire resonances for high-frequency, large coupling strength quantum dot hybrid nanomechanics” Rana Thanos, Hajer Tlili, Yoann Curé, Matteo Finazzer, Alberto Artioli, Saptarshi Kotal, Yann Genuist, Pierre Verlot, Joël Bleuse, Jean-Michel Gérard, and Julien Claudon. Submitted.

- “Resonant excitation of a quantum dot in a nanopost optical cavity” Matteo Finazzer*, Maxime Gaignard*, et al. (* = equal contribution) In preparation.

# References

[1] Scott Aaronson and Alex Arkhipov. “The computational complexity of linear optics”. In: *Proceedings of the forty-third annual ACM symposium on Theory of computing*. STOC’11: Symposium on Theory of Computing. San Jose California USA: ACM, June 6, 2011, pp. 333–342. ISBN: 978-1-4503-0691-1. DOI: `10.1145/1993636.1993682`. URL: `https://dl.acm.org/doi/10.1145/1993636.1993682` (visited on 12/07/2023) (cit. on p. 2).

[2] C. Adami and N. J. Cerf. *Quantum computation with linear optics*. June 13, 1998. DOI: `10.48550/arXiv.quant-ph/9806048`. arXiv: `quant-ph/9806048`. URL: `http://arxiv.org/abs/quant-ph/9806048` (visited on 12/05/2023) (cit. on p. 2).

[3] Charles S. Adams, Jonathan D. Pritchard, and James P. Shaffer. “Rydberg atom quantum technologies”. In: *Journal of Physics B: Atomic, Molecular and Optical Physics* 53.1 (2019). Publisher: IOP Publishing, p. 012002. URL: `https://iopscience.iop.org/article/10.1088/1361-6455/ab52ef/meta` (visited on 12/08/2023) (cit. on p. 1).

[4] Yoshihiro Akahane, Takashi Asano, Bong-Shik Song, and Susumu Noda. “High-Q photonic nanocavity in a two-dimensional photonic crystal”. In: *nature* 425.6961 (2003). Publisher: Nature Publishing Group UK London, pp. 944–947. URL: `https://www.nature.com/articles/nature02063` (visited on 10/30/2023) (cit. on p. 36).

[5] M. Arcari, I. Söllner, A. Javadi, S. Lindskov Hansen, S. Mahmoodian, J. Liu, H. Thyrrestrup, E. H. Lee, J. D. Song, S. Stobbe, and P. Lodahl. “Near-Unity Coupling Efficiency of a Quantum Emitter to a Photonic Crystal Waveguide”. In: *Physical Review Letters* 113.9 (Aug. 29, 2014), p. 093603. ISSN: 0031-9007, 1079-7114. DOI: `10.1103/PhysRevLett.113.093603`. URL: `https://link.aps.org/doi/10.1103/PhysRevLett.113.093603` (visited on 11/28/2023) (cit. on p. 31).

[6] M. Arcari, I. Söllner, A. Javadi, S. Lindskov Hansen, S. Mahmoodian, J. Liu, H. Thyrrestrup, E.H. Lee, J.D. Song, S. Stobbe, and P. Lodahl. "Near-Unity Coupling Efficiency of a Quantum Emitter to a Photonic Crystal Waveguide". In: *Phys. Rev. Lett.* 113 (2014), p. 093603 (cit. on pp. 40, 77).

[7] O. Arcizet, V. Jacques, A. Siria, P. Poncharal, P. Vincent, and S. Seidelin. "A single nitrogen-vacancy defect coupled to a nanomechanical oscillator". In: *Nature Phys.* 7 (2011), pp. 879–883 (cit. on p. 102).

[8] Juan M. Arrazola, Ville Bergholm, Kamil Brádler, Thomas R. Bromley, Matt J. Collins, Ish Dhand, Alberto Fumagalli, Thomas Gerrits, Andrey Goussev, and Lukas G. Helt. "Quantum circuits with many photons on a programmable nanophotonic chip". In: *Nature* 591.7848 (2021). Publisher: Nature Publishing Group UK London, pp. 54–60. URL: `https://www.nature.com/articles/s41586-021-03202-1` (visited on 12/07/2023) (cit. on p. 2).

[9] M. Aspelmeyer, T. J. Kippenberg, and F. Marquardt. "Cavity optomechanics". In: *Rev. Mod. Phys.* 86 (2014), pp. 1391–1452 (cit. on pp. 126, 130).

[10] P.-L. de Assis, I. Yeo, A. Gloppe, H. A. Nguyen, D. Tumanov, E. Dupont-Ferrier, N. S. Malik, E. Dupuy, J. Claudon, J.-M. Gérard, A. Auffèves, O. Arcizet, M. Richard, and J.-Ph. Poizat. "Strain-Gradient Position Mapping of Semiconductor Quantum Dots". In: *Phys. Rev. Lett.* 118 (2017), p. 117401 (cit. on pp. 83, 102, 117).

[11] A. Badolato, K. Hennessy, M. Atatüre, J. Dreiser, E. Hu, P. M. Petroff, and A. Imamoğlu. "Deterministic Coupling of Single Quantum Dots to Single Nanocavity Modes". In: *Science* 308 (2005), pp. 1158–1161 (cit. on p. 38).

[12] W.L. Barnes, G. Björk, J.M. Gérard, P. Jonsson, J.A.E. Wasey, P.T. Worthing, and V. Zwiller. "Solid-state single photon sources: light collection strategies". In: *The European Physical Journal D - Atomic, Molecular and Optical Physics* 18.2 (Feb. 1, 2002), pp. 197–210. ISSN: 1434-6060, 1434-6079. DOI: `10.1140/epjd/e20020024`. URL: `http://link.springer.com/10.1140/epjd/e20020024` (visited on 12/12/2023) (cit. on p. 47).

[13] Ben Bartlett and Shanhui Fan. "Universal programmable photonic architecture for quantum information processing". In: *Physical Review A* 101.4 (Apr. 20, 2020), p. 042319. ISSN: 2469-9926, 2469-9934. DOI: `10.1103/PhysRevA.101.042319`. URL: `https://link.aps.org/`

doi/10.1103/PhysRevA.101.042319 (visited on 12/07/2023) (cit. on p. 2).

[14] Gerald Bastard. “Wave mechanics applied to semiconductor heterostructures”. In: (1990). Publisher: New York, NY (USA); John Wiley and Sons Inc. URL: https://www.osti.gov/biblio/5095386 (visited on 11/27/2023) (cit. on p. 11).

[15] M. B. Bavinck, M. Zieliński, B. J. Witek, T. Zehender, E. P. A. M. Bakkers, and V. Zwiller. “Controlling a Nanowire Quantum Dot Band Gap Using a Straining Dielectric Envelope”. In: *Nano. Lett.* 12 (2012), pp. 6206–6211 (cit. on p. 97).

[16] H. Benisty, C. M. Sotomayor-Torrès, and C. Weisbuch. “Intrinsic mechanism for the poor luminescence properties of quantum-box systems”. In: *Physical Review B* 44.19 (Nov. 15, 1991), pp. 10945–10948. ISSN: 0163-1829, 1095-3795. DOI: 10.1103/PhysRevB.44.10945. URL: https://link.aps.org/doi/10.1103/PhysRevB.44.10945 (visited on 11/30/2023) (cit. on pp. 21, 22).

[17] Alice Berthelot, Ivan Favero, Guillaume Cassabois, Christophe Voisin, Claude Delalande, Ph Roussignol, Robson Ferreira, and Jean-Michel Gérard. “Unconventional motional narrowing in the optical spectrum of a semiconductor quantum dot”. In: *Nature Physics* 2.11 (2006). Publisher: Nature Publishing Group UK London, pp. 759–764 (cit. on pp. 23, 66).

[18] G. L. Bir and G. Pikus. *Symmetry and Strain-Induced Effects in Semiconductors.* Wiley, New York, 1974 (cit. on pp. 102, 103).

[19] Gennadi Levikovich Bir, Grigori Ezekielevich Pikus, and David Louvish. *Symmetry and strain-induced effects in semiconductors.* Vol. 484. Wiley New York, 1974 (cit. on p. 82).

[20] J. Bleuse, J. Claudon, M. Creasey, N. S. Malik, J.-M. Gérard, I. Maksymov, J.-P. Hugonin, and P. Lalanne. “Inhibition, Enhancement, and Control of Spontaneous Emission in Photonic Nanowires”. In: *Phys. Rev. Lett.* 106 (2011), p. 103601 (cit. on pp. 41, 96, 98, 102, 120, 126, 130, 131).

[21] N. Bloembergen, E. M. Purcell, and R. V. Pound. “Relaxation Effects in Nuclear Magnetic Resonance Absorption”. In: *Physical Review* 73.7 (Apr. 1, 1948), pp. 679–712. ISSN: 0031-899X. DOI: 10.1103/PhysRev.73.679. URL: https://link.aps.org/doi/10.1103/PhysRev.73.679 (visited on 11/28/2023) (cit. on p. 31).

[22] U. Bockelmann and G. Bastard. "Phonon scattering and energy relaxation in two-, one-, and zero-dimensional electron gases". In: *Physical Review B* 42.14 (Nov. 15, 1990), pp. 8947–8951. ISSN: 0163-1829, 1095-3795. DOI: `10.1103/PhysRevB.42.8947`. URL: `https://link.aps.org/doi/10.1103/PhysRevB.42.8947` (visited on 11/30/2023) (cit. on p. 21).

[23] Wim Bogaerts, Daniel Pérez, José Capmany, David AB Miller, Joyce Poon, Dirk Englund, Francesco Morichetti, and Andrea Melloni. "Programmable photonic circuits". In: *Nature* 586.7828 (2020). Publisher: Nature Publishing Group UK London, pp. 207–216. URL: `https://www.nature.com/articles/s41586-020-2764-0` (visited on 12/07/2023) (cit. on p. 2).

[24] Louis Bouet, M. Vidal, T. Mano, N. Ha, T. Kuroda, M. V. Durnev, M. M. Glazov, E. L. Ivchenko, Xavier Marie, and Thierry Amand. "Charge tuning in [111] grown GaAs droplet quantum dots". In: *Applied Physics Letters* 105.8 (2014). Publisher: AIP Publishing. URL: `https://pubs.aip.org/aip/apl/article/105/8/082111/1077904` (visited on 10/11/2023) (cit. on p. 27).

[25] Samuel L. Braunstein and Peter Van Loock. "Quantum information with continuous variables". In: *Reviews of Modern Physics* 77.2 (June 29, 2005), pp. 513–577. ISSN: 0034-6861, 1539-0756. DOI: `10.1103/RevModPhys.77.513`. URL: `https://link.aps.org/doi/10.1103/RevModPhys.77.513` (visited on 12/06/2023) (cit. on p. 1).

[26] M. A. Broome, A. Fedrizzi, S. Rahimi-Keshari, J. Dove, S. Aaronson, T. C. Ralph, and A. G. White. "Photonic Boson Sampling in a Tunable Circuit". In: *Science* 339.6121 (Feb. 15, 2013), pp. 794–798. ISSN: 0036-8075, 1095-9203. DOI: `10.1126/science.1231440`. URL: `https://www.sciencemag.org/lookup/doi/10.1126/science.1231440` (visited on 12/07/2023) (cit. on p. 2).

[27] Colin D. Bruzewicz, John Chiaverini, Robert McConnell, and Jeremy M. Sage. "Trapped-ion quantum computing: Progress and challenges". In: *Applied Physics Reviews* 6.2 (2019). Publisher: AIP Publishing. URL: `https://pubs.aip.org/aip/apr/article-abstract/6/2/021314/570103` (visited on 12/08/2023) (cit. on p. 1).

[28] Jacques Carolan, Christopher Harrold, Chris Sparrow, Enrique Martín-López, Nicholas J. Russell, Joshua W. Silverstone, Peter J. Shadbolt, Nobuyuki Matsuda, Manabu Oguma, Mikitaka Itoh, Graham D. Marshall, Mark G. Thompson, Jonathan C. F. Matthews, Toshikazu

Hashimoto, Jeremy L. O'Brien, and Anthony Laing. "Universal linear optics". In: *Science* 349.6249 (Aug. 14, 2015), pp. 711–716. ISSN: 0036-8075, 1095-9203. DOI: `10.1126/science.aab3642`. URL: `https://www.science.org/doi/10.1126/science.aab3642` (visited on 12/07/2023) (cit. on p. 2).

[29] Jacques Carolan, Jasmin DA Meinecke, Peter J. Shadbolt, Nicholas J. Russell, Nur Ismail, Kerstin Wörhoff, Terry Rudolph, Mark G. Thompson, Jeremy L. O'brien, and Jonathan CF Matthews. "On the experimental verification of quantum complexity in linear optics". In: *Nature Photonics* 8.8 (2014). Publisher: Nature Publishing Group UK London, pp. 621–626. URL: `https://www.nature.com/articles/nphoton.2014.152` (visited on 12/07/2023) (cit. on p. 2).

[30] G. Cassabois. "Origines et limites du modèle de l'atome artificiel pour une boîte quantique de semiconducteurs". PhD thesis. Université Paris VI, 2006 (cit. on pp. 12, 14, 22).

[31] Guillaume Cassabois. "Origines et limites du modèle de l'atome artificiel pour une boîte quantique de semiconducteurs". thesis. Université Pierre et Marie Curie - Paris VI, Jan. 27, 2006. URL: `https://theses.hal.science/tel-00011932` (visited on 09/04/2023) (cit. on p. 12).

[32] A. Catellani and P. Ballone. "Islands at semiconductor interfaces". In: *Physical Review B* 45.24 (June 15, 1992). Publisher: American Physical Society, pp. 14197–14203. DOI: `10.1103/PhysRevB.45.14197`. URL: `https://link.aps.org/doi/10.1103/PhysRevB.45.14197` (visited on 10/09/2023) (cit. on p. 12).

[33] J. Chan, T. P. Mayer Alegre, A. H. Safavi-Naeini, J. T. Hill, A. Krause, S. Gröblacher, M. Aspelmeyer, and O. Painter. "Laser cooling of a nanomechanical oscillator into its quantum ground state". In: *Nature* 478 (2011), pp. 89–92 (cit. on p. 126).

[34] Y. Chen, J. Zhang, M. Zopf, K. Jung, Y. Zhang, R. Keil, F. Ding, and O. G. Schmidt. "Wavelength-tunable entangled photons from silicon-integrated III-V quantum dots". In: *Nat. Commun.* 7 (2016), p. 10387 (cit. on p. 77).

[35] Y. Chu, P. Kharel, T. Yoon, L. Frunzio, P. T. Rakich, and R. J. Schoelkopf. "Creation and control of multi-phonon Fock states in a bulk acoustic-wave resonator". In: *Nature* 563 (2018), pp. 666–670 (cit. on pp. 101, 102).

[36] J. Claudon, J. Bleuse, N. S. Malik, M. Bazin, P. Jaffrennou, N. Gregersen, C. Sauvan, P. Lalanne, and J.-M. Gérard. “A highly efficient single-photon source based on a quantum dot in a photonic nanowire”. In: *Nature Photon.* 4 (2010), pp. 174–177 (cit. on pp. 77, 126).

[37] Julien Claudon, Joël Bleuse, Nitin Singh Malik, Maela Bazin, Périne Jaffrennou, Niels Gregersen, Christophe Sauvan, Philippe Lalanne, and Jean-Michel Gérard. “A highly efficient single-photon source based on a quantum dot in a photonic nanowire”. In: *Nature Photonics* 4.3 (2010). Publisher: Nature Publishing Group UK London, pp. 174–177 (cit. on pp. 31, 40, 41).

[38] Julien Claudon, Niels Gregersen, Philippe Lalanne, and Jean-Michel Gérard. “Harnessing Light with Photonic Nanowires: Fundamentals and Applications to Quantum Optics”. In: *ChemPhysChem* 14.11 (Aug. 5, 2013), pp. 2393–2402. ISSN: 1439-4235, 1439-7641. DOI: `10.1002/cphc.201300033`. URL: `https://chemistry-europe.onlinelibrary.wiley.com/doi/10.1002/cphc.201300033` (visited on 10/31/2023) (cit. on p. 41).

[39] R. J. Coles, D. M. Price, J. E. Dixon, B. Royall, E. Clarke, P. Kok, M. S. Skolnick, A. M. Fox, and M. N. Makhonin. “Chirality of nanophotonic waveguide with embedded quantum emitter for unidirectional spin transfer”. In: *Nat. Commun.* 7 (2016), p. 11183 (cit. on p. 40).

[40] S. Cortez, O. Krebs, P. Voisin, and J. M. Gérard. “Polarization of the interband optical dipole in InAs GaAs self-organized quantum dots”. In: *Phys. Rev. B* 63 (2001), p. 233306 (cit. on p. 103).

[41] Andrea Crespi, Roberto Osellame, Roberta Ramponi, Daniel J. Brod, Ernesto F. Galvao, Nicolo Spagnolo, Chiara Vitelli, Enrico Maiorino, Paolo Mataloni, and Fabio Sciarrino. “Integrated multimode interferometers with arbitrary designs for photonic boson sampling”. In: *Nature photonics* 7.7 (2013). Publisher: Nature Publishing Group UK London, pp. 545–549. URL: `https://www.nature.com/articles/nphoton.2013.112` (visited on 12/07/2023) (cit. on p. 2).

[42] Shantanu Debnath, Norbert M. Linke, Caroline Figgatt, Kevin A. Landsman, Kevin Wright, and Christopher Monroe. “Demonstration of a small programmable quantum computer with atomic qubits”. In: *Nature* 536.7614 (2016). Publisher: Nature Publishing Group UK London, pp. 63–66. URL: `https://www.nature.com/articles/nature18648` (visited on 12/07/2023) (cit. on p. 2).

[43] Carole Diederichs. “The resonance fluorescence of single semiconductor quantum dots for the generation of indistinguishable photons.” thesis. Université Pierre et Marie Curie (UPMC), Dec. 7, 2016. URL: `https://theses.hal.science/tel-01416901` (visited on 08/10/2023) (cit. on p. 72).

[44] Xing Ding, Yu He, Z.-C. Duan, Niels Gregersen, M.-C. Chen, S. Unsleber, Sebastian Maier, Christian Schneider, Martin Kamp, and Sven Höfling. “On-demand single photons with high extraction efficiency and near-unity indistinguishability from a resonantly driven quantum dot in a micropillar”. In: *Physical review letters* 116.2 (2016). Publisher: APS, p. 020401 (cit. on p. 47).

[45] J. Doster, S. Hoenl, H. Lorenz, P. Paulitschke, and E. M. Weig. “Collective dynamics of strain-coupled nanomechanical pillar resonators”. In: *Nat. Commun.* 10 (2019), p. 5246 (cit. on pp. 121, 126).

[46] J. Doster, T. Shah, T. Fösel, P. Paulitschke, F. Marquardt, and E. M. Weig. “Observing polarization patterns in the collective motion of nanomechanical arrays”. In: *Nat. Commun.* 13 (2022), p. 2478 (cit. on pp. 121, 126).

[47] Artur K. Ekert. “Quantum cryptography based on Bell’s theorem”. In: *Physical Review Letters* 67.6 (Aug. 5, 1991), pp. 661–663. ISSN: 0031-9007. DOI: `10.1103/PhysRevLett.67.661`. URL: `https://link.aps.org/doi/10.1103/PhysRevLett.67.661` (visited on 12/07/2023) (cit. on pp. 1, 2).

[48] A. W. Elshaari, E. Büyüközer, I. E. Zadeh, T. Lettner, P. Zhao, E. Schöll, S. Gyger, M. E. Reimer, D. Dalacu, P. J. Poole, K. D. Jöns, and V. Zwiller. “Strain-Tunable Quantum Integrated Photonics”. In: *Nano Lett.* 18 (2018), pp. 7969–7976 (cit. on p. 78).

[49] Dirk Englund, David Fattal, Edo Waks, Glenn Solomon, Bingyang Zhang, Toshihiro Nakaoka, Yasuhiko Arakawa, Yoshihisa Yamamoto, and Jelena Vučković. “Controlling the Spontaneous Emission Rate of Single Quantum Dots in a Two-Dimensional Photonic Crystal”. In: *Physical Review Letters* 95.1 (July 2005), p. 013904. ISSN: 0031-9007, 1079-7114. DOI: `10.1103/PhysRevLett.95.013904`. URL: `https://link.aps.org/doi/10.1103/PhysRevLett.95.013904` (visited on 10/30/2023) (cit. on p. 36).

[50] A. Faraon, D. Englund, I. Fushman, J. Vučković, N. Stoltz, and P. Petroff. “Local quantum dot tuning on photonic crystal chips”. In: *Appl. Phys. Lett.* 90 (2007), p. 213110 (cit. on p. 77).

[51] Andrei Faraon, Dirk Englund, Ilya Fushman, Jelena Vučković, Nick Stoltz, and Pierre Petroff. “Local quantum dot tuning on photonic crystal chips”. In: *Applied Physics Letters* 90.21 (2007). Publisher: AIP Publishing. URL: `https://pubs.aip.org/aip/apl/article/90/21/213110/333484` (visited on 10/10/2023) (cit. on p. 24).

[52] I. Favero, A. Berthelot, G. Cassabois, C. Voisin, C. Delalande, Ph. Roussignol, R. Ferreira, and J. M. Gérard. “Temperature dependence of the zero-phonon linewidth in quantum dots: An effect of the fluctuating environment”. In: *Physical Review B* 75.7 (Feb. 28, 2007), p. 073308. ISSN: 1098-0121, 1550-235X. DOI: `10.1103/PhysRevB.75.073308`. URL: `https://link.aps.org/doi/10.1103/PhysRevB.75.073308` (visited on 11/28/2023) (cit. on p. 23).

[53] Saimon Filipe Covre da Silva, Gabriel Undeutsch, Barbara Lehner, Santanu Manna, Tobias M. Krieger, Marcus Reindl, Christian Schimpf, Rinaldo Trotta, and Armando Rastelli. “GaAs quantum dots grown by droplet etching epitaxy as quantum light sources”. In: *arXiv e-prints* (2021), arXiv–2109. URL: `https://ui.adsabs.harvard.edu/abs/2021arXiv210901507F/abstract` (visited on 12/21/2023) (cit. on p. 3).

[54] J. J. Finley, M. Sabathil, P. Vogl, G. Abstreiter, R. Oulton, A. I. Tartakovskii, D. J. Mowbray, M. S. Skolnick, S. L. Liew, A. G. Cullis, and M. Hopkinson. “Quantum-confined Stark shifts of charged exciton complexes in quantum dots”. In: *Physical Review B* 70.20 (Nov. 24, 2004), p. 201308. ISSN: 1098-0121, 1550-235X. DOI: `10.1103/PhysRevB.70.201308`. URL: `https://link.aps.org/doi/10.1103/PhysRevB.70.201308` (visited on 10/10/2023) (cit. on p. 27).

[55] J. J. Finley, M. Sabathil, P. Vogl, G. Abstreiter, R. Oulton, A. I. Tartakovskii, D. J. Mowbray, M. S. Skolnick, S. L. Liew, A. G. Cullis, and M. Hopkinson. “Quantum-confined Stark shifts of charged exciton complexes in quantum dots”. In: *Phys. Rev. B* 70 (2004), 201308(R) (cit. on p. 77).

[56] E. B. Flagg, A. Muller, S. V. Polyakov, A. Ling, A. Migdall, and G. S. Solomon. “Interference of Single Photons from Two Separate Semiconductor Quantum Dots”. In: *Phys. Rev. Lett.* 104 (2010), p. 137401 (cit. on p. 77).

[57] I. Friedler, C. Sauvan, J. P. Hugonin, P. Lalanne, J. Claudon, and J. M. Gérard. “Solid-state single photon sources: the nanowire antenna”. In: *Opt. Express* 17 (2009), pp. 2095–2110 (cit. on p. 40).

[58] Inbal Friedler, Philippe Lalanne, Jean-Paul Hugonin, Julien Claudon, Jean-Michel Gérard, Alexios Beveratos, and Isabelle Robert-Philip. "Efficient photonic mirrors for semiconductor nanowires". In: *Optics letters* 33.22 (2008). Publisher: Optica Publishing Group, pp. 2635–2637 (cit. on pp. 41, 44).

[59] P. W. Fry, I. E. Itskevich, D. J. Mowbray, M. S. Skolnick, J. J. Finley, J. A. Barker, E. P. O'Reilly, L. R. Wilson, I. A. Larkin, P. A. Maksym, M. Hopkinson, M. Al-Khafaji, J. P. R. David, A. G. Cullis, G. Hill, and J. C. Clark. "Inverted Electron-Hole Alignment in InAs-GaAs Self-Assembled Quantum Dots". In: *Physical Review Letters* 84.4 (Jan. 24, 2000), pp. 733–736. ISSN: 0031-9007, 1079-7114. DOI: `10.1103/PhysRevLett.84.733`. URL: `https://link.aps.org/doi/10.1103/PhysRevLett.84.733` (visited on 10/10/2023) (cit. on p. 27).

[60] Erik M. Gauger, Simon C. Benjamin, Ahsan Nazir, and Brendon W. Lovett. "High-fidelity all-optical control of quantum dot spins: Detailed study of the adiabatic approach". In: *Physical Review B* 77.11 (Mar. 14, 2008), p. 115322. ISSN: 1098-0121, 1550-235X. DOI: `10.1103/PhysRevB.77.115322`. URL: `https://link.aps.org/doi/10.1103/PhysRevB.77.115322` (visited on 10/17/2023) (cit. on p. 29).

[61] Jean-Michel Gerard, Yoann CURE, and Julien Claudon. "Light source adapted to emit pairs of polarization-entangled photons". U.S. pat. 20210194213A1. Commissariat a lEnergie Atomique et aux Energies Alternatives CEA. June 24, 2021. URL: `https://patents.google.com/patent/US20210194213A1/en` (visited on 12/21/2023) (cit. on p. 130).

[62] Jean-Michel Gerard and Bruno Gayral. "Strong Purcell effect for InAs quantum boxes in three-dimensional solid-state microcavities". In: *Journal of lightwave technology* 17.11 (1999). Publisher: IEEE, p. 2089. URL: `https://opg.optica.org/abstract.cfm?uri=jlt-17-11-2089` (visited on 10/21/2023) (cit. on p. 31).

[63] J. Gérard, B. Sermage, B. Gayral, B. Legrand, E. Costard, and V. Thierry-Mieg. "Enhanced Spontaneous Emission by Quantum Boxes in a Monolithic Optical Microcavity". In: *Physical Review Letters* 81.5 (Aug. 1998), pp. 1110–1113. ISSN: 0031-9007, 1079-7114. DOI: `10.1103/PhysRevLett.81.1110`. URL: `https://link.aps.org/doi/10.1103/PhysRevLett.81.1110` (visited on 11/28/2023) (cit. on pp. 31, 47).

[64] J. M. Gérard, B. Legrand, B. Gayral, E. Costard, B. Sermage, R. Kuszelewicz, D. Barrier, V. Thierry-Mieg, T. Rivera, and J. Y. Marzin. “InAs quantum boxes in GaAs/AlAs pillar microcavities: From spectroscopic investigations to spontaneous emission control”. In: *Physica E: Low-dimensional Systems and Nanostructures* 2.1 (1998). Publisher: Elsevier, pp. 804–808. URL: `https://www.sciencedirect.com/science/article/pii/S1386947798001647` (visited on 10/21/2023) (cit. on p. 31).

[65] Jean-Michel Gérard. “Prospects of High-Efficiency Quantum Boxes Obtained by Direct Epitaxial Growth”. In: *Confined Electrons and Photons*. Ed. by Elias Burstein and Claude Weisbuch. Vol. 340. Series Title: NATO ASI Series. Boston, MA: Springer US, 1995, pp. 357–381. ISBN: 978-1-4613-5807-7 978-1-4615-1963-8. DOI: `10.1007/978-1-4615-1963-8_13`. URL: `http://link.springer.com/10.1007/978-1-4615-1963-8_13` (visited on 11/30/2023) (cit. on pp. 22, 23).

[66] Jean-Michel Gérard. “Solid-State Cavity-Quantum Electrodynamics with Self-Assembled Quantum Dots”. In: *Single Quantum Dots*. Vol. 90. Series Title: Topics in Applied Physics. Berlin, Heidelberg: Springer Berlin Heidelberg, Nov. 4, 2003, pp. 269–314. ISBN: 978-3-540-14022-1 978-3-540-39180-7. DOI: `10.1007/978-3-540-39180-7_7`. URL: `http://link.springer.com/10.1007/978-3-540-39180-7_7` (visited on 11/29/2023) (cit. on p. 34).

[67] Jean-Michel Gérard, J. B. Genin, J. Lefebvre, J. M. Moison, N. Lebouche, and F. Barthe. “Optical investigation of the self-organized growth of InAs/GaAs quantum boxes”. In: *Journal of crystal growth* 150 (1995). Publisher: Elsevier, pp. 351–356 (cit. on pp. 8, 12, 89).

[68] L. Goldstein, F. Glas, J. Y. Marzin, M. N. Charasse, and G. Le Roux. “Growth by molecular beam epitaxy and characterization of InAs/GaAs strained-layer superlattices”. In: *Applied Physics Letters* 47.10 (1985). Publisher: American Institute of Physics, pp. 1099–1101 (cit. on p. 7).

[69] Hayato Goto. “Universal quantum computation with a nonlinear oscillator network”. In: *Physical Review A* 93.5 (May 10, 2016), p. 050301. ISSN: 2469-9926, 2469-9934. DOI: `10.1103/PhysRevA.93.050301`. URL: `https://link.aps.org/doi/10.1103/PhysRevA.93.050301` (visited on 12/07/2023) (cit. on p. 2).

[70] P. Goy, J. M. Raimond, M. Gross, and S. Haroche. “Observation of Cavity-Enhanced Single-Atom Spontaneous Emission”. In: *Physical Review Letters* 50.24 (June 13, 1983), pp. 1903–1906. ISSN: 0031-9007.

DOI: 10.1103/PhysRevLett.50.1903. URL: https://link.aps.org/doi/10.1103/PhysRevLett.50.1903 (visited on 10/21/2023) (cit. on p. 31).

[71] N. Gregersen, D. P. S. McCutcheon, J. Mørk, J.-M. Gérard, and J. Claudon. "A broadband tapered nanocavity for efficient nonclassical light emission". In: *Opt. Express* 24 (2016), pp. 20904–20924 (cit. on p. 77).

[72] N. Gregersen, T. R. Nielsen, J. Claudon, J. M. Gérard, and J. Mørk. "Controlling the emission profile of a nanowire with a conical taper". In: *Opt. Lett.* 33 (2008), pp. 1693–1695 (cit. on p. 41).

[73] J. Q. Grim, A. S. Bracker, M. Zalalutdinov, S. G. Carter, A. C. Kozen, M. Kim, C. S. Kim, J. T. Mlack, M. Yakes, B. Lee, and D. Gammon. "Scalable in operando strain tuning in nanophotonic waveguides enabling three-quantum-dot superradiance". In: *Nat. Mater.* 18 (2019), pp. 963–969 (cit. on pp. 98, 130).

[74] Gilbert Grynberg, Alain Aspect, and Claude Fabre. *Introduction to quantum optics: from the semi-classical approach to quantized light.* Cambridge university press, 2010 (cit. on p. 55).

[75] M. Gschrey, A. Thoma, P. Schnauber, M. Seifried, R. Schmidt, B. Wohlfeil, L. Krüger, J. H. Schulze, T. Heindel, S. Burger, F. Schmidt, A. Strittmatter, S. Rodt, and S. Reitzenstein. "Highly indistinguishable photons from deterministic quantum-dot microlenses utilizing three-dimensional *in situ* electron-beam lithography". In: *Nat. Commun.* 6 (2015), p. 7662 (cit. on p. 77).

[76] Rajeev Gupta, Rajesh Singh, Anita Gehlot, Shaik Vaseem Akram, Neha Yadav, Ranjeet Brajpuriya, Ashish Kumar Yadav, Yongling Wu, Hongyu Zheng, and Abhijit Biswas. "Silicon photonics interfaced with microelectronics for integrated photonic quantum technologies: a new era in advanced quantum computers and quantum communications?" In: *Nanoscale* (2023). Publisher: Royal Society of Chemistry. URL: https://pubs.rsc.org/en/content/articlehtml/2023/nr/d2nr05610k (visited on 12/07/2023) (cit. on p. 2).

[77] S. Hameau, Y. Guldner, O. Verzelen, R. Ferreira, G. Bastard, J. Zeman, A. Lemaître, and J. M. Gérard. "Strong Electron-Phonon Coupling Regime in Quantum Dots: Evidence for Everlasting Resonant Polarons". In: *Physical Review Letters* 83.20 (Nov. 15, 1999), pp. 4152–4155. ISSN: 0031-9007, 1079-7114. DOI: 10.1103/PhysRevLett.83.4152. URL: https://link.aps.org/doi/10.1103/PhysRevLett.83.4152 (visited on 11/30/2023) (cit. on p. 21).

[78] R. Hanson, L. P. Kouwenhoven, J. R. Petta, S. Tarucha, and L. M. K. Vandersypen. “Spins in few-electron quantum dots”. In: *Reviews of Modern Physics* 79.4 (Oct. 1, 2007), pp. 1217–1265. ISSN: 0034-6861, 1539-0756. DOI: `10.1103/RevModPhys.79.1217`. URL: `https://link.aps.org/doi/10.1103/RevModPhys.79.1217` (visited on 10/15/2023) (cit. on p. 1).

[79] Kevin Hennessy, Antonio Badolato, Martin Winger, D. Gerace, Mete Atatüre, S. Gulde, S. Fält, Evelyn L. Hu, and A. Imamoğlu. “Quantum nature of a strongly coupled single quantum dot–cavity system”. In: *Nature* 445.7130 (2007). Publisher: Nature Publishing Group UK London, pp. 896–899. URL: `https://www.nature.com/articles/nature05586` (visited on 10/10/2023) (cit. on pp. 33, 35, 38).

[80] Ryszard Horodecki. “Quantum information”. In: *Acta Physica Polonica A* 139.3 (Mar. 2021), pp. 197–2018. ISSN: 1898-794X, 0587-4246. DOI: `10.12693/APhysPolA.139.197`. arXiv: `2103.07712[quant-ph]`. URL: `http://arxiv.org/abs/2103.07712` (visited on 12/05/2023) (cit. on p. 1).

[81] D. Huber, M. Reindl, J. Aberl, A. Rastelli, and R. Trotta. “Semiconductor quantum dots as an ideal source of polarization-entangled photon pairs on-demand: a review”. In: *J. Opt.* 20 (2018), p. 073002 (cit. on p. 77).

[82] Tobias Huber, Ana Predojevic, Milad Khoshnegar, Dan Dalacu, Philip J. Poole, Hamed Majedi, and Gregor Weihs. “Polarization entangled photons from quantum dots embedded in nanowires”. In: *Nano letters* 14.12 (2014). Publisher: ACS Publications, pp. 7107–7114 (cit. on p. 19).

[83] P. Imany, Z. Wang, R. A. DeCrescent, R. C. Boutelle, C. A. McDonald, T. Autry, S. Berweger, P. Kabos, S. W. Nam, R. P. Mirin, and K. L. Silverman. “Quantum phase modulation with acoustic cavities and quantum dots”. In: *Optica* 9 (2022), pp. 501–504 (cit. on pp. 102, 125, 126).

[84] Martin Arentoft Jacobsen, Yujing Wang, Luca Vannucci, Julien Claudon, Jean-Michel Gérard, and Niels Gregersen. “Performance of the nanopost single-photon source: beyond the single-mode model”. In: *arXiv preprint arXiv:2301.02556* (2023) (cit. on pp. 35, 44–49).

[85] Ali Jaffal, Walid Redjem, Philippe Regreny, Hai Son Nguyen, Sébastien Cueff, Xavier Letartre, Gilles Patriarche, Emmanuel Rousseau, Guillaume Cassabois, and Michel Gendry. “InAs quantum dot in a needle-

like tapered InP nanowire: a telecom band single photon source monolithically grown on silicon". In: *Nanoscale* 11.45 (2019). Publisher: Royal Society of Chemistry, pp. 21847–21855. URL: `https://pubs.rsc.org/en/content/articlehtml/2019/nr/c9nr06114b` (visited on 12/21/2023) (cit. on p. 3).

[86] Aleksandar Jankovic. "Etats électroniques des boîtes quantiques de semiconducteur : rôle de l'environnement et couplage dépendant du spin". These de doctorat. Paris 6, Jan. 1, 2004. URL: `https://www.theses.fr/2004PA066464` (visited on 10/06/2023) (cit. on p. 13).

[87] J. Johansen, S. Stobbe, I. S. Nikolaev, T. Lund-Hansen, P. T. Kristensen, J. M. Hvam, W. L. Vos, and P. Lodahl. "Size dependence of the wavefunction of self-assembled InAs quantum dots from time-resolved optical measurements". In: *Phys. Rev. B* 77 (2008), p. 073303 (cit. on p. 102).

[88] J. R. Johansson, P. D. Nation, and Franco Nori. "QuTiP 2: A Python framework for the dynamics of open quantum systems". In: *Computer Physics Communications* 184.4 (Apr. 1, 2013), pp. 1234–1240. ISSN: 0010-4655. DOI: `10.1016/j.cpc.2012.11.019`. URL: `https://www.sciencedirect.com/science/article/pii/S0010465512003955` (visited on 11/22/2023) (cit. on p. 70).

[89] H. Kamada and T. Kutsuwa. "Broadening of single quantum dot exciton luminescence spectra due to interaction with randomly fluctuating environmental charges". In: *Physical Review B* 78.15 (Oct. 27, 2008), p. 155324. ISSN: 1098-0121, 1550-235X. DOI: `10.1103/PhysRevB.78.155324`. URL: `https://link.aps.org/doi/10.1103/PhysRevB.78.155324` (visited on 12/13/2023) (cit. on p. 66).

[90] Fumihiro Kaneda, Bradley G. Christensen, Jia Jun Wong, Hee Su Park, Kevin T. McCusker, and Paul G. Kwiat. "Time-multiplexed heralded single-photon source". In: *Optica* 2.12 (2015). Publisher: Optica Publishing Group, pp. 1010–1013. URL: `https://opg.optica.org/abstract.cfm?uri=optica-2-12-1010` (visited on 12/07/2023) (cit. on p. 3).

[91] J. Kettler, N. Vaish, L. Mercier de Lépinay, B. Besga, P.-L. de Assis, O. Bourgeois, A. Auffèves, M. Richard, J. Claudon, J.-M. J.-M. Gérard, B. Pigeau, O. Arcizet, P. Verlot, and J.-P. Poizat. "Inducing micromechanical motion by optical excitation of a single quantum dot". In: *Nat. Nanotechnol.* 16 (2021), pp. 283–287 (cit. on pp. 96, 102).

[92] Morten Kjaergaard, Mollie E. Schwartz, Jochen Braumüller, Philip Krantz, Joel I.-J. Wang, Simon Gustavsson, and William D. Oliver. "Superconducting Qubits: Current State of Play". In: *Annual Review of Condensed Matter Physics* 11.1 (Mar. 10, 2020), pp. 369–395. ISSN: 1947-5454, 1947-5462. DOI: `10.1146/annurev-conmatphys-031119-050605`. URL: `https://www.annualreviews.org/doi/10.1146/annurev-conmatphys-031119-050605` (visited on 12/07/2023) (cit. on p. 1).

[93] E. Knill, R. Laflamme, and G. J. Milburn. "A scheme for efficient quantum computation with linear optics". In: *Nature* 409 (Jan. 1, 2001). ADS Bibcode: 2001Natur.409...46K, pp. 46–52. ISSN: 0028-0836. DOI: `10.1038/35051009`. URL: `https://ui.adsabs.harvard.edu/abs/2001Natur.409...46K` (visited on 12/05/2023) (cit. on p. 2).

[94] Pieter Kok, W. J. Munro, Kae Nemoto, T. C. Ralph, Jonathan P. Dowling, and G. J. Milburn. "Review article: Linear optical quantum computing". In: *Reviews of Modern Physics* 79.1 (Jan. 24, 2007), pp. 135–174. ISSN: 0034-6861, 1539-0756. DOI: `10.1103/RevModPhys.79.135`. arXiv: `quant-ph/0512071`. URL: `http://arxiv.org/abs/quant-ph/0512071` (visited on 12/05/2023) (cit. on p. 1).

[95] S. Kotal, A. Artioli, Y. Wang, A. D. Osterkryger, M. Finazzer, R. Fons, Y. Genuist, J. Bleuse, J.-M. Gérard, N. Gregersen, and J. Claudon. "A nanowire optical nanocavity for broadband enhancement of spontaneous emission". In: *Appl. Phys. Lett.* 118 (2021), p. 194002 (cit. on p. 77).

[96] Saptarshi Kotal. "Controlling the spectral properties of quantum light sources based on a quantum dot in a nanowire". PhD thesis. UGA, Jan. 12, 2022. 181 pp. URL: `http://www.theses.fr/2021GRALY039/document` (cit. on pp. 45, 52, 89).

[97] Saptarshi Kotal, Alberto Artioli, Yujing Wang, Andreas Dyhl Osterkryger, Matteo Finazzer, Romain Fons, Yann Genuist, Joël Bleuse, Jean-Michel Gérard, and Niels Gregersen. "A nanowire optical nanocavity for broadband enhancement of spontaneous emission". In: *Applied Physics Letters* 118.19 (2021). Publisher: AIP Publishing LLC, p. 194002 (cit. on pp. 4, 31, 35, 47, 127).

[98] P. E. Kremer, A. C. Dada, P. Kumar, Y. Ma, S. Kumar, E. Clarke, and B. D. Gerardot. "A strain-tunable quantum dot embedded in a nanowire antenna". In: *Phys. Rev. B* 90 (2014), p. 201408 (cit. on p. 78).

[99] A. V. Kuhlmann, J. Houel, A. Ludwig, L. Greuter, D. Reuter, A. D. Wieck, M. Poggio, and R. J. Warburton. “Charge noise and spin noise in a semiconductor quantum device”. In: *Nature Phys.* 9 (2013), pp. 570–575 (cit. on p. 102).

[100] Andreas V Kuhlmann, Julien Houel, Daniel Brunner, Arne Ludwig, Dirk Reuter, Andreas D Wieck, and Richard J Warburton. “A dark-field microscope for background-free detection of resonance fluorescence from single semiconductor quantum dots operating in a set-and-forget mode”. In: *Review of scientific instruments* 84.7 (2013). Publisher: American Institute of Physics, p. 073905 (cit. on pp. 54, 62).

[101] Andreas V. Kuhlmann, Jonathan H. Prechtel, Julien Houel, Arne Ludwig, Dirk Reuter, Andreas D. Wieck, and Richard J. Warburton. “Transform-limited single photons from a single quantum dot”. In: *Nature communications* 6.1 (2015). Publisher: Nature Publishing Group UK London, p. 8204 (cit. on p. 29).

[102] C. E. Kuklewicz, R. N. E. Malein, P. M. Petroff, and B. D. Gerardot. “Electro-Elastic Tuning of Single Particles in Individual Self-Assembled Quantum Dots”. In: *Nano Lett.* 12 (2012), pp. 3761–3765 (cit. on p. 94).

[103] Christian Kurtsiefer, Sonja Mayer, Patrick Zarda, and Harald Weinfurter. “Stable Solid-State Source of Single Photons”. In: *Physical Review Letters* 85.2 (July 10, 2000). Publisher: American Physical Society, pp. 290–293. DOI: `10.1103/PhysRevLett.85.290`. URL: `https://link.aps.org/doi/10.1103/PhysRevLett.85.290` (visited on 12/21/2023) (cit. on p. 3).

[104] D. Labilloy, H. Benisty, C. Weisbuch, T. F. Krauss, C. J. M. Smith, R. Houdre, and U. Oesterle. “High-finesse disk microcavity based on a circular Bragg reflector”. In: *Applied physics letters* 73.10 (1998). Publisher: American Institute of Physics, pp. 1314–1316. URL: `https://pubs.aip.org/aip/apl/article-abstract/73/10/1314/69138` (visited on 10/30/2023) (cit. on p. 37).

[105] Patrick Laferrière, Aria Yin, Edith Yeung, Leila Kusmic, Marek Korkusinski, Payman Rasekh, David B. Northeast, Sofiane Haffouz, Jean Lapointe, Philip J. Poole, Robin L. Williams, and Dan Dalacu. “Approaching transform-limited photons from nanowire quantum dots using excitation above the band gap”. In: *Phys. Rev. B* 107 (2023), p. 155422 (cit. on p. 126).

[106] Y. Lai, S. Pirotta, G. Urbinati, Dario Gerace, M. Minkov, V. Savona, A. Badolato, and Matteo Galli. “Genetically designed L3 photonic crystal nanocavities with measured quality factor exceeding one million”. In: *Applied Physics Letters* 104.24 (2014). Publisher: AIP Publishing. URL: `https://pubs.aip.org/aip/apl/article/104/24/241101/385107` (visited on 10/30/2023) (cit. on p. 37).

[107] Ph Lalanne, Jean-Paul Hugonin, and Jean-Michel Gérard. “Electromagnetic study of the quality factor of pillar microcavities in the small diameter limit”. In: *Applied Physics Letters* 84.23 (2004). Publisher: American Institute of Physics, pp. 4726–4728. URL: `https://pubs.aip.org/aip/apl/article-abstract/84/23/4726/116742` (visited on 11/29/2023) (cit. on p. 36).

[108] Mikkel V. Larsen, Xueshi Guo, Casper R. Breum, Jonas S. Neergaard-Nielsen, and Ulrik L. Andersen. “Deterministic multi-mode gates on a scalable photonic quantum computing platform”. In: *Nature Physics* 17.9 (2021). Publisher: Nature Publishing Group UK London, pp. 1018–1023. URL: `https://www.nature.com/articles/s41567-021-01296-y` (visited on 12/07/2023) (cit. on p. 2).

[109] G. Lecamp, P. Lalanne, and J. P. Hugonin. “Very Large Spontaneous-Emission $\beta$ Factors in Photonic-Crystal Waveguides”. In: *Phys. Rev. Lett.* 99 (2007), p. 023902 (cit. on p. 39).

[110] Sheng-Kai Liao et al. “Satellite-Relayed Intercontinental Quantum Network”. In: *Physical Review Letters* 120.3 (Jan. 19, 2018), p. 030501. ISSN: 0031-9007, 1079-7114. DOI: `10.1103/PhysRevLett.120.030501`. URL: `https://link.aps.org/doi/10.1103/PhysRevLett.120.030501` (visited on 12/05/2023) (cit. on p. 2).

[111] Qing Lin and Jian Li. “Quantum control gates with weak cross-Kerr nonlinearity”. In: *Physical Review A* 79.2 (Feb. 2, 2009), p. 022301. ISSN: 1050-2947, 1094-1622. DOI: `10.1103/PhysRevA.79.022301`. URL: `https://link.aps.org/doi/10.1103/PhysRevA.79.022301` (visited on 12/07/2023) (cit. on p. 2).

[112] F. Liu, A. J. Brash, J. O’Hara, L. M. P. P. Martins, C. L. Phillips, R. J. Coles, B. Royall, E. Clarke, C. Bentham, N. Prtljaga, I. E. Itskevich, L. R. Wilson, M. S. Skolnick, and A. M. Fox. “High Purcell factor generation of indistinguishable on-chip single photons”. In: *Nature Nanotech.* 13 (2018), pp. 835–840 (cit. on p. 77).

[113] J. Liu, R. Su, Y. Wei, B. Yao, S. Filipe Covre da Silva, Y. Yu, J. Iles-Smith, K. Srinivasan, A. Rastelli, J. Li, and X. Wang. “A solid-state source of strongly entangled photon pairs with high brightness and indistinguishability”. In: *Nat. Nanotechnol.* 14 (2019), pp. 586–593 (cit. on p. 77).

[114] Jin Liu, Rongbin Su, Yuming Wei, Beimeng Yao, Saimon Filipe Covre da Silva, Ying Yu, Jake Iles-Smith, Kartik Srinivasan, Armando Rastelli, and Juntao Li. “A solid-state source of strongly entangled photon pairs with high brightness and indistinguishability”. In: *Nature nanotechnology* 14.6 (2019). Publisher: Nature Publishing Group UK London, pp. 586–593 (cit. on pp. 35, 37, 47).

[115] P Lodahl, S. Mahmoodian, and S. Stobbe. “Interfacing single photons and single quantum dots with photonic nanostructures”. In: *Rev. Mod. Phys.* 87 (2015), pp. 347–400 (cit. on pp. 77, 102).

[116] Peter Lodahl, Sahand Mahmoodian, and Søren Stobbe. “Interfacing single photons and single quantum dots with photonic nanostructures”. In: *Reviews of Modern Physics* 87.2 (2015). Publisher: APS, p. 347 (cit. on p. 4).

[117] V. Loo, L. Lanco, A. Lemaître, I. Sagnes, O. Krebs, P. Voisin, and P. Senellart. “Quantum dot-cavity strong-coupling regime measured through coherent reflection spectroscopy in a very high-Q micropillar”. In: *Appl. Phys. Lett.* 97 (2010), p. 241110 (cit. on p. 36).

[118] T. Lund-Hansen, S. Stobbe, B. Julsgaard, H. Thyrrestrup, T. Sünner, M. Kamp, A. Forchel, and P. Lodahl. “Experimental Realization of Highly Efficient Broadband Coupling of Single Quantum Dots to a Photonic Crystal Waveguide”. In: *Phys. Rev. Lett.* 101 (2008), p. 113903 (cit. on p. 40).

[119] Lars S. Madsen, Fabian Laudenbach, Mohsen Falamarzi Askarani, Fabien Rortais, Trevor Vincent, Jacob FF Bulmer, Filippo M. Miatto, Leonhard Neuhaus, Lukas G. Helt, and Matthew J. Collins. “Quantum computational advantage with a programmable photonic processor”. In: *Nature* 606.7912 (2022). Publisher: Nature Publishing Group UK London, pp. 75–81. URL: `https://www.nature.com/articles/s41586-022-04725-x` (visited on 12/07/2023) (cit. on p. 2).

[120] V. S. C. Manga Rao and S. Hughes. “Single quantum-dot Purcell factor and $\beta$ factor in a photonic crystal waveguide”. In: *Phys. Rev. B* 75 (2007), p. 205437 (cit. on p. 39).

[121] Petr Marek, Radim Filip, Hisashi Ogawa, Atsushi Sakaguchi, Shuntaro Takeda, Jun-ichi Yoshikawa, and Akira Furusawa. "General implementation of arbitrary nonlinear quadrature phase gates". In: *Physical Review A* 97.2 (Feb. 20, 2018), p. 022329. ISSN: 2469-9926, 2469-9934. DOI: `10.1103/PhysRevA.97.022329`. URL: `https://link.aps.org/doi/10.1103/PhysRevA.97.022329` (visited on 12/07/2023) (cit. on p. 2).

[122] J. Martín-Sánchez, R. Trotta, A. Mariscal, R. Serna, G. Piredda, S. Stroj, J. Edlinger, C. Schimpf, J. Aberl, T. Lettner, J. Wildmann, H. Huang, X. Yuan, D. Ziss, J. Stangl, and A. Rastelli. "Strain-tuning of the optical properties of semiconductor nanomaterials by integration onto piezoelectric actuators". In: *Semicond. Sci. Technol.* 33 (2018), p. 013001 (cit. on p. 77).

[123] J. Y. Marzin and J. M. Gérard. "Strained-Layer Superlattices: Physics". In: *Semiconductors and Semimetals*. Ed. by T. P. Pearsall. Elsevier, 1990. Chap. Optical Studies of Strained III-V Heterolayers, p. 55 (cit. on pp. 11, 102).

[124] J.-Y. Marzin and G. Bastard. "Calculation of the energy levels in InAsGaAs quantum dots". In: *Solid state communications* 92.5 (1994). Publisher: Elsevier, pp. 437–442 (cit. on p. 11).

[125] Matteo Finazzer, Rana Tanos, Yoann Curé, Alberto Artioli, Saptarshi Kotal, Joël Bleuse, Yann Genuist, Jean-Michel Gérard, Fabrice Donatini, and Julien Claudon. "On-Chip Electrostatic Actuation of a Photonic Wire Antenna Embedding Quantum Dots". In: *Nano Letters* 23.6 (2023). Publisher: ACS Publications, pp. 2203–2209 (cit. on pp. 77, 101).

[126] R. Melet, V. Voliotis, A. Enderlin, D. Roditchev, X. L. Wang, T. Guillet, and R. Grousson. "Resonant excitonic emission of a single quantum dot in the Rabi regime". In: *Physical Review B* 78.7 (Aug. 5, 2008), p. 073301. ISSN: 1098-0121, 1550-235X. DOI: `10.1103/PhysRevB.78.073301`. URL: `https://link.aps.org/doi/10.1103/PhysRevB.78.073301` (visited on 10/30/2023) (cit. on p. 33).

[127] M. Metcalfe, S. M. Carr, A. Muller, G. S. Solomon, and J. Lawall. "Resolved Sideband Emission of InAs/GaAs Quantum Dots Strained by Surface Acoustic Waves". In: *Phys. Rev. Lett.* 105 (2010), p. 037401 (cit. on p. 102).

[128] P. Michler, A. Kiraz, C. Becher, W. V. Schoenfeld, P. M. Petroff, Lidong Zhang, E. Hu, and A. Imamoglu. "A Quantum Dot Single-Photon Turnstile Device". In: *Science* 290.5500 (Dec. 22, 2000). Publisher: American Association for the Advancement of Science, pp. 2282–2285. DOI: `10.1126/science.290.5500.2282`. URL: `https://www.science.org/doi/10.1126/science.290.5500.2282` (visited on 12/21/2023) (cit. on p. 3).

[129] M. Moczała-Dusanowska, Ł. Dusanowski, O. Iff, T. Huber, S. Kuhn, T. Czyszanowski, C. Schneider, and S. Höfling. "Strain-Tunable Single-Photon Source Based on a Circular Bragg Grating Cavity with Embedded Quantum Dots". In: *ACS Photonics* 7 (2020), pp. 3474–3480 (cit. on p. 78).

[130] M. Montinaro, G. Wüst, M. Munsch, Y. Fontana, E. Russo-Averchi, M. Heiss, A. Fontcuberta i Morral, R. J. Warburton, and M. Poggio. "Quantum Dot Opto-Mechanics in a Fully Self-Assembled Nanowire". In: *Nano Lett.* 14 (2014), pp. 4454–4460 (cit. on p. 102).

[131] M. Munsch, J. Claudon, J. Bleuse, N. S. Malik, E. Dupuy, J.-M. Gérard, Y. Chen, N. Gregersen, and J. Mørk. "Linearly Polarized, Single-Mode Spontaneous Emission in a Photonic Nanowire". In: *Phys. Rev. Lett.* 108 (2012), p. 077405 (cit. on pp. 98, 126, 130).

[132] M. Munsch, A. V. Kuhlmann, D. Cadeddu, J.-M. Gérard, J. Claudon, M. Poggio, and R. J. Warburton. "Resonant driving of a single photon emitter embedded in a mechanical oscillator". In: *Nat. Commun.* 8 (2017), p. 76 (cit. on pp. 96, 102, 126, 130).

[133] M. Munsch, N. S. Malik, E. Dupuy, A. Delga, J. Bleuse, J.-M. Gérard, J. Claudon, N. Gregersen, and J. Mørk. "Dielectric GaAs-antenna ensuring an efficient broadband coupling between an InAs quantum-dot light emitter and a Gaussian optical beam". In: *Phys. Rev. Lett.* 110 (2013), p. 177402 (cit. on pp. 77, 78).

[134] Mathieu Munsch, Andreas V. Kuhlmann, Davide Cadeddu, Jean-Michel Gérard, Julien Claudon, Martino Poggio, and Richard J. Warburton. "Resonant driving of a single photon emitter embedded in a mechanical oscillator". In: *Nature communications* 8.1 (2017). Publisher: Nature Publishing Group UK London, p. 76 (cit. on p. 131).

[135] Daniel Najer, Immo Söllner, Pavel Sekatski, Vincent Dolique, Matthias C. Löbl, Daniel Riedel, Rüdiger Schott, Sebastian Starosielec, Sascha R. Valentin, and Andreas D. Wieck. "A gated quantum dot strongly coupled to an optical microcavity". In: *Nature* 575.7784 (2019). Publisher: Nature Publishing Group UK London, pp. 622–627. URL: `https:`

//www.nature.com/articles/s41586-019-1709-y (visited on 10/12/2023) (cit. on pp. 35, 37, 76, 128).

[136] H. A. Nguyen, T. Grange, B. Reznychenko, I. Yeo, P.-L. de Assis, D. Tumanov, F. Fratini, N. S. Malik, E. Dupuy, N. Gregersen, A. Auffèves, J.-M. Gérard, J. Claudon, and J.-P. Poizat. "Giant non-linear interaction between two optical beams via a quantum dot embedded in a photonic wire". In: *Phys. Rev. B* 97 (2018), 201106(R) (cit. on p. 96).

[137] Hai-Son Nguyen, Gregory Sallen, Christophe Voisin, Ph Roussignol, Carole Diederichs, and Guillaume Cassabois. "Optically gated resonant emission of single quantum dots". In: *Physical review letters* 108.5 (2012). Publisher: APS, p. 057401 (cit. on p. 72).

[138] A Nick Vamivakas, Yong Zhao, Chao-Yang Lu, and Mete Atatüre. "Spin-resolved quantum-dot resonance fluorescence". In: *Nature Physics* 5.3 (2009). Publisher: Nature Publishing Group UK London, pp. 198–202 (cit. on p. 62).

[139] A. D. O'Connell, M. Hofheinz, M. Ansmann, R. C. Bialczak, M. Lenander, E. Lucero, M. Neeley, D. Sank, H. Wang, M. Weides, J. Wenner, J. M. Martinis, and A. N. Cleland. "Quantum ground state and single-phonon control of a mechanical resonator". In: *Nature* 464 (2010), pp. 697–703 (cit. on pp. 101, 102).

[140] R. Ohta, L. Herpin, V. M. Bastidas, T. Tawara, H. Yamaguchi, and H. Okamoto. "Rare-Earth-Mediated Optomechanical System in the Reversed Dissipation Regime". In: *Phys. Rev. Lett.* 126 (2021), p. 047404 (cit. on p. 102).

[141] A. D. Osterkryger, J. Claudon, J.-M. Gérard, and N. Gregersen. "Photonic "hourglass" design for efficient quantum light emission". In: *Opt. Lett.* 44 (2019), pp. 2617–2620 (cit. on p. 77).

[142] P. Ovartchaiyapong, K. W. Lee, B. A. Myers, and A. C. B. Jayich. "Dynamic strain-mediated coupling of a single diamond spin to a mechanical resonator". In: *Nat. Commun.* 5 (2014), p. 4429 (cit. on p. 102).

[143] F. Patella, S. Nufris, F. Arciprete, M. Fanfoni, E. Placidi, A. Sgarlata, and A. Balzarotti. "Tracing the two- to three-dimensional transition in the InAs/GaAs(001) heteroepitaxial growth". In: *Physical Review B* 67.20 (May 12, 2003), p. 205308. ISSN: 0163-1829, 1095-3795. DOI: 10.1103/PhysRevB.67.205308. URL: https://link.aps.org/

`doi/10.1103/PhysRevB.67.205308` (visited on 10/09/2023) (cit. on p. 12).

[144] Emanuele Pelucchi, Giorgos Fagas, Igor Aharonovich, Dirk Englund, Eden Figueroa, Qihuang Gong, Hübel Hannes, Jin Liu, Chao-Yang Lu, and Nobuyuki Matsuda. "The potential and global outlook of integrated photonics for quantum technologies". In: *Nature Reviews Physics* 4.3 (2022). Publisher: Nature Publishing Group UK London, pp. 194–208. URL: `https://www.nature.com/articles/s42254-021-00398-z` (visited on 12/07/2023) (cit. on p. 2).

[145] E. Peter, P. Senellart, D. Martrou, A. Lemaître, J. Hours, J. M. Gérard, and J Bloch. "Exciton-Photon Strong-Coupling Regime for a Single Quantum Dot Embedded in a Microcavity". In: *Phys. Rev. Lett.* 95 (2005), p. 067401 (cit. on p. 33).

[146] Y. U. Peter and Manuel Cardona. *Fundamentals of semiconductors: physics and materials properties*. Springer Science & Business Media, 2010 (cit. on pp. 10, 11).

[147] P. Rabl, S. J. Kolkowitz, F. H. L. Koppens, J. G. E. Harris, P. Zoller, and M. D. Lukin. "A quantum spin transducer based on nanoelectromechanical resonator arrays". In: *Nature Phys* 6 (2010), pp. 602–608 (cit. on p. 102).

[148] A. J. Ramsay, Achanta Venu Gopal, E. M. Gauger, Ahsan Nazir, Brendon William Lovett, A. M. Fox, and M. S. Skolnick. "Damping of exciton Rabi rotations by acoustic phonons in optically excited InGaAs/GaAs quantum dots". In: *Physical review letters* 104.1 (2010). Publisher: APS, p. 017402 (cit. on p. 29).

[149] W. Redjem, A. Durand, T. Herzig, A. Benali, S. Pezzagna, J. Meijer, A. Yu Kuznetsov, H. S. Nguyen, S. Cueff, J.-M. Gérard, I. Robert-Philip, B. Gil, D. Caliste, P. Pochet, M. Abbarchi, V. Jacques, A. Dréau, and G. Cassabois. "Single artificial atoms in silicon emitting at telecom wavelengths". In: *Nature Electronics* 3.12 (Dec. 2020). Number: 12 Publisher: Nature Publishing Group, pp. 738–743. ISSN: 2520-1131. DOI: `10.1038/s41928-020-00499-0`. URL: `https://www.nature.com/articles/s41928-020-00499-0` (visited on 12/21/2023) (cit. on p. 3).

[150] Antoine Reigue, Richard Hostein, and Valia Voliotis. "Resonance fluorescence of a single semiconductor quantum dot: The impact of a fluctuating electrostatic environment". In: *Semiconductor Science and Technology* 34.11 (2019). Publisher: IOP Publishing, p. 113001 (cit. on p. 68).

[151] M. E. Reimer, G. Bulgarini, N. Akopian, M. Hocevar, M. B. Bavinck, M. A. Verheijen, E. P. A. M. Bakkers, L. P. Kouwenhoven, and V. Zwiller. “Bright single-photon sources in bottom-up tailored nanowires”. In: *Nat. Commun.* 3 (2012), p. 737 (cit. on pp. 77, 126).

[152] J. P. Reithmaier, G. S k, A. Löffler, C. Hofmann, S. Kuhn, S. Reitzenstein, L. V. Keldysh, V. D. Kulakovskii, T. L. Reinecke, and A. Forchel. “Strong coupling in a single quantum dot-semiconductor microcavity system”. In: *Nature* 432 (2004), pp. 197–200 (cit. on p. 35).

[153] J. Pelal Reithmaier, G. Sęk, A. Löffler, C. Hofmann, S. Kuhn, S. Reitzenstein, L. V. Keldysh, V. D. Kulakovskii, T. L. Reinecke, and A. Forchel. “Strong coupling in a single quantum dot–semiconductor microcavity system”. In: *Nature* 432.7014 (2004). Publisher: Nature Publishing Group UK London, pp. 197–200. URL: https://www.nature.com/articles/nature02969 (visited on 10/30/2023) (cit. on pp. 33, 37).

[154] S. Reitzenstein, C. Hofmann, A. Gorbunov, M. Strauß, S. H. Kwon, C. Schneider, A. Löffler, S. Höfling, M. Kamp, and A. Forchel. “AlAs/GaAs micropillar cavities with quality factors exceeding 150.000”. In: *Appl. Phys. Lett.* 90 (2007), p. 251109 (cit. on p. 36).

[155] S. Reitzenstein, S. Münch, P. Franeck, A. Rahimi-Iman, A. Löffler, S. Höfling, L. Worschech, and A. Forchel. “Control of the Strong Light-Matter Interaction between an Elongated $In_{0.3}Ga_{0.7}As$ Quantum Dot and a Micropillar Cavity Using External Magnetic Fields”. In: *Phys. Rev. Lett.* 103 (2009), p. 127401 (cit. on p. 77).

[156] T. Rivera, J.-P. Debray, J. M. Gérard, B. Legrand, L. Manin-Ferlazzo, and J. L. Oudar. “Optical losses in plasma-etched AlGaAs microresonators using reflection spectroscopy”. In: *Applied physics letters* 74.7 (1999). Publisher: American Institute of Physics, pp. 911–913. URL: https://pubs.aip.org/aip/apl/article-abstract/74/7/911/519343 (visited on 11/29/2023) (cit. on p. 36).

[157] L. Sapienza, H. Thyrrestrup, S. Stobbe, P. D. Garcia, S. Smolka, and P. Lodahl. “Cavity Quantum Electrodynamics with Anderson-Localized Modes”. In: *Science* 327 (2010), pp. 1352–1355 (cit. on p. 40).

[158] Luca Sapienza, Marcelo Davanço, Antonio Badolato, and Kartik Srinivasan. “Nanoscale optical positioning of single quantum dots for bright and pure single-photon emission”. In: *Nature communications* 6.1 (2015). Publisher: Nature Publishing Group UK London, p. 7833. URL: https:

//www.nature.com/articles/ncomms8833 (visited on 10/30/2023) (cit. on p. 37).

[159] M. Schmidt, M.V. Helversen, S. Fischbach, A. Kaganskiy, R. Schmidt, A. Schliwa, T. Heindel, S. Rodt, and S. Reitzenstein. "Deterministically fabricated spectrally-tunable quantum dot based single-photon source". In: *Opt. Mater. Express* 10 (2020), pp. 76–87 (cit. on p. 78).

[160] F. J. R. Schülein, E. Zallo, P. Atkinson, O. G. Schmidt, R. Trotta, A. Rastelli, A. Wixforth, and H. J. Krenner. "Fourier synthesis of radiofrequency nanomechanical pulses with different shapes". In: *Nature Nanotech.* 10 (2015), pp. 512–516 (cit. on p. 102).

[161] S. Seidl, A. Högele, M. Kroner, K. Karrai, A. Badolato, P. M. Petroff, and R. J. Warburton. "Tuning the cross-gap transition energy of a quantum dot by uniaxial stress". In: *Physica E: Low-dimensional Systems and Nanostructures* 32.1 (2006). Publisher: Elsevier, pp. 14–16. URL: https://www.sciencedirect.com/science/article/pii/S1386947705004418 (visited on 10/10/2023) (cit. on p. 27).

[162] Stefan Seidl, Martin Kroner, Alexander Högele, Khaled Karrai, Richard J. Warburton, Antonio Badolato, and Pierre M. Petroff. "Effect of uniaxial stress on excitons in a self-assembled quantum dot". In: *Applied Physics Letters* 88.20 (2006). Publisher: AIP Publishing. URL: https://pubs.aip.org/aip/apl/article-abstract/88/20/203113/331527 (visited on 10/10/2023) (cit. on p. 27).

[163] P. Senellart, G. Solomon, and A. White. "High-performance semiconductor quantum-dot single-photon sources". In: *Nature Nanotech.* 12 (2017), pp. 1026–1039 (cit. on pp. 77, 102).

[164] Ranber Singh and Gabriel Bester. "Lower Bound for the Excitonic Fine Structure Splitting in Self-Assembled Quantum Dots". In: *Physical Review Letters* 104.19 (May 12, 2010), p. 196803. ISSN: 0031-9007, 1079-7114. DOI: 10.1103/PhysRevLett.104.196803. URL: https://link.aps.org/doi/10.1103/PhysRevLett.104.196803 (visited on 10/14/2023) (cit. on p. 27).

[165] Niccolo Somaschi, Valerian Giesz, Lorenzo De Santis, J. C. Loredo, Marcelo P. Almeida, Gaston Hornecker, S. Luca Portalupi, Thomas Grange, Carlos Anton, and Justin Demory. "Near-optimal single-photon sources in the solid state". In: *Nature Photonics* 10.5 (2016). Publisher: Nature Publishing Group UK London, pp. 340–345 (cit. on pp. 38, 47, 76, 128).

[166] Nicolo Spagnolo, Chiara Vitelli, Marco Bentivegna, Daniel J. Brod, Andrea Crespi, Fulvio Flamini, Sandro Giacomini, Giorgio Milani, Roberta Ramponi, and Paolo Mataloni. “Experimental validation of photonic boson sampling”. In: *Nature Photonics* 8.8 (2014). Publisher: Nature Publishing Group UK London, pp. 615–620. URL: https://www.nature.com/articles/nphoton.2014.135 (visited on 12/07/2023) (cit. on p. 2).

[167] Clemens Spinnler, Giang N. Nguyen, Ying Wang, Liang Zhai, Alisa Javadi, Marcel Erbe, Sven Scholz, Andreas D. Wieck, Arne Ludwig, Peter Lodahl, Leonardo Midolo, and Richard J. Warburton. *A single-photon emitter coupled to a phononic-crystal resonator in the resolved-sideband regime*. Nov. 9, 2023. arXiv: 2311.05342[cond-mat,physics:physics,physics:quant-ph]. URL: http://arxiv.org/abs/2311.05342 (visited on 12/11/2023) (cit. on p. 131).

[168] J. B. Spring, B. J. Metcalf, P. C. Humphreys, W. S. Kolthammer, X.-M. Jin, M. Barbieri, A. Datta, N. Thomas-Peter, N. K. Langford, D. Kundys, J. C. Gates, B. J. Smith, P. G. R. Smith, and I. A. Walmsley. “Boson Sampling on a Photonic Chip”. In: *Science* 339.6121 (Feb. 15, 2013), pp. 798–801. ISSN: 0036-8075, 1095-9203. DOI: 10.1126/science.1231692. URL: https://www.sciencemag.org/lookup/doi/10.1126/science.1231692 (visited on 12/07/2023) (cit. on p. 2).

[169] Kartik Srinivasan and Oskar Painter. “Linear and nonlinear optical spectroscopy of a strongly coupled microdisk–quantum dot system”. In: *Nature* 450.7171 (2007). Publisher: Nature Publishing Group UK London, pp. 862–865. URL: https://www.nature.com/articles/nature06274 (visited on 10/30/2023) (cit. on p. 35).

[170] P. Stepanov, A. Delga, N. Gregersen, E. Peinke, M. Munsch, J. Teissier, J. Mørk, M. Richard, J. Bleuse, J.-M. Gérard, and J. Claudon. “Highly directive and Gaussian far-field emission from ‘giant’ photonic trumpets”. In: *Appl. Phys. Lett.* 107 (2015), p. 141106 (cit. on p. 78).

[171] P. Stepanov, M. Elzo-Aizarna, J. Bleuse, N. S. Malik, Y. Curé, E. Gautier, V. Favre-Nicolin, J.-M. Gérard, and J. Claudon. “Large and Uniform Optical Emission Shifts in Quantum Dots Strained along Their Growth Axis”. In: *Nano Lett.* 16 (2016), pp. 3215–3220 (cit. on pp. 83, 125).

[172] R. Mark Stevenson, Andrew J. Hudson, Anthony J. Bennett, Robert J. Young, Christine A. Nicoll, David A. Ritchie, and Andrew J. Shields. “Evolution of entanglement between distinguishable light states”. In:

*Physical review letters* 101.17 (2008). Publisher: APS, p. 170501 (cit. on p. 19).

[173] Damien Stucki, Nicolas Gisin, Olivier Guinnard, Grégoire Ribordy, and Hugo Zbinden. "Quantum key distribution over 67 km with a plug&play system". In: *New Journal of Physics* 4.1 (2002). Publisher: IOP Publishing, p. 41. URL: https://iopscience.iop.org/article/10.1088/1367-2630/4/1/341/meta (visited on 12/07/2023) (cit. on p. 2).

[174] Shuntaro Takeda and Akira Furusawa. "Toward large-scale fault-tolerant universal photonic quantum computing". In: *APL Photonics* 4.6 (2019). Publisher: AIP Publishing. URL: https://pubs.aip.org/aip/app/article-abstract/4/6/060902/123159 (visited on 12/07/2023) (cit. on p. 2).

[175] J. Teissier, A. Barfuss, P. Appel, E. Neu, and P. Maletinsky. "Strain Coupling of a Nitrogen-Vacancy Center Spin to a Diamond Mechanical Oscillator". In: *Phys. Rev. Lett.* 113 (2014), p. 020503 (cit. on p. 102).

[176] H. Thyrrestrup, G. Kiršanskė, H. Le Jeannic, T. Pregnolato, L. Zhai, L. Raahauge, L. Midolo, N. Rotenberg, A. Javadi, R. Schott, A. D. Wieck, A. Ludwig, M. C. Löbl, I. Söllner, R. J. Warburton, and P. Lodahl. "Quantum Optics with Near-Lifetime-Limited Quantum-Dot Transitions in a Nanophotonic Waveguide". In: *Nano Lett.* 18 (2018), pp. 1801–1806 (cit. on p. 77).

[177] Y. Tian, P. Navarro, and M. Orrit. "Single Molecule as a Local Acoustic Detector for Mechanical Oscillators". In: *Phys. Rev. Lett.* 113 (2014), p. 135505 (cit. on p. 102).

[178] Max Tillmann, Borivoje Dakić, René Heilmann, Stefan Nolte, Alexander Szameit, and Philip Walther. "Experimental boson sampling". In: *Nature photonics* 7.7 (2013). Publisher: Nature Publishing Group UK London, pp. 540–544. URL: https://www.nature.com/articles/nphoton.2013.102 (visited on 12/07/2023) (cit. on p. 2).

[179] Natasha Tomm, Alisa Javadi, Nadia Olympia Antoniadis, Daniel Najer, Matthias Christian Löbl, Alexander Rolf Korsch, Rüdiger Schott, Sascha René Valentin, Andreas Dirk Wieck, and Arne Ludwig. "A bright and fast source of coherent single photons". In: *Nature Nanotechnology* 16.4 (2021). Publisher: Nature Publishing Group UK London, pp. 399–403 (cit. on pp. 38, 47).

[180] P. Treutlein, C. Genes, K. Hammerer, M. Poggio, and P. Rabl. “Cavity Optomechanics”. In: ed. by M. Aspelmeyer, T. J. Kippenberg, and F. Marquardt. Berlin: Springer, 2014. Chap. Hybrid Mechanical Systems (cit. on p. 101).

[181] R. Trivedi, K. A. Fischer, J. Vučković, and K. Müller. “Generation of Non-Classical Light Using Semiconductor Quantum Dots”. In: *Adv. Quantum Technol.* 3 (2020), p. 1900007 (cit. on p. 77).

[182] R. Trotta, J. Martín-Sánchez, J. S. Wildmann, G. Piredda, M. Reindl, C. Schimpf, E. Zallo, S. Stroj, J. Edlinger, and A. Rastelli. “Wavelength-tunable sources of entangled photons interfaced with atomic vapours”. In: *Nat. Commun.* 7 (2016), p. 10375 (cit. on p. 77).

[183] R. Trotta, E. Zallo, C. Ortix, P. Atkinson, J. D. Plumhof, J. Van Den Brink, A. Rastelli, and O. G. Schmidt. “Universal Recovery of the Energy-Level Degeneracy of Bright Excitons in InGaAs Quantum Dots without a Structure Symmetry”. In: *Physical Review Letters* 109.14 (Oct. 1, 2012), p. 147401. ISSN: 0031-9007, 1079-7114. DOI: `10.1103/PhysRevLett.109.147401`. URL: `https://link.aps.org/doi/10.1103/PhysRevLett.109.147401` (visited on 10/14/2023) (cit. on pp. 27, 97, 129).

[184] Rinaldo Trotta, Javier Martín-Sánchez, Johannes S. Wildmann, Giovanni Piredda, Marcus Reindl, Christian Schimpf, Eugenio Zallo, Sandra Stroj, Johannes Edlinger, and Armando Rastelli. “Wavelength-tunable sources of entangled photons interfaced with atomic vapours”. In: *Nature Communications* 7.1 (Jan. 27, 2016). Number: 1 Publisher: Nature Publishing Group, p. 10375. ISSN: 2041-1723. DOI: `10.1038/ncomms10375`. URL: `https://www.nature.com/articles/ncomms10375` (visited on 10/11/2023) (cit. on pp. 27, 28, 128).

[185] Rinaldo Trotta, Johannes S. Wildmann, Eugenio Zallo, Oliver G. Schmidt, and Armando Rastelli. “Highly Entangled Photons from Hybrid Piezoelectric-Semiconductor Quantum Dot Devices”. In: *Nano Letters* 14.6 (June 11, 2014), pp. 3439–3444. ISSN: 1530-6984, 1530-6992. DOI: `10.1021/nl500968k`. URL: `https://pubs.acs.org/doi/10.1021/nl500968k` (visited on 10/11/2023) (cit. on p. 128).

[186] Rinaldo Trotta, Eugenio Zallo, Elisabeth Magerl, Oliver G. Schmidt, and Armando Rastelli. “Independent control of exciton and biexciton energies in single quantum dots via electroelastic fields”. In: *Physical Review B* 88.15 (Oct. 15, 2013). Publisher: American Physical Society, p. 155312. DOI: `10.1103/PhysRevB.88.155312`. URL: `https://`

link.aps.org/doi/10.1103/PhysRevB.88.155312 (visited on 10/13/2023) (cit. on p. 27).

[187] Ming-Fu Tsai, Hsuan Lin, Chia-Hsien Lin, Sheng-Di Lin, Sheng-Yun Wang, Ming-Cheng Lo, Shun-Jen Cheng, Ming-Chih Lee, and Wen-Hao Chang. “Diamagnetic Response of Exciton Complexes in Semiconductor Quantum Dots”. In: *Physical Review Letters* 101.26 (Dec. 24, 2008), p. 267402. ISSN: 0031-9007, 1079-7114. DOI: 10.1103/PhysRevLett.101.267402. URL: https://link.aps.org/doi/10.1103/PhysRevLett.101.267402 (visited on 10/11/2023) (cit. on p. 25).

[188] D. Tumanov, N. Vaish, H. A. Nguyen, Y. Curé, J.-M. Gérard, J. Claudon, F. Donatini, and Poizat J.-Ph. “Static strain tuning of quantum dots embedded in a photonic wire”. In: *Appl. Phys. Lett.* 112 (2018), p. 123102 (cit. on p. 78).

[189] Leslie G. Valiant. “The complexity of computing the permanent”. In: *Theoretical computer science* 8.2 (1979). Publisher: Elsevier, pp. 189–201. URL: https://www.sciencedirect.com/science/article/pii/0304397579900446 (visited on 12/07/2023) (cit. on p. 2).

[190] A. Vasanelli, R. Ferreira, and G. Bastard. “Continuous Absorption Background and Decoherence in Quantum Dots”. In: *Physical Review Letters* 89.21 (Nov. 4, 2002). Publisher: American Physical Society, p. 216804. DOI: 10.1103/PhysRevLett.89.216804. URL: https://link.aps.org/doi/10.1103/PhysRevLett.89.216804 (visited on 10/04/2023) (cit. on p. 21).

[191] O. Verzelen, R. Ferreira, and G. Bastard. “Polaron lifetime and energy relaxation in semiconductor quantum dots”. In: *Physical Review B* 62.8 (Aug. 15, 2000), R4809–R4812. ISSN: 0163-1829, 1095-3795. DOI: 10.1103/PhysRevB.62.R4809. URL: https://link.aps.org/doi/10.1103/PhysRevB.62.R4809 (visited on 11/30/2023) (cit. on p. 23).

[192] Y. A. Vlasov, M. O’Boyle, H. F. Hamann, and S. J. McNab. “Active control of slow light on a chip with photonic crystal waveguides”. In: *Nature* 438 (2005), pp. 65–69 (cit. on p. 40).

[193] A. Vogele, M. M. Sonner, B. Mayer, X. Yuan, M. Weiß, E. D. S. Nysten, S. F. Covre da Silva, A. Rastelli, and H. J. Krenner. “Quantum Dot Optomechanics in Suspended Nanophononic Strings”. In: *Adv. Quantum Technol.* 3 (2020), p. 1900102 (cit. on pp. 102, 125).

[194] I. Vurgaftman, J. R. Meyer, and L. R. Ram-Mohan. “Band parameters for III–V compound semiconductors and their alloys”. In: *J. Appl. Phys.* 89 (2001), pp. 5815–5875 (cit. on pp. 83, 125).

[195] H. Wang, H. Hu, T.-H. Chung, J. Qin, X. Yang, J.-P. Li, R.-Z. Liu, H.-S. Zhong, Y.-M. He, X. Ding, Y.-H. Deng, Q. Dai, Y.-H. Huo, S. Höfling, C.-Y. Lu, and J.-W. Pan. "On-Demand Semiconductor Source of Entangled Photons Which Simultaneously Has High Fidelity, Efficiency, and Indistinguishability". In: *Phys. Rev. lett.* 122 (2019), p. 113602 (cit. on p. 77).

[196] Hui Wang, Yu-Ming He, T.-H. Chung, Hai Hu, Ying Yu, Si Chen, Xing Ding, M.-C. Chen, Jian Qin, and Xiaoxia Yang. "Towards optimal single-photon sources from polarized microcavities". In: *Nature Photonics* 13.11 (2019). Publisher: Nature Publishing Group UK London, pp. 770–775 (cit. on p. 47).

[197] Hui Wang, Hai Hu, T.-H. Chung, Jian Qin, Xiaoxia Yang, J.-P. Li, R.-Z. Liu, H.-S. Zhong, Y.-M. He, Xing Ding, Y.-H. Deng, Qing Dai, Y.-H. Huo, Sven Höfling, Chao-Yang Lu, and Jian-Wei Pan. "On-Demand Semiconductor Source of Entangled Photons Which Simultaneously Has High Fidelity, Efficiency, and Indistinguishability". In: *Physical Review Letters* 122.11 (Mar. 22, 2019), p. 113602. ISSN: 0031-9007, 1079-7114. DOI: `10.1103/PhysRevLett.122.113602`. URL: `https://link.aps.org/doi/10.1103/PhysRevLett.122.113602` (visited on 10/30/2023) (cit. on p. 37).

[198] Bi-Ying Wang, Emil V. Denning, Uğur Meriç Gür, Chao-Yang Lu, and Niels Gregersen. "Micropillar single-photon source design for simultaneous near-unity efficiency and indistinguishability". In: *Physical Review B* 102.12 (2020). Publisher: APS, p. 125301 (cit. on p. 47).

[199] M. Weiß, D. Wigger, M. Nägele, K. Müller, J. J. Finley, T. Kuhn, P. Machnikowski, and H. J. Krenner. "Optomechanical wave mixing by a single quantum dot". In: *Optica* 8 (2021), pp. 291–300 (cit. on pp. 102, 126).

[200] I. Wilson-Rae, P. Zoller, and A. Imamoğlu. "Laser Cooling of a Nanomechanical Resonator Mode to its Quantum Ground State". In: *Phys. Rev. Lett.* 92 (2004), p. 075507 (cit. on pp. 102, 126).

[201] X. Wu, X. Dou, K. Ding, P. Zhou, H. Ni, Z. Niu, D. Jiang, and B. Sun. "In situ tuning the single photon emission from single quantum dots through hydrostatic pressure". In: *Appl. Phys. Lett.* 103 (2013), p. 252108 (cit. on p. 77).

[202] E. Yablonovitch. "Photonic band-gap crystals". In: *Journal of Physics: Condensed Matter* 5.16 (1993). Publisher: IOP Publishing, p. 2443. URL: `https://iopscience.iop.org/article/10.1088/0953-8984/5/16/004/meta` (visited on 11/28/2023) (cit. on p. 31).

[203] Beimeng Yao, Rongbin Su, Yuming Wei, Zhuojun Liu, Tianming Zhao, and Jin Liu. “Design for hybrid circular Bragg gratings for a highly efficient quantum-dot single-photon source”. In: *Journal of the Korean Physical Society* 73 (2018). Publisher: Springer, pp. 1502–1505 (cit. on p. 47).

[204] I. Yeo, P.-L. de Assis, A. Gloppe, E. Dupont-Ferrier, P. Verlot, N. S. Malik, E. Dupuy, J. Claudon, J.-M. Gérard, A. Auffèves, G. Nogues, S. Seidelin, J.-Ph. Poizat, O. Arcizet, and M. Richard. “Strain-mediated coupling in a quantum dot-mechanical oscillator hybrid system”. In: *Nature Nanotech.* 9 (2014), pp. 106–110 (cit. on p. 102).

[205] Liang Zhai, Matthias C. Löbl, Giang N. Nguyen, Julian Ritzmann, Alisa Javadi, Clemens Spinnler, Andreas D. Wieck, Arne Ludwig, and Richard J. Warburton. “Low-noise GaAs quantum dots for quantum photonics”. In: *Nature Communications* 11.1 (Sept. 21, 2020). Number: 1 Publisher: Nature Publishing Group, p. 4745. ISSN: 2041-1723. DOI: `10.1038/s41467-020-18625-z`. URL: `https://www.nature.com/articles/s41467-020-18625-z` (visited on 10/11/2023) (cit. on pp. 26, 27, 128).

[206] Xiaoyan Zhou, Liang Zhai, and Jin Liu. “Epitaxial quantum dots: a semiconductor launchpad for photonic quantum technologies”. In: *Photonics Insights* 1.2 (2023). Publisher: Society of Photo-Optical Instrumentation Engineers, R07–R07. URL: `https://www.spiedigitallibrary.org/journals/photonics-insights/volume-1/issue-2/R07/Epitaxial-quantum-dots--a-semiconductor-launchpad-for-photonic-quantum/10.3788/PI.2022.R07.short` (visited on 12/08/2023) (cit. on p. 3).